

October 2021

RADICAL POLYMERIZATION: CHEMISTRIES, APPLICATIONS, DEVELOPMENTS, AND PERSPECTIVES

Yifeng Du
University of Massachusetts Amherst

Follow this and additional works at: https://scholarworks.umass.edu/dissertations_2

Recommended Citation

Du, Yifeng, "RADICAL POLYMERIZATION: CHEMISTRIES, APPLICATIONS, DEVELOPMENTS, AND PERSPECTIVES" (2021). *Doctoral Dissertations*. 2307.
<https://doi.org/10.7275/24597547> https://scholarworks.umass.edu/dissertations_2/2307

This Open Access Dissertation is brought to you for free and open access by the Dissertations and Theses at ScholarWorks@UMass Amherst. It has been accepted for inclusion in Doctoral Dissertations by an authorized administrator of ScholarWorks@UMass Amherst. For more information, please contact scholarworks@library.umass.edu.

University of Massachusetts Amherst

ScholarWorks@UMass Amherst

Doctoral Dissertations

Dissertations and Theses

**RADICAL POLYMERIZATION: CHEMISTRIES, APPLICATIONS,
DEVELOPMENTS, AND PERSPECTIVES**

Yifeng Du

Follow this and additional works at: https://scholarworks.umass.edu/dissertations_2

**RADICAL POLYMERIZATION: CHEMISTRIES, APPLICATIONS,
DEVELOPMENTS, AND PERSPECTIVES**

A Dissertation Presented

by

YIFENG DU

Submitted to the Graduate School of the
University of Massachusetts Amherst in partial fulfillment
of the requirements for the degree of

DOCTOR OF PHILOSOPHY

September 2021

Polymer Science and Engineering

© Copyright by Yifeng Du 2021

All Rights Reserved

**RADICAL POLYMERIZATION: CHEMISTRIES, APPLICATIONS,
DEVELOPMENTS, AND PERSPECTIVES**

A Dissertation Presented

by

YIFENG DU

Approved as to style and content by:

E. Bryan Coughlin, Chair

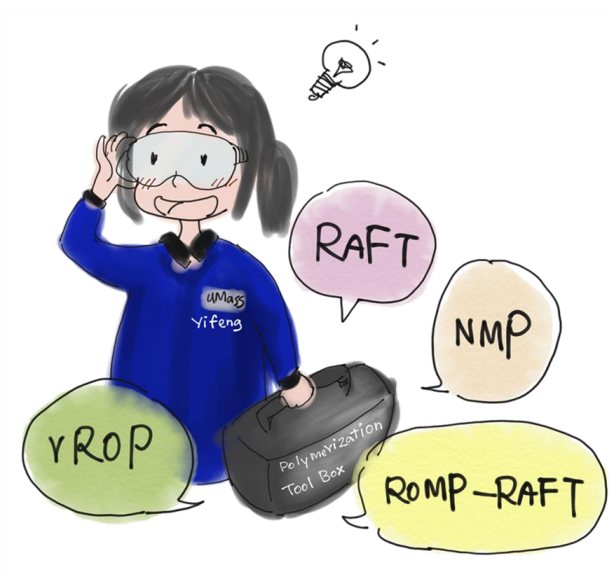
Jessica D. Schiffman, Member

Thomas J. McCarthy, Member

David A. Hoagland, Department Head
Polymer Science and Engineering

DEDICATION

To Yifeng's unique journey and to her beloved family.



ACKNOWLEDGMENTS

First and foremost, I express my deepest appreciation to my advisor, Professor E. Bryan Coughlin. Bryan is a great research advisor and a kind mentor who trained me with all professional skills and scientific attitude to become a scientist today from a curious naive student in 2016. Bryan always says humbly, “we are collaborators”. I am very glad that we were indeed able to expand our advisor-student relationship into an official academia-industry collaboration, and I can continue learning from someone that I look up to after my graduation.

I would like to thank my current committee members, Professors Jessica Schiffman, Tom McCarthy, and my former committee member, Professor Ryan Hayward. I am appreciative for the time and effort you spent on evaluating my science. I have thoroughly enjoyed our discussions. Your insightful comments, questions and inter-disciplinary perspectives left meaningful impact upon my graduate-school learning.

It’s my great pleasure and honor to be able to work with several exceptional scientists. I would like to thank all my collaborators, who exposed me with polymer physics and engineering knowledge and inspired me to become a better scientist. Dr. Austin Barnes and Professor Steve Buratto (UCSB) helped me with AFM and EFM characterization on ionomer membranes. Nora Buggy, Mei-Chen Kuo and Prof. Andrew Herring (Colorado School of Mines) supported me with comprehensive characterization with ionomer membranes for their application performance evaluations. Dr. Zoey X. Meng, Professors Jessica Schiffman and Sarah Perry (UMass) used the polyelectrolytes from our lab to make coacervate and studied the rheology and electrospinning properties. Dr. Weiguo Hu

provided enormous support with my DOSY experiments. The core team members for the collaborative project about rROP include Dr. Stefano Lazzari, Dr. Tom Holcombe, Dr. Rupert Konradi, Dr. Liqun Ren, Dr. Yang Yang (BASF), Helen Y. Du and Bryan (UMass). They are the best mentors and collaborators who offered me great support during my early career in BASF.

I hope to thank the Coughlin group. Throughout the first three years of my graduate-school, I have been surrounded by awesome groupmates. In the past two years I spent in Shanghai, China, I also managed to keep contact with the group via Zoom, got to know and shared fun with new members. I would like to thank Dr. Pirl Ertem, Dr. Wenxu Zhang, Dr. Haomiao Yuan, Dr. Rohit Gupta, Dr. Chinomso Nwosu, Dr. Joshua Enokida, Dr. Huyen Vu, Ria Ghosh, Roshni Chethalen, Anne Radzanowski and Helen Du.

I appreciate the time I spent with the Class of 2016 as we traveled this journey together and shared many difficulties and accomplishments. I would like to thank my dear friends in Amherst and across the world, especially Min Zeng, Qingyang Sun, Xiayu Peng, Dr. Yangming Kou, Zihan Yang, Jingyu Sun, Lanxi Luo, Pei Xie, You Wu, Mark Ma and Yi Zhao. Toast to the good time we had together and also to the difficult time when I still have you all on my side.

Lastly, I would like to express my gratitude to my dear family, my dad, Mr. Dexiang Du and my mom, Ms. Ping Li. You are the best parents that you well preserved the curiosity in me from my childhood and carefully nurtured it to become the courage, passion and creativity towards life and science. I am lucky to have you and I hope that I can make you proud.

ABSTRACT

RADICAL POLYMERIZATION: CHEMISTRIES, APPLICATIONS, DEVELOPMENTS, AND PERSPECTIVES

SEPTEMBER 2021

YIFENG DU, B.S., FUDAN UNIVERSITY

M.S., UNIVERSITY OF MASSACHUSETTS AMHERST

Ph.D., UNIVERSITY OF MASSACHUSETTS AMHERST

Directed by: Professor E. Bryan Coughlin

Radical polymerization is one of most versatile and easily implemented chain-growth polymerization methods for obtaining polymers, copolymers and polymer composites. As a synthetic process with over seventy years of investigation, it has enabled the production of materials that enriched the daily lives of humankind. The polymerization mechanism involves the fundamental steps of initiation, propagation, and termination events. This radical-based synthetic route provides many advantages, such as the reaction conditions are usually not as demanding as ionic and coordination-insertion polymerizations regarding the tolerance of water, chemical functionalities and impurities. This polymerization technique can be applied to a wide variety of monomers.

The major challenge during the early development of controlled radical polymerization resulted from the presence of radical combination, atom transfer and abstraction reactions, which bring difficulties in understanding polymerization kinetics and achieving well-defined polymer structures. Thereby, industrial and academic effort has been focusing on developing techniques that offered the prospect of control over radical

polymerization. The seeds were laid for the major growth of controlled radical polymerization techniques in the 1990s. These approaches allow for the facile production of polymer architectures with complexities, from simple chains with narrow dispersity to di-block, tri-block and multi-block copolymers.

In Chapters 2 and 4 of this dissertation, radical addition fragmentation chain transfer (RAFT) polymerization was utilized to investigate well-defined polymer structures, enabling subsequent structure-property relationship investigations of polyelectrolyte solutions and multi-block copolymer membranes. In Chapter 3, nitroxide mediated polymerization (NMP) was performed to prepare polyisoprene that was successfully chain extended with chloromethyl styrene. The resulting diblock copolymer was quaternized for ionomer preparation. The analysis of their bulk as well as surface morphology was investigated.

Cyclic ketene acetals (CKA) can be polymerized through concomitant radical rearrangement and ring-opening mechanisms, to yield ester-based scission points on the resultant polymer backbone. An aliphatic and an aromatic CKAs were investigated in Chapter 5 to develop a fundamental understanding of CKA radical-mediated polymerization and charge transfer as a main competitive reaction.

Chapter 6 concludes on the areas of research and development that I believe will lead to further progress in the future.

PREFACE

The discovery of living anionic polymerization by Michael Szwarc in the 1950s has left significant impacts on polymer science.^{1,2} The development of ultra-high vacuum techniques to minimize moisture and air during the polymerization enabled the elimination of transfer and termination events during chain-growth polymerization. The technique was then quickly implemented in industry, enabling mass production of commercial products, such as well-defined block copolymer thermoplastic elastomers. While anionic polymerization was being discovered and developed, radical polymerization was already flourishing. Free radical polymerization was driven by technological progress and its commercialization preceded scientific understanding. For example, polystyrene and poly(methyl methacrylate) have been in commercial production before their polymerization process were understood. Since mid-1980s, understanding and exploitation of radical polymerization has begun to occur, including the mechanistic investigations of radical processes from Szwarc³⁻⁵ and a comprehensive theory of radical polymerization from other pioneering researchers.⁶⁻¹⁰

In spite of attempts to tune the overall polymerization rate,^{11,12} molecular weights and distributions essentially could not be controlled during free radical polymerization and the technique early on could not yield block copolymers. Another feature of conventional radical polymerizations results from the propagation mechanism. During a typical propagation step, sp^2 hybridized carbon radicals undergo successive addition to monomers, which leads to the formation of carbon-carbon bonds. As a result, C-C backbone-based polymers are obtained, which cannot easily bio-degrade in nature. As the biological and environmental fate of polymeric materials becomes a growing concern, the capability to

build biodegradable polymer portfolios has been recognized as one of the most significant aspects for radical polymerization technique development.

Following the earlier effect to confer livingness, controlled radical polymerization was first demonstrated in early 1990s, with a stable radical or a cobalt complex as the capping agents for the polymerizations of styrene and acrylate monomers, respectively.^{13,14} Based on the same principle of establishing a dynamic equilibrium between propagating radicals and dormant species, various living radical polymerization techniques have been developed, including nitroxide-mediated polymerization (NMP), stable free radical polymerization (SFRP), atom transfer radical polymerization (ATRP), degenerative transfer polymerization, reversible addition-fragmentation chain transfer (RAFT) polymerization, etc.¹⁵ In Chapters 2 and 4 of this dissertation, RAFT polymerization was investigated to achieve well-defined polymer structures, enabling subsequent structure-property relationship investigations of polyelectrolyte solutions and multi-block copolymer membranes. In Chapter 3, NMP was performed to overcome the sluggish polymerization rate of isoprene. The polyisoprene was successfully chain extended with chloromethyl styrene and the resulting block copolymer was quaternized for ionomer preparation. The analysis of their bulk as well as surface morphology was investigated.

Regarding bio-degradability concerns, radical ring-opening polymerization (rROP) provides a sustainable solution, where cyclic ketene acetals (CKA) can be polymerized through concomitant radical rearrangement and ring-opening mechanisms, to yield ester-based scission points on the resultant polymer backbone.¹⁶ An aliphatic and an aromatic CKAs were investigated in Chapter 5 to develop a fundamental understanding of CKA radical-mediated polymerization and charge transfer as a main competitive reaction.

References

- (1) SZWARC, M. 'Living' Polymers. *Nature* **1956**, 178 (4543), 1168–1169.
- (2) Szwarc, M.; Levy, M.; Milkovich, R. POLYMERIZATION INITIATED BY ELECTRON TRANSFER TO MONOMER. A NEW METHOD OF FORMATION OF BLOCK POLYMERS¹. *J. Am. Chem. Soc.* **1956**, 78 (11), 2656–2657.
- (3) Szwarc, M. Remarks on the Calculating Rates of Some Radical Reactions. *J. Chem. Phys.* **1951**, 19 (2), 256–257.
- (4) Szwarc, M. Reactions of Methyl Radicals and Their Applications to Polymer Chemistry. *J. Polym. Sci.* **1955**, 16 (82), 367–382.
- (5) Buckley, R. P.; Rembaum, A.; Szwarc, M. Methyl Affinities of Vinyl Monomers. Ethylene and Its Homologues. *J. Polym. Sci.* **1957**, 24 (105), 135–137.
- (6) Bagdasarian, H. S. *Theory of Radical Polymerization*; Akademii Nauk: Moscow, 1959.
- (7) Bamford, C. H. *The Kinetics of Vinyl Polymerization by Radical Mechanisms*; Academic Press: New York, 1958.
- (8) Walling, C. *Free Radicals in Solution*; Wiley, 1957.
- (9) Moad, G.; Solomon, D. H. *The Chemistry of Radical Polymerization*, 2nd ed.; Elsevier: Oxford, UK, 2006.
- (10) Davis, T. P.; Matyjaszewski, K. *Handbook of Radical Polymerization*; Wiley-

Interscience: Hoboken, 2002.

- (11) Boutevin, B.; Pietrasanta, Y. Telomerization. *Pergamon Press plc, Compr. Polym. Sci. Synth. Charact. React. Appl. Polym.* **1989**, *3*, 185–194.
- (12) Bengough, W. I.; Fairservice, W. H. Effects of Salts of Metals on Vinyl Polymerization. Part 1. Polymerization of Methyl Methacrylate in Presence of Cupric Chloride. *Trans. Faraday Soc.* **1965**, *61*, 1206–1215.
- (13) Georges, M. K.; Veregin, R. P. N.; Kazmaier, P. M.; Hamer, G. K. Narrow Molecular Weight Resins by a Free-Radical Polymerization Process. *Macromolecules* **1993**, *26* (11), 2987–2988.
- (14) Wayland, B. B.; Poszmik, G.; Mukerjee, S. L.; Fryd, M. Living Radical Polymerization of Acrylates by Organocobalt Porphyrin Complexes. *J. Am. Chem. Soc.* **1994**, *116* (17), 7943–7944.
- (15) Braunecker, W. A.; Matyjaszewski, K. Controlled/Living Radical Polymerization: Features, Developments, and Perspectives. *Prog. Polym. Sci.* **2007**, *32* (1), 93–146.
- (16) Tardy, A.; Nicolas, J.; Gimes, D.; Lefay, C.; Guillaneuf, Y. Radical Ring-Opening Polymerization: Scope, Limitations, and Application to (Bio) Degradable Materials. *Chem. Rev.* **2017**, *117*, 1319–1406.

TABLE OF CONTENTS

	Page
ACKNOWLEDGMENTS	v
ABSTRACT.....	vii
PREFACE.....	ix
LIST OF TABLES	xi
LIST OF FIGURES	xiii
LIST OF ABBREVIATIONS.....	xxi
CHAPTER 1 INTRODUCTION	24
1.1 Introduction to Ion-Containing Polymers	24
1.2 Polyelectrolytes and Ionomers	25
1.3 Polyelectrolyte Solution Properties and Applications	26
1.4 Ionomer Membranes and Applications in Clean Energy Devices	30
1.5 Synthetic Approaches for Degradable Functional Polymers	34
1.6 Dissertation Objectives	35
1.7 References	36
CHAPTER 2 USING DOSY TO INVESTIGATE THE DIFFUSION OF POLYELECTROLYTES IN SALT-FREE SOLUTIONS	54
2.1 Introduction.....	54
2.2 Experimental	56
2.2.1 Materials	56

2.2.2 Silicon-based CTA Synthesis	57
2.2.3 Styrene RAFT Polymerization with Si-based CTA or 2- cyano-2-propyl benzodithioate (CPBT).....	58
2.2.4 (Vinylbenzyl)trimethylammonium chloride (VBTMA) RAFT Polymerization with Si-based CTA	58
2.2.5 Block polyelectrolytes, P(EO- <i>b</i> -VBTMA), Synthesis.....	59
2.2.6 Characterization.	60
2.3 Results and Discussion	61
2.3.1 Silicon-based CTA Synthesis	61
2.3.2 Synthesis of Homo-Polyelectrolytes, PVBTMA, with Si- based CTA.	68
2.3.3 Synthesis of Block-Polyelectrolytes, P(EO- <i>b</i> -VBTMA).....	70
2.3.4 DOSY Characterization.	77
2.4 Conclusions.....	90
2.5 References.....	92

CHAPTER 3 NEUTRAL – CHARGED BLOCK COPOLYMER MEMBRANES:

BULK AND SURFACE MORPHOLOGY AND THE EFFECTS ON

CONNECTIVITY.....	97
3.1 Introduction.....	97
3.2 Experimental	100
3.2.1 Materials	100

3.2.2	Synthesis of Macro-Initiator, Polyisoprene– <i>N</i> -tert-Butyl- <i>N</i> - [1-diethylphosphono-(2,2-dimethylpropyl)]nitroxide (PIp–SG1), by NMP	100
3.2.3	Synthesis of Block Copolymers, Polyisoprene–Polychloromethylstyrene (PIp–PCMS).....	101
3.2.4	Polymer Quaternization	101
3.2.5	Partial Quaternization	102
3.2.6	Membrane Fabrication	102
3.2.7	Characterization	103
3.3	Results and Discussion	106
3.3.1	Polymer Synthesis.....	106
3.3.2	Quaternization Agent Effect on Morphology	109
3.3.3	Quaternization Level and Morphology	112
3.3.4	Bulk versus Surface Morphology with Various IECs	115
3.3.5	Humidity-Dependent Bulk Morphology Investigation.....	119
3.3.6	Humidity-Dependent Surface Morphology Investigation	121
3.3.7	Morphology Reversibility by Humidity Cycling.....	123
3.3.8	Effect of Surface Alignment on Ionic Domain Connectivity	124
3.4	Conclusions.....	135
3.5	References.....	137
CHAPTER 4 MULTI-BLOCK COPOLYMERS OF ISOPRENE AND CHLOROMETHYLSTYRENE SYNTHESIS AND CHARACTERIZATION.....		146
4.1	Introduction.....	146

4.2 Results and Discussion	149
4.2.1 Synthesis of Diblock Copolymer PIp- <i>b</i> -PCMS	149
4.2.2 Synthesis of Tri- and Penta-block Copolymers of Ip and CMS	151
4.2.3 Morphology Investigation of Multi-block Copolymers of Ip and CMS	158
4.3 Future Prospective	166
4.3.1 Mechanical Properties Characterization of the Multi-block Copolymers	166
4.3.2 Investigation on the Morphology of Charged-neutral Multi- block Copolymers	166
4.4 Reference	167
 CHAPTER 5 INVESTIGATION ON RADICAL RING-OPENING POLYMERIZATION AND CHARGE TRANFER OF CYCLIC KETENE ACETALS	
5.1 Introduction	172
5.2 Materials and Methods	174
5.3 Results and Discussion	177
5.4 Conclusion	188
5.5 Reference	189
 CHAPTER 6 CONCLUSIONS AND PERSPECTIVE	
6.1 Polyelectrolyte Coacervates in Electrospinning	194
6.2 Interactions in Polymer Composite Systems	195

6.3CKA Charge-Transfer versus Radical Co-Polymerization with Anhydride Containing Comonomers.....	196
6.4CKA Monomer Synthesis	196
6.5Reference	198
BIBLIOGRAPHY.....	202

LIST OF TABLES

Table	Page
Table 2. 1 PS molecular weights from ^1H NMR end-group analysis and GPC.....	67
Table 2. 2 Peak assignment from the PEO-OH ESI spectrum in Figure 2.5B	73
Table 2.3 Peak assignment from the PEO-CTA ESI spectrum in Figure 2.6B	75
Table 2. 4 PVBTMA ₁₂₁ D ₂ O solutions DOSY biexponential analysis.....	80
Table 2. 5 PVBTMA molecular weights, dispersity (D) and diffusion coefficients in 5 mg/ml D ₂ O solutions.....	80
Table 2. 6 P(EO ₄₆ - <i>b</i> -VBTMA) chemical compositions and diffusion coefficients of the PEO block.	85
Table 2. 7 P(EO- <i>b</i> -VBTMA) chemical compositions and diffusion coefficients of the PEO block.	88
Table 3. 1 Chemical composition and morphology of PIp- <i>b</i> -P(R ₃ P ⁺)MS synthesized by NMP.....	107
Table 4. 1 Chemical composition and morphology of diblock copolymer PIp- <i>b</i> -PCMS synthesized by NMP.	150
Table 4. 2 Chemical composition and morphology of triblock copolymer PCMS- <i>b</i> -PIp- <i>b</i> - PCMS.....	160

Table 4. 3 Chemical composition and morphology of pentablock copolymer PIp-b-PCMS-b-PIp-b-PCMS-b-PIp.	161
Table 4. 4 Chemical composition and morphology of triblock copolymer PIp-b-PCMS-b-PIp.	161
Table 4. 5 Chemical composition and morphology of pentablock copolymer PCMS-b-PIp-b-PCMS-b-PIp-b-PCMS.	162
Table 5. 1 the half-life time ($t_{(1/2)}$) of CKAs and optical bandgap values of the intermediates during the charge-transfer reactions between CKAs and unsaturated cyclic anhydrides in THF (0.5 mol/L).	186
Table 5. 2 Molecular weights and DP ratios of the copolymers of CKA and electron deficient comonomers.	188

LIST OF FIGURES

Figure	Page
Figure 1. 1 Depiction of (A) polyelectrolytes and (B) ionomers.....	25
Figure 1. 2 Sketch of a single-stranded RNA solution. Chain connectivity, charges on the polymer backbone, counterions, salt ions, excluded volume effects, hydrogen bonding, and the water solvent contribute to the polyelectrolyte behaviors.....	26
Figure 1. 3 Illustration of several dipole–dipole pairings responsible for polyelectrolyte aggregate formation. Red arrows denote dipoles formed by adsorbed counterions on the polymer backbone. u_0 is the magnitude of the average attractive energy between two adjacent dipoles in contact. N is the number of segments between two such physical cross-links.	28
Figure 1. 4 (A) Chemical structure of Nafion® and (B) proposed ionic channel models with various structures in Nafion® membranes.	31
Figure 1. 5 Schematic comparison of (A) a proton exchange membrane (PEM) and (B) an anion exchange membrane (AEM) used in fuel cells that are supplied with H ₂ and air.....	33
Figure 1. 6 Schematic of synthetic approaches for biodegradable polymers.	34
Figure 2. 1 (A) ESI mass spectrometry and (B) ¹ H NMR spectroscopy of Si-based CTA.	63

Figure 2. 2 Structure comparison of CTBT and Si-based CTA, ^1H NMR of PS polymerized by CPBT or Si-based CTA.	66
Figure 2. 3 GPC traces of PVBTMA.	69
Figure 2. 4 ^1H NMR of PEO-CTA.	71
Figure 2. 5 (A) MALDI-TOF of PEO-OH and (B) a close-up of the squared region of the mass spectrum in (A).	73
Figure 2. 6 (A) MALDI-TOF of PEO-CTA and (B) a close-up of the squared region of the mass spectrum in (A).	75
Figure 2. 7 GPC traces of P(EO-b-VBTMA) with different DPs of PEO and PVBTMA blocks.	77
Figure 2. 8 ^1H NMR of P(EO-b-PVBTMA).	77
Figure 2. 9 (A) ^1H NMR spectra, (B) DOSY spectrum by automatic Bayesian transform, and (C) biexponential fitting curve of peak integration vs. diffusion gradient strength from characteristic peaks a, b, and c from PVBTMA ₁₂₁ in D ₂ O, with the concentration of 5 mg/ml.	79
Figure 2. 10 Dependence of fast diffusion coefficient D_f (■) and slow diffusion coefficient D_s (●) on polyelectrolyte molecular weights. PVBTMA in D ₂ O, with concentration of 5 mg/ml.	81
Figure 2. 11 DOSY spectra of P(EO ₄₆ -b-VBTMA ₆₄).	82

Figure 2. 12 Schematic of PEO homopolymer and P(EO-*b*-VBTMA) neutral-block copolymer with the same PEO block and different molecular weights of the PVBTMA blocks. The “acceleration effect” from PVBTMA blocks on the fast-mode PEO blocks increases with the molecular weight.86

Figure 2. 13 Dependence of ***Df*** (■) and ***Ds*** (●) of P(EO₄₆-*b*-VBTMA), with the same DP_{PEO} = 46 and different DP_{PVBTMA}, = 0, 6, 20, 64, on molecular weights.
Acceleration ratio = Df – DPEO homopolymer / DPEO homopolymer × 100%.....87

Figure 2. 14 Dependence of ***Df*** (■) and ***Ds*** (●) of P(EO-*b*-VBTMA), with similar DP ratios of the PEO block versus the PVBTMA block, on molecular weights. The diffusion coefficient of the PEO macro-precursor, *DPEO homopolymer* (▲), was also plotted against the molecular weight of the corresponding P(EO-*b*-VBTMA) after chain extension.89

Figure 2. 15 Schematic of PEO homopolymer and P(EO-*b*-VBTMA) neutral-block copolymer with the same ***DP PEO / DPVBTMA*** and different molecular weights. The “acceleration effect” from PVBTMA as well as the “deceleration effect” from PEO on the fast-mode PEO blocks increases with the molecular weight.....90

Figure 3.1 ³¹P NMR spectra of two quaternization agents and AEM 19 after quaternization. (A) P(Ph(OMe)₃)₃ and (B) P(Ph)₃.....109

Figure 3.2 ¹ H NMR spectra of neutral block copolymer PIp- <i>b</i> -PCMS and neutral-charged block copolymer AEM 19 PIp- <i>b</i> -P(R ₃ P ⁺)MS, quaternized by P(Ph(OMe) ₃) ₃ and P(Ph) ₃ respectively.....	110
Figure 3.3 (A) SAXS comparison of AEM 16 quaternized by P(Ph(OMe) ₃) ₃ in black trace and P(Ph) ₃ in red trace. (B) Phase images of AEM 16 quaternized by P(Ph(OMe) ₃) ₃ and P(Ph) ₃ , respectively. Bright phase contrast is assigned to the hydrophilic domains.....	111
Figure 3.4 SAXS of (A) AEM 17 (B) AEM 18 and (C) AEM 19, quaternized by P(Ph(OMe) ₃) ₃ (black trace) and P(Ph) ₃ (red trace).	111
Figure 3.5 ¹ H NMR spectra, chemical composite and corresponding peak integration results of partially quaternized AEM 19 by P(Ph) ₃	113
Figure 3.6 (A) SAXS of un-quaternized and partially quaternized AEM 17. (B) Phase images of AEM 17 (i) 0.25_ <i>P</i> , (ii) 0.5_ <i>P</i> , (iii) 0.75_ <i>P</i> , and (iv) 1_ <i>P</i>	114
Figure 3.7 Cartoon illustration of d-spacing vs. QL dependency.	115
Figure 3.8 (A-C) SAXS, (D-F) TEM, and (G-I) AFM phase of AEM 13 (A, D, G), AEM 17 (B,E,H), AEM 18 (C,F,I). Dark contrast in TEM and AFM is the hydrophobic domains.....	118
Figure 3.10 SAXS of (A) AEM 13 and (B) AEM 19 under dry (black trace) and 95% RH (red trace). The dashed red lines mark the peak position shift between dry and 95% RH.....	119

Figure 3.9 SAXS of (A) AEM 17_0.25P and (B) AEM 17_IP, quaternized by P(Ph)₃, through three humidity cycles. Where the black traces were under dry conditions and red traces are under 95% RH.120

Figure 3.11 (A-I) Repulsive mode phase images of AEM 13 (A-C), AEM 16 (D-F), and AEM 19 (G-I) under 18% (A,D,G), 50% (B,E,H), and 80% RH (C,F,I).121

Figure 3.12 (A) Repulsive mode phase images of AEM 13 at a fixed scan area for 1 humidity cycle ranging from 50 – 80% RH. (A-i) the first scan at 50% RH. (A-ii) after 2 h exposure at 80% RH. (A-iii) after 2 h drying and equilibrated at 50% RH. (B) SAXS of AEM 13 for three humidity cycles for dry-95% RH-dry.123

Figure 3. 13 Bulk and surface morphology comparison of AEM 13 and 16. SAXS of (A) AEM 13 and (E) 16. Cross-sectional TEM of (B) AEM 13 and (F) 16, where dark contrast is from PIP domains. Repulsive mode phase images of (C) AEM 13 and (G) 16, where dark contrast corresponds to PIP domains. Radially-averaged power spectral density (PSD) of phase images of (D) AEM 13 and (H) 16.125

Figure 3. 14 Cartoons illustrating the proposed structure leading to variation in connectivity. The red cylinders represent the PIP phase, while blue represents the continuous ionic phase. (A) Parallel-aligned cylinders can either block surface charge migration or provide a connected path. (B) Perpendicularly aligned cylinders give rise to only connected ionic pathways.127

Figure 3. 15 (A) First pass repulsive-mode phase image of AEM 13. EFM images taken in the second pass at (B) $V_{EFM} = +5$ V and (C) $V_{EFM} = -5$ V sample bias. (D) Repulsive-mode phase image of AEM 16 taken in the first pass. EFM images during the second pass at (E) -5 V sample bias and (F) +5 V sample bias. Parabolic response of EFM phase as a function of $VEFM$ for two regions highlighted (G) in A-C of AEM 13 and (H) in D-F of AEM 16.129

Figure 3. 16 (I) Scatter plot of the linear fit term A vs. quadratic fit term B for several features of AEM 13 in black circles and AEM 16 in red circles. Inset shows a close-up of the scatter plot (I-i) AEM 13 and (I-ii) AEM 16. (II) Histogram of A/B data from (4I) for AEM 13 (gray) and AEM 16 (red).....133

Figure 4. 1 Phase diagram for melts of (A) AB diblock copolymers, (B) ABA triblock copolymers, and (C) infinite linear ABAB... multiblock copolymers. The ordered regions comprise of lamellar (L), cylindrical (C), bcc spherical (S), hcp spherical (S_{cp}), gyroid (G), and $Fddd$ (O^{70}) morphologies.147

Figure 4. 2 Typical looping and bridging illustration of ABA triblock copolymers in a (A) cylinder morphology and (B) lamellar morphology. (C) Bridging fractions of ABA triblock copolymers as a function of copolymer composition fA at $\chi N = 15, 20, 30$. The upper, middle, and lower curves correspond to the S, C, and L phases, respectively. The solid dots denote phase transitions, and the dotted lines are simply there to connect curves of the same χN . (Images adapted from Ref. 1 and 8.).....148

Figure 4. 3 (A) GPC traces and (B) ¹ H NMR of PIP-SG1 macro-initiator and PIP-b-PCMS.....	150
Figure 4. 4 (A) ¹ H NMR and (B) ESI mass spectra of difunctional CTA.	153
Figure 4. 5 GPC for (A) HSH-6, (B) SHSHS-1, (C) SHS-7 and (D) HSHSH-1.....	158
Figure 4. 6 ¹ H NMR for (A) HSH-6, (B) SHSHS-1, (C) SHS-7 and (D) HSHSH-1.....	158
Figure 4. 7 TEM for (A) HSH-6, (B) SHSHS-1, (C) SHS-7 and (D) HSHSH-1.	159
Figure 4. 8 SAXS for (A) SH-1, (B) SHS-8 and (C) SHSHS-1.	160
Figure 4. 9 SAXS for weak-segregation SHS samples.....	163
Figure 4. 10 SAXS for weak-segregation SHS-3 with small N and strong-segregation SHS-7 with large χ^N	164
Figure 4. 11 d-spacings D* as a function of composition f_A at a fixed $\chi^N=30$	165
Figure 5. 1 ¹ H NMR of (A) 5,6-benzo-2-(bromomethyl)-1,3-dioxepane and (B) BMDO.	179
Figure 5. 2 ¹ H NMR of (A) 2-(bromomethyl)-1,3,6-trioxocane and (B) MTC.	180
Figure 5. 3 Intermolecular acetal exchange leads to the formation of poly(acetal-ether). (A) ¹ H NMR and (B) GPC (polystyrene as the standards) of the resultant poly(acetal-ether).	180

Figure 5. 4 Kinetic characterization of the reactions between MTC and maleic anhydride by ¹ H NMR in 1 mol/L <i>d</i> -THF solution at 25 °C, the possible intermediate and decomposition products annotated.....	182
Figure 5. 5 Kinetic characterization of the reactions between MTC and (A) citraconic anhydride, (B) itaconic anhydride by ¹ H NMR in 1 mol/L <i>d</i> -THF solution at 25 °C.	183
Figure 5. 6 Kinetic ¹ H NMR of the reactions between BMDO and (A) maleic anhydride, (B) citraconic anhydride, and (C) itaconic anhydride in 1 mol/L <i>d</i> -THF solution at 25 °C.	184
Figure 5. 7 Real-time absorption characterization of the reactions between CKAs and unsaturated cyclic anhydrides.	185
Figure 6. 1 Chemical structures of polyelectrolytes used for methacryloyl-based coacervate preparation. Electrostatic interactions in coacervates can facilitate the formation of a continuous fiber jet during electrospinning.....	194
Figure 6. 2 Water absorption and crystallinity of polymer-silver composites were highly dependent on cation species.....	195
Figure 6. 3 CKA syntheses based on (A) carbonate route using triphosgene, ²⁰ (B) carbonate route using ethylchloroformate, ¹⁶ (C) ortho-ester pyrolysis ¹⁷ and (D) Pinner reaction. ¹⁹	198

LIST OF ABBREVIATIONS

°C	degree Celsius
\bar{D}	Molecular Weight Dispersity, M_w/M_n
δ	Chemical shift
χ	Flory-Huggins Parameter
AIBN	2,2'-Azobis(2-methylpropionitrile)
AEM	Anion Exchange Membrane
AFM	Atomic Force Microscope
CTA	Chain Transfer Agent
CKA	Cyclic Ketene Acetal
BMDO	5,6-Benzo-2-methylene-1,3-dioxepane
CPBT	2-Cyano-2-Propyl Benzodithioate
d-spacing	Domain Spacing
DCC	<i>N,N'</i> -Dicyclohexylcarbodiimide
DCM	Dichloromethane
D_f	Fast-Mode Diffusion Coefficient
DMAP	4-Dimethylaminopyridine
DME	Dimethyl Maleate
DMMAAnH	2,3-Dimethylmaleic Anhydride
DOSY	Diffusion-Ordered NMR Spectroscopy
DP	Degree of Polymerization
D_s	Slow-Mode Diffusion Coefficient
equiv.	Molar equivalent

EFM	Electrostatic Force Microscopy
ESI	Electrospray Ionization Mass Spectrometry
GPC	Gel Permeation Chromatography
IEC	Ion Exchange Capacity
ITDE	Dimethyl Itaconate
MALDI-TOF	Matrix-Assisted Laser Desorption/Ionization Time-Of-Flight Mass Spectrometry
M_n	Number Average Molecular Weight
mmol	Millimole
mol	Mole
MTC	2-Methylene-1,3,6-trioxocane
M_w	Weight Average Molecular Weight
NMR	Nuclear Magnetic Resonance Spectroscopy
NMP	Nitroxide Mediated Polymerization
<i>N</i> PhMI	<i>N</i> -Penylmaleimide
<i>N</i> PrMI	<i>N</i> -Propylmaleimide
PEO	Poly(Ethylene Oxide)
ppm	Parts Per Million
q	Scattering Wave Factor
RAFT	Reversible Addition-Fragmentation Chain Transfer
rROP	Radical Ring-Opening Polymerization
SAXS	Small Angle X-Ray Scattering
TEM	Transmission Electron Microscopy

T_g	Glass transition temperature
VBTMA	Vinylbenzyltrimethylammonium chloride

CHAPTER 1

INTRODUCTION

1.1 Introduction to Ion-Containing Polymers

Ion-containing polymers represent a broad class of materials. Natural ion-containing polymers have existed before life began. Basic life requires replicating charged polymers, polynucleotides, that contain information. Beyond these information-encrypting polymers, various organisms and their behaviors rely on versatile proteins, assembled from amino acids bearing charges. New bio-inspired synthetic ion-containing polymers are emerging from laboratories with novel properties, carrying on the responsibility of improving human health care and our planet's sustainability.

Because of the diversities of polymeric materials which contain ions a comprehensive classification can be difficult. For specific polymers containing quaternary ions, Hoover classified the system into ammonium, sulfonium, and phosphonium.¹ On a broader scope, Holliday divided the materials into networks, long covalent chains, short covalent chains, each category comprising sub-categories of organics, inorganics, hybrids, and polyelectrolytes.² Over the years, various categories have been proposed based on polymer characteristics of interest, such as ion contents (polyelectrolyte, ionomer), ionic group identities (polycation, polyanion, or polyzwitterion), and polymer backbone structures (inorganics, organics).³ The work presented in this chapter, and throughout the dissertation, will differentiate ion-containing polymers based on the ion content.

1.2 Polyelectrolytes and Ionomers

As demonstrated previously, polymers with one type of ion covalently bonded can be classified as two types: polyelectrolytes and ionomers.^{4,5} Historically, polymers with more than 15 mol% ionic moieties were termed as polyelectrolytes, while those containing a lower content of ionic moieties as ionomers.⁶⁻⁸ A depiction of a polyelectrolyte and an ionomer is shown in Figure 1.1A and 1.1B, respectively.

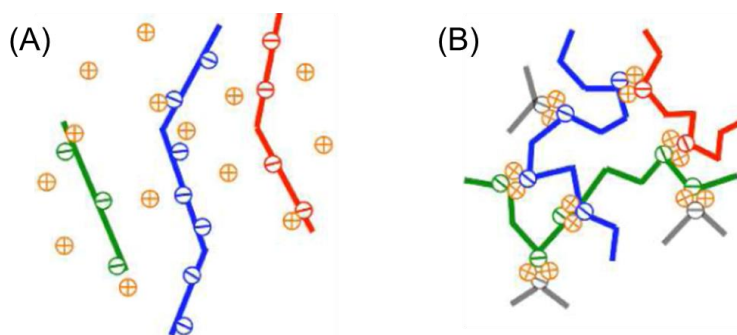


Figure 1. 1 Depiction of (A) polyelectrolytes and (B) ionomers.

(Image taken from reference ⁵)

Bulk polyelectrolytes usually exhibit extremely high glass transition temperatures (T_g) which limits their applications. Therefore, polyelectrolytes are usually dissolved in high-dielectric-constant solvents and investigated in solutions, where ion pairs can dissociate to some extent. As a result, the polyelectrolyte chains are highly charged and locally extended, as presented in Figure 1.1A.⁹

In contrast, an ionomer is essentially an ionized copolymer whose major component is a nonionic backbone and the minor component consists of ionic comonomers with associated counterions. Since neutral backbone materials usually have dielectric constants lower than ionic moieties, polar ionic groups tend to aggregate and overall dynamics of bulk ionomers can be strongly affected by those aggregates, as shown in Figure 1.1B.^{5,7}

1.3 Polyelectrolyte Solution Properties and Applications

In polyelectrolyte solutions, ionizable groups can dissociate, leaving charges on polymer backbones and releasing counterions in the solution, resulting in a multi-component system with polyions, counterions, co-ions, and solvent. An aqueous solution of single-stranded RNA with additional salt is present in Figure 1.2, as an example.¹⁰

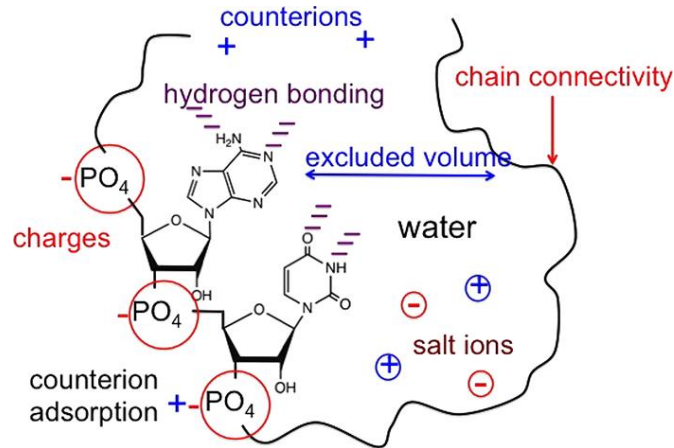


Figure 1. 2 Sketch of a single-stranded RNA solution. Chain connectivity, charges on the polymer backbone, counterions, salt ions, excluded volume effects, hydrogen bonding, and the water solvent contribute to the polyelectrolyte behaviors.

(Image taken from reference ¹⁰)

The collective effects from long-ranged electrostatic forces, hydrogen-bonding, dipolar interactions, *van der Waals* interactions, and chain connectivity in the system lead to unique properties, which are unseen in the neutral analogues.^{6,10} For example, (1) The crossover from dilute to semi-dilute solution regime occurs at much lower polymer concentrations in polyelectrolyte solutions than that in neutral polymers. Polyelectrolyte chains in the semi-dilute regime follow unentangled dynamics in a much broader concentration range and the crossover to the entangled dynamics occurs further away from

the chain overlap concentration, in comparison with solutions of uncharged polymers. (2) There is a well-pronounced peak, known as the polyelectrolyte peak, and enhanced intensity at near zero scattering angles in the light scattering of salt-free polyelectrolyte solutions, which was not observed in scattering profiles from neutral polymer solutions. If additional salt is present, the polyelectrolyte peak disappears, and the scattering is analogous to that of a neutral polymer solution. (3) The osmotic pressure of polyelectrolytes in salt-free solutions exceeds that of neutral polymers at similar polymer concentrations by several orders of magnitude. The osmotic pressure is independent of molecular weights but increases with polymer concentrations, which can be tuned with additional salts. (4) The viscosity of polyelectrolyte solutions is governed by the *Fuoss* law,¹¹ where the reduced viscosity is proportional to the square root of the polymer concentration, in contrast, a linear relationship was observed between the reduced viscosity and the polymer concentration for neutral polymer solutions. (5) Multiple dynamic modes exist in polyelectrolyte solutions, with various diffusion coefficients, whereas the diffusion behaviors of neutral polymer solutions are dictated by the *Stokes-Einstein* law.¹²⁻²⁶

These characteristic phenomena in polyelectrolyte solutions have been addressed by a variety of theoretical and simulation investigations. The theoretical studies on polyelectrolyte solutions mainly include scaling theories,⁹ field-theory-based analytical theories,²⁷ and liquid-state theories.^{28,29} The simulation efforts can be classified into two groups: (1) united-atom-based molecular dynamics, Brownian dynamics, Langevin dynamics, and Monte Carlo simulations,³⁰⁻³² focusing on the investigation of counterion condensation, osmotic pressure, electrostatic correlations, and complexation between oppositely charged polymers. (2) field-theoretic simulations, providing insights into the

formation of large-scale structures. Despite some contradictions in the field, it has been thought that the existence of polymer aggregates in polyelectrolyte solutions can have a great impact on their physical behaviors. As shown in Figure 1.3, a number of counterions can be adsorbed onto the charged backbone, leading to the formation of dipoles. The dipole-dipole interaction further results in the formation of quadrupoles. If several quadrupoles are formed between intermingling chains, the resultant net attractive forces can effectively compete against the electrostatic repulsion between the chains and polymer aggregates arise.³³

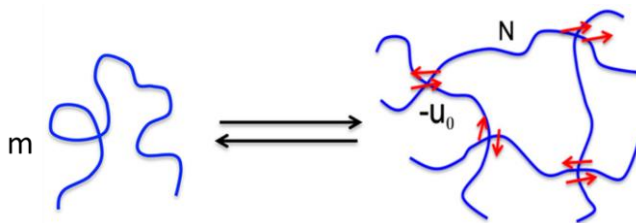


Figure 1. 3 Illustration of several dipole–dipole pairings responsible for polyelectrolyte aggregate formation. Red arrows denote dipoles formed by adsorbed counterions on the polymer backbone. u_0 is the magnitude of the average attractive energy between two adjacent dipoles in contact. N is the number of segments between two such physical cross-links.

(Image reproduced from reference ³³)

The developments of polyelectrolytes and their medical applications have dramatically improved the treatment of many diseases. By tailoring molecular structures, polymers can be created that interact with the external environment in a pre-programmed and intelligent manner. Environmentally responsive polyelectrolytes have possible applications in pharmaceutical preparations, since drug could be released in the human body when and where needed. One of the most widely investigated candidates are pH-

sensitive polymers, *e.g.* poly(methacrylic acid) and poly(acrylic acid), which have been used to prepare porous materials for drug delivery with adjustable release rates.³⁴⁻³⁶ Temperature responsive polymers are another widely studied system, mostly based on poly(*N*-isopropylacrylamide) (PNIPAAm) and derivatives. Because of the lower critical solution temperature (LCST) character of PNIPAAm, these polymer systems undergo a reversible volume phase transition with a change in the temperature. A variety of applications including drug delivery and tissue engineering of these thermo-sensitive polyelectrolytes have been investigated.^{37,38}

In addition to the physical environmental response, polyelectrolytes can have shield effects on specific cell antigens, which enables the application on cell surface engineering to create molecular camouflages.³⁹⁻⁴⁴ In a recent study, Tang and Wang *et al.* developed a new technique to engineer cell surfaces with polysialic acid-tyramine polyelectrolyte conjugates for the production of Rhesus D (RhD)-negative red blood cells. The technique can potentially be used for RhD-negative blood transfusion and transplantation medicines, which faces critical shortages in current clinical practice.⁴⁵

Another unique property of ion-containing polymers is anti-fouling which is gaining interest in different biotechnological applications.⁴⁶ It has been demonstrated that surface structure, hydrophilicity and charges are crucial factors on membrane fouling properties.⁴⁶⁻⁴⁸ Positively and negatively charged polyelectrolytes, as well as zwitterionic polymers, have been used as the surface modifiers to improve high flux and membrane antifouling properties.⁴⁹⁻⁵² For polyzwitterion coatings, the close proximity of oppositely charged groups facilitates the formation of hydrogen bonds with water molecules, resulting in an aqueous layer which resists the adsorption of organic and biological materials.^{53,54}

Polyelectrolyte coacervates formed from oppositely charged polymers have recently been investigated as an alternative means of addressing biological fouling.⁵⁵ It has been hypothesized that the positive and negative charges present in coacervates can mirror the functionality of polyelectrolytes, creating a barrier against bacterial attachment.^{53,54,56}

1.4 Ionomer Membranes and Applications in Clean Energy Devices

Ionomer structures and properties can be drastically affected by the incorporation of relatively low fractions of ions into nonionic backbones. The extent to which the properties are altered depends on various factors, including ion contents, the dielectric constant of the backbone, positions and types of ionic groups, the counterion, the degree of neutralization, etc.⁵⁷ In terms of polymer backbone structures, the most common studies on ionomers have focused on polyethylene (low T_g , semi-crystalline)⁵⁸⁻⁶¹ and polystyrene (high T_g , amorphous)⁶²⁻⁶⁶ backbones. Other backbones have also been explored to some extent, such as polyisoprene,^{67,68} polybutadiene,⁶⁹ poly(ethyl acrylate),⁷⁰ polyester,⁷¹ and polytetrafluoroethylene.^{72,73} The last is the basis of a unique ionomer developed by DuPont under the name Nafion[®], which has found extensive applications in fuel cells.

As mentioned in 1.1.1, due to the incompatibility between ions and the neutral backbone materials, ionic groups in ionomers can microphase-separate into nanoscale aggregates, usually referred to as “ion clusters” (Figure 1.1B). These structures can act as reversible physical crosslinks as well as a strong reinforcing filler dispersed in the backbone matrix. As a result, the ion clusters greatly affect the overall polymer behavior, accountable for the similarity of the thermo-mechanical properties of ionomers to block copolymers; improved mechanical strength, melt viscosity, and puncture/scratch

resistance.^{5,7,57} In the case of Nafion[®], considerable research effort has been devoted to exploring the morphology of hydrophilic and hydrophobic components of Nafion[®] in the solid state, in order to decipher its proton conduction properties. The nanophase morphological structure in Nafion[®] membranes has been demonstrated to be a significant factor, as the ion clusters can form “channels” with different configurations for water and ion transportation (Figure 1.4).^{74,75}

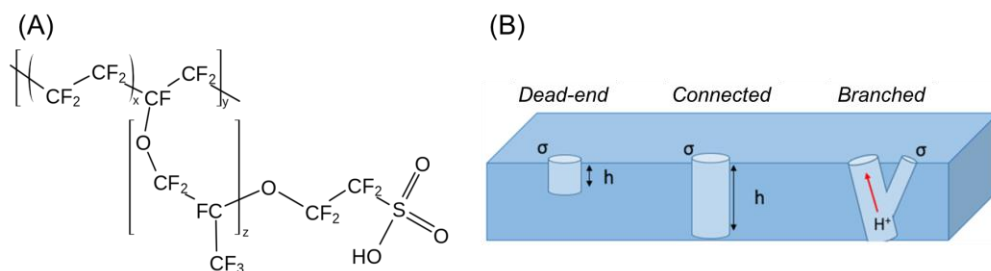


Figure 1. 4 (A) Chemical structure of Nafion[®] and (B) proposed ionic channel models with various structures in Nafion[®] membranes.

(Image reproduced from reference ⁷⁴)

Additionally, many other physical behaviors of ionomers can also be attributed to the formation of ion clusters. For example, the strong electrostatic interactions restrict polymer chain mobility, resulting in an increased T_g for the ionomer;^{65,70} at the melt state, the inhibited chain mobility leads to a characteristic plateau modulus, which is a consequence of the ion clusters acting as physical crosslinks between polymer chains, effectively increasing the polymer-polymer connectivity and prolonging their relaxation times.⁶⁶

The drastic property changes of polymeric materials resulting from the introduction of the *Coulombic* interaction bring an enormous range of applications of these materials. A comprehensive ion-containing polymer application review has been summarized by Eisenberg, including processing aids, modifiers, additives, etc.³ Despite the extensive

studies and publications in the field, herein, selective applications on bio-medicine and energy are discussed in this section.

Ionomers play an important role in energy storage and conversion technologies and have received significant research investment over the last few decades due to the increasing energy demands worldwide and the rising awareness on global warming, climate change, and environmental degradation. Robust reverse osmosis membranes can be formed from crosslinked sulfonated polymers for water treatment.^{76,77} Another application is seawater desalination by electrodialysis, which employs a current to drive ions out of a saline water stream. Electrodialysis membranes are typically composed of aminated or sulfonated crosslinked polystyrene, reinforced with hydrophobic polymers or inert mesh supports.⁷⁸

A broad class of ionomers with promising features have been created for proton exchange membranes (PEM) fuel cell development, as a promising alternative to conventional hydrocarbon fuel systems for transportation.⁷⁹ Poly(perfluorosulfonic acid) (PFSA)-based membranes, *e.g.*, Nafion[®], Aquivion[®] and 3M ionomer, are the leading materials in the field, because of the outstanding chemical resistance and proton conductivity. These perfluorinated polymers have pendent sulfonic acid groups that provide the membrane with moderate hydrophilicity and sufficient proton concentration to achieve high conductivity.^{75,80} New molecular designs for PFSA alternatives include aromatic polymers with poly(imide),^{81–84} poly(phenylene),^{85,86} poly(ketone),⁷⁶ and poly(sulfone).^{87,88} Those alternative ionomer membranes have undergone extensive device testing in a research environment, however, wide-scale commercialization has not yet been achieved.

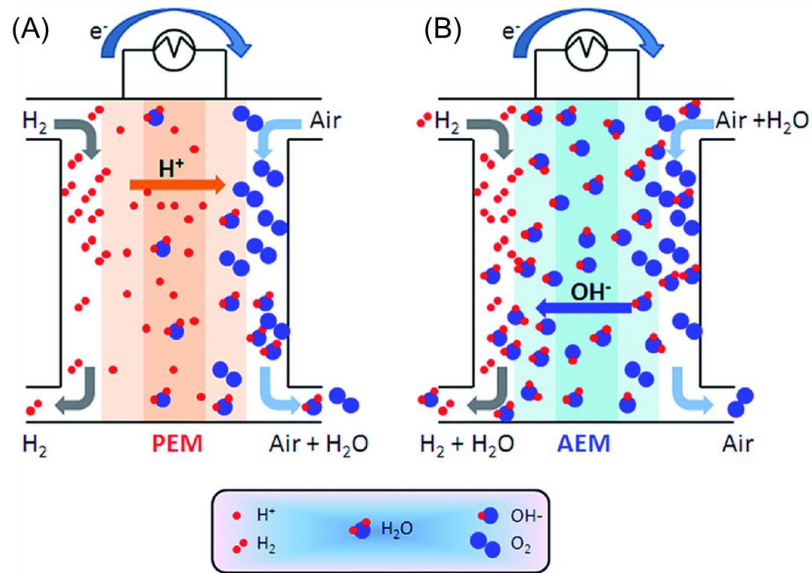


Figure 1. 5 Schematic comparison of (A) a proton exchange membrane (PEM) and (B) an anion exchange membrane (AEM) used in fuel cells that are supplied with H₂ and air.

(Image taken from reference ⁷⁹)

A counterpart to PEM materials are anion exchange membrane (AEM) polymers with tethered cationic groups. The electrochemical reactions for fuel cell operation are performed in an alkaline environment, which enables the use of non-platinum-group metal (non-PGM) catalysts.⁸⁹⁻⁹¹ The United States space programs played a predominant role in AEM fuel cells development. NASA successfully equipped the Gemini (1963) and Apollo (1968) spaceships with alkaline fuel cells, because of a more efficient electrolyte than PEM fuel cells.⁹²

1.5 Synthetic Approaches for Degradable Functional Polymers

The biological and environmental fate of polymeric materials has been a significant concern of humankind and the ability for polymers to break down to benign products after use has become increasingly important. Therefore, biodegradable polymer syntheses and certain chemical functionality have received growing research interest. With versatile synthesis routes, desired biodegradability can be embedded with desired characteristics for various applications (Figure 1.6).⁹³

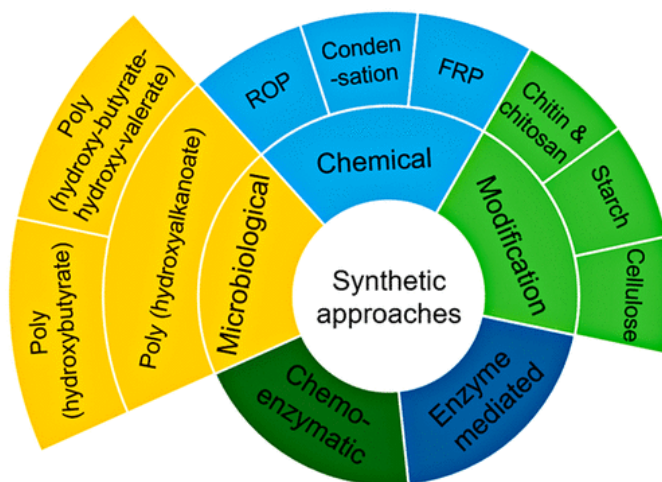


Figure 1. 6 Schematic of synthetic approaches for biodegradable polymers.

(Image taken from reference ⁹³)

As demonstrated in Figure 1.6, polyhydroxyalkanoates (PHA) are biopolyesters that accumulate in microorganisms as an energy source.^{94,95} In the versatile PHAs family, poly(hydroxybutyrate) (PHB) is the most prominent member and can be found in estuarine microflora,⁹⁶ soil bacteria,⁹⁷ blue-green algae,⁹⁸ microbially treated sewage,⁹⁹ etc. The first isolation and characterization of PHB, poly(3-hydroxybutyrate) in *Bacillus megaterium*, were performed by Lemoigne in 1925, which denoted the first discovery of PHA in history.¹⁰⁰ Years later, extensive research has been conducted to investigate

microbiological approaches for functional PHA synthesis.¹⁰¹ Chemo-enzymatic and enzyme mediated methods have been developed which combines conventional polymerization with an efficient enzymatic approach.^{102,103} Natural polymers are a readily biodegradable platform which can be functionalized via various chemical modifications, such as hydroxylation, alkylation, sulfonation, nitration, acylation, phosphorylation, thiolation, xanthation, quaternization, and graft copolymerization.^{104–110} Intensive chemical synthetic effort has been dedicated to polymer backbones resembling natural materials, which are usually with ester, amide, and peptide degradable groups. Ring-opening polymerization (ROP) of lactones, such as caprolactone and lactide,^{111–113} is one of the most versatile methods for the synthesis of major groups of biopolymers to procure products in large quantities. Ring-opening metathesis polymerization (ROMP) can be used to prepare degradable functional polymers. Degradable linkages including acetal, disulfide, ester, etc, can be incorporated onto the backbone with tunable degradation kinetics.^{114–122} Radical ring-opening polymerization (rROP) of cyclic ketene acetals (CKAs) provides a route to synthesize biodegradable polyesters and confer biodegradability into traditional vinyl polymers.

1.6 Dissertation Objectives

Based on the existing studies on ion-containing copolymers as a framework, this dissertation aims to further investigate the behaviors of polyelectrolytes in solutions and solid-state ionomers, for a better understanding of the collective nature among charged polymer systems.

In Chapter 2, polyelectrolyte homopolymers and neutral-charged block polyelectrolytes were synthesized by direct polymerizations. The salt-free dilute polymer solutions were characterized by diffusion-ordered NMR spectroscopy (DOSY), which enables a correlation between the diffusion behaviors and the specific chemical structures, to which polymer the diffusion coefficients belong. In Chapters 3 and 4, multi-block copolymers with a low T_g “soft” segment, polyisoprene, and a high T_g “hard” segment, poly(chloromethyl styrene), were synthesized. Pendant cations were then installed via quaternization reaction with tertiary amines or phosphines, resulting in mechanically robust ionomers. The ionomer membranes were then prepared and characterized by X-ray scattering, electron microscopy, etc, for a detailed investigation on structure-morphology-property relationships. In Chapter 5, a novel technique, Radical ring-opening polymerization (rROP) of cyclic ketene acetals (CKAs), was investigated, which demonstrated a route to synthesize biodegradable polyesters and confer biodegradability into traditional vinyl polymers. Finally, Chapter 6 summarizes the conclusions of the presented work and outlines future directions for sustainable chemistry development.

1.7 References

- (1) Hoover, M. F. Cationic Quaternary Polyelectrolytes—A Literature Review. *J. Macromol. Sci. Part A - Chem.* **1970**, *4* (6), 1327–1418.
- (2) Holliday, L. *Ionic Polymers*; Applied Science Publishers: London, 1975.
- (3) Eisenberg, A.; King, M. Ion-Containing Polymers: Physical Properties and Structure (Chapter I - Introduction); Academic Press, 1977; pp 1–14.

- (4) Chen, Q.; Bao, N.; Wang, J.-H. H. H.; Tunic, T.; Liang, S.; Colby, R. H. Linear Viscoelasticity and Dielectric Spectroscopy of Ionomer/Plasticizer Mixtures: A Transition from Ionomer to Polyelectrolyte. *Macromolecules* **2015**, *48* (22), 8240–8252.
- (5) Eisenberg, A.; Rinaudo, M. Polyelectrolytes and Ionomers. *Polym. Bull.* **1990**, *24* (6), 671.
- (6) Dobrynin, A. V.; Rubinstein, M. Theory of Polyelectrolytes in Solutions and at Surfaces. *Prog. Polym. Sci.* **2005**, *30* (11), 1049–1118.
- (7) Eisenberg, A.; Kim, J.-S. *Introduction to Ionomers*; Wiley: New York, 1998.
- (8) Colby, R. H. Structure and Linear Viscoelasticity of Flexible Polymer Solutions: Comparison of Polyelectrolyte and Neutral Polymer Solutions. *Rheol. Acta* **2010**, *49* (5), 425–442.
- (9) De Gennes, P.-G.; Pincus, P.; Velasco, R. M.; Brochard, F. Remarks on Polyelectrolyte Conformation. *J. Phys.* **1976**, *37* (12), 1461–1473.
- (10) Muthukumar, M. 50th Anniversary Perspective: A Perspective on Polyelectrolyte Solutions. *Macromolecules* **2017**, *50* (24), 9528–9560.
- (11) Fuoss, R. M. Viscosity Function for Polyelectrolytes. *J. Polym. Sci.* **1948**, *3* (4), 603–604.
- (12) Prabhu, V. M. Counterion Structure and Dynamics in Polyelectrolyte Solutions. *Curr. Opin. Colloid Interface Sci.* **2005**, *10* (1), 2–8.

- (13) Sedlák, M. What Can Be Seen by Static and Dynamic Light Scattering in Polyelectrolyte Solutions and Mixtures? *Langmuir* **1999**, *15* (12), 4045–4051.
- (14) Nishida, K.; Kaji, K.; Kanaya, T.; Shibano, T. Added Salt Effect on the Intermolecular Correlation in Flexible Polyelectrolyte Solutions: Small-Angle Scattering Study. *Macromolecules* **2002**, *35* (10), 4084–4089.
- (15) Jia, D.; Muthukumar, M. Effect of Salt on the Ordinary-Extraordinary Transition in Solutions of Charged Macromolecules. *J. Am. Chem. Soc.* **2019**, *141* (14), 5886–5896.
- (16) Sehgal, A.; Seery, T. A. P. The Ordinary–Extraordinary Transition Revisited: A Model Polyelectrolyte in a Highly Polar Organic Solvent. *Macromolecules* **1998**, *31* (21), 7340–7346.
- (17) Förster, S.; Schmidt, M. Polyelectrolytes in Solution. *Adv. Polym. Sci.* **1995**, *120*, 51–133.
- (18) Muthukumar, M. Collective Dynamics of Semidilute Polyelectrolyte Solutions with Salt. *J. Polym. Sci. Part B Polym. Phys.* **2019**, *57*, 1263–1269.
- (19) Lin, S. -C S.-C.; Lee, W. I.; Schurr, J. M. Brownian Motion of Highly Charged Poly(L-lysine). Effects of Salt and Polyion Concentration. *Biopolymers* **1978**, *17* (4), 1041–1064.
- (20) Chen, K.; Zheng, K.; Xu, G.; Yang, J.; Zhao, J. Diffusive Motion of Single Polyelectrolyte Molecules under Electrostatic Repulsion. *Macromolecules* **2019**, *52*

- (10), 3925–3934.
- (21) Sehgal, A.; Seery, T. A. P. The Ordinary-Extraordinary Transition Revisited: A Model Polyelectrolyte in a Highly Polar Organic Solvent. *Macromolecules* **1998**, *31* (21), 7340–7346.
- (22) Sedláč, M.; Amis, E. J. Dynamics of Moderately Concentrated Salt-Free Polyelectrolyte Solutions: Molecular Weight Dependence. *J. Chem. Phys.* **1992**, *96* (1), 817–825.
- (23) Prabhu, V. M.; Muthukumar, M.; Wignall, G. D.; Melnichenko, Y. B. Dimensions of Polyelectrolyte Chains and Concentration Fluctuations in Semidilute Solutions of Sodium-Poly(Styrene Sulfonate) as Measured by Small-Angle Neutron Scattering. *Polymer (Guildf)*. **2001**, *42* (21), 8935–8946.
- (24) Zhang, Y.; Douglas, J. F.; Ermi, B. D.; Amis, E. J. Influence of Counterion Valency on the Scattering Properties of Highly Charged Polyelectrolyte Solutions. *J. Chem. Phys.* **2001**, *114* (7), 3299–3313.
- (25) Prabhu, V. M.; Muthukumar, M.; Wignall, G. D.; Melnichenko, Y. B. Polyelectrolyte Chain Dimensions and Concentration Fluctuations near Phase Boundaries. *J. Chem. Phys.* **2003**, *119* (7), 4085–4098.
- (26) Förster, S.; Schmidt, M.; Antonietti, M. Static and Dynamic Light Scattering by Aqueous Polyelectrolyte Solutions: Effect of Molecular Weight, Charge Density and Added Salt. *Polymer (Guildf)*. **1990**, *31* (5), 781–792.

- (27) Levy, A.; Andelman, D.; Orland, H. Dielectric Constant of Ionic Solutions: A Field-Theory Approach. *Phys. Rev. Lett.* **2012**, *108* (22), 227801.
- (28) Yethiraj, A. Liquid State Theory of Polyelectrolyte Solutions. *J. Phys. Chem. B* **2009**, *113* (6), 1539–1551.
- (29) Yethiraj, A. Theory for Chain Conformations and Static Structure of Dilute and Semidilute Polyelectrolyte Solutions. *J. Chem. Phys.* **1998**, *108* (3), 1184–1192.
- (30) Mahalik, J. P.; Muthukumar, M. Langevin Dynamics Simulation of Polymer-Assisted Virus-like Assembly. *J. Chem. Phys.* **2012**, *136* (13), 135101.
- (31) Liu, S.; Muthukumar, M. Langevin Dynamics Simulation of Counterion Distribution around Isolated Flexible Polyelectrolyte Chains. *J. Chem. Phys.* **2002**, *116* (22), 9975–9982.
- (32) Shew, C.-Y.; Yethiraj, A. Monte Carlo Simulations and Self-Consistent Integral Equation Theory for Polyelectrolyte Solutions. *J. Chem. Phys.* **1999**, *110* (11), 5437–5443.
- (33) Muthukumar, M. Ordinary-Extraordinary Transition in Dynamics of Solutions of Charged Macromolecules. *Proc. Natl. Acad. Sci. U. S. A.* **2016**, *113* (45), 12627–12632.
- (34) Osada, Y.; Honda, K.; Ohta, M. Control of Water Permeability by Mechanochemical Contraction of Poly(Methacrylic Acid)-Grafted Membranes. *J. Memb. Sci.* **1986**, *27* (3), 327–338.

- (35) Tarvainen, T.; Svarfvar, B.; Åkerman, S.; Savolainen, J.; Karhu, M.; Paronen, P.; Järvinen, K. Drug Release from a Porous Ion-Exchange Membrane in Vitro. *Biomaterials* **1999**, *20* (22), 2177–2183.
- (36) Åkerman, S.; Viinikka, P.; Svarfvar, B.; Järvinen, K.; Kontturi, K.; Näsman, J.; Urtti, A.; Paronen, P. Transport of Drugs across Porous Ion Exchange Membranes. *J. Control. Release* **1998**, *50* (1), 153–166.
- (37) Sershen, S.; West, J. Implantable, Polymeric Systems for Modulated Drug Delivery. *Adv. Drug Deliv. Rev.* **2003**, *55* (3), 439.
- (38) Jeong, B.; Kim, S. W.; Bae, Y. H. Thermosensitive Sol-Gel Reversible Hydrogels. *Adv. Drug Deliv. Rev.* **2002**, *54* (1), 37–51.
- (39) Rossi, N. A. A.; Constantinescu, I.; Brooks, D. E.; Scott, M. D.; Kizhakkedathu, J. N. Enhanced Cell Surface Polymer Grafting in Concentrated and Nonreactive Aqueous Polymer Solutions. *J. Am. Chem. Soc.* **2010**, *132* (10), 3423–3430.
- (40) Rossi, N. A. A.; Constantinescu, I.; Kainthan, R. K.; Brooks, D. E.; Scott, M. D.; Kizhakkedathu, J. N. Red Blood Cell Membrane Grafting of Multi-Functional Hyperbranched Polyglycerols. *Biomaterials* **2010**, *31* (14), 4167–4178.
- (41) Mansouri, S.; Merhi, Y.; Winnik, F. M.; Tabrizian, M. Investigation of Layer-by-Layer Assembly of Polyelectrolytes on Fully Functional Human Red Blood Cells in Suspension for Attenuated Immune Response. *Biomacromolecules* **2011**, *12* (3), 585–592.

- (42) Wang, D.; Toyofuku, W. M.; Scott, M. D. The Potential Utility of Methoxypoly(Ethylene Glycol)-Mediated Prevention of Rhesus Blood Group Antigen RhD Recognition in Transfusion Medicine. *Biomaterials* **2012**, *33* (10), 3002–3012.
- (43) Wang, B.; Wang, G.; Zhao, B.; Chen, J.; Zhang, X.; Tang, R. Antigenically Shielded Universal Red Blood Cells by Polydopamine-Based Cell Surface Engineering. *Chem. Sci.* **2014**, *5* (9), 3463–3468.
- (44) Scott, M. D.; Murad, K. L.; Koumpouras, F.; Talbot, M.; Eaton, J. W. Chemical Camouflage of Antigenic Determinants: Stealth Erythrocytes. *Proc. Natl. Acad. Sci.* **1997**, *94* (14), 7566 LP – 7571.
- (45) Zhao, Y.; Fan, M.; Chen, Y.; Liu, Z.; Shao, C.; Jin, B.; Wang, X.; Hui, L.; Wang, S.; Liao, Z.; Ling, D.; Tang, R.; Wang, B. Surface-Anchored Framework for Generating RhD-Epitope Stealth Red Blood Cells. *Sci. Adv.* **2020**, *6* (12), 1–12.
- (46) Howell, J. A.; Nyström, M. Fouling Phenomena BT - Membranes in Bioprocessing: Theory and Applications; Howell, J. A., Sanchez, V., Field, R. W., Eds.; Springer Netherlands: Dordrecht, 1993; pp 203–241.
- (47) Dalsin, J. L.; Messersmith, P. B. Bioinspired Antifouling Polymers. *Mater. Today* **2005**, *8* (9), 38–46.
- (48) Rana, D.; Matsuura, T. Surface Modifications for Antifouling Membranes. *Chem. Rev.* **2010**, *110* (4), 2448–2471.

- (49) Combe, C.; Molis, E.; Lucas, P.; Riley, R.; Clark, M. M. The Effect of CA Membrane Properties on Adsorptive Fouling by Humic Acid. *J. Memb. Sci.* **1999**, *154* (1), 73–87.
- (50) Ulbricht, M.; Richau, K.; Kamusewitz, H. Chemically and Morphologically Defined Ultrafiltration Membrane Surfaces Prepared by Heterogeneous Photo-Initiated Graft Polymerization | Part 11 of the Series: Photomodification of Ultrafiltration Membranes. *Colloids Surfaces A Physicochem. Eng. Asp.* **1998**, *138* (2), 353–366.
- (51) Kato, K.; Sano, S.; Ikada, Y. Protein Adsorption onto Ionic Surfaces. *Colloids Surfaces B Biointerfaces* **1995**, *4* (4), 221–230.
- (52) Susanto, H.; Ulbricht, M. Photografted Thin Polymer Hydrogel Layers on PES Ultrafiltration Membranes: Characterization, Stability, and Influence on Separation Performance. *Langmuir* **2007**, *23* (14), 7818–7830.
- (53) White, A.; Jiang, S. Local and Bulk Hydration of Zwitterionic Glycine and Its Analogues through Molecular Simulations. *J. Phys. Chem. B* **2011**, *115* (4), 660–667.
- (54) Hower, J. C.; Bernards, M. T.; Chen, S.; Tsao, H.-K.; Sheng, Y.-J.; Jiang, S. Hydration of “Nonfouling” Functional Groups. *J. Phys. Chem. B* **2009**, *113* (1), 197–201.
- (55) Kurtz, I. S.; Sui, S.; Hao, X.; Huang, M.; Perry, S. L.; Schiffman, J. D. Bacteria-Resistant, Transparent, Free-Standing Films Prepared from Complex Coacervates. *ACS Appl. Bio Mater.* **2019**, *2* (9), 3926–3933.

- (56) Leng, C.; Huang, H.; Zhang, K.; Hung, H.-C.; Xu, Y.; Li, Y.; Jiang, S.; Chen, Z. Effect of Surface Hydration on Antifouling Properties of Mixed Charged Polymers. *Langmuir* **2018**, *34* (22), 6538–6545.
- (57) Bazuin, C. G.; Eisenberg, A. Ion-Containing Polymers: Ionomers. *J. Chem. Educ.* **1981**, *58* (11), 938–943.
- (58) Taubert, A.; Winey, K. I. Imaging and X-Ray Microanalysis of a Poly(Ethylene-Ran-Methacrylic Acid) Ionomer Melt Neutralized with Sodium. *Macromolecules* **2002**, *35* (19), 7419–7426.
- (59) Buitrago, C. F.; Jenkins, J. E.; Opper, K. L.; Aitken, B. S.; Wagener, K. B.; Alam, T. M.; Winey, K. I. Room Temperature Morphologies of Precise Acid- and Ion-Containing Polyethylenes. *Macromolecules* **2013**, *46* (22), 9003–9012.
- (60) Seitz, M. E.; Chan, C. D.; Opper, K. L.; Baughman, T. W.; Wagener, K. B.; Winey, K. I. Nanoscale Morphology in Precisely Sequenced Poly(Ethylene-Co-Acrylic Acid) Zinc Ionomers. *J. Am. Chem. Soc.* **2010**, *132* (23), 8165–8174.
- (61) Nagayama, K.; Kapur, J.; Morris, B. A. Influence of Two-Phase Behavior of Ethylene Ionomers on Diffusion of Water. *J. Appl. Polym. Sci.* **2020**, *137*, 48929.
- (62) Zhou, N. C.; Chan, C. D.; Winey, K. I. Reconciling STEM and X-Ray Scattering Data To Determine the Nanoscale Ionic Aggregate Morphology in Sulfonated Polystyrene Ionomers. *Macromolecules* **2008**, *41* (16), 6134–6140.
- (63) Castagna, A. M.; Wang, W.; Winey, K. I.; Runt, J. Influence of the Degree of

- Sulfonation on the Structure and Dynamics of Sulfonated Polystyrene Copolymers. *Macromolecules* **2010**, *43* (24), 10498–10504.
- (64) Castagna, A. M.; Wang, W.; Winey, K. I.; Runt, J. Influence of Cation Type on Structure and Dynamics in Sulfonated Polystyrene Ionomers. *Macromolecules* **2011**, *44* (13), 5420–5426.
- (65) Yang, S.; Sun, K.; Risen Jr., W. M. Preparation and Thermal Characterization of the Glass Transition Temperatures of Sulfonated Polystyrene-Metal Ionomers. *J. Polym. Sci. Part B Polym. Phys.* **1990**, *28* (10), 1685–1697.
- (66) Weiss, R. A.; Fitzgerald, J. J.; Kim, D. Viscoelastic Behavior of Lightly Sulfonated Polystyrene Ionomers. *Macromolecules* **1991**, *24* (5), 1071–1076.
- (67) Enokida, J. S.; Tanna, V. A.; Winter, H. H.; Coughlin, E. B. Progression of the Morphology in Random Ionomers Containing Bulky Ammonium Counterions. *Macromolecules* **2018**, *51* (18), 7377–7385.
- (68) Enokida, J. S.; Hu, W.; Fang, H.; Morgan, B. F.; Beyer, F. L.; Winter, H. H.; Coughlin, E. B. Modifying the Structure and Dynamics of Ionomers through Counterion Sterics. *Macromolecules* **2020**, *53* (5), 1767–1776.
- (69) Nandi, A.; DuttaGupta, M.; Banthia, A. K. Sulfonated Polybutadiene Ionomer Templates Nanonickel Composite. *Mater. Lett.* **2002**, *52* (3), 203–205.
- (70) Matsuura, H.; Eisenberg, A. Glass Transitions of Ethyl Acrylate-Based Ionomers. *J. Polym. Sci. Polym. Phys. Ed.* **1976**, *14* (7), 1201–1209.

- (71) Chen, Q.; Tudryn, G. J.; Colby, R. H. Ionomer Dynamics and the Sticky Rouse Model. *J. Rheol. (N. Y. N. Y.)* **2013**, *57* (5), 1441–1462.
- (72) Page, K. A.; Landis, F. A.; Phillips, A. K.; Moore, R. B. SAXS Analysis of the Thermal Relaxation of Anisotropic Morphologies in Oriented Nafion Membranes. *Macromolecules* **2006**, *39* (11), 3939–3946.
- (73) Nguyen, H.-D.; Jestin, J.; Porcar, L.; Iojoiu, C.; Lyonard, S. Aromatic Copolymer/Nafion Blends Outperforming the Corresponding Pristine Ionomers. *ACS Appl. Energy Mater.* **2018**, *1* (2), 355–367.
- (74) Barnes, A. M.; Buratto, S. K. Imaging Channel Connectivity in Nafion Using Electrostatic Force Microscopy. *J. Phys. Chem. B* **2018**, *122* (3), 1289–1295.
- (75) Hickner, M. A. Water-Mediated Transport in Ion-Containing Polymers. *J. Polym. Sci. Part B Polym. Phys.* **2012**, *50* (1), 9–20.
- (76) Wang, F.; Hickner, M.; Kim, Y. S.; Zawodzinski, T. A.; McGrath, J. E. Direct Polymerization of Sulfonated Poly(Arylene Ether Sulfone) Random (Statistical) Copolymers: Candidates for New Proton Exchange Membranes. *J. Memb. Sci.* **2002**, *197* (1), 231–242.
- (77) Paul, M.; Park, H. B.; Freeman, B. D.; Roy, A.; McGrath, J. E.; Riffle, J. S. Synthesis and Crosslinking of Partially Disulfonated Poly(Arylene Ether Sulfone) Random Copolymers as Candidates for Chlorine Resistant Reverse Osmosis Membranes. *Polymer (Guildf.)* **2008**, *49* (9), 2243–2252.

- (78) Van der Bruggen, B.; Vandecasteele, C. Distillation vs. Membrane Filtration: Overview of Process Evolutions in Seawater Desalination. *Desalination* **2002**, *143* (3), 207–218.
- (79) Varcoe, J. R.; Atanassov, P.; Dekel, D. R.; Herring, A. M.; Hickner, M. A.; Kohl, P. A.; Kucernak, A. R.; Mustain, W. E.; Nijmeijer, K.; Scott, K.; Xu, T.; Zhuang, L. Anion-Exchange Membranes in Electrochemical Energy Systems. *Energy Environ. Sci.* **2014**, *7* (10), 3135–3191.
- (80) Hickner, M. A. Ion-Containing Polymers: New Energy & Clean Water. *Mater. Today* **2010**, *13* (5), 34–41.
- (81) Asano, N.; Aoki, M.; Suzuki, S.; Miyatake, K.; Uchida, H.; Watanabe, M. Aliphatic/Aromatic Polyimide Ionomers as a Proton Conductive Membrane for Fuel Cell Applications. *J. Am. Chem. Soc.* **2006**, *128* (5), 1762–1769.
- (82) Einsla, B. R.; Hong, Y.-T.; Seung Kim, Y.; Wang, F.; Gunduz, N.; McGrath, J. E. Sulfonated Naphthalene Dianhydride Based Polyimide Copolymers for Proton-Exchange-Membrane Fuel Cells. I. Monomer and Copolymer Synthesis. *J. Polym. Sci. Part A Polym. Chem.* **2004**, *42* (4), 862–874.
- (83) Fang, J.; Guo, X.; Harada, S.; Watari, T.; Tanaka, K.; Kita, H.; Okamoto, K. Novel Sulfonated Polyimides as Polyelectrolytes for Fuel Cell Application. 1. Synthesis, Proton Conductivity, and Water Stability of Polyimides from 4,4'-Diaminodiphenyl Ether-2,2'-Disulfonic Acid. *Macromolecules* **2002**, *35* (24), 9022–9028.
- (84) Genies, C.; Mercier, R.; Sillion, B.; Cornet, N.; Gebel, G.; Pineri, M. Soluble

- Sulfonated Naphthalenic Polyimides as Materials for Proton Exchange Membranes. *Polymer (Guildf)*. **2001**, 42 (2), 359–373.
- (85) Ghassemi, H.; McGrath, J. E. Synthesis and Properties of New Sulfonated Poly(p-Phenylene) Derivatives for Proton Exchange Membranes. I. *Polymer (Guildf)*. **2004**, 45 (17), 5847–5854.
- (86) Fujimoto, C. H.; Hickner, M. A.; Cornelius, C. J.; Loy, D. A. Ionomeric Poly(Phenylene) Prepared by Diels–Alder Polymerization: Synthesis and Physical Properties of a Novel Polyelectrolyte. *Macromolecules* **2005**, 38 (12), 5010–5016.
- (87) Schuster, M.; Kreuer, K.-D.; Andersen, H. T.; Maier, J. Sulfonated Poly(Phenylene Sulfone) Polymers as Hydrolytically and Thermooxidatively Stable Proton Conducting Ionomers. *Macromolecules* **2007**, 40 (3), 598–607.
- (88) Karlsson, L. E.; Jannasch, P. Polysulfone Ionomers for Proton-Conducting Fuel Cell Membranes: Sulfoalkylated Polysulfones. *J. Memb. Sci.* **2004**, 230 (1), 61–70.
- (89) Merle, G.; Wessling, M.; Nijmeijer, K. Anion Exchange Membranes for Alkaline Fuel Cells: A Review. *J. Memb. Sci.* **2011**, 377 (1–2), 1–35.
- (90) Hickner, M. A.; Herring, A. M.; Coughlin, E. B. Anion Exchange Membranes: Current Status and Moving Forward. *J. Polym. Sci. Part B Polym. Phys.* **2013**, 51 (24), 1727–1735.
- (91) Gottesfeld, S.; Dekel, D. R.; Page, M.; Bae, C.; Yan, Y.; Zelenay, P.; Kim, Y. S. Anion Exchange Membrane Fuel Cells: Current Status and Remaining Challenges.

J. Power Sources **2018**, 375, 170–184.

- (92) Couture, G.; Alaaeddine, A.; Boschet, F.; Ameduri, B. Polymeric Materials as Anion-Exchange Membranes for Alkaline Fuel Cells. *Prog. Polym. Sci.* **2011**, 36 (11), 1521–1557.
- (93) Panchal, S. S.; Vasava, D. V. Biodegradable Polymeric Materials: Synthetic Approach. *ACS Omega* **2020**, 5 (9), 4370–4379.
- (94) Luo, Z.; Wu, Y. L.; Li, Z.; Loh, X. J. Recent Progress in Polyhydroxyalkanoates-Based Copolymers for Biomedical Applications. *Biotechnol. J.* **2019**, 1900283, 1–16.
- (95) Koller, M. Polyhydroxyalkanoate Biosynthesis at the Edge of Water Activity-Haloarchaea as Biopolyester Factories. *Bioengineering* **2019**, 6 (2), 34.
- (96) Herron, J. S.; King, J. D.; White, D. C. Recovery of Poly- β -Hydroxybutyrate from Estuarine Microflora. *Appl. Environ. Microbiol.* **1978**, 35 (2), 251 LP – 257.
- (97) Luo, S.; Netravali, A. N. Interfacial and Mechanical Properties of Environment-Friendly ‘green’ Composites Made from Pineapple Fibers and Poly(Hydroxybutyrate-Co-Valerate) Resin. *J. Mater. Sci.* **1999**, 34 (15), 3709–3719.
- (98) Carr, N. G. The Occurrence of Poly- β -Hydroxybutyrate in the Blue-Green Alga, *Chlorogloea Fritschii*. *Biochim. Biophys. Acta - Biophys. Incl. Photosynth.* **1966**, 120 (2), 308–310.

- (99) Wallen, L. L.; Rohwedder, W. K. Poly-. Beta.-Hydroxyalkanoate from Activated Sludge. *Environ. Sci. Technol.* **1974**, 8 (6), 576–579.
- (100) Lemoigne, M. Etudes Sur L'autolyse Microbienne Acidification Par Formation D'acide β -Oxybutyrique. *Ann. Inst. Pasteur* **1925**, 39, 144–173.
- (101) Roy, I.; Visakh, P. M. *Polyhydroxyalkanoate (PHA) Based Blends, Composites and Nanocomposites*; Royal Society of Chemistry, 2014; Vol. 30.
- (102) Knani, D.; Gutman, A. L.; Kohn, D. H. Enzymatic Polyesterification in Organic Media. Enzyme-Catalyzed Synthesis of Linear Polyesters. I. Condensation Polymerization of Linear Hydroxyesters. II. Ring-Opening Polymerization of ϵ -Caprolactone. *J. Polym. Sci. Part A Polym. Chem.* **1993**, 31 (5), 1221–1232.
- (103) Pellis, A.; Comerford, J. W.; Weinberger, S.; Guebitz, G. M.; Clark, J. H.; Farmer, T. J. Enzymatic Synthesis of Lignin Derivable Pyridine Based Polyesters for the Substitution of Petroleum Derived Plastics. *Nat. Commun.* **2019**, 10 (1), 1762.
- (104) Eichhorn, S. J.; Dufresne, A.; Aranguren, M.; Marcovich, N. E.; Capadona, J. R.; Rowan, S. J.; Weder, C.; Thielemans, W.; Roman, M.; Renneckar, S.; Gindl, W.; Veigel, S.; Keckes, J.; Yano, H.; Abe, K.; Nogi, M.; Nakagaito, A. N.; Mangalam, A.; Simonsen, J.; et al. *Review: Current International Research into Cellulose Nanofibres and Nanocomposites*; 2010; Vol. 45.
- (105) Wohlhauser, S.; Delepierre, G.; Labet, M.; Morandi, G.; Thielemans, W.; Weder, C.; Zoppe, J. O. Grafting Polymers from Cellulose Nanocrystals: Synthesis, Properties, and Applications. *Macromolecules* **2018**, 51 (16), 6157–6189.

- (106) Heinze, T.; Liebert, T. Unconventional Methods in Cellulose Functionalization. *Prog. Polym. Sci.* **2001**, *26* (9), 1689–1762.
- (107) Carvalho, L. C. R.; Queda, F.; Santos, C. V. A.; Marques, M. M. B. Selective Modification of Chitin and Chitosan: En Route to Tailored Oligosaccharides. *Chem. - An Asian J.* **2016**, *11* (24), 3468–3481.
- (108) Kurita, K.; Mori, S.; Nishiyama, Y.; Harata, M. N-Alkylation of Chitin and Some Characteristics of the Novel Derivatives. *Polym. Bull.* **2002**, *48* (2), 159–166.
- (109) Kurita, K.; Kojima, T.; Nishiyama, Y.; Shimojoh, M. Synthesis and Some Properties of Nonnatural Amino Polysaccharides: Branched Chitin and Chitosan. *Macromolecules* **2000**, *33* (13), 4711–4716.
- (110) Kurita, K.; Akao, H.; Yang, J.; Shimojoh, M. Nonnatural Branched Polysaccharides: Synthesis and Properties of Chitin and Chitosan Having Disaccharide Maltose Branches. *Biomacromolecules* **2003**, *4* (5), 1264–1268.
- (111) Silvernail, C. M.; Yao, L. J.; Hill, L. M. R.; Hillmyer, M. A.; Tolman, W. B. Structural and Mechanistic Studies of Bis(Phenolato)Amine Zinc(II) Catalysts for the Polymerization of ϵ -Caprolactone. *Inorg. Chem.* **2007**, *46* (16), 6565–6574.
- (112) Gou, M.; Gong, C.; Zhang, J.; Wang, X.; Wang, X.; Gu, Y.; Guo, G.; Chen, L.; Luo, F.; Zhao, X.; Wei, Y.; Qian, Z. Polymeric Matrix for Drug Delivery: Honokiol-Loaded PCL-PEG-PCL Nanoparticles in PEG-PCL-PEG Thermosensitive Hydrogel. *J. Biomed. Mater. Res. Part A* **2010**, *93A* (1), 219–226.

- (113) Lowe, J. R.; Martello, M. T.; Tolman, W. B.; Hillmyer, M. A. Functional Biorenewable Polyesters from Carvone-Derived Lactones. *Polym. Chem.* **2011**, *2* (3), 702–708.
- (114) Fraser, C.; Hillmyer, M. A.; Gutierrez, E.; Grubbs, R. H. Degradable Cyclooctadiene/Acetal Copolymers: Versatile Precursors to 1,4-Hydroxytelechelic Polybutadiene and Hydroxytelechelic Polyethylene. *Macromolecules* **1995**, *28* (21), 7256–7261.
- (115) Hilf, S.; Kilbinger, A. F. M. Heterotelechelic Ring-Opening Metathesis Polymers. *Macromolecules* **2010**, *43* (1), 208–212.
- (116) Hilf, S.; Kilbinger, A. F. M. Sacrificial Synthesis of Hydroxy-Telechelic Metathesis Polymers via Multiblock-Copolymers. *Macromolecules* **2009**, *42* (4), 1099–1106.
- (117) Hilf, S.; Grubbs, R. H.; Kilbinger, A. F. M. Sacrificial Synthesis of Hydroxy-Functionalized ROMP Polymers: An Efficiency Study. *Macromolecules* **2008**, *41* (16), 6006–6011.
- (118) Hilf, S.; Berger-Nicoletti, E.; Grubbs, R. H.; Kilbinger, A. F. M. Monofunctional Metathesis Polymers via Sacrificial Diblock Copolymers. *Angew. Chemie - Int. Ed.* **2006**, *45* (47), 8045–8048.
- (119) Chang, C. C.; Emrick, T. Functional Polyolefins Containing Disulfide and Phosphoester Groups: Synthesis and Orthogonal Degradation. *Macromolecules* **2014**, *47* (4), 1344–1350.

- (120) Nagarkar, A. A.; Crochet, A.; Fromm, K. M.; Kilbinger, A. F. M. Efficient Amine End-Functionalization of Living Ring-Opening Metathesis Polymers. *Macromolecules* **2012**, *45* (11), 4447–4453.
- (121) Shieh, P.; Nguyen, H. V. T.; Johnson, J. A. Tailored Silyl Ether Monomers Enable Backbone-Degradable Polynorbornene-Based Linear, Bottlebrush and Star Copolymers through ROMP. *Nat. Chem.* **2019**, *11* (12), 1124–1132.
- (122) Hilf, S.; Kilbinger, A. F. M. Thiol-Functionalized ROMP Polymers via Sacrificial Synthesis. *Macromolecules* **2009**, *42* (12), 4127–4133.

CHAPTER 2

USING DOSY TO INVESTIGATE THE DIFFUSION OF POLYELECTROLYTES IN SALT-FREE SOLUTIONS

2.1 Introduction

Polyelectrolyte solutions are multi-component systems consisting of polyions, counterions, co-ions, and solvent. The collective effects from long-range electrostatic forces, hydrogen-bonding, dipolar interaction, *van der Waals* interaction, and chain connectivity lead to unique properties, which are unseen in neutral polymer analogues.¹ One of the attributes is the existence of multiple dynamic modes in solutions under salt-free or low-salt conditions, commonly referred to as “ordinary–extraordinary” transition.^{2,3,12–16,4–11} The “ordinary” behavior, represented by a “fast” relaxation mode, is interpreted as the coupled diffusion of polyion single chains with the counterions. The diffusion coefficient of the “fast” mode (D_f) has been found to be independent of the molar mass over three decades in molecular weight. This behavior is in stark contrast with neutral polymer solutions, where diffusion coefficient $D = \frac{kT}{6\pi\eta R_H}$, where R_H is the polymer hydrodynamic radius, proportional to molecular weight by a power law. The “extraordinary” behavior is attributed to the presence of multichain aggregates, whose diffusion coefficient (D_s) is usually several orders of magnitude smaller than D_f , and dependent on the molecular weight. Therefore, these aggregates display a “slow” relaxation mode.^{3,4}

Many scenarios have been proposed to interpret the physical mechanisms of these dynamic modes. The coupled mode theories attribute the higher diffusion rate of the “fast”

mode to the coupling of the polyion motion with the dynamics of small and more mobile counterions.^{4,17} More recently, Muthukumar derived a general mean-field theory combining the Flory–Huggins theory of polymer solutions and the Debye–Hückel theory¹⁸ of simple electrolytes, which has been successfully applied to polyelectrolyte solutions.^{19,20} In addition to intensive theoretical study, numerous experiments on synthetic polyelectrolytes, proteins, polynucleotides and charged polysaccharides have been performed.^{3,7,11,12,21–23} Typically, dynamic light scattering (DLS) and small-angle light scattering (SALS) have been commonly employed to measure diffusion coefficients in solution. The apparent scattering intensity by DLS contains contributions from different particles or dynamic modes, which can be distinguished based on various time autocorrelation functions decay at different time scales.³ Nevertheless, the measurement from DLS is prone to the influence of dust particles. Only a few larger particles are necessary to influence the DLS results yielding misleading data. This makes the interpretation of the scattering from polyelectrolyte solutions even more difficult. There have always been controversies on whether the slow modes detected from scattering profiles were due to impurities.¹⁵

Diffusion-ordered NMR spectroscopy (DOSY) has been utilized as a powerful tool in recent years to investigate structures in solutions.²⁴ By relating the chemical shifts of NMR resonances from analytes to the translational diffusion coefficient of that species, the influence from irrelevant impurities in solution can be easily eliminated. In addition, DOSY is especially helpful for the investigation of local molecular dynamics in polyelectrolyte solutions.

In contrast to the intense theoretical and experimental effort on homopolyelectrolyte solutions, the studies on block copolymers of electrolytes and other neutral moieties are still at an early stage of development. The dynamic studies and solution properties of block polyelectrolytes were first reported by Tenhu *et al.* Dynamic light scattering was used to characterize both linear and branched block copolymers of ethylene oxide and methacrylic acid, where the fast and the slow diffusion modes were observed and the relationship with polymer concentration and pH were revealed.²⁵ Limited by the instrumental resolution of light scattering, the investigation on diffusion behavior of individual blocks in block polyelectrolytes has rarely been performed. In our study, DOSY was utilized for the dynamic investigation on both homo- and block- polyelectrolytes in D₂O. The results provide insights into the fundamental understanding of polyelectrolyte diffusion and self-assembly in salt-free dilution solutions, which can further enlighten the application of polyelectrolytes in industry, for example, multichain aggregates of nontoxic, biocompatible, and biodegradable polymers in pharmaceutical, biotechnology, and cosmetic applications.^{26,27}

2.2 Experimental

2.2.1 Materials

2,2'-Azobis(2-methylpropionitrile) (AIBN) was recrystallized from methanol and stored under -20 °C before the use as the initiator during RAFT polymerization. For Si-based CTA synthesis, crude AIBN was used without purification. All other chemicals were used as received.

2.2.2 Silicon-based CTA Synthesis

Silicon-based CTA was synthesized according to a modified protocol based on previously reported methods.²⁸⁻³⁰ *Step 1:* Bromo-4-(trimethylsilyl)benzene (12.6 mL, 0.12 mol) in 90 mL of dry tetrahydrofuran (THF) was added dropwise to magnesium turnings (3 g, 0.12 mol) in 100 mL of dry THF with stirring under nitrogen. After 6 h, the solution was cooled to 0 °C and carbon disulfide (9.15 g, 0.12 mol) was added dropwise to the Grignard mixture. After 6 hours, the Grignard reagent was hydrolyzed by the slow addition of water (20 mL). The magnesium salts were removed by filtration and rinsed with deionized water. The solution was then acidified by HCl aqueous solution (200 mL, 1.0 M) to generate dithiol carboxylic acid and partitioned between water and diethyl ether. The ether layer was collected and re-deprotonated by NaOH solution (350 mL, 1.0 M) and partitioned again, leaving a dark red solution of the sodium salt of dithiobenzoic acid. A solution of potassium ferricyanide (21.4 g, 0.065 mol) in 100 mL deionized water was added dropwise to the solutions of the sodium salt of dithiobenzoic acid, with vigorous stirring. After 1.5 h, a red precipitate was collected by liquid-liquid separation. After removing the solvent by rotary evaporation, the disulfide intermediate was obtained, which was used directly in the next step. *Step 2:* A Schlenk flask was charged with the disulfide intermediate (9 g), crude 2,2'-azobis(2-methylpropionitrile) (AIBN, 3.3 g, 0.02 mol), and ethyl acetate (20 mL). The mixture was degassed by nitrogen purge for 20 minutes and then sealed with a rubber septum, before being heated to 80 °C to initiate the reaction. A needle was left in the septum to balance the pressure because a large amount of nitrogen can be produced during this radical coupling reaction. After 48 hours, the mixture was filtrated and concentrated. Column chromatography was used with hexane: ethyl acetate (v:v = 9:1)

as eluent to isolate the product. Then, the product was recrystallized from hexane. Yield = 80%.

2.2.3 Styrene RAFT Polymerization with Si-based CTA or 2-cyano-2-propyl benzodithioate (CPBT)

In a typical procedure, PS-Si CTA-1 was synthesized by RAFT polymerization with Si-based CTA. Recrystallized AIBN (11 mg, 0.06 mmol) and Si-based CTA (94 mg, 0.32 mmol), and styrene (2 g, 19.2 mmol) were dissolved in dioxane (10 ml) in a vial. After purging with nitrogen for 30 minutes, the vial was immersed in an oil bath at 70 °C for 16 hours and then quenched in an ice bath. The solution was precipitated in hexane. The precipitate was redissolved in dichloromethane and the solution was precipitated in hexane for three times to remove excess styrene monomers. The product was dried in vacuum oven overnight. By using either Si-based CTA or CPBT and modulating the feed ratio of styrene, polystyrene with various molecular weights and different end-groups can be obtained.

2.2.4 (Vinylbenzyl)trimethylammonium chloride (VBTMA) RAFT Polymerization with Si-based CTA

In a typical procedure, PVBTMA₇₇ (poly[(vinylbenzyl)trimethylammonium chloride], DP = 77) was synthesized by RAFT polymerization with Si-based CTA. Recrystallized AIBN (3.86 mg, 0.02 mmol) and Si-based CTA (34.5 mg, 0.11 mmol), and VBTMA (2 g, 10 mmol) were dissolved in dioxane (10 ml) in a vial. After purging with dry nitrogen for 30 minutes, the vial was immersed in an oil bath at 70 °C for 16 hours and then quench in an ice bath. The excess monomer was removed by dialysis (molecular weight

cut-off = 2 kDa) for 3 days. After lyophilization for 5 days, a light pink product was obtained. By modulating the feed ratio of VBTMA monomer, a series of PVBTMAs with different molecular weights were synthesized.

2.2.5 Block polyelectrolytes, P(EO-*b*-VBTMA), Synthesis.

PEO-CTA synthesis. In a typical procedure, PEO₄₆-CTA was synthesized as follows: PEO₄₆-OH (6.6 g, 3.33 mmol) and CTA 1 (3-cyano-3-(butylthiocarbonothioylthio)-butanoic acid, 1.38 g, 5 mmol) was dissolved in 150 mL of dichloromethane with a catalytic amount of 4-dimethylaminopyridine (DMAP, 100 mg, 0.82 mmol). The solution was homogenized by stirring before being placed into ice bath, then *N,N'*-dicyclohexylcarbodiimide (DCC, 1.03 g, 5 mmol) in dichloromethane (10 mL) was added into the cold solution. After stirring at room temperature for 36 h, the solution was kept in a -20 °C freezer overnight to allow the dicyclohexylurea (DCU) to precipitate from the solution before removal by filtration. The filtrate was concentrated and precipitated in excess cold diethyl ether. The product, with a yellow color, was obtained by filtering and drying under vacuum before NMR and MALDI-TOF characterization.

Chain extension with VBTMA. In a typical procedure, P(EO₄₆-*b*-VBTMA₆) was synthesized as follows: VBTMA (0.42 g, 2 mmol), PEO₄₆-CTA (0.18 g, 0.09 mmol) and recrystallized AIBN (2.96 mg, 0.018 mmol) were dissolved in 3 ml methanol in a Schlenk flask. Three cycles of freeze–pump–thaw were applied to degas the mixture, then the flask was backfilled with nitrogen and placed in an oil bath at 75 °C for 12h. The chain extension was quenched by immersing the flask into an ice bath for 10 min before dialysis against deionized water for 3 days and lyophilization for 5 days.

2.2.6 Characterization.

Gel Permeation Chromatography (GPC). GPC was performed in tetrafluoroethylene (TFE) at a flow rate of 1.0 mL/min using a refractive index detector on a Polymer Laboratories PL-GPC 50 integrated GPC system.

Matrix-Assisted Laser Desorption/Ionization-Time of Flight (MALDI-TOF) mass spectrometry. MALDI-TOF were performed on a Bruker UltrafleXtreme MALDI-TOF instrument. For the two PEO analytes (PEO-OH and PEO-CTA), 2,5-dihydroxybenzoic acid (DHB) matrix was used to facilitate the ionization (matrix : polymer concentration = 10:1, weight ratio). The measurements were conducted in positive mode.

Nuclear Magnetic Resonance (NMR) Spectroscopy. ^1H NMR were performed in 5 mm diameter tubes in deuterated water (D_2O) performed at 25 °C on a 400 MHz Bruker Advanced NMR spectrometer. Diffusion Ordered Spectroscopy (DOSY) experiments were conducted on the same instrument equipped with an Accustar z-axis gradient amplifier and an ATMA BBO probe with a z axis gradient coil. Samples ($c_p = 5 \text{ mg/ml}$) were stabilized at 25 °C for 5 min before data collection. All experiments were performed without spinning to avoid convection. 90° pulse was calibrated before each measurement. Bipolar rectangular gradients were used with a total duration of 0.5–10 ms. Gradient recovery delays were 0.1–0.5 μs . The number of gradient steps was set to be 16. Individual rows of the quasi-2-D diffusion databases were phase corrected and baseline subtracted.

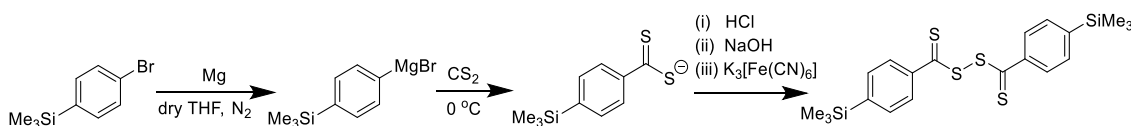
2.3 Results and Discussion

2.3.1 Silicon-based CTA Synthesis

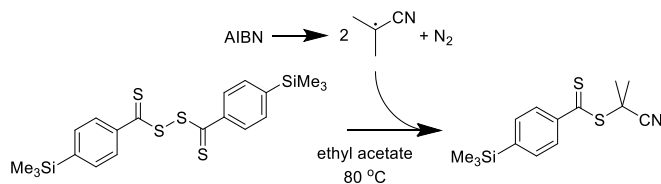
In order to obtain a series of homo-polyelectrolyte standards, RAFT was chosen to synthesize poly(vinylbenzyltrimethylammonium chloride) (PVBtMA) over a range of molecular weights, all with narrow dispersity. A functional RAFT chain transfer agent (CTA) was needed to provide living character for polymerization and having a traceable end-group in ^1H NMR, so that end-group analysis would result in a reliable M_n , even at relatively high degrees of polymerization (DP).

Scheme 2. 1 Synthesis of Si-based CTA.

Step 1:



Step 2:



Commercially available phenyl or alkyl CTA provide good control over RAFT polymerization, however, in ^1H NMR, peaks from end-groups usually overlap with those from polymer backbones, and this renders end-group analysis less accurate, or impossible, in the determination of molecular weights. Due to high electron density of silicon, methyl groups attached to silicon are strongly shielded and appear at high-field chemical shift in

^1H NMR spectroscopy. For example, tetramethylsilane (TMS) is commonly used as a NMR chemical shift reference ($\delta = 0$ ppm). Therefore, a trimethyl silyl functionalized CTA was designed to provide an end-group with high-field chemical shift in ^1H NMR, *i.e.* $\delta \sim 0$ ppm, where polymer peaks are generally absent. Because of no overlap with polymer backbone peaks, there is less analytical error from baseline or phase correction. Therefore, RAFT polymerization by the silicon-based (Si-based) CTA is a promising method to synthesize polymers with reliable M_n determination from end-group analysis.

As shown in Scheme 2.1, the Si-based CTA was synthesized through a Grignard reaction (Step 1) and a subsequent radical coupling reaction (Step 2). In order to confirm the structure of the Si-based CTA, the product was analyzed by electrospray ionization mass spectrometry (ESI), as shown in Figure 2.1A. A distinct peak at ~ 294 m/z was detected from the molecular ion of the target Si-based CTA with molecular weight of 293.52 g/mol. The structure and purity were further confirmed by ^1H NMR, Figure 2.1B, the singlet from three methyl groups on silicon appears at a high-field chemical shift of $\delta = 0.26$ ppm.

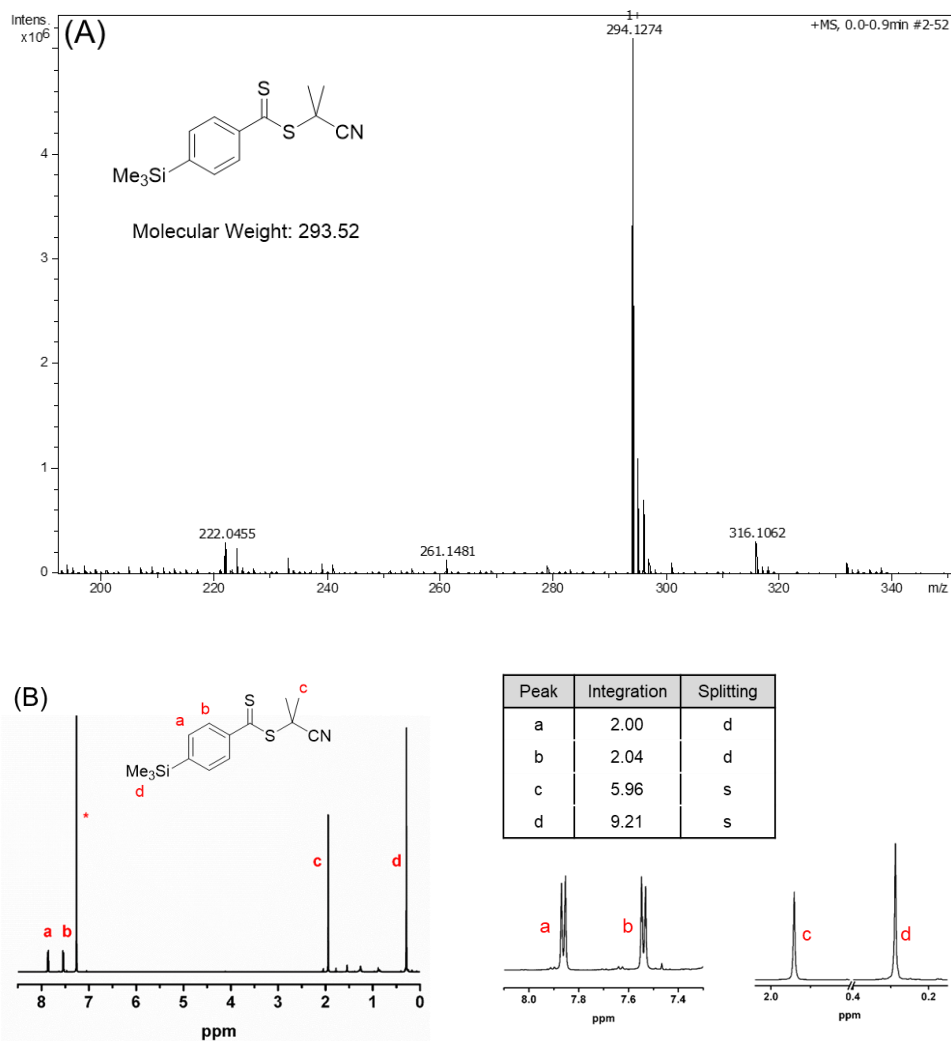
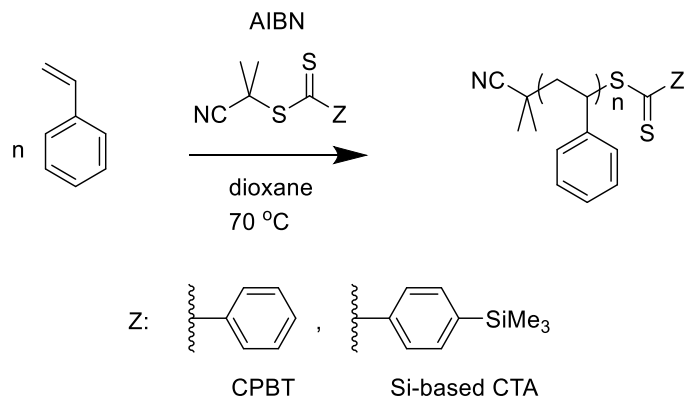


Figure 2. 1 (A) ESI mass spectrometry and (B) ^1H NMR spectroscopy of Si-based CTA.

After the successful synthesis of Si-based CTA, RAFT polymerization of styrene was performed with the Si-based CTA, as shown in Scheme 2.2. For comparison, the polymerization of styrene was conducted using a commercially available CTA, 2-cyano-2-propyl benzodithioate (CPBT), under the same reaction conditions, to answer the two following questions. Do both CTAs exhibit living character during RAFT polymerization and result in polymers with narrow dispersity? Will the Si-based CTA provide accurate molecular weight determination by end-group analysis in ^1H NMR spectroscopy?

Scheme 2. 2 Styrene polymerization by CPBT or Si-based CTA.



In order to answer the two questions, two polymerizations were conducted for each CTA. The molecular weight and distribution results from THF GPC are listed in Table 2.1. Polystyrene (PS) standards were used to provide reliable molecular weight results for comparison with M_n determined by ^1H NMR. The analysis by GPC shows narrow dispersity ($D < 1.1$) for all samples, indicating living character provided by either CTA. As shown in Figure 2.2, CTA are usually dithiocarbonate species with desired R and Z groups. During RAFT polymerization, the R group is responsible for efficient fragmentation to ensure the reinitiation process occurs in a short time frame to obtain a narrow molecular weight distribution. The Z group aids with the stabilization of the intermediate radical to favor radical addition on C=S bonds.³¹ The structures of Si-based CTA and CPBT, both have the same R group, 2-methyl-propionitrile, but different Z groups, either trimethylsilyl benzodithioate for Si-based CTA, or benzodithioate for CPBT. As demonstrated by the narrow dispersity in all of the GPC results, no deleterious side effects from the trimethylsilyl group on the stability of the intermediate species in RAFT polymerization was observed. Thus, the C=S bond remains more reactive than the C=C bond of the monomer for both CTAs, which is a key aspect for a successful RAFT polymerization.

The ^1H NMR spectroscopy in Figure 2.2 reveals the remarkable difference regarding end-group peak integrations between two CTAs. According to RAFT mechanism, the same R group from both CTAs, caps one end of the PS chain after polymerization, while the other end is terminated by a different Z group, as shown in Figure 2.2 as well as two PS structures in Figure 2.2.^{31,32} The ^1H NMR resonance from two methyl groups on R group overlap with that from PS alkyl backbone, thus Z group is investigated for end-group analysis for both cases.

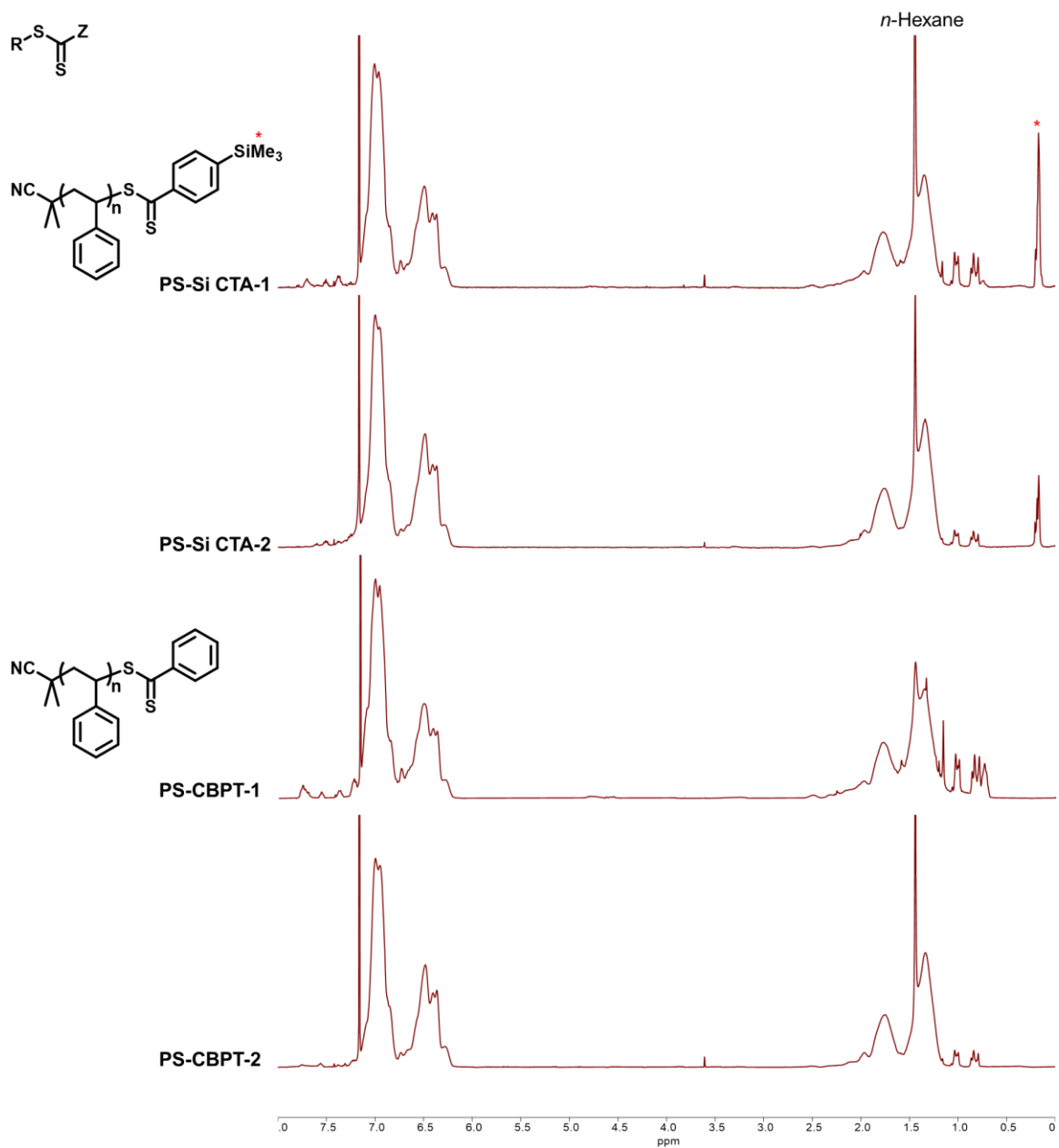


Figure 2. 2 Structure comparison of CTBT and Si-based CTA, ^1H NMR of PS polymerized by CPBT or Si-based CTA.

For PS-CPBT, protons at *para*, *meta* and *ortho* positions of the phenyl group show up as three peaks in ^1H NMR (Figure 2.2). Thus, an integration over a wide range of chemical shift is required ($\delta = 7.4\text{-}7.8$ ppm) for end-group analysis. In this case, baseline correction brings serious error even under low DP, which results in large deviation of

molecular weight estimation. For PS-Si-based CTA, a sharp narrow singlet from the silyl methyl group appears at $\delta \sim 0.2$ ppm, and end-group integration does not suffer from overlapping or baseline-correction error. Therefore, M_n calculated from Si-based end-group analysis was much closer to that from GPC, in comparison with PS-CPBT. Quantitative calculation of deviations from end-group analysis against GPC results are shown in Table 2.1. It has been demonstrated that Si-based CTA is a functional living agent for RAFT polymerization as well as ^1H NMR end-group marker for M_n determination.

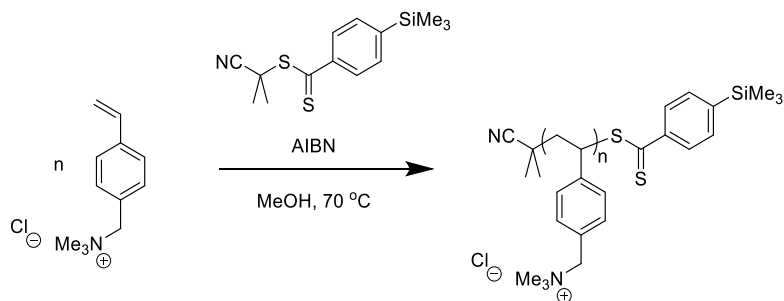
Table 2. 1 PS molecular weights from ^1H NMR end-group analysis and GPC.

Sample	GPC			^1H NMR	Deviation ^a
	M_n (g/mol)	M_w (g/mol)	\mathcal{D}	M_n (g/mol)	
PS-Si CTA-1	2,700	2,800	1.07	2,660	1%
PS-CPBT-1	2,200	2,300	1.07	1,550	30%
PS-Si CTA-2	5,200	5,600	1.09	5,790	11%
PS-CPBT-2	4,700	5,100	1.09	9,800	109%

^aDeviation was calculated by referring M_n from end-group analysis to M_n from GPC

$$\text{(PS standards). } Deviation = \left| \frac{M_n(NMR) - M_n(GPC)}{M_n(GPC)} \right| \times 100\%.$$

Scheme 2. 3 Synthesis of PVBTMA standards by Si-based CTA.



2.3.2 Synthesis of Homo-Polyelectrolytes, PVBTMA, with Si-based CTA.

The Si-based CTA has proven to be a functional end-group marker, as well as a living chain transfer agent in RAFT. Next, as shown in Scheme 2.3, RAFT polymerization of an ionic monomer, vinylbenzyltrimethylammonium chloride (VBTMA), was performed using the Si-based CTA. The resultant polyelectrolyte, PVBTMA, is expected to have narrow dispersity and reliable molecular weight determination by ¹H NMR end-group analysis.

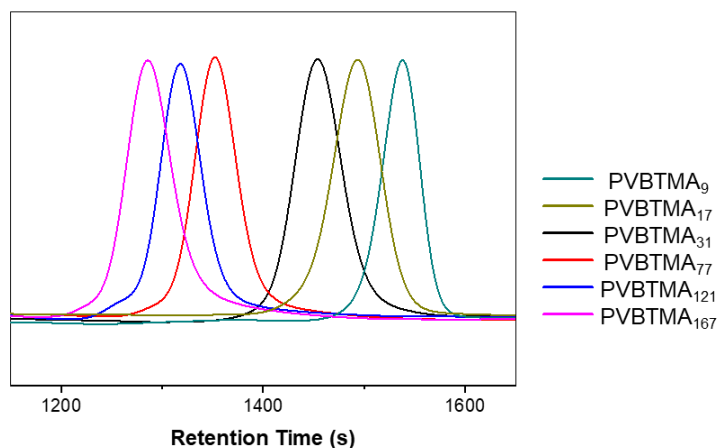


Figure 2. 3 GPC traces of PVBTMA.

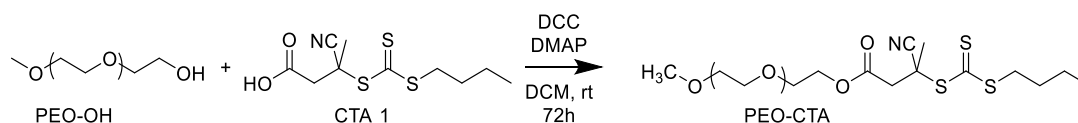
The molar ratio of Si-based CTA and initiator was kept at 10:1. By modulating the feed ratio of monomer, a series of PVBTMAs with molecular weights ranging from ~2 to ~35 kg/mol, were synthesized. They were characterized by GPC in 2,2,2-trifluoroethanol (TFE), using PMMA standards. Although PMMA is not the ideal standard, the GPC traces provide a reliable evaluation of dispersity and retention time comparisons between various PVBTMAs. Unimodal distribution was observed in all GPC traces as shown in Figure 2.3. In addition, end-group analysis was performed based on the integration of trimethyl silyl end-groups in ^1H NMR. The GPC and ^1H NMR analysis results are listed in Table 2.5.

2.3.3 Synthesis of Block-Polyelectrolytes, P(EO-*b*-VBTMA).

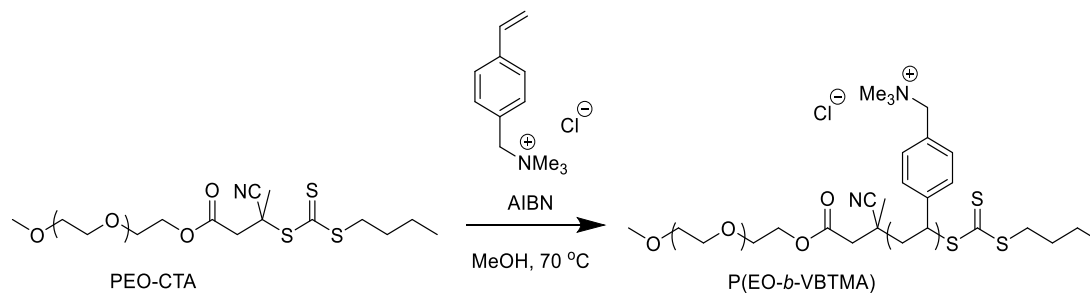
Having developed a reliable method for polyelectrolyte molecular weight determination, neutral-charged block polyelectrolytes, poly(ethylene oxide)-*b*-poly(vinylbenzyltrimethylammonium) (PEO-*b*-PVBTMA), were successfully synthesized via the route presented in Scheme 2.4.

Scheme 2. 4 Synthesis of Block Polyelectrolytes, P(EO-*b*-VBTMA).

Step 1:



Step 2:



Hydroxy-group terminated PEO (PEO-OH) was used as received. The other end of PEO is capped by an inert methoxy group. Esterification with excess CTA 1 with a carboxyl group and PEO-OH was performed at room temperature over three days in the presence of *N,N'*-dicyclohexylcarbodiimide (DCC) and 4-dimethylaminopyridine (DMAP). After precipitation, the excess reactants and side product dicyclohexylurea (DCU) was fully removed and the resulting PEO-CTA appears light yellow in color, indicating that the trithiocarbonate has been incorporated. As shown in Figure 2.4, ^1H NMR spectroscopy reveals the appearance of characteristic peaks from CTA, confirming the

formation of ester carbonyl group and the successful synthesis of PEO-CTA. The capping efficiency of CTA 1 was calculated from integration of peaks a, e, g, h, f, versus peak c, which was 85%.

Additionally, matrix assisted laser desorption ionization-time of flight mass spectrometry (MALDI-TOF) was used to confirm the structures of both PEO-OH and PEO-CTA, as shown in Figure 2.5A and Figure 2.6A, respectively. Accordingly, representative regions were expanded for clarification in Figure 2.5B and Figure 2.6B.

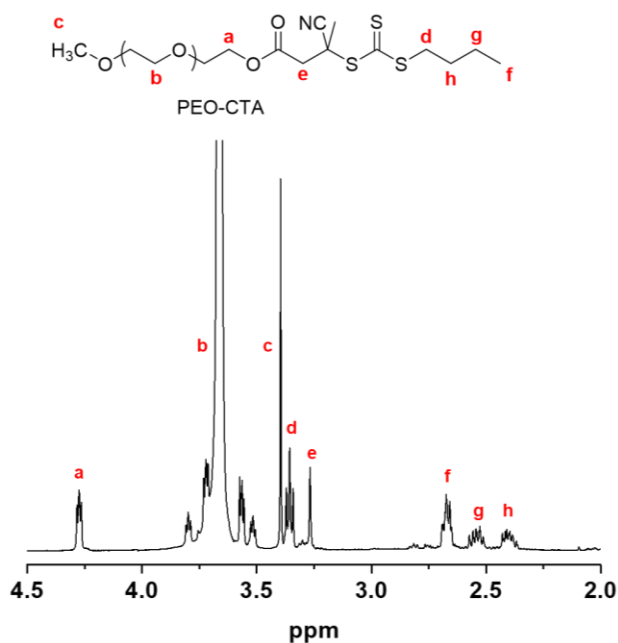


Figure 2. 4 ¹H NMR of PEO-CTA.

The mass spectra allow for a detailed structural characterization including the repeating unit chemistry and end-group determination.³³ Before CTA capping (Figure 2.5), PEO-OH exhibits two sets of peaks, each with an interval of ~44 m/z, which corresponds to the molecular weight of the ethylene oxide repeating unit. The individual DP for each peak is calculated by subtracting the molecular weights of adduct ions, either sodium or potassium, methoxy and hydroxide end-groups, then dividing the value by the molecular

weight of the ethylene oxide repeating unit. The DP calculation result for Figure 2.5B region is summarized in Table 2.2 as an example. Both the sodium and potassium cation adduct of PEO-OH were detected, corresponding to the two sets of peaks observed in Figure 2.5A and B. Peaks from end-group or backbone fragmentation were not observed, due to good chemical stability of end-group and backbone structures.

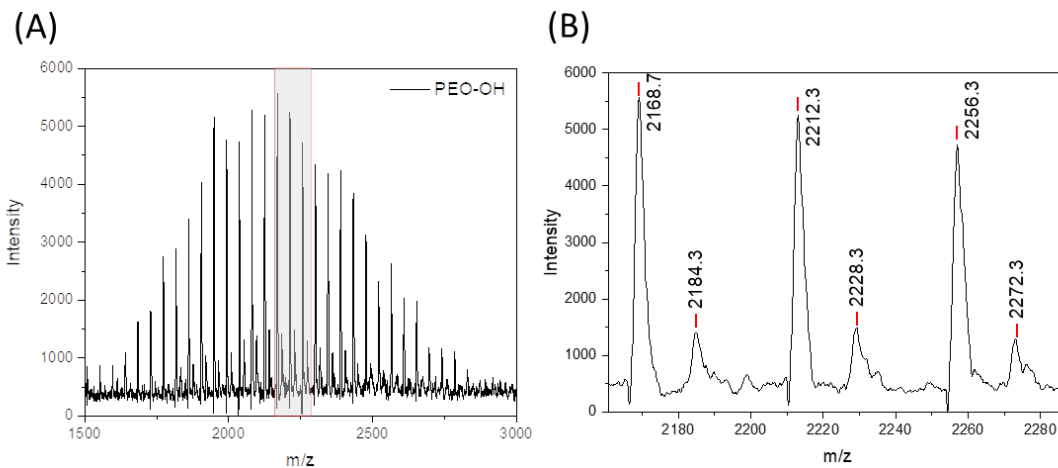


Figure 2. 5 (A) MALDI-TOF of PEO-OH and (B) a close-up of the squared region of the mass spectrum in (A).

Table 2. 2 Peak assignment from the PEO-OH ESI spectrum in Figure 2.5B

m/z	Structures	DP	Molecular mass (g/mol)
2168.7		47	2168
2184.3			2184
2212.3		48	2212
2228.3			2228
2256.3		49	2256
2272.3			2272

After CTA end capping, the PEO-CTA can undergo fracturing at either the ester groups or the tri-thiol carbonate positions, under the experimental conditions (ionization temperature over 200 °C), resulting in more sub-structures observed in Figure 2.6. Representative assignments of one primary and four fragmentation peaks from Figure 2.7B are listed in Table 2.3. Taking the molecular weights of the residual end-group structures into consideration, the specific DP was calculated and marked as subscripts in chemical structures. The corresponding molecular weights were summarized in Table 2.3 for comparison. The primary peak at 2189.9 m/z might be from protonated hydroxide terminated species. As the protonated PEO-OH peak was not observed in Figure 2.6A, this primary peak is presumably not from the unreacted precursor PEO-OH, but from the fractured PEO-CTA at the ester group instead. Fractionation of tri-thiol carbonate could result in two species, cyanide terminated PEO, whose lithium ion adduct was detected at 2206.7 m/z, and thiol terminated PEO. The peaks at 2210.1 and 2222.9 m/z are assigned to the sodium and potassium ion adducts of the thiol terminated PEO, respectively.

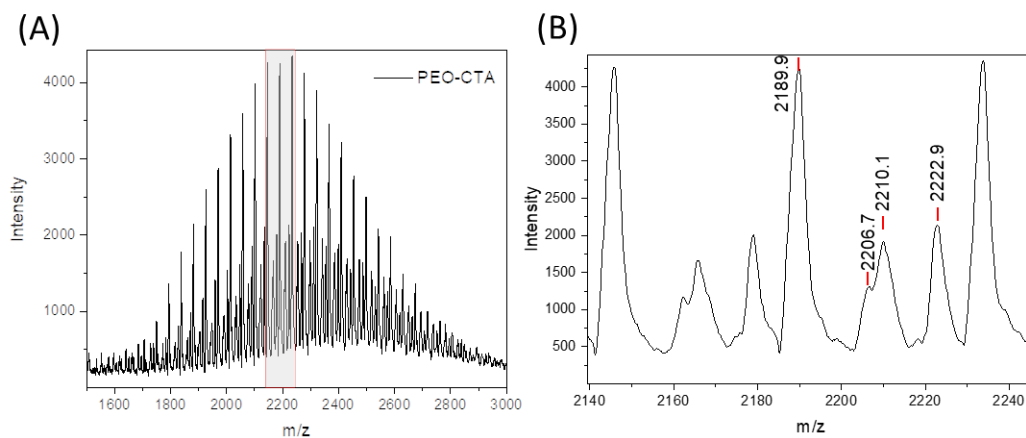


Figure 2. 6 (A) MALDI-TOF of PEO-CTA and (B) a close-up of the squared region of the mass spectrum in (A).

Table 2.3 Peak assignment from the PEO-CTA ESI spectrum in Figure 2.6B

m/z	Structures	Molecular mass (g/mol)
2189.9		2190
2206.7		2206
2210.1		2210
2222.9		2223

In the next step, macro PEO-CTA was subject to chain extension by polymerization with VBTMA to synthesize PEO-*b*-PVBTMA. After 12 h reaction, ~90% conversion was achieved. Following dialysis (molecular weight cut-off = 2 kDa) and lyophilization, a light yellow products were obtained. The color indicates the preservation of the end-functionalities after chain extension. By starting from PEO-OH with different molecular weights and changing the feeding ratio of the second monomer, VBTMA, during chain extension, various DP of PEO and PVBTMA can be achieved.

The block polyelectrolytes, PEO-*b*-PVBTMA, were characterized by GPC in TFE and ¹H NMR in D₂O. The GPC traces and ¹H NMR spectra are presented in Figure 2.7 and Figure 2.8, respectively. The characterization results are summarized in Table 2.5. Narrow dispersity (<1.1) was observed for all block copolymers, indicating living character provided by PEO macro-CTA. As shown in Figure 2.7, all three block copolymer peaks shifted to higher molecular weight position compared to that of the PEO₄₅-CTA, indicating the formation of block copolymer. Small shoulders were observed in all block copolymer GPC traces, which might be from trace amount of PEO homopolymer. The presence of PEO is probably due to the failure of fully converting all PEO into macro CTA precursor. The esterification efficiency is less than 100% after three days of reaction. A possible explanation for this may be that due to hydroxy end-group missing on some PEO, which precludes the full esterification.

As shown in Figure 2.8, peak m from PEO backbone was normalized by area, and peaks from PVBTMA block ($\delta = 7.5\text{-}6.5, 4.5\text{-}4.2, 3.3\text{-}2.7, 2.5\text{-}1.5$ ppm) increased with increasing DP. Peaks a~e were integrated and averaged to calculate DP (Table 2.5).

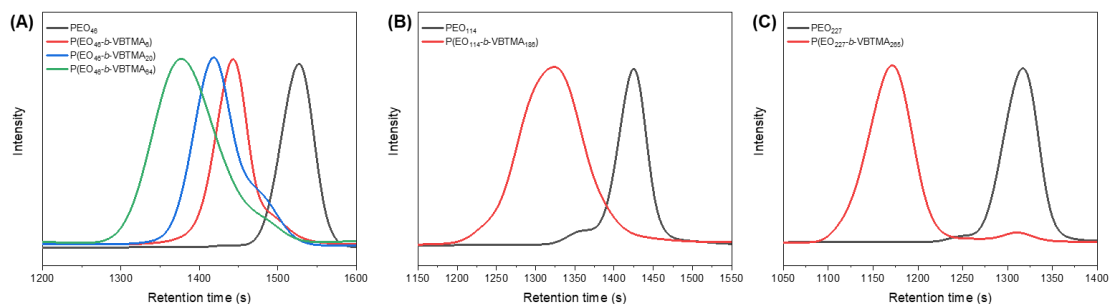


Figure 2. 7 GPC traces of P(EO-b-VBTMA) with different DPs of PEO and PVBTMA blocks.

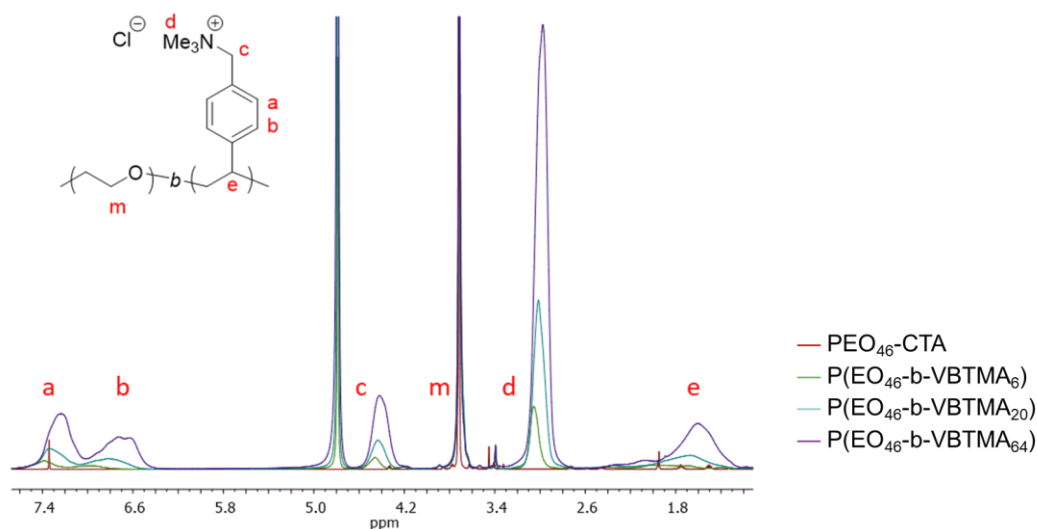


Figure 2. 8 ^1H NMR of P(EO-b-PVBTMA).

2.3.4 DOSY Characterization.

2.3.4.1 Homo-polyelectrolyte: PVBTMA

^1H NMR end-group analysis was performed to obtain the PVBTMA molecular weight (Figure 2.9A). The same D_2O solution was subject to DOSY measurement, which spread the ^1H NMR spectra along a second diffusion axis (Figure 2.9B). The projections of signals onto the diffusion axis indicate corresponding diffusion coefficients of specific chemical shifts.³⁴ Taking PVBTMA₁₂₁ as an example, only one dominant diffusion

coefficient for all characteristic peaks was observed in Figure 2.9B, because the DOSY spectra were analyzed by Dynamic Center software, where the diffusion dimension was generated using a Bayesian transform. However, this automatic processing method could overlook some diffusion modes with minor distribution. Therefore, further quantitative analysis was performed manually on peaks a, b, and c from the PVBTMA polymer backbone, which are free from overlap with solvents. The peak integration decay as a function of the diffusion gradient strength (G) was fit to a biexponential function as shown in Figure 2.9C and the results were listed in Table 2.4. Two diffusion times, t_1 and t_2 , can be detected, indicating the existence of two diffusion modes, the fast and the slow modes, respectively. All six PVBTMA solutions were characterized by DOSY. The same dilute polymer concentration (5 mg/ml) was adopted to ensure consistent viscosity and density conditions for all the measurements. The same biexponential fitting methodology was used to analyze the DOSY spectra and the results are listed in Table 2.5.

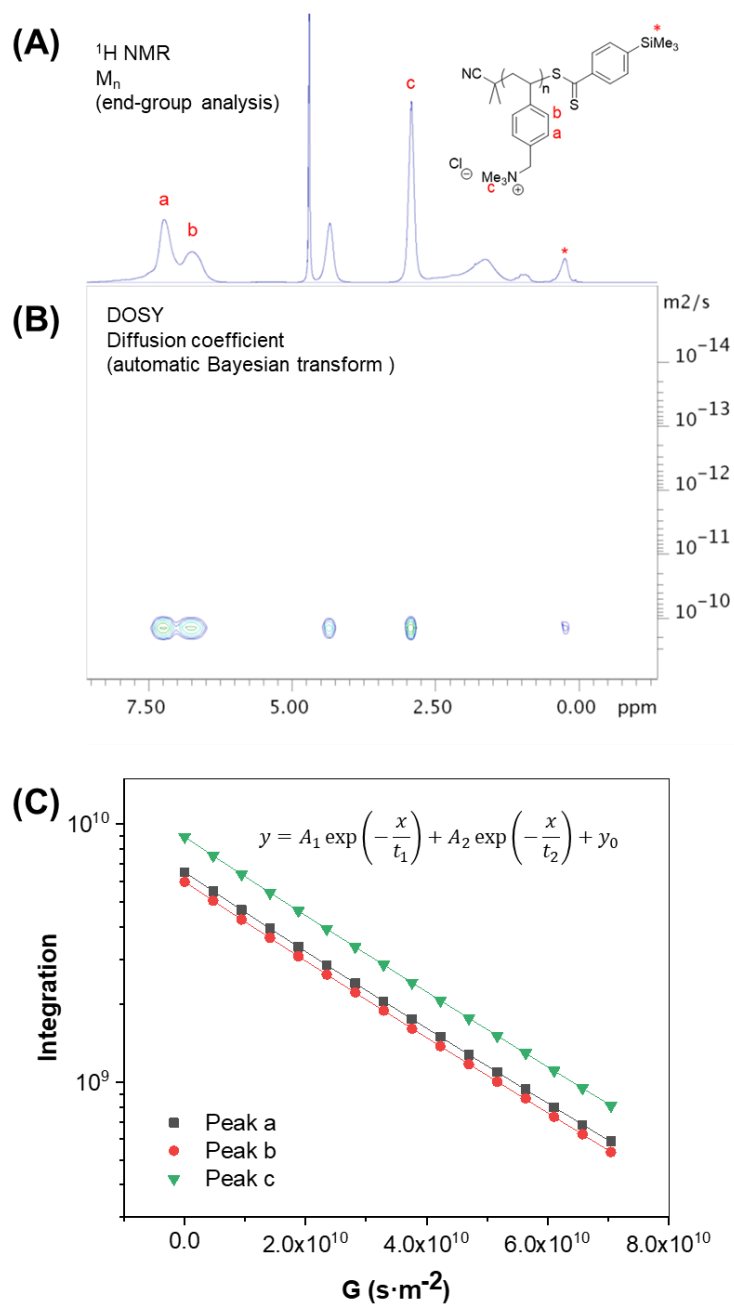


Figure 2. 9 (A) ^1H NMR spectra, (B) DOSY spectrum by automatic Bayesian transform, and (C) biexponential fitting curve of peak integration vs. diffusion gradient strength from characteristic peaks a, b, and c from PVBTMA121 in D_2O , with the concentration of 5 mg/ml.

Table 2. 4 PVBTMA₁₂₁ D₂O solutions DOSY biexponential analysis.

Peak	t_1 ($\times 10^9$)	D_1^a ($\times 10^{-11}$ m ² /s)	d^b (%)	A_1 ($\times 10^8$)	D_f^c ($\times 10^{-11}$ m ² /s)	t_2 ($\times 10^{10}$)	D_2^a ($\times 10^{-11}$ m ² /s)	d^b (%)	A_2 ($\times 10^9$)	D_s^c ($\times 10^{-11}$ m ² /s)
a	3.8	26.32	22.2	0.6	25.47	2.8	3.52	0.4	3.9	3.59
b	4.1	24.45	20.8	2.4		2.8	3.52	0.5	8.7	
c	3.9	25.63	38.1	1.1		2.7	3.72	2.9	5.5	

^a D_1 or D_2 was calculated by: $D = \frac{1}{t}$.

^b d , standard error.

^c D_f or D_s is the average of D_1 or D_2 of peaks a, b, c.

Table 2. 5 PVBTMA molecular weights, dispersity (\mathcal{D}) and diffusion coefficients in 5 mg/ml D₂O solutions.

Sample	¹ H NMR ^a	GPC ^b	DOSY ^c	
	M_n (g/mol)	\mathcal{D}	D_f ($\times 10^{-11}$ m ² /s)	D_s ($\times 10^{-11}$ m ² /s)
PVBTMA ₉	1,950	1.01	17.3 ± 0.0	17.3 ± 0.0
PVBTMA ₁₇	3,660	1.03	29.1 ± 16.9	13.5 ± 0.3
PVBTMA ₃₁	7,710	1.03	30.2 ± 21.3	8.6 ± 0.2
PVBTMA ₇₇	16,390	1.03	23.4 ± 14.0	4.8 ± 0.2
PVBTMA ₁₂₁	25,700	1.04	25.5 ± 9.7	3.6 ± 0.1
PVBTMA ₁₆₇	35,400	1.07	22.2 ± 7.3	2.6 ± 0.1

^a M_n calculated from ¹H NMR end-group analysis.

^bDispersity (\mathcal{D}) from GPC.

^cDiffusion coefficients of the fast mode (D_f) and the slow mode (D_s) measured by DOSY.

In addition to the diffusion time, from the biexponential fitting, the value of $\frac{A_2}{A_1}$ reflects the ratio between the polyelectrolytes in the slow mode and in the fast mode, which is more than 25 for all PVBTMA solutions. Therefore, more than 95% of the chains form polyelectrolyte aggregates in the dilute D₂O solutions, regardless of molecular weights. Less than 5% of the polymers stay as single chains in the solution. The small ratio of the fast-mode polymer chains leads to inaccuracies during the biexponential fitting for the fast mode term and resulted in much larger standard errors for D_f measurements than D_s in Table 2.4, as well as much larger error bars for D_f (■) than D_s (●) in Figure 2.10.

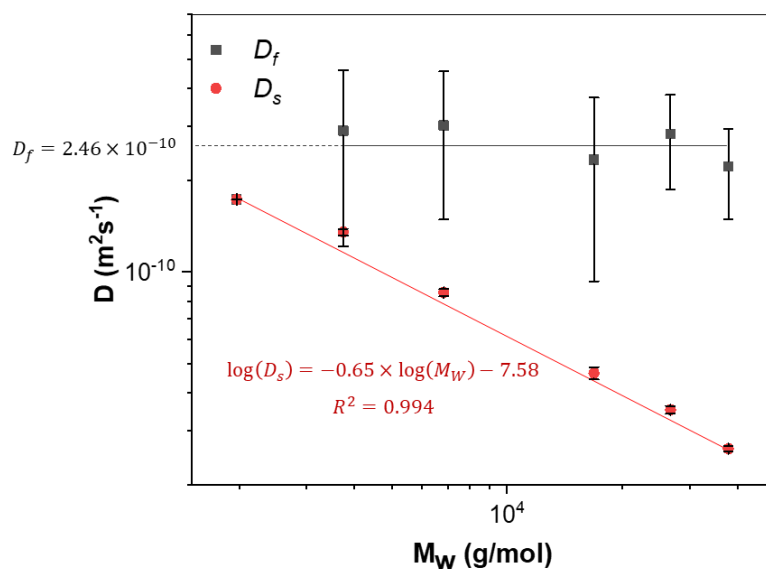


Figure 2. 10 Dependence of fast diffusion coefficient D_f (■) and slow diffusion coefficient D_s (●) on polyelectrolyte molecular weights. PVBTMA in D₂O, with concentration of 5 mg/ml.

The D_s shows a logarithmic-linear relationship with the PVBTMA molecular weight. The slope was calculated to be -0.65 for the dilute D₂O solutions for the molecular

weight ranging from $\sim 10^3$ to $\sim 10^4$ g/mol. In contrast, the D_f has been found to be independent of the molecular weight, with the average diffusion coefficient of 2.46×10^{-10} m^2/s^{-1} , which is in agreement with the D_f measured by light scattering for salt-free polyelectrolyte solutions in the literature and based on theories established over the past four decades.^{1,7,35} When the D_s keeps increasing with the decrease of molecular weights, the D_s and D_f become very close to each other and eventually not distinguishable for the molecular weight of ~ 1.9 kg/mol, where two diffusion coefficients overlapped in Figure 2.10.

2.3.4.2 Block-polyelectrolyte: P(EO-*b*-VBTMA)

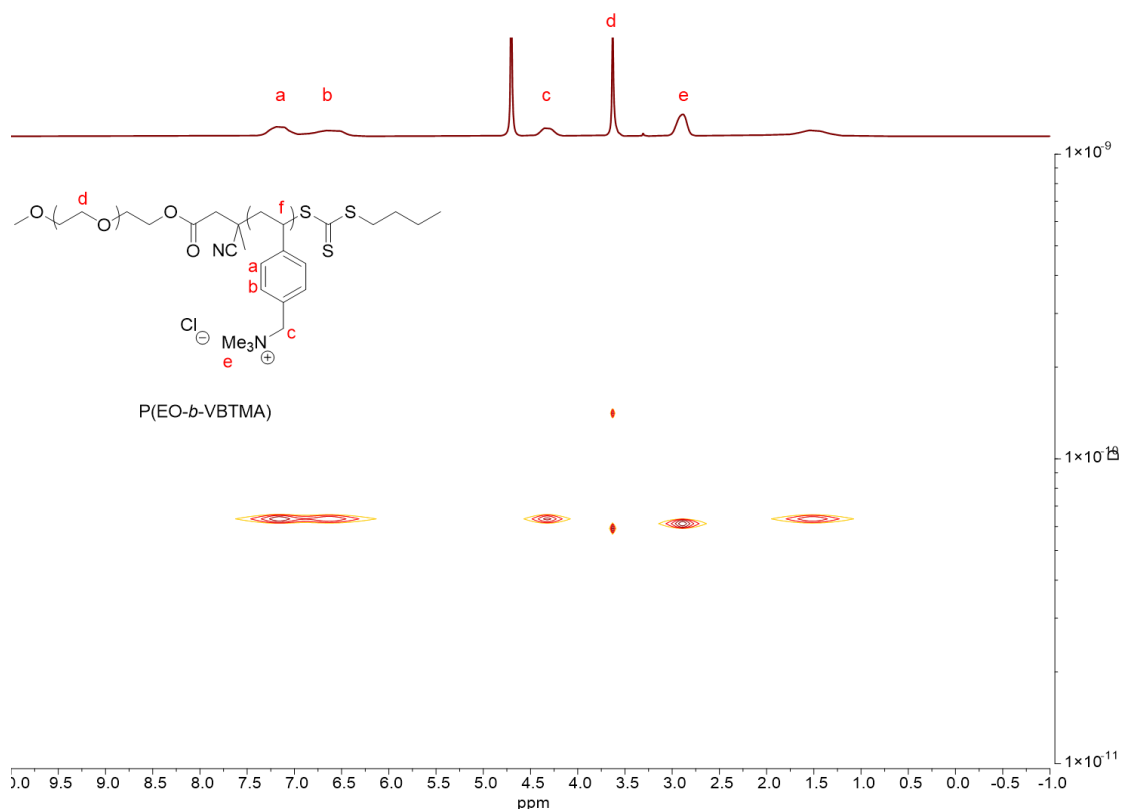


Figure 2. 11 DOSY spectra of P(EO₄₆-*b*-VBTMA₆₄).

Drastic difference was observed between the diffusion behaviors of PEO neutral block than that of the PVBTMA block in block polyelectrolyte D₂O solutions, even though the two blocks are connected by covalent bonds. A representative DOSY spectrum of P(EO₄₆-*b*-VBTMA₆₄) is shown in Figure 2.11, where PEO exhibits two distinct diffusion modes (Figure 2.11, peak *d*) but PVBTMA appears dominant with just one diffusion coefficient (Figure 2.11, peaks *a-c*, *e*). Based on the PVBTMA homo-polyelectrolyte investigation discussed above, a possible explanation is that the slow mode is still the majority for the PVBTMA block in block-polyelectrolyte solutions, as it was in the homo-polyelectrolyte system. The following discussion will be focused on the diffusion behavior of PEO.

In the solution, the diffusion behaviors of PEO moieties are dependent on polymer chemical structures (either a homopolymer or a block copolymer) as well as polyelectrolyte intermolecular physical structures. Due to incomplete conversion of modifying all PEO-OH into macro CTA precursor and the nature of RAFT polymerization,³¹ a small amount of PEO homopolymer is left in the system after chain extension, as observed in GPC traces for P(EO-*b*-VBTMA) in Figure 2.8. For the PEO covalently bonded with the PVBTMA block, there are various species with different diffusion modes. First, similar to the fast mode in homo-polyelectrolyte solution, the single chains of block polyelectrolytes also exist in the D₂O solutions. But the PEO block on the fast-mode block polyelectrolytes will not be affected by counterions as much as the electrolyte block. In the case of the block polyelectrolytes aggregates, the PEO restrained inside the PVBTMA aggregates display a similar diffusion mode as the electrolyte block, therefore, having a diffusion coefficient close to D_s . However, the P(EO-*b*-VBTMA) aggregates can form micelle structures,³⁶

where some PEO chains covalently attached to the aggregate still have one free end toward outside, resulting in a more mobile diffusion mode. The diffusion coefficient of those PEO chains can also be affected by the ratio between the volumes free from, and restrained within the aggregates. Therefore, there are differences from D_s or D_f of the electrolyte block.

The apparent diffusion behaviors of PEO is a collective result from at least four forms of PEO discussed above. As a result, a complicated signal decay along with the diffusion gradient strength was observed. Even though the signal decay of PEO block in DOSY is a result from multi-diffusion modes, the biexponential fitting methodology can be a basic approximation to start with, in order to fully understand the diffusion behavior of the PEO block in block polyelectrolyte solutions. Therefore, the methylene (CH_2) peak on PEO ($\delta \sim 3.7$ ppm) was analyzed to yield two diffusion coefficients, as shown in Tables 2.6, 2.7 and Figures 2.12, 2.14.

P(EO_{46} -*b*-VBTMA) with the same DP_{PEO} and various $\text{DP}_{\text{PVBTMA}}$:

A series of P(EO_{46} -*b*-VBTMA) copolymers chain extended from the same PEO_{46} were first investigated to study the effect from the polyelectrolyte block molecular weight on diffusion behaviors of the neutral PEO block. A schematic of the structure comparison is present in Figure 2.13.

As shown in Figure 2.12, the negative correlation between the molecular weight and D_s observed in homo-polyelectrolytes still stand for block-polyelectrolytes. The serious inaccuracy during the diffusion coefficient measurement of P(EO_{46} -*b*-VBTMA₆) with the shortest PVBTMA block ($\text{DP}_{\text{PVBTMA}} = 6$) might indicate the instability of the aggregates, during the early phase of block polyelectrolyte aggregates formation. A longer

PVBTMA block contributes to a larger enthalpy term due to stronger Columbic interactions, which favors the formation of aggregates. Therefore, better accuracy was obtained during the measurements for P(EO₄₆-*b*-VBTMA₂₀) and P(EO₄₆-*b*-VBTMA₆₄).

Table 2. 6 P(EO₄₆-*b*-VBTMA) chemical compositions and diffusion coefficients of the PEO block.

Sample ^a	GPC ^b	DOSY ^c	
	\bar{D}	$D_f (\times 10^{-11} \text{ m}^2/\text{s})$	$D_s (\times 10^{-11} \text{ m}^2/\text{s})$
PEO ₄₆ -CTA	1.07	11.2 ± 0.0	-
P(EO ₄₆ - <i>b</i> -VBTMA ₆)	1.03	12.0 ± 1.7	8.7 ± 1.3
P(EO ₄₆ - <i>b</i> -VBTMA ₂₀)	1.06	12.3 ± 0.5	8.0 ± 0.2
P(EO ₄₆ - <i>b</i> -VBTMA ₆₄)	1.10	14.2 ± 0.3	6.0 ± 0.1

^aThe DPs of PEO and PVBTMA are marked as footnotes, respectively.

^bDispersity obtained from TFE GPC.

^cDiffusion coefficients of the fast mode (D_f) and the slow mode (D_s) of the PEO block measured by DOSY.

It is surprising that the D_f of the PEO block appears larger than the diffusion coefficient of PEO homopolymer before chain extension. This “acceleration effect” from the PVBTMA block was observed for all three block polyelectrolyte solutions, in comparison to the diffusion coefficient of the corresponding PEO macro-precursor ($D_{PEO} = 1.12 \times 10^{-10} \text{ m}^2/\text{s}^{-1}$). Even though the D_f of PVBTMA is $\sim 2.46 \times 10^{-10} \text{ m}^2/\text{s}^{-1}$, independent of molecular weight, or DP. When a PVBTMA block is covalently connected to a PEO block with a slower diffusion rate, the “acceleration effect” from PVBTMA on the PEO block can be affected by the DP of PVBTMA (DP_{PVBTMA}). For the same DP of the PEO

block (DP_{PEO}), a larger DP_{PVBTMA} leads to a larger D_f of the PEO block, indicating greater “acceleration effect”, as shown in Figure 2.12.

It has been demonstrated that in the homo-polyelectrolyte, PVBTMA, solutions, the D_s can get very close to the D_f at lower molecular weights. The two diffusion modes were not distinguishable when $DP = 9$, or molecular weight is ~ 1.9 kg/mol. However, the attachment with PEO block can facilitate the aggregate formation, even for a very short PVBTMA chain with $DP = 6$, where two distinct diffusion modes can be observed (Figure 2.13).

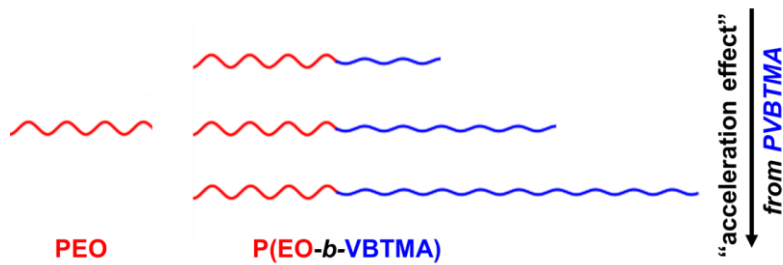


Figure 2. 12 Schematic of PEO homopolymer and P(EO-*b*-VBTMA) neutral-block copolymer with the same PEO block and different molecular weights of the PVBTMA blocks. The “acceleration effect” from PVBTMA blocks on the fast-mode PEO blocks increases with the molecular weight.

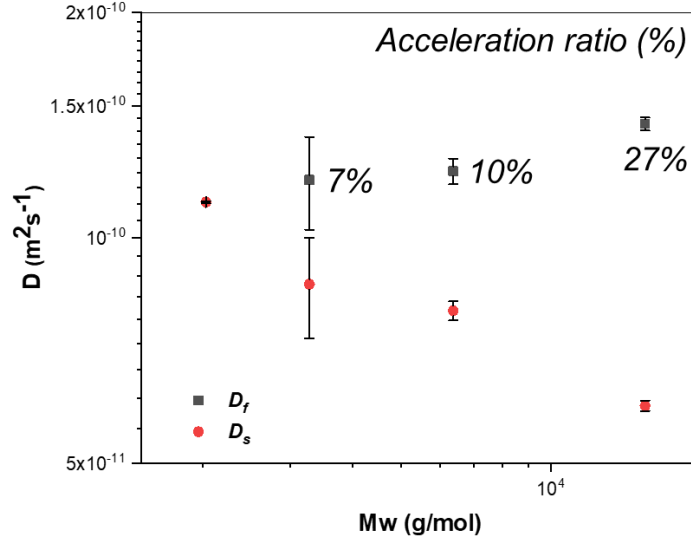


Figure 2.13 Dependence of D_f (■) and D_s (●) of P(EO₄₆-*b*-VBTMA), with the same $DP_{PEO} = 46$ and different DP_{VBTMA} , = 0, 6, 20, 64, on molecular weights.

$$Acceleration\ ratio = \frac{D_f - D_{PEO\ homopolymer}}{D_{PEO\ homopolymer}} \times 100\%.$$

P(EO-*b*-VBTMA) with a similar $\frac{DP_{PEO}}{DP_{VBTMA}}$ and various molecular weights:

The following discussion involves the diffusion characterization of three block polyelectrolytes with similar DP ratio of ethylene oxide and VBTMA but different overall molecular weights, P(EO₄₆-*b*-VBTMA₆₄), P(EO₁₁₄-*b*-VBTMA₁₈₆), and P(EO₂₂₇-*b*-VBTMA₂₆₅), as shown in Figure 2.15 for the structure comparison schematic. The block polymers are equipped with the PVBtMA block as the “engine”, able to form stable aggregates in their slow mode, meanwhile in their fast mode, diffuse much faster and bring the “acceleration effect” on the neutral block. On the other hand, the polymers are loaded with the PEO block with a proportionally smaller size as the “cargo”. The comparison between these three P(EO-*b*-VBTMA) is intended to reveal the effect from polymer sizes,

or molecular weights, on the diffusion coefficients of the PEO block. The diffusion coefficient measurement results are present in Table 2.7 and Figure 2.14. The DP_{PVBTMA} versus the DP_{PEO} are 1.4, 1.6, and 1.2, respectively.

Table 2. 7 P(EO-*b*-VBTMA) chemical compositions and diffusion coefficients of the PEO block.

Sample ^a	GPC ^b	DOSY ^c	
	\bar{D}	D_f ($\times 10^{-11}$ m ² /s)	D_s ($\times 10^{-11}$ m ² /s)
PEO ₄₆	1.01	11.2 ± 0.0	-
P(EO ₄₆ - <i>b</i> -VBTMA ₆₄)	1.10	14.2 ± 0.3	6.0 ± 0.1
PEO ₁₁₄	1.04	7.9 ± 0.1	-
P(EO ₁₁₄ - <i>b</i> -VBTMA ₁₈₆)	1.12	8.8 ± 0.3	3.3 ± 0.0
PEO ₂₂₇	1.04	6.1 ± 0.0	-
P(EO ₂₂₇ - <i>b</i> -VBTMA ₂₆₅)	1.12	5.8 ± 0.1	0.9 ± 0.1

^aThe DPs of PEO and PVBTMA are marked as footnotes, respectively.

^bDispersity obtained from TFE GPC.

^cDiffusion coefficients of the fast mode (D_f) and the slow mode (D_s) of the PEO block measured by DOSY.

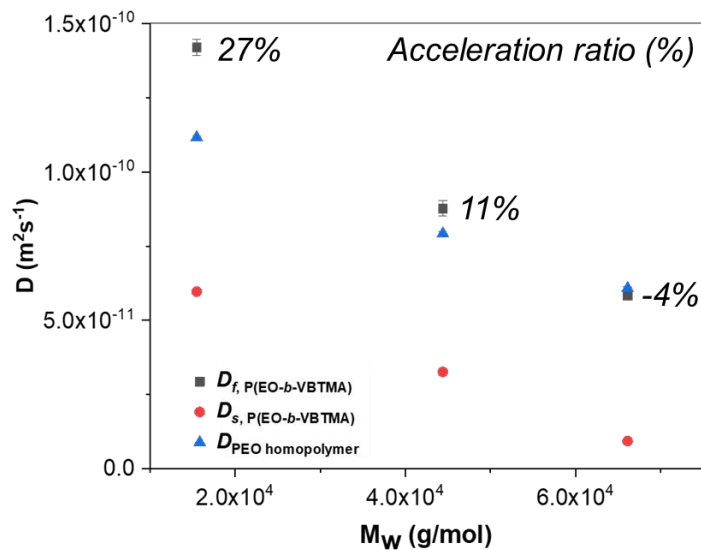


Figure 2. 14 Dependence of D_f (■) and D_s (●) of P(EO-*b*-VBTMA), with similar DP ratios of the PEO block versus the PVBTMA block, on molecular weights. The diffusion coefficient of the PEO macro-precursor, $D_{PEO\ homopolymer}$ (▲), was also plotted against the molecular weight of the corresponding P(EO-*b*-VBTMA) after chain extension.

As shown in Figure 2.14, the linear relationship between the diffusion coefficients of the PEO block and the molecular weights was observed for both the fast mode and the slow mode. The diffusion coefficients of the PEO macro-precursors ($D_{PEO\ homopolymer}$) were also plotted in Figure 2.14 for comparison. Please note the molecular weight (x axis) does not correspond to the molecular weight of PEO, but to that of the P(EO-*b*-VBTMA) after chain extension, in order for easier comparison. It has been discussed that the D_f of PVBTMA homo-polyelectrolyte is $\sim 2.46 \times 10^{-10} \text{ m}^2/\text{s}^{-1}$, independent on molecular weight. However, after a PVBTMA chain is covalently connected to a neutral PEO chain, the PVBTMA block in the fast mode brings the “acceleration effect” to the PEO block, resulting in a faster diffusion coefficient than a sole PEO homopolymer chain in solution.

On the other hand, an increase of PEO molecular weight leads to a larger friction factor, driving the diffusion coefficient to decrease, as a “deceleration effect”. The D_f in Figure 2.14 is a coupling result from these two antagonistic effects. As a result, the D_f of the PEO block is larger than the corresponding $D_{PEO \text{ homopolymer}}$ for P(EO₄₆-*b*-VBTMA₆₄) and P(EO₁₁₄-*b*-VBTMA₁₈₆). Nevertheless, the “acceleration effect” from the PVBTMA block was leveraged by “deceleration effect” from the PEO block at molecular weight ~66 kg/mol, leading to the diffusion coefficient similarity of the PEO blocks either with or without a proportional PVBTMA block.

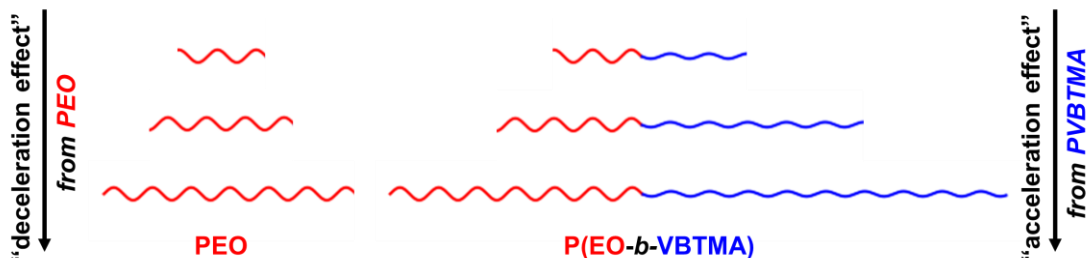


Figure 2. 15 Schematic of PEO homopolymer and P(EO-*b*-VBTMA) neutral-block copolymer with the same $\frac{DP_{PEO}}{DP_{VBTMA}}$ and different molecular weights. The “acceleration effect” from PVBTMA as well as the “deceleration effect” from PEO on the fast-mode PEO blocks increases with the molecular weight.

2.4 Conclusions

A novel silicon-based chain transfer agent (Si-based CTA) was synthesized to mediate RAFT polymerization, yielding greatly improved accuracy of molecular weight determination in ¹H NMR end-group analysis. A series of poly(vinylbenzyltrimethylammonium) (PVBTMA) with different molecular weights were

synthesized with Si-based CTA and characterized by diffusion-ordered spectroscopy (DOSY). Fast and slow modes with different diffusion coefficients were detected and their relationship with molecular weights were studied. The diffusion coefficient of the fast mode (D_f), resulted from the diffusion of single polyelectrolyte chains and counterions, shows independence on molecular weights. The diffusion coefficient of the slow mode (D_s), from large polyelectrolyte aggregates, show inverse logarithmic-linear correlation with molecular weights ($\log D_s \propto -0.65 \times \log M_w$). Neutral-charged block copolymers of ethylene oxide and vinylbenzyltrimethylammonium, P(EO-*b*-VBTMA), were synthesized. The diffusion behavior of the PEO block was investigated. The PEO attached to the aggregates presents a slow diffusion mode. Whereas in the fast mode, the “acceleration effect” from the PVBTMA block on the PEO block was observed, *i.e.* the diffusion rate of PEO in the block polyelectrolyte was faster than the PEO block alone as a homopolymer. The “acceleration effect” is dependent on the molecular weights of PVBTMA, which is in contrast to the independence of the homo-polyelectrolyte D_f on molecular weights. For the block polyelectrolytes with a similar degree of polymerization (DP) ratio between ethylene oxide and VBTMA, by increasing the molecular weight, the “deceleration effect” from the PEO block effectively leverages the “acceleration effect” from the PVBTMA block, resulting in a similar diffusion coefficient of PEO in the block polyelectrolyte to the corresponding PEO homopolymer at ~66 kg/mol. Future studies will be required to explore the diffusion behavior of neutral-charged block polyelectrolytes in solutions with added salts. The addition of salt can screen the interactions and gradually destabilize polyelectrolyte aggregates.¹⁵ DOSY technique can be utilized to monitor the transitions of

the intermolecular structural formed by P(EO-*b*-VBTMA) along the salt concentration change.

2.5 References

- (1) Muthukumar, M. 50th Anniversary Perspective: A Perspective on Polyelectrolyte Solutions. *Macromolecules* **2017**, *50* (24), 9528–9560.
- (2) Prabhu, V. M. Counterion Structure and Dynamics in Polyelectrolyte Solutions. *Curr. Opin. Colloid Interface Sci.* **2005**, *10* (1), 2–8.
- (3) Sedlák, M. What Can Be Seen by Static and Dynamic Light Scattering in Polyelectrolyte Solutions and Mixtures? *Langmuir* **1999**, *15* (12), 4045–4051.
- (4) Lin, S. -C S.-C.; Lee, W. I.; Schurr, J. M. Brownian Motion of Highly Charged Poly(L-lysine). Effects of Salt and Polyion Concentration. *Biopolymers* **1978**, *17* (4), 1041–1064.
- (5) Chen, K.; Zheng, K.; Xu, G.; Yang, J.; Zhao, J. Diffusive Motion of Single Polyelectrolyte Molecules under Electrostatic Repulsion. *Macromolecules* **2019**, *52* (10), 3925–3934.
- (6) Sehgal, A.; Seery, T. A. P. The Ordinary-Extraordinary Transition Revisited: A Model Polyelectrolyte in a Highly Polar Organic Solvent. *Macromolecules* **1998**, *31* (21), 7340–7346.
- (7) Sedlák, M.; Amis, E. J. Dynamics of Moderately Concentrated Salt-Free Polyelectrolyte Solutions: Molecular Weight Dependence. *J. Chem. Phys.* **1992**, *96*

- (1), 817–825.
- (8) Prabhu, V. M.; Muthukumar, M.; Wignall, G. D.; Melnichenko, Y. B. Dimensions of Polyelectrolyte Chains and Concentration Fluctuations in Semidilute Solutions of Sodium-Poly(Styrene Sulfonate) as Measured by Small-Angle Neutron Scattering. *Polymer (Guildf)*. **2001**, *42* (21), 8935–8946.
- (9) Zhang, Y.; Douglas, J. F.; Ermi, B. D.; Amis, E. J. Influence of Counterion Valency on the Scattering Properties of Highly Charged Polyelectrolyte Solutions. *J. Chem. Phys.* **2001**, *114* (7), 3299–3313.
- (10) Prabhu, V. M.; Muthukumar, M.; Wignall, G. D.; Melnichenko, Y. B. Polyelectrolyte Chain Dimensions and Concentration Fluctuations near Phase Boundaries. *J. Chem. Phys.* **2003**, *119* (7), 4085–4098.
- (11) Förster, S.; Schmidt, M.; Antonietti, M. Static and Dynamic Light Scattering by Aqueous Polyelectrolyte Solutions: Effect of Molecular Weight, Charge Density and Added Salt. *Polymer (Guildf)*. **1990**, *31* (5), 781–792.
- (12) Nishida, K.; Kaji, K.; Kanaya, T.; Shibano, T. Added Salt Effect on the Intermolecular Correlation in Flexible Polyelectrolyte Solutions: Small-Angle Scattering Study. *Macromolecules* **2002**, *35* (10), 4084–4089.
- (13) Jia, D.; Muthukumar, M. Effect of Salt on the Ordinary-Extraordinary Transition in Solutions of Charged Macromolecules. *J. Am. Chem. Soc.* **2019**, *141* (14), 5886–5896.

- (14) Sehgal, A.; Seery, T. A. P. The Ordinary–Extraordinary Transition Revisited: A Model Polyelectrolyte in a Highly Polar Organic Solvent. *Macromolecules* **1998**, *31* (21), 7340–7346.
- (15) Förster, S.; Schmidt, M. Polyelectrolytes in Solution. *Adv. Polym. Sci.* **1995**, *120*, 51–133.
- (16) Muthukumar, M. Collective Dynamics of Semidilute Polyelectrolyte Solutions with Salt. *J. Polym. Sci. Part B Polym. Phys.* **2019**, 1263–1269.
- (17) Tivant, P.; Turq, P.; Drifford, M.; Magdelenat, H.; Menez, R. Effect of Ionic Strength on the Diffusion Coefficient of Chondroitin Sulfate and Heparin Measured by Quasielastic Light Scattering. *Biopolymers* **1983**, *22* (2), 643–662.
- (18) Meller, A.; Nivon, L.; Branton, D. Voltage-Driven DNA Translocations through a Nanopore. *Phys. Rev. Lett.* **2001**, *86* (15), 3435–3438.
- (19) Muthukumar, M. Phase Diagram of Polyelectrolyte Solutions: Weak Polymer Effect. *Macromolecules* **2002**, *35* (24), 9142–9145.
- (20) Lee, C.-L.; Muthukumar, M. Phase Behavior of Polyelectrolyte Solutions with Salt. *J. Chem. Phys.* **2009**, *130* (2), 24904.
- (21) Mori, S. Secondary Effects in Aqueous Size Exclusion Chromatography of Sodium Poly(Styrenesulfonate) Compounds. *Anal. Chem.* **1989**, *61* (6), 530–534.
- (22) Liu, Y.; Fratini, E.; Baglioni, P.; Chen, W.-R.; Chen, S.-H. Effective Long-Range Attraction between Protein Molecules in Solutions Studied by Small Angle Neutron

- Scattering. *Phys. Rev. Lett.* **2005**, *95* (11), 118102.
- (23) Sedláč, M.; Amis, E. J. Concentration and Molecular Weight Regime Diagram of Salt-Free Polyelectrolyte Solutions as Studied by Light Scattering. *J. Chem. Phys.* **1992**, *96* (1), 826–834.
- (24) Scheler, U. NMR on Polyelectrolytes. *Curr. Opin. Colloid Interface Sci.* **2009**, *14* (3), 212–215.
- (25) Holappa, S.; Karesoja, M.; Shan, J.; Tenhu, H. Solution Properties of Linear and Branched Block Copolymers Consisting of Acidic and PEO Blocks. *Macromolecules* **2002**, *35* (12), 4733–4738.
- (26) Sinha, V. R.; Singla, A. K.; Wadhawan, S.; Kaushik, R.; Kumria, R.; Bansal, K.; Dhawan, S. Chitosan Microspheres as a Potential Carrier for Drugs. *Int. J. Pharm.* **2004**, *274* (1), 1–33.
- (27) Kumar, M. N. V. R.; Muzzarelli, R. A. A.; Muzzarelli, C.; Sashiwa, H.; Domb, A. J. Chitosan Chemistry and Pharmaceutical Perspectives. *Chem. Rev.* **2004**, *104* (12), 6017–6084.
- (28) Gondi, S. R.; Vogt, A. P.; Sumerlin, B. S. Versatile Pathway to Functional Telechelics via RAFT Polymerization and Click Chemistry. *Macromolecules* **2007**, *40* (3), 474–481.
- (29) Bouhadir, G.; Legrand, N.; Quiclet-Sire, B.; Zard, S. Z. A New Practical Synthesis of Tertiary S-Alkyl Dithiocarbonates and Related Derivatives. *Tetrahedron Lett.*

- 1999**, *40* (2), 277–280.
- (30) Moad, G.; Chong, Y. K.; Postma, A.; Rizzardo, E.; Thang, S. H. Advances in RAFT Polymerization: The Synthesis of Polymers with Defined End-Groups. *Polymer (Guildf)*. **2005**, *46* (19), 8458–8468.
- (31) Perrier, S. 50th Anniversary Perspective: RAFT Polymerization - A User Guide. *Macromolecules* **2017**, *50* (19), 7433–7447.
- (32) Keddie, D. J.; Moad, G.; Rizzardo, E.; Thang, S. H. RAFT Agent Design and Synthesis. *Macromolecules* **2012**, *45* (13), 5321–5342.
- (33) Weidner, S. M.; Trimpin, S. Mass Spectrometry of Synthetic Polymers. *Anal. Chem.* **2008**, *80* (12), 4349–4361.
- (34) Cohen, Y.; Avram, L.; Frish, L. Diffusion NMR Spectroscopy in Supramolecular and Combinatorial Chemistry: An Old Parameter - New Insights. *Angew. Chemie - Int. Ed.* **2005**, *44* (4), 520–554.
- (35) Muthukumar, M. Ordinary-Extraordinary Transition in Dynamics of Solutions of Charged Macromolecules. *Proc. Natl. Acad. Sci. U. S. A.* **2016**, *113* (45), 12627–12632.
- (36) Stuart, M. A. C.; Hofs, B.; Voets, I. K.; Keizer, A. De. Assembly of Polyelectrolyte-Containing Block Copolymers in Aqueous Media. *Curr. Opin. Colloid Interface Sci.* **2005**, *10*, 30–36.

CHAPTER 3

NEUTRAL – CHARGED BLOCK COPOLYMER MEMBRANES: BULK AND SURFACE MORPHOLOGY AND THE EFFECTS ON CONNECTIVITY

3.1 Introduction

Anion exchange membranes (AEMs) have attracted significant research interest for application in alkaline fuel cells.¹⁻³ Compared to the acidic environment of proton exchange membrane (PEM) fuel cells, AEM allows for reduced loading of expensive platinum catalyst, or replacement by silver or gold.⁴ Despite the similar transport mechanisms in both AEMs and PEMs,⁵ including Grotthuss transfer,^{6,7} surface-site hopping,^{7,8} and diffusion,⁹ AEMs exhibit lower overall conductivity at today's level of development. In pursuit of higher conductivity, fundamental studies on membrane structure-property relationship are needed. Nafion[®] is the current state-of-the-art PEM and a benchmark for future membrane development, however, its random sulfonated backbone structure makes interpretation of scattering data difficult. Although several models have accurately described the scattering characteristics, they are still under debate.¹⁰⁻¹² On the contrary, ion-containing block copolymers provide tunable ordered morphologies, thus, can serve as a model system for morphology-channel connectivity study, which leads to the ultimate goal of achieving a favorable ion transport environment and improving conductivity.

To date, the most commonly characterized AEMs are quaternary ammonium based polymers because of the facile synthesis routes established in the literature.³ However, quaternary ammonium containing polymers lack long term stability in alkaline

environment.¹³⁻¹⁶ One method to improve stability is by utilizing bulky quaternary phosphonium (QP) cations. These larger functional groups provide steric hindrance, which inhibits degradation.¹⁷⁻¹⁹ In addition, QP polymers are solvent processable, showing solubility in DMF, alcohols, toluene, dichloromethane and chloroform, which makes them promising candidates for not only fuel cell membranes, but also ionomeric binder materials at the catalyst layer.¹⁶ Furthermore, the basicity of phosphonium hydroxide was higher than the ammonium counterpart, which contributes to higher hydroxide conductivity.¹⁶ Although these findings have established important design principles for AEM materials, structural characterization revealing the impact of chemical modifications on size, shape, and connectivity of the ionic domains still needs further investigation.

Zhang *et al.* synthesized block copolymers of polyisoprene and quaternary phosphonium containing styrenic block (PIp-*b*-P(R₃P⁺)MS).²⁰ Membranes with a range of ion exchange capacities (IECs) were prepared. Lamellar and hexagonal morphologies were observed from SAXS and TEM, at low to moderate IECs. Bulk chloride ion conductivities were then correlated with the morphology. Higher conductivity was achieved for a hexagonal morphology over lamellar morphology at similar IECs, likely a result of improved channel connectivity. We expand on this work by developing a new synthetic strategy to achieve higher IEC (0.87-2.35 mmol/g) phosphonium diblock copolymers by utilizing nitroxide-mediated radical polymerization (NMP) and implementing a smaller quaternization agent. The bulk and surface phase behaviors of neutral block copolymers have been studied, but detailed understanding of charged block copolymers is still rather incomplete. Experimental and computational analysis have shown charge cohesion effects can induce the formation of nanostructures that are inaccessible to conventional uncharged

block copolymers, depending on the charge fraction.²¹⁻²⁵ Hybrid self-consistent field theory and liquid state theory (SCFT-LS) models have recently shown that chain length, charge fraction, charge size, and the strength of Coulombic interactions can lead to considerable morphology shifts.²⁵⁻³² What has not been addressed is a comprehensive comparison between the bulk and surface morphologies as a function of quaternization level. Bulk and surface morphologies of PIP-*b*-P(R₃P⁺)MS membranes were investigated and their dependence on IEC, type of pendant phosphonium ion, the degree of quaternization and relative humidity will be discussed.

In this study, both parallel and perpendicular alignments were observed for membranes with cylindrical morphology. What remains to be seen is how the alignment of surface domains influences channel connectivity. Although it has been hypothesized that parallel alignment can impede charge transport at the membrane-electrode interface,²³ there has so far been no direct supporting evidence. Therefore, relationship between AEM surface morphology and ionic domain connectivity were investigated by electrostatic force microscopy (EFM). As a tapping-mode AFM based technique, EFM probes the electrostatic force gradient and has been used to investigate the surface charge characteristics of isolated nanostructures³³⁻³⁶ and structures imbedded in thin films.^{37,38} Previously, EFM has been demonstrated to be a useful tool to study the disconnected dead-end channels in Nafion[®].³⁹ Variation in EFM phase with respect to change in bias voltage is indicative of regions where charge is trapped due to the disconnection in channels.⁴⁰ Thus, from different EFM responses as a function of bias voltage, the channel structures and connectivity can be evaluated. These findings provide direct evidence of the relationship between membrane preparation methods, morphology and channel

connectivity, which in turn helps direct the synthesis and processing methods of these promising AEM materials.

3.2 Experimental

3.2.1 Materials

Isoprene (Ip) was distilled and stored under $-20\text{ }^{\circ}\text{C}$ before use. Chloromethylstyrene (CMS) (mixture of para- and meta- isomers) was passed through basic alumina and stored at $-20\text{ }^{\circ}\text{C}$ before use. All other chemicals were used as received.

3.2.2 Synthesis of Macro-Initiator, Polyisoprene-*N*-tert-Butyl-*N*-[1-diethylphosphono-(2,2-dimethylpropyl)]nitroxide (PIp-SG1), by NMP

In a typical procedure, *N*-tert-Butyl-*N*-[1-diethylphosphono-(2,2-dimethylpropyl)]nitroxide (SG1, 38.14 mg, 0.1 mmol) was added to a Teflon-sealed Schlenk flask containing isoprene (4 g, 5.87 mL, 58.7 mmol) and pyridine (5.87 mL) with equal volume fraction. Three cycles of freeze-pump-thaw were applied to degas the mixture; then, the flask was backfilled with nitrogen and placed in an oil bath at $115\text{ }^{\circ}\text{C}$. After the polymerization, the reaction was quenched by immersing the flask into an ice bath for 10 min. The contents were transferred to a pre-weighed vial. Solvent and unreacted isoprene were removed by purging with dry nitrogen overnight and then kept in a vacuum oven for 24 h. The viscous light-yellow liquid was obtained and weighed.

3.2.3 Synthesis of Block Copolymers, Polyisoprene–Polychloromethylstyrene (PIp–PCMS)

In a typical procedure, PIp–SG1 (1 g, Mn 9.3 kg/mol, Đ 1.16), CMS (3.22 g, 3 mL, 21.1 mmol), and *o*-xylene (6 mL) were added to a Schlenk flask. Three cycles of freeze–pump–thaw were applied to degas the mixture; then, the flask was backfilled with nitrogen and placed in an oil bath at 105 °C for 12 h. The chain extension was quenched by immersing the flask into an ice bath for 10 min and then precipitated into hexane three times to remove excess monomer CMS and dormant PIp homopolymer without chain extension. A white powder was obtained.

3.2.4 Polymer Quaternization

A typical quaternization procedure consisted of dissolving PIp–PCMS (AEM 17, 100 mg, with CMS moieties 0.55 mmol) and tris(2,4,6-trimethoxyphenyl)phosphine (P(Ph(OMe)₃)₃, 445 mg, 0.84 mmol) in 5 mL of dichloromethane (DCM). The solution was purged with dry nitrogen for 10 min before placing into 40 °C oil bath while stirring for 3 days. After the quaternization, the solution was precipitated into methanol to remove the excess P(Ph(OMe)₃)₃ and P(R₃P⁺MS homopolymers (PCMS homopolymer, the side product during chain extension of PIp–SG1, after quaternization). A white powder was obtained and dried in a vacuum oven overnight.

3.2.5 Partial Quaternization

PIp-PCMS (AEM 17, 20 mg, with CMS moieties 0.11 mmol) and triphenylphosphine ($P(Ph)_3$) with reaction stoichiometries of 0.25, 0.5, 0.75, and 1 (7.28, 14.56, 21.85, 29.13 mg) were dissolved in 2 mL of chloroform, respectively. The solutions with different $P(Ph)_3$ feeding ratios were purged with dry nitrogen for 10 min before placing into an oil bath at 40 °C for 3 days. After the quaternization, the solutions were precipitated into methanol to remove the excess $P(Ph)_3$ and $P(R_3P^+)MS$ homopolymers. A white powder was obtained and dried in a vacuum oven overnight.

3.2.6 Membrane Fabrication

Membrane Casting. For drop-cast membranes, a solution of the quaternized diblock copolymer, PIp- $P(R_3P^+)MS$, in chloroform (~ 50 mg/mL, 1 mL) was drop-cast onto a clean polytetrafluorethylene sheet and allowed to dry slowly overnight. The membranes were then solvent annealed by tetrahydrofuran (THF) vapor for 24 h before being peeled off the substrate and dried under vacuum. The thicknesses of the membranes, measured by AFM, were ~ 6 μm . For spun-cast membranes, the solution of the quaternized diblock copolymer was spun-cast on a conductive fluorine-doped tin oxide (FTO) substrate. Only AEM 16 was spun-cast. FTO was cut into 2×2 cm squares. The substrates were cleaned by sonicating in a 1:1 EtOH/DI water bath for 15 min followed by a DI water bath for 15 min. FTO was then air-dried in a Petri dish. The as-received membranes were recast from THF. A 5 wt% solution was sonicated for 5 min and spun-cast on clean FTO at 3000 rpm. The thicknesses of the membrane were measured by AFM to be ~ 40 nm.

3.2.7 Characterization

Gel Permeation Chromatography (GPC). GPC was performed in THF at a flow rate of 1.0 mL/min using a refractive index detector on a Polymer Laboratories PL-GPC 50 integrated GPC system.

Nuclear Magnetic Resonance (NMR) Spectroscopy. NMR spectroscopy was performed in 5 mm diameter tubes in deuterated chloroform (CDCl_3) at 25 °C. ^1H and ^{31}P NMR spectroscopies were performed on a Bruker 500 spectrometer at 500 MHz (^1H) and 202 MHz (^{31}P), respectively.

Small-Angle X-ray Scattering (SAXS). SAXS measurements were performed using a GANESHA 300 XL SAXS. Humidity-dependent SAXS measurements were performed at The Basic Energy Sciences Synchrotron Radiation Center at the Advanced Photon Source at Argonne National Lab on beamline 12 ID-B. A Pilatus 2 M SAXS detector was used to collect scattering data with an exposure time of 1 s. The X-ray beam had a wavelength of 1 Å and a power of 12 keV. The intensity (I) is a radial integration of the two-dimensional scattering pattern with respect to the scattering vector (q). Temperature and relative humidity (RH) were controlled within a custom sample oven. Typical experiments studied three membrane samples and one empty window; so, a background spectrum of the scattering through the Kapton windows and a nitrogen environment could be obtained for each experimental condition. The RH of the sample environment was controlled by mixing heated streams of saturated and dry nitrogen. Sample holders were inserted into an oven environment of 40 °C and <10% RH. The samples were allowed to dry for 40 min before the X-ray test started. RH was then increased to 95% while the temperature was maintained at 40 °C. X-ray spectrum was taken after 1 h equilibration.

Similarly, for the drying process, RH was set to 0% while the temperature was maintained, and the X-ray spectrum was taken after 1 h equilibration.

Transmission Electron Microscopy (TEM). The TEM specimens were prepared by a Leica CryoUltramicrotome. The microtome chamber was cooled down to $-100\text{ }^{\circ}\text{C}$ by liquid nitrogen, where the bulk sample was microtomed with a diamond knife to a thickness of around 40 nm. The cutting sections were then collected by 400-mesh copper support grids and stained by OsO₄ vapor for 20 min at room temperature. TEM characterization was performed on a JEOL 2000FX TEM operated at an accelerating voltage of 200 kV.

Atomic Force Microscopy (AFM). Height and phase images were acquired in tapping mode using an atomic force microscope (Asylum Research MFP3D). Standard silicon probes (XSC11, MikroMasch) with resonant frequency ($\sim 300\text{ kHz}$) and spring constant (40 N/m) were used. A closed fluid cell (modified PolyHeater, Asylum Research) was used to control the relative humidity (RH). Membranes were mounted by epoxy resin to a metal puck, which could be screwed in place inside the closed fluid cell. Membranes were hydrated by equilibrating at 80% RH for 2 h. Humidified nitrogen was supplied to the cell at 100 mL/min. Humidity was measured in the cell using an external humidity sensor (Honeywell). Membranes were dehydrated in a vacuum oven at $70\text{ }^{\circ}\text{C}$ for 24 h and then imaged in a nitrogen environment at 18% RH. The sizes of the hydrophilic and hydrophobic domains were measured using the particle analysis tool in Igor Pro by applying a threshold to the sample using the iterative method. The spacing between the cylindrical aggregates (d-spacing) of the lamellar surfaces was measured by measuring both line profiles and the radially averaged one-dimensional power spectral density (PSD). The phase images were used for analyses because the phase offered greater contrast than

topography. The PSDs were computed in Gwyddion and plotted in Igor Pro. The position of the peak indicates the maximum spatial frequency of the AFM phase images. The first peak in the PSD is taken as (q_1). The d-spacing is defined as $\frac{2\pi}{q_1}$.

Electrostatic Force Microscopy (EFM). An amplitude contrast tapping-mode AFM technique is based on the two-pass interleave scan, in which the height and phase are measured in the first pass and a lift height of 20 nm is applied to the tip in the second pass. A constant dc bias is applied to the electrode substrate, while the tip is held at ground. A platinum-coated tip provided by Micromasch (model HQ:XSC11/Pt) with a resonant frequency of ~ 325 kHz and a tip radius of curvature < 27 nm was used. The same region was scanned with different voltage biases applied to the substrate from the microscope controller, 0, ± 1 , ± 3 , and ± 5 V. The measurements were performed under ambient conditions and at room temperature. All the images were acquired using the retrace image. The (x, y) position of the domains in the phase image was marked by a cursor which highlights the (x, y) position in the EFM images. The EFM phase as a function of V_{EFM} ($V_{EFM} = V_{tip} - V_{substrate}$) was plotted for each domain and was fit to a third-order polynomial.

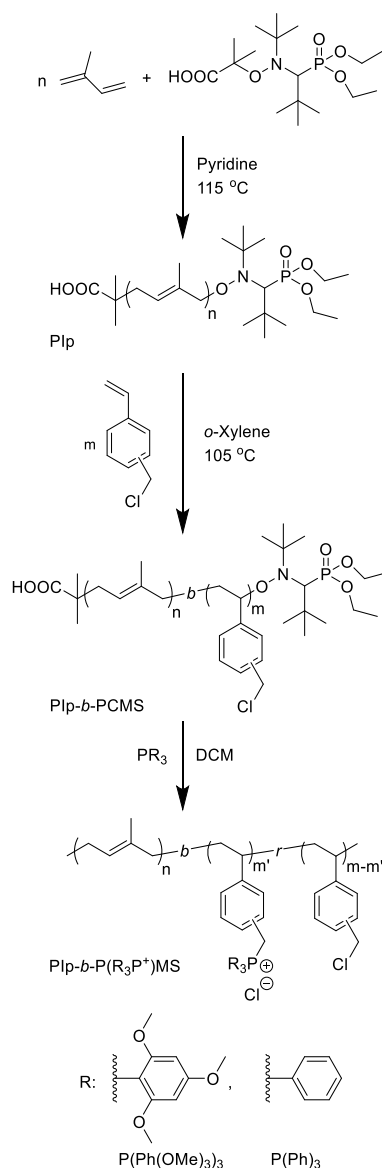
3.3 Results and Discussion

3.3.1 Polymer Synthesis

Previously, the phosphonium-pendant diblock and triblock copolymers were synthesized by reversible addition-fragmentation chain transfer (RAFT) polymerization.²⁰ Chloromethylstyrene (CMS) was polymerized first, and then chain extended with isoprene (Ip). The benzylic position on CMS is electrophilic for subsequent quaternization by nucleophilic attack. Polyisoprene (PIp) was chosen because of its low glass-transition temperature (T_g) and attendant flexibility.

In this study, NMP was chosen for block copolymer synthesis due to its fast propagation rate at high temperature (120 °C). The use of *N-tert*-butyl-*N*-[1-diethylphosphono-(2,2-dimethylpropyl)] nitroxide (SG1) to mediate the polymerization of Ip provides living character. By using pyridine, a polar solvent, intramolecular hydrogen-bonding is disrupted, therefore, the polar SG1 initiator was stabilized, providing further control over polymerization.⁴¹ By modulating the feeding ratio of Ip and initiator SG1,

Scheme 3.1 Synthesis of PIp-*b*-P(R₃P⁺)MS by NMP.



molecular weights of ~9 and 62 kg/mol PIP were successfully synthesized with narrow dispersity ($D_{PIp} < 1.2$), as shown in Table 3.1. The conversion can also be calculated from ^1H NMR to be ~50% after 14 hours of reaction time. Molecular weights were determined by GPC using THF as solvent against polystyrene standards.

The macro-initiator, PIP-SG1, was then chain extended with CMS in *o*-xylene. By changing the feeding ratio of CMS and PIP-SG1, molecular weight of the second PCMS block can be tuned. From ^1H NMR, the integration of the alkene peak from PIP (δ : 4.9-5.1 ppm, CDCl_3) was normalized to 1, while peaks from the aromatic ring (δ : 6.1-6.6, 6.6-7.1 ppm, CDCl_3) and benzylic position (δ : 4.2-4.5 ppm, CDCl_3) were integrated and averaged to calculate the DP ratio between PCMS and PIP. Due to fast propagation rate of NMP, ~80% conversion of CMS was achieved within short reaction time (10 h) and high degree of polymerization (DP) of CMS was easily obtained. Analysis by GPC in THF revealed the molecular weight and distribution, using polystyrene standards. The increased dispersity was observed, which might be resulted from the chain transfer of benzylic site on CMS, facilitated by conjugation with the aromatic ring.⁴²

Table 3. 1 Chemical composition and morphology of PIP-*b*-P(R₃P⁺)MS synthesized by NMP.

AEM	PIp		PIp- <i>b</i> -PCMS			PIp- <i>b</i> -P(R ₃ P ⁺)MS, R = Ph(OMe) ₃			PIp- <i>b</i> -P(R ₃ P ⁺)MS, R = Ph		
	M _w ^a (g/mol)	Đ ^a	M _w ^a (g/mol)	Đ ^a	f (%) ^b	IEC ^c (mmol/g)	d- spacing ^g (nm)	M ^h	IEC ^c (mmol/g)	d- spacing ^d (nm)	M ^d
16	62,000	1.15	89,000	1.35	80	0.87	20	C	2.24	22	C
17			110,000	1.34	82	0.88	23	C	2.26	24	C
18	9,400	1.14	28,000	1.89	88	0.91	41	S	2.31	43	S
19			29,000	1.84	92	0.93	70	S	2.35	72	S

^aWeight-average molecular weight (M_w) and dispersity (\bar{D}) of the polymers from THF GPC.

^bVolume fraction of the PCMS block, calculated by DP from ¹H NMR and the densities of homopolymers.

^cTheoretical ion exchange capacity (IEC) of the copolymer PIp-*b*-P(R₃P⁺)MS, calculated from ¹H NMR.

^dD-spacing and morphology inferred from SAXS, where C denotes cylinder and S denotes sphere.

Block copolymer PIp-*b*-PCMS was then quaternized with P(Ph(OMe)₃)₃ or P(Ph)₃, using dichloromethane (DCM) as solvent. The solution was purged by nitrogen in advance to inhibit the oxidation of the phosphine during quaternization. The reaction was conducted at 50 °C for three days, then the quaternized polymers were precipitated in methanol. Peaks from phosphine oxide or excess quaternization agent were not observed in ³¹P NMR, as shown in Figure 3.1.

The quaternization efficiency for the conventional quaternization agents, $P(\text{Ph}(\text{OMe})_3)_3$, was $\sim 30\%$.²⁰ Whereas the quaternization efficiency of $P(\text{Ph})_3$ is close to 100%, indicated by full disappearance of the peak from PCMS benzylic position in Figure 3.2, ^1H NMR. Thus, quaternization efficiency of 30% and 100% were used to calculate the theoretical IEC for $P(\text{Ph}(\text{OMe})_3)_3$ and $P(\text{Ph})_3$ quaternized polymers, respectively.

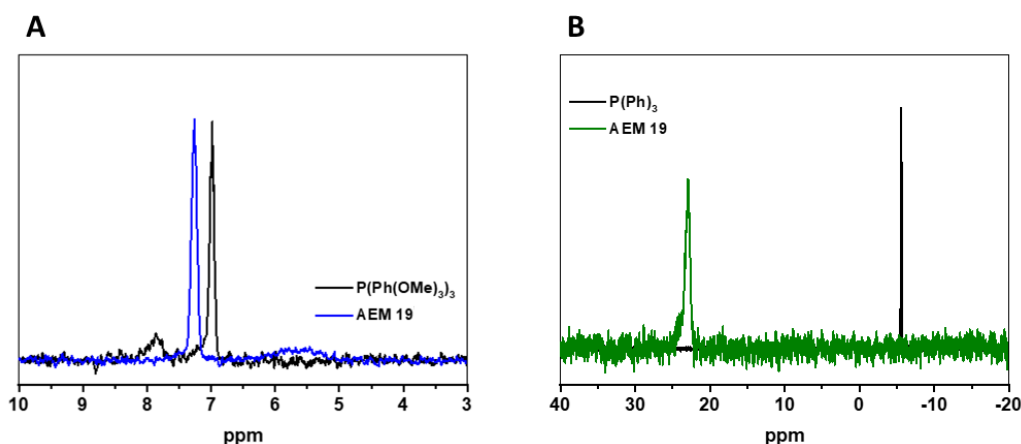


Figure 3.1 ^{31}P NMR spectra of two quaternization agents and AEM 19 after quaternization. (A) $P(\text{Ph}(\text{OMe})_3)_3$ and (B) $P(\text{Ph})_3$.

After quaternization, the polymer solution in chloroform was drop cast onto a clean polytetrafluoroethylene sheet and left to dry. The membranes were then exposed to THF vapor for solvent annealing for 24 hours, resulting in transparent and uniform membranes $\sim 5 \mu\text{m}$ thick.

3.3.2 Quaternization Agent Effect on Morphology

The influence on bulk and surface morphologies were investigated by SAXS and AFM for comparison of the two quaternization agents. As discussed above, $P(\text{Ph}(\text{OMe})_3)_3$ has a lower quaternization efficiency, due to the steric hindrance of nine methoxy groups

on the benzene rings, while $P(\text{Ph})_3$, a less bulky counterpart, has a higher quaternization efficiency for the same reaction time. The quaternization efficiency difference directly results in a two-fold increase in IEC, as shown in Table 3.1.

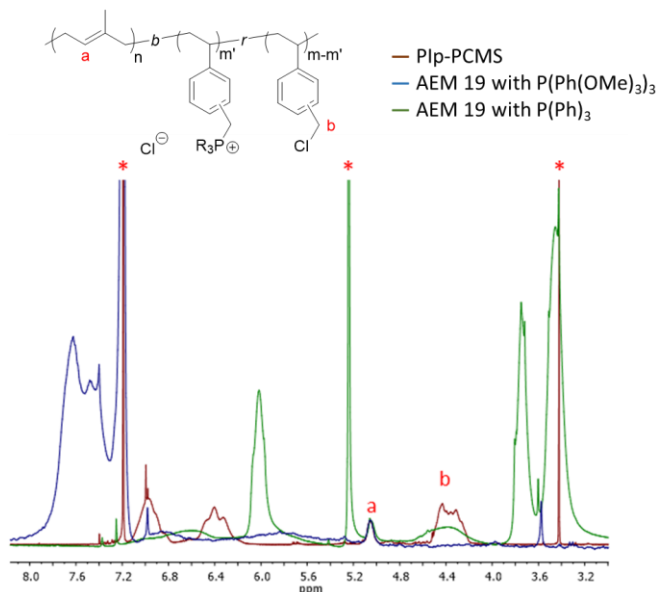


Figure 3.2 ^1H NMR spectra of neutral block copolymer PIp-*b*-PCMS and neutral-charged block copolymer AEM 19 PIp-*b*- $P(\text{R}_3\text{P}^+)\text{MS}$, quaternized by $P(\text{Ph}(\text{OMe})_3)_3$ and $P(\text{Ph})_3$ respectively.

In terms of their morphological effect, the SAXS profiles of AEM 16 quaternized with $P(\text{Ph})_3$ and $P(\text{Ph}(\text{OMe})_3)_3$ are shown in Figure 3.3A, where the primary peak position determines the *d*-spacing and peak positions of higher order relative to the primary peak indicates bulk morphology. Figure 3.3B shows the repulsive-mode phase images of the two membranes by AFM, which reveals surface morphology. Bright contrast in the phase images is assigned to the hydrophilic domains. Despite such a large difference in IEC, membranes from both quaternization agents show cylindrical morphology. A small shift of ~ 2 nm larger *d*-spacing was observed in $P(\text{Ph})_3$ from SAXS, as well as larger cluster size in AFM, than those of $P(\text{Ph}(\text{OMe})_3)_3$.

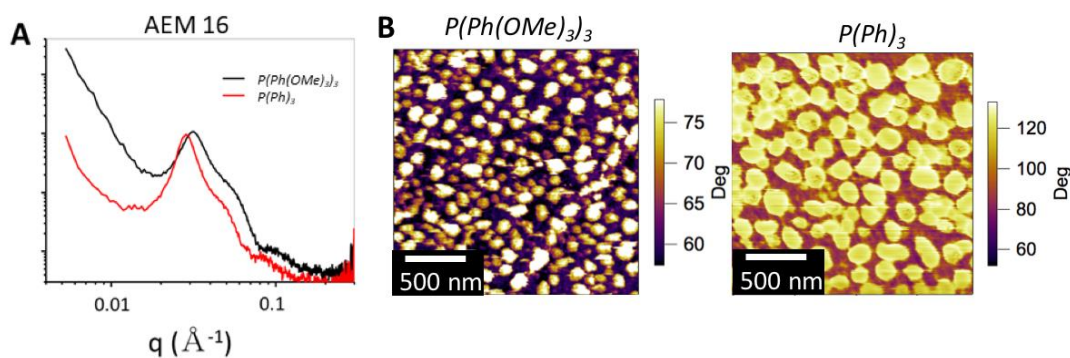


Figure 3.3 (A) SAXS comparison of AEM 16 quaternized by $P(\text{Ph}(\text{OMe})_3)_3$ in black trace and $P(\text{Ph})_3$ in red trace. (B) Phase images of AEM 16 quaternized by $P(\text{Ph}(\text{OMe})_3)_3$ and $P(\text{Ph})_3$, respectively. Bright phase contrast is assigned to the hydrophilic domains.

In addition, AEM 17, 18, and 19 were quaternized by $P(\text{Ph}(\text{OMe})_3)_3$ and $P(\text{Ph})_3$. The SAXS profiles are shown in Figure 3.3 for different quaternization agents comparison. Smaller d-spacing was obtained for the conventional quaternization agent, $P(\text{Ph}(\text{OMe})_3)_3$. D-spacing difference varies between 0.5 to 3 nm, depending on the amount of quaternizable component in the precursor block copolymer, PIp-*b*-PCMS.

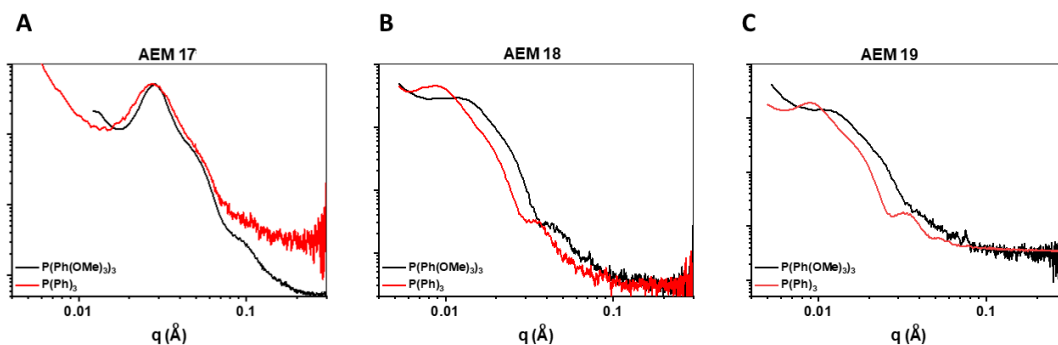


Figure 3.4 SAXS of (A) AEM 17 (B) AEM 18 and (C) AEM 19, quaternized by $P(\text{Ph}(\text{OMe})_3)_3$ (black trace) and $P(\text{Ph})_3$ (red trace).

3.3.3 Quaternization Level and Morphology

In order to evaluate the impact of quaternization level (QL) on phase behavior of PIp-*b*-P(R₃P⁺)MS membranes, a range of QL was achieved by partial quaternization of AEM 17 with P(Ph)₃. The QL was altered by adjusting the reaction stoichiometries of P(Ph)₃ to PIp-*b*-PCMS. Quaternization were performed with ratios of P(Ph)₃ to PIp-*b*-PCMS of 1:4, 2:4, 3:4 and 4:4, as well as with a two-fold excess of P(Ph)₃ to ensure the highest QL. They are noted as *0.25_P*, *0.5_P*, *0.75_P*, *1_P* and *full_P*, respectively, while the un-quaternized membrane of AEM 17 was denoted as *0_P*, as listed in Figure 3.6A. The QL was confirmed by ¹H NMR in Figure 3.5. The peak from PIp was normalized by area, gradual decrease of the peak from benzyl chloride positions on PCMS and increase of the peaks from phosphonium phenyl positions were observed. For *full_P* sample, the complete absence of the benzyl chloride peak indicates the QL is close to 100%.

With an increase in QL, cylinder morphology was maintained throughout all membranes with scattering peaks located at q , $\sqrt{3}q$ and $\sqrt{7}q$, for *0.25_P* to *full_P*. For *0_P*, peaks locate at q , $2q$, $\sqrt{7}q$, and $3q$. The absence of $\sqrt{3}q$ in *0_P* followed by its appearance after quaternization might indicate some degree of morphology change. The attenuation of the $2q$ peak in cylinder morphologies for PIp-*b*-P(R₃P⁺)MS is typical and likely due to the form factor cancelling out the structure factor.²⁰

A decrease followed by a subsequent increase in d-spacing was observed with increasing QL. The trend in d-spacing was also supported by the change in domain size in the repulsive mode phase images of *0.25_P*, *0.5_P*, *0.75_P*, and *1_P* shown in Figure 3.6B. Bright phase contrast is assigned to the hydrophilic domains. Figure 3.6B-i initially shows relatively large domains. With further increase in QL at *0.5_P*, Figure 3.6B-ii domains

decrease in size and are spaced further apart. At 0.75_P , Figure 3.6B-iii shows a subsequent increase in domain size with decreased spacing, while Figure 3.6B-iv shows smaller domain size with ordered packing at 1_P .

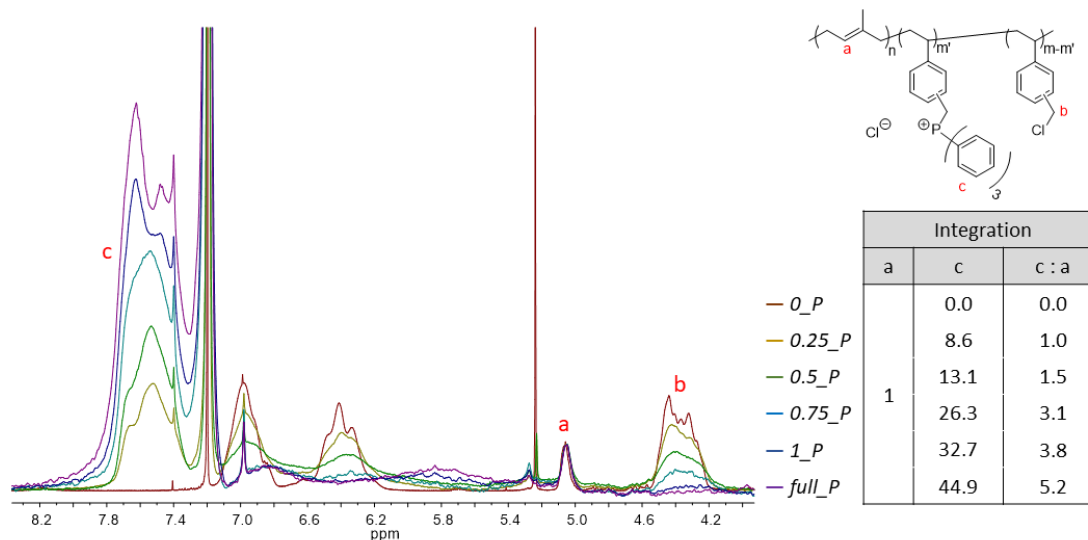


Figure 3.5 ^1H NMR spectra, chemical composite and corresponding peak integration results of partially quaternized AEM 19 by $\text{P}(\text{Ph})_3$.

A small loading of charges in 0.25_P resulted in a d-spacing decrease from 28 nm in 0_P to 21 nm. The onset of electrostatic cohesion lowers the separation distance between PCMS chains. D-spacing further decreased to 20 nm in 0.5_P , which is likely due to two reasons: first, the Coulombic interactions between the chloride counterions and phosphonium cations drives the ionic phase to be more tightly packed, while the distance between two phosphonium cations is sufficiently far apart to avoid repulsion. Second, the QL could also affect the separation distance in a way similar to triblock architectures. At low QL, the quaternized $\text{P}(\text{R}_3\text{P}^+)\text{MS}$ could behave as a third block with high χ value.²⁰ This pseudo triblock copolymer, 0.5_P , can undergo chain frustration, as the ionic block

tend to form continuous phase while the two other neutral moieties, PIP and PCMS, remain phase separated.

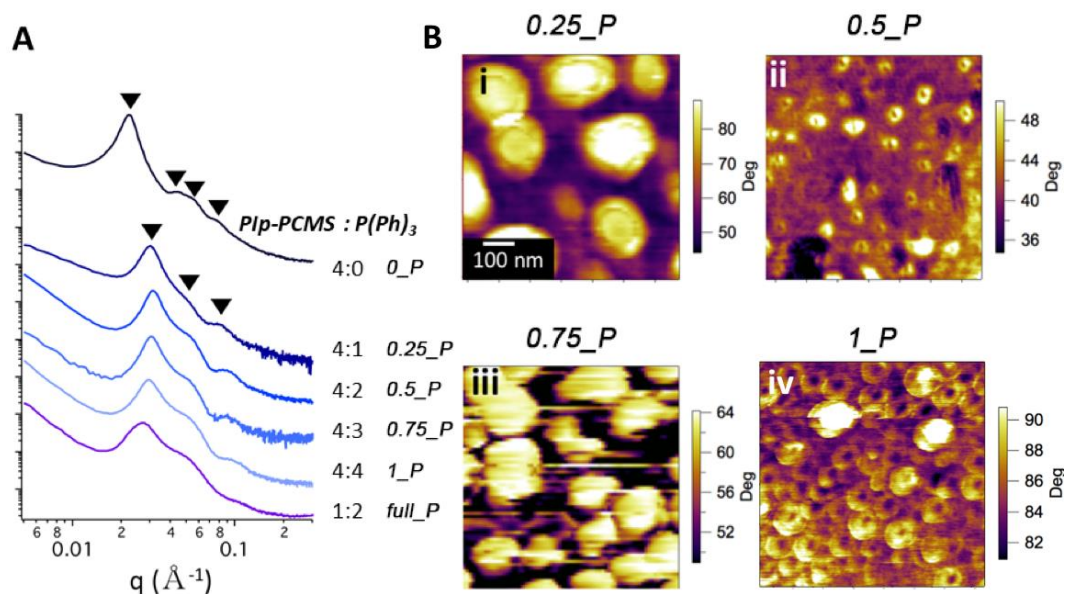


Figure 3.6 (A) SAXS of un-quaternized and partially quaternized AEM 17. (B) Phase images of AEM 17 (i) 0.25_P , (ii) 0.5_P , (iii) 0.75_P , and (iv) 1_P .

Upon further increasing QL from 0.5_P to $full_P$, a monotonic increase in d-spacing was observed, shown both in SAXS and AFM in Figure 2. It is likely due to the following reasons: first, steric repulsion from bulky phosphonium ions leads to the size increase of the ionic domains. Second, as more charges were installed onto the polymer backbone, the distance between two phosphonium cations is decreased. Due to the Columbic repulsion between adjacent charges, polymer chains were more extended, resembling the behavior of rod-like polyelectrolyte, which resulted in the observed d-spacing increase.

The collective effects from the Columbic interactions and steric hindrance on the d-spacing change are illustrated by the cartoon in Figure 3.7. Similar electrostatic interaction induced non-monotonic change was predicted in a computational study of

lamellar block polyelectrolyte by Sing *et al.*, where the dependence of lamellar d-spacing on charge fraction was investigated via SCFT-LS calculations. For weak Coulombic interactions, the introduction of charge decreases d-spacing; while for stronger Coulombic interactions, charge introduced into the block polyelectrolyte has the opposite effect and results in increasing d-spacing.²⁸

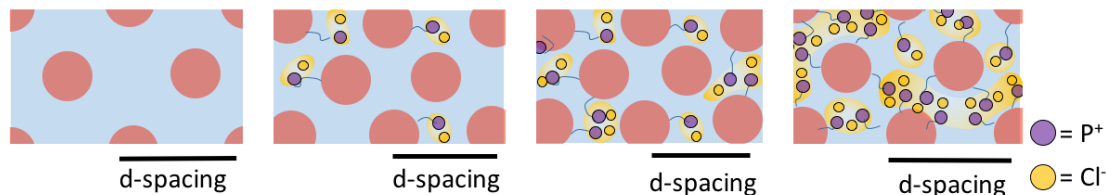


Figure 3.7 Cartoon illustration of d-spacing versus QL dependency.

3.3.4 Bulk versus Surface Morphology with Various IECs

Representative membranes of low (AEM 13), moderate (AEM 17) and high (AEM 18) IECs, quaternized with $P(\text{Ph}(\text{OMe})_3)_3$, were investigated by SAXS, TEM and AFM for bulk and surface morphology characterization. AEM 13 was a previously synthesized diblock copolymer with IEC of 0.44 mmol/g,²⁰ while AEM 17 and 18 were synthesized in this study with IEC of 0.88 and 0.91 mmol/g, respectively. Bulk morphologies were inferred from SAXS (Figure 3.8A-C), further confirmed by cross-sectional TEM (Figure 3.8D-F). Prior to TEM, membranes were microtomed and stained by OsO_4 , which selectively stain PIP.^{43,44} Thus, dark contrast in Figure 3.8D-F corresponds to the PIP and bright region corresponds to the ionic $P(\text{R}_3\text{P}^+)\text{MS}$ block.

For AEM 13, the d-spacing was 42 nm and shows peak positions at q , $\sqrt{3}q$, $\sqrt{7}q$, indicating cylinder morphology (Figure 3.8A). Both short-range parallel and perpendicular cylinders were observed (Figure 3.8D). The cylinder morphology was also observed for

AEM 17, with d-spacing of 23 nm. The decrease in d-spacing is supported by TEM in Figure 3.8E, where smaller and more tightly packed hydrophobic cylinders were observed. An average diameter of the hydrophobic aggregates in AEM 17 was measured from TEM to be ~20 nm. Upon further increasing IEC, AEM 18 exhibits a spherical body-centered cubic (BCC) morphology with d-spacing of 41 nm, indicated by peak positions of q and $\sqrt{6}q$. Less ordered morphology was observed in Figure 3.8F, where hydrophobic domains were loosely packed. Despite the increase in IEC, the hydrophobic domains increased in size. The average diameter of the hydrophobic domains was 30 nm, which is in agreement with the d-spacing. Modelling of neutral polyisoprene-polystyrene diblock (PIp-*b*-PS) copolymer ($\chi_N \gg 10$) has shown that a spherical morphology is expected for polystyrene volume fractions > 0.77 .⁴⁵

Surface morphology and relevant sizes of the hydrophilic and hydrophobic surface domains were revealed by AFM (Figure 3.8G-I). The hydrophobic PIp block has a low T_g and is more compliant than the P(R₃P⁺)MS hydrophilic block. Careful analysis of the size and frequency of the bright clusters in repulsive mode phase images upon increasing quaternization (shown in Figure 3.7B), assigned the bright contrast to be the hydrophilic domains. Interestingly, different surface alignments were observed for the two cylinder-morphology membranes, AEM 13 and 17. For AEM 13, cylinders were observed to align parallel to the surface of the membrane (Figure 3.8G), despite perpendicular bulk alignment shown by TEM. Similar phenomenon for PS-*b*-PIp diblock copolymer with a PS volume fraction of 52% was observed by Hasegawa *et al.*,⁴⁶ where PIp block tends to cover the surface regardless of microdomain alignment in bulk. Cross-sectional AFM imaging was used by Komura *et al.* to show the difference in surface alignment of cylinders

of PEO-*b*-PMA(Az) membranes.^{47,48} In addition, Khanna *et al.* observed parallel alignment of lamellar sheets for polycyclohexylethylene-*b*-polyethylene (PCHE-*b*-PE) diblock polymer films and the author noted that PE, with lower surface energy, preferred to orient toward the surface and lay parallel.⁴⁹ Furthermore, upon increasing the volume fraction of PCHE, the surface domains formed perpendicular to the surface. Nevertheless, perpendicularly aligned domains are observed in AEM 17 with moderate IEC (Figure 3.8H), resembling the cylinder morphology in TEM. Although the Coulombic interactions can influence the morphology in charged block copolymers,²⁵ we suggest that a similar phenomenon is taking place for our PIp-*b*-P(R₃P⁺)MS membranes in which the volume fraction of PIp plays an important role for the alignment of domains and difference in surface energy between the PIp and P(R₃P⁺)MS blocks can account for the surface alignment.

In terms of domain size and spacing, larger domains on the surface were observed than in the bulk for both AEM 13 and 17. By taking line profiles perpendicular to the cylinder, a cylinder width of AEM 13 is measured to be ~40 nm and spacing between cylinders was ~17 nm (Figure 3.8D). For AEM 17, the bright clusters, interpreted as the ionic domains, are 50-70 nm in diameter, nearly twice as large as domains in the bulk. The d-spacing was evaluated by power spectral density (PSD) analysis was 126.0 nm. Size discrepancy of ionic domains between the surface and bulk can result from phase rearrangement occurring at the air-membrane interface during the membrane casting process. In Nafion[®], ionic domains are ~4 nm in diameter in the bulk¹² while ~10 nm in diameter on the surface.⁵⁰ Similarly, a combination of water adsorption by the ionic

domains and the segmental motion of the PIP block could account for such a rearrangement.

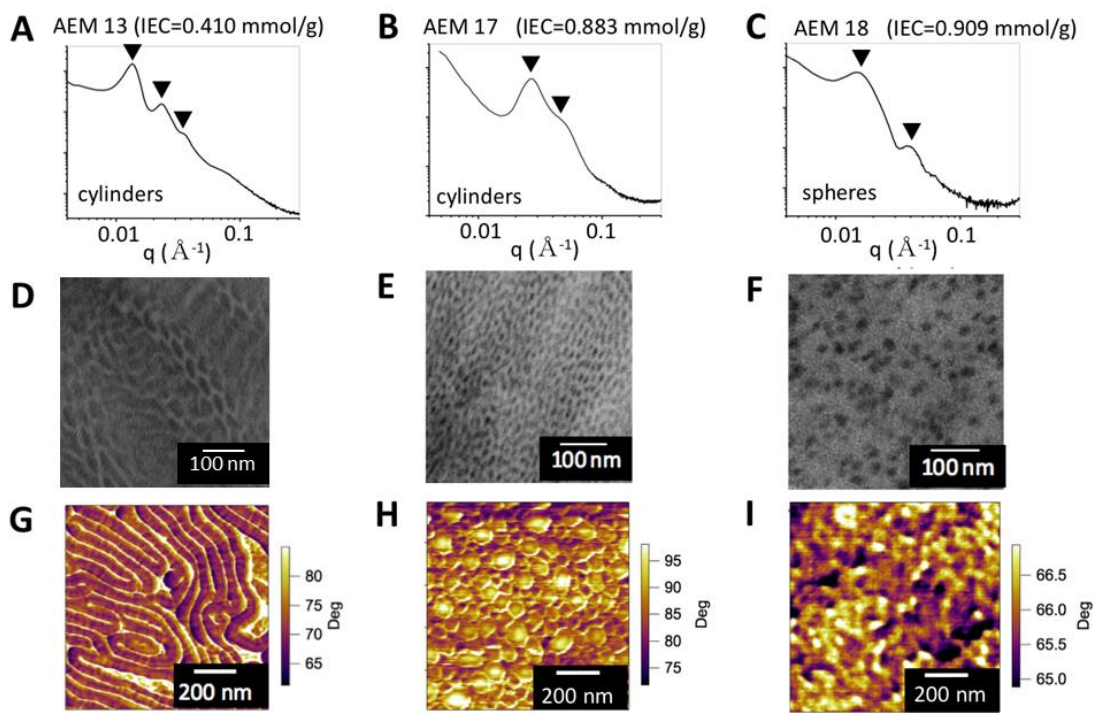


Figure 3.8 (A-C) SAXS, (D-F) TEM, and (G-I) AFM phase of AEM 13 (A, D, G), AEM 17 (B,E,H), AEM 18 (C,F,I). Dark contrast in TEM and AFM is the hydrophobic domains.

For AEM 18, a less ordered morphology was observed, where spheres were loosely packed (Figure 3.8I), resembling the TEM. The disagreement between the results inferred from SAXS and TEM of AEM 18 (Figure 3.8C, F) while qualitative similarities between the AFM and TEM images (Figure 3.8F, I) is peculiar. Typically, BCC forming membranes exhibit scattering peaks at q , $\sqrt{2}q$, $\sqrt{3}q$, $\sqrt{4}q$, ... The broad higher order peak at $\sqrt{6}q$ could suggest a liquid-like short range order with lack of true long range order of BCC membranes.^{51,52} Average diameter of bright ionic domains was measured to be ~ 25 nm and

that of dark hydrophobic domains was ~40 nm. The d-spacing by PSD analysis was 100.1 nm.

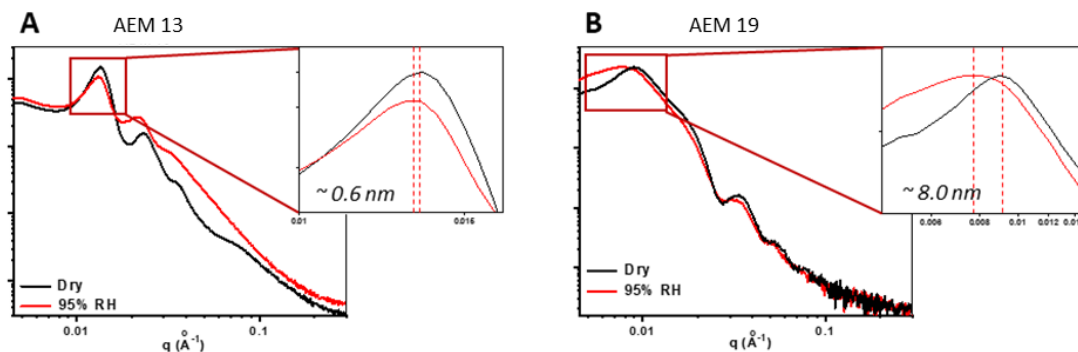


Figure 3.9 SAXS of (A) AEM 13 and (B) AEM 19 under dry (black trace) and 95% RH (red trace). The dashed red lines mark the peak position shift between dry and 95% RH.

3.3.5 Humidity-Dependent Bulk Morphology Investigation

In these AEM membranes, the ionic phase is hydrophilic and PIp phase is hydrophobic. The hydrophilicity of the membranes can lead to humidity-dependent morphology. Thus, the humidity-dependent bulk morphologies of AEM 13 and AEM 19 were investigated by SAXS.

Prior to the SAXS measurement, AEM 13 and AEM 19, quaternized with $\text{P}(\text{Ph}(\text{OMe})_3)_3$, were equilibrated in a RH-controlled environment for 1h. SAXS was first collected under dry conditions ($<5\%$ RH, black trace), then 95% RH (red trace). As shown in Figure 3.9A and B, the presence of higher order peaks under both RH conditions indicates that the ordered morphologies was maintained throughout dry to humid conditions for both AEMs. A d-spacing shift of $\sim 0.6 \text{ nm}$ was observed in AEM 13, between dry and 95% RH, whereas a larger shift in d-spacing of $\sim 8.0 \text{ nm}$ for AEM 19 was observed.

The minimal morphological change in AEM 13 with lower IEC could be due to low degree of water uptake inherent to bulky QP pendant polymers.^{17,18} Although AEM 13 has a lower IEC than AEM 19, the difference in orientation of the surface domains could also influence

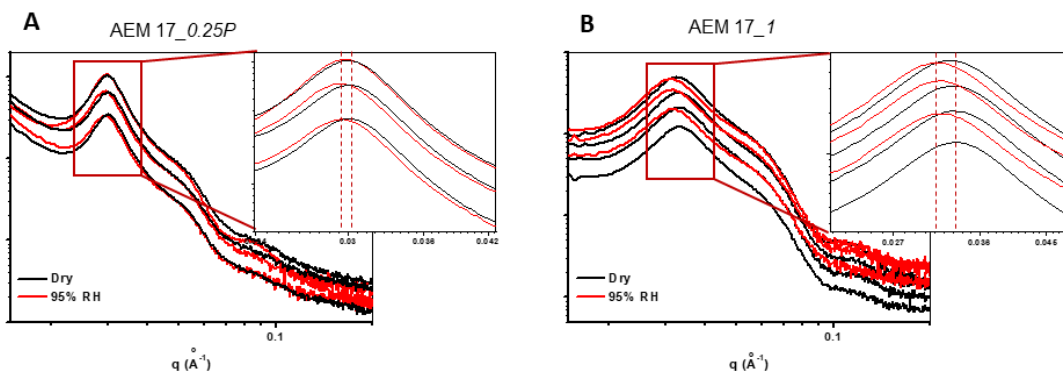


Figure 3.10 SAXS of (A) AEM 17_0.25P and (B) AEM 17_1P, quaternized by P(Ph)₃, through three humidity cycles. Where the black traces were under dry conditions and red traces are under 95% RH.

the swelling behavior. For example, the surface of AEM 13 consists of parallel hydrophobic PIP cylinders, which could shield more water from adsorbing than domains that would be perpendicularly aligned.

Control experiments were performed on two partially quaternized AEM 17 membranes with different QL (0.25_P and 1_P) at dry and 95% RH, as shown in Figure 3.10. Both membranes consist of perpendicularly aligned cylinders, but the difference in IEC accounts for a d-spacing shift of ~0.6 nm for AEM 17-0.25_P and ~1.3 nm for AEM 17-1_P.

3.3.6 Humidity-Dependent Surface Morphology Investigation

Phase imaging of ion exchange membranes at controlled environmental conditions is a useful tool in observing changes in surface morphology as a result of changes in RH.⁵³ Figure 3.11 provides a comparison of repulsive mode phase images of AEM 13, AEM 16, and AEM 19, quaternized with P(Ph(OMe)₃)₃, at a wide range of RH. It is important to note that AEM 16 and AEM 17 showed similar hexagonal morphology as well as AEM 18 and AEM 19 showed similar BCC morphology according to SAXS, TEM, and AFM.

With the lowest IEC (0.44 mmol/g), AEM 13 showed no significant change in morphology, only differences in spacing. The spacing between cylindrical aggregates measured by line profiles from Figure 3.11A-C was 14 nm at 18% RH, 17 nm at 50% RH,

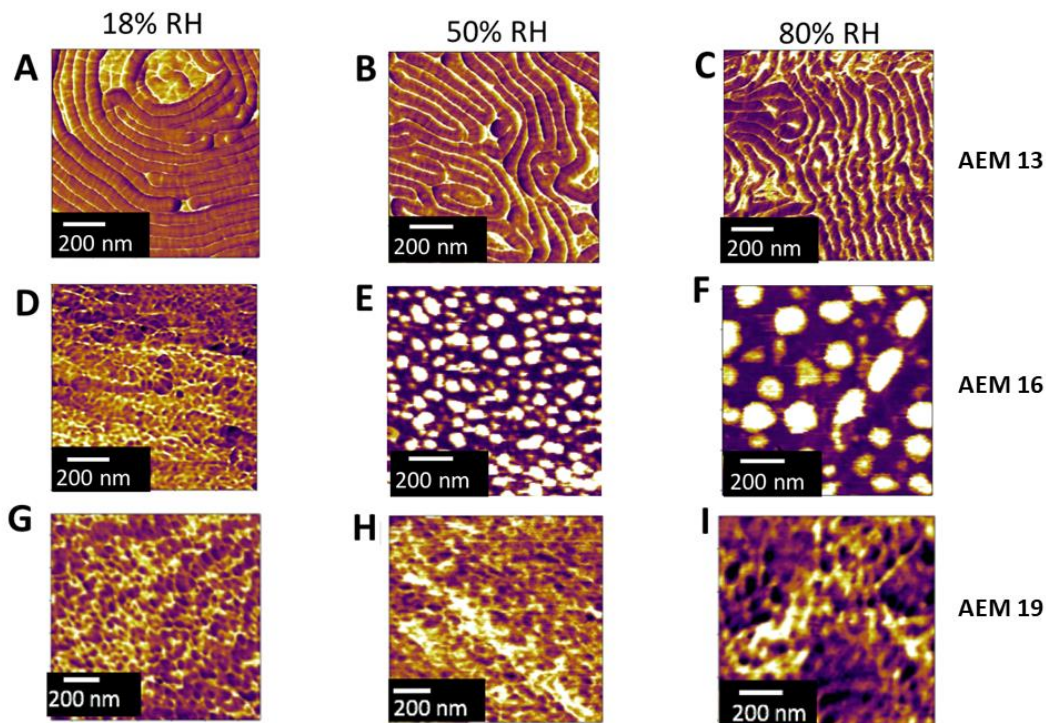


Figure 3.11 (A-I) Repulsive mode phase images of AEM 13 (A-C), AEM 16 (D-F), and AEM 19 (G-I) under 18% (A,D,G), 50% (B,E,H), and 80% RH (C,F,I).

and 23 nm at 80% RH. The d-spacing was calculated by measuring the peak position in the power spectral density (PSD) of Figures 3.11A-C. An increase in d-spacing with increasing RH was observed, from 31 nm at 18% RH to 61 nm at 50% RH, and 65 nm at 80% RH.

With an IEC of 0.87 mmol/g, the phase image of AEM 16 (Figure 3.11E) resembled the morphology of AEM 17 in Figure 3.8H at ambient conditions. The bright ionic domains were not as tightly packed as AEM 17 due to the difference in IEC. The average diameter of the domains in Figure 3.11E was 42 nm with 16% coverage. Under dry conditions, we observed an absence of bright ionic domains and a disordered morphology (Figure 3.11D). At 80% RH, the surface became more ordered and domain size increased in which the average diameter is 59 nm with 10% coverage (Figure 3.11F).

Upon further increasing IEC, AEM 19 showed a similar disordered morphology as AEM 18 in Figure 3.8I. We have interpreted regions of dark contrast as the hydrophobic domains given the striking qualitative similarity with TEM. Control experiments in which un-quaternized AEM 19 was imaged under ambient conditions and showed a similar morphology as shown in Figure 3.8I. Under ambient conditions, the average diameter of the hydrophobic domain was 20 nm at 26% coverage. At hydrated conditions, phase contrast increased, indicating increasing water uptake by the continuous ionic phase. The hydrophobic domains increased in size to 38 nm with 30% coverage. The increasing size, although at a similar area coverage, can be due to stretching of the PIP block to accommodate increase in water uptake. At dehydrated conditions, the phase contrast between the hydrophilic and hydrophobic domains was lower. There was no change in size of the hydrophobic domains between ambient and dehydrated conditions, but the area coverage decreased to 20%. The surface, which displays a different morphology-humidity

behavior than bulk, could be explained by increased chain flexibility near the surface that can more easily release internal stress.

3.3.7 Morphology Reversibility by Humidity Cycling

The morphological reversibility after cycling the RH was analyzed for AEM 13 by both AFM and SAXS. Small, but detectable changes in size and spacing of domains under dry and humidified conditions were observed as shown in Figure 3.11A-C. Excessive

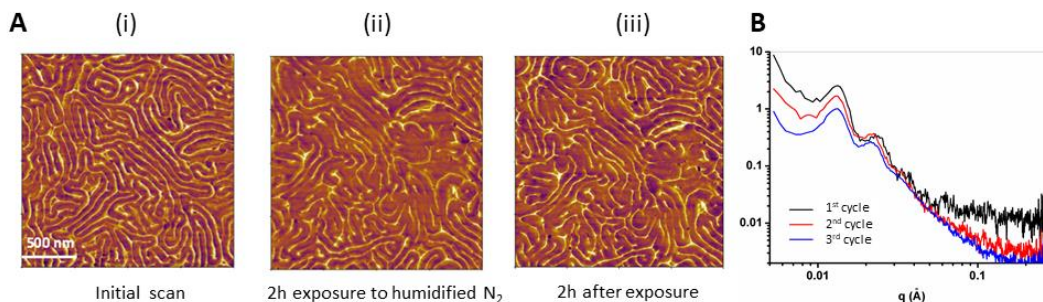


Figure 3.12 (A) Repulsive mode phase images of AEM 13 at a fixed scan area for 1 humidity cycle ranging from 50 – 80% RH. (A-i) the first scan at 50% RH. (A-ii) after 2 h exposure at 80% RH. (A-iii) after 2 h drying and equilibrated at 50% RH. (B) SAXS of AEM 13 for three humidity cycles for dry-95% RH-dry.

swelling was avoided in AEM 13, thus tip-sample contact could be maintained for a long period of time.

Repulsive mode phase images of AEM 13 through one humidity cycle between ambient (50% RH) and humidified (80% RH) were collected in Figure 3.12A. The experiment was conducted in a closed humidity-controlled fluid cell. The first scan, shown in Figure 3.12A-i, was conducted under ambient conditions. The parallel-aligned cylinder morphology is clearly shown, similar to Figure 3.8G. Humidified nitrogen was supplied to the fluid cell. After 2 h, equilibrium was reached and a second image, shown in Figure

3.12A-ii, was collected. A decrease in the connectivity of the bright ionic regions was observed, which was a result of the swelling behavior. The humidified nitrogen flow was then turned off, after 2 h, a third image, shown in Figure 3.12A-iii was collected, where a gradual restoration of the initial scan can be observed. The d-spacing was also measured by taking the PSD of the images. The spacing showed an increase from 66 nm in Figure 3.12A-i to 74 nm in Figure 3.12A-ii and a subsequent decrease to 71 nm in Figure 3.12A-iii.

In addition, Figure 6B shows SAXS of AEM 13 for three humidity cycles. Initially, AEM 13 was equilibrated in a humidity chamber with 95% RH over night at 40° C. The membrane was then dried under vacuum overnight before SAXS profile was collected (first cycle in Figure 3.12B). This process was repeated twice. After each cycle, SAXS profile was collected. Although a shift in d-spacing of ~0.6 nm was observed between dry and 95% RH cycles (Figure 3.9A), Figure 3.12B shows no drift in d-spacing between cycles, which indicates that the expansion and contraction of channels between the humidified and dry conditions are reversible.

3.3.8 Effect of Surface Alignment on Ionic Domain Connectivity

The following investigation involves specifically AEM 13 (IEC = 0.44 mmol/g) and AEM 16 (IEC = 0.87 mmol/g). Bulk morphologies were investigated by SAXS and TEM, as shown in Figure 3.13, which are indicative of hexagonal cylinder morphology. The surface morphology was revealed by AFM. The phase images were collected in repulsive mode. The bright contrast is from the ionic P(R₃P⁺)MS domains and the dark contrast is indicative of the hydrophobic PIP domains. The images show stark differences

between the surface alignment between the two membranes. Figure 3.13C shows cylinders forming parallel to the surface, while Figure 3.13G indicates perpendicularly aligned cylinders. This implies that in AEM 13, perpendicular channels convert to parallel channels at the surface as the film dries. In AEM 16, on the other hand, shows perpendicular alignment of the channels. Surface alignment was further confirmed by PSD analysis for both AFM phase images, as shown in Figure 3.13D and H, respectively. The PSD is useful

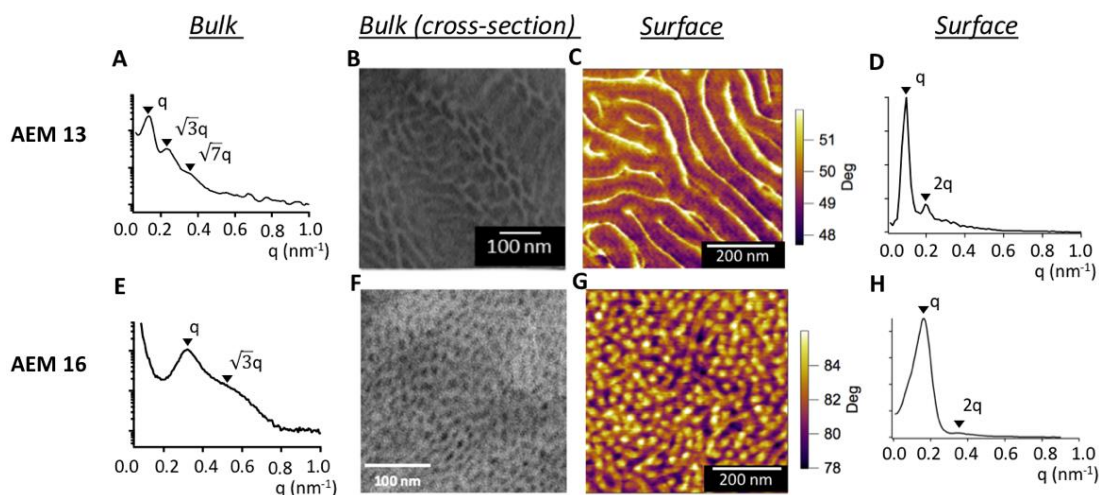


Figure 3. 13 Bulk and surface morphology comparison of AEM 13 and 16. SAXS of (A) AEM 13 and (E) 16. Cross-sectional TEM of (B) AEM 13 and (F) 16, where dark contrast is from PIp domains. Repulsive mode phase images of (C) AEM 13 and (G) 16, where dark contrast corresponds to PIp domains. Radially-averaged power spectral density (PSD) of phase images of (D) AEM 13 and (H) 16.

in analyzing spatial frequencies of AFM images. Surface ordering information of block copolymer membranes can be revealed through analysis of peak positions.^{54,55} In Figure 3.13D, the peaks are positioned at q and $2q$, which signifies regular periodic order typically observed in lamellar phases. In Figure 3.13H, the peak positions for AEM 16 at q and $2q$ is with much weaker intensity, signifying short-range order.

The surface free energy difference between two blocks influences the alignment of domains at the air-membrane interface.^{45,46,49} In addition, different sample preparation methods play a significant role in affecting bulk and surface morphologies, via different film formation kinetics.^{56,57} AEM 13 was prepared by drop-casting from CHCl₃ solution onto a PTFE sheet. AEM 16 was spun-cast from THF solution onto a fluorine doped tin oxide (FTO) substrate. Drop-cast films were ~6 μm thick while spun-cast films were ~40 nm thick. Film deposition by fast solvent extraction via spin-casting or solvent vapor annealing can trap the block copolymer in a non-equilibrium morphology.⁵⁶ In drop-cast films, the solvent evaporates slowly (over 6 h) under ambient RH, which favors the formation of larger ionic domains on the surface than bulk. In spun-cast films, the bulk structure is trapped at the surface because the film is not given enough time to reach equilibrium at ambient RH, thus giving rise to smaller ionic domains distributed on the surface. Since the alignment, ordering, and size of domains at the surface of spun-cast AEM 16 are commensurate with bulk measurements of drop-cast AEM 16, we use AEM 16 as a benchmark hexagonal membrane with well-connected channels to compare with AEM 13. Furthermore, the similarities in bulk morphologies of AEM 13 and AEM 16 make them good candidates for comparing the influence of different surface alignments on charge migration and channel connectivity.

A cartoon illustration of the proposed structures with different alignments is shown in Figure 3.14. Mixed alignments of PIp cylinders in the bulk with parallel alignment on the surface for AEM 13 is shown in Figure 3.14A. It is possible that these misalignments between the surface and bulk can result in coverage of the ionic phase and prevent charges from reaching the air-membrane interface. The discontinuities between the bulk and the

surface can be readily seen within the two-dimensional plane of the surface of AEM 13 shown in Figure 3.13C. Therefore, it is possible that these discontinuities could exist within the bulk further impeding ion mobility. Additionally, the expanded diameters of the PIP cylinders of AEM 13 cover most of the surface of the membrane, which can lead to lower connectivity. Figure 3.14B illustrates that at a high volume fraction of the $P(R_3P^+)MS$ block, the cylinders only align perpendicular to the air–membrane interface throughout the membrane, leading solely to connected paths. Additionally, AEM 16 exposes significantly more of the conductive blue region on the surface, which can lead to better connectivity through the membrane and hence better conductivity. In both cases, continuous ionic regions allow charges to migrate throughout the entire membrane. Thus, the conductivity of block copolymer AEMs is dependent on the extent of coverage and alignment of the PIP phase at the surface.²³

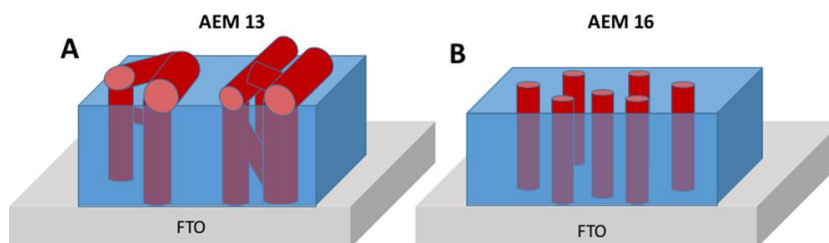


Figure 3. 14 Cartoons illustrating the proposed structure leading to variation in connectivity. The red cylinders represent the PIP phase, while blue represents the continuous ionic phase. (A) Parallel-aligned cylinders can either block surface charge migration or provide a connected path. (B) Perpendicularly aligned cylinders give rise to only connected ionic pathways.

EFM is a tapping-mode AFM based technique that probes the electrostatic force gradient via two-pass interleave scans. In the first pass, the height and phase are gathered. In the second pass, phase deviations are influenced by the electrostatic force gradient,

which is attributed to surface charge, dielectric permittivity, and film capacitance. The conductive tip is raised above the surface by 20 nm. A constant DC bias is applied to the electrode FTO sample substrate (V_{sample}) while the platinum-coated tip is held at ground ($V_{tip} = 0$). Conventionally, the bias voltage is defined as $V_{EFM} = V_{tip} - V_{sample}$. Hence, $V_{EFM} = -V_{sample}$. The ions migrate depending on the sign of the bias voltage, for example, a $V_{EFM} = +5$ V implies a negative sample voltage and would bias the ions toward the surface. Figure 3.15A and D shows first pass phase images of AEM 13 and 16 showing the same morphology from images shown in Figure 3.13. Figure 3.15B and C shows EFM images of AEM 13 at -5 V and +5 V FTO sample bias, respectively.

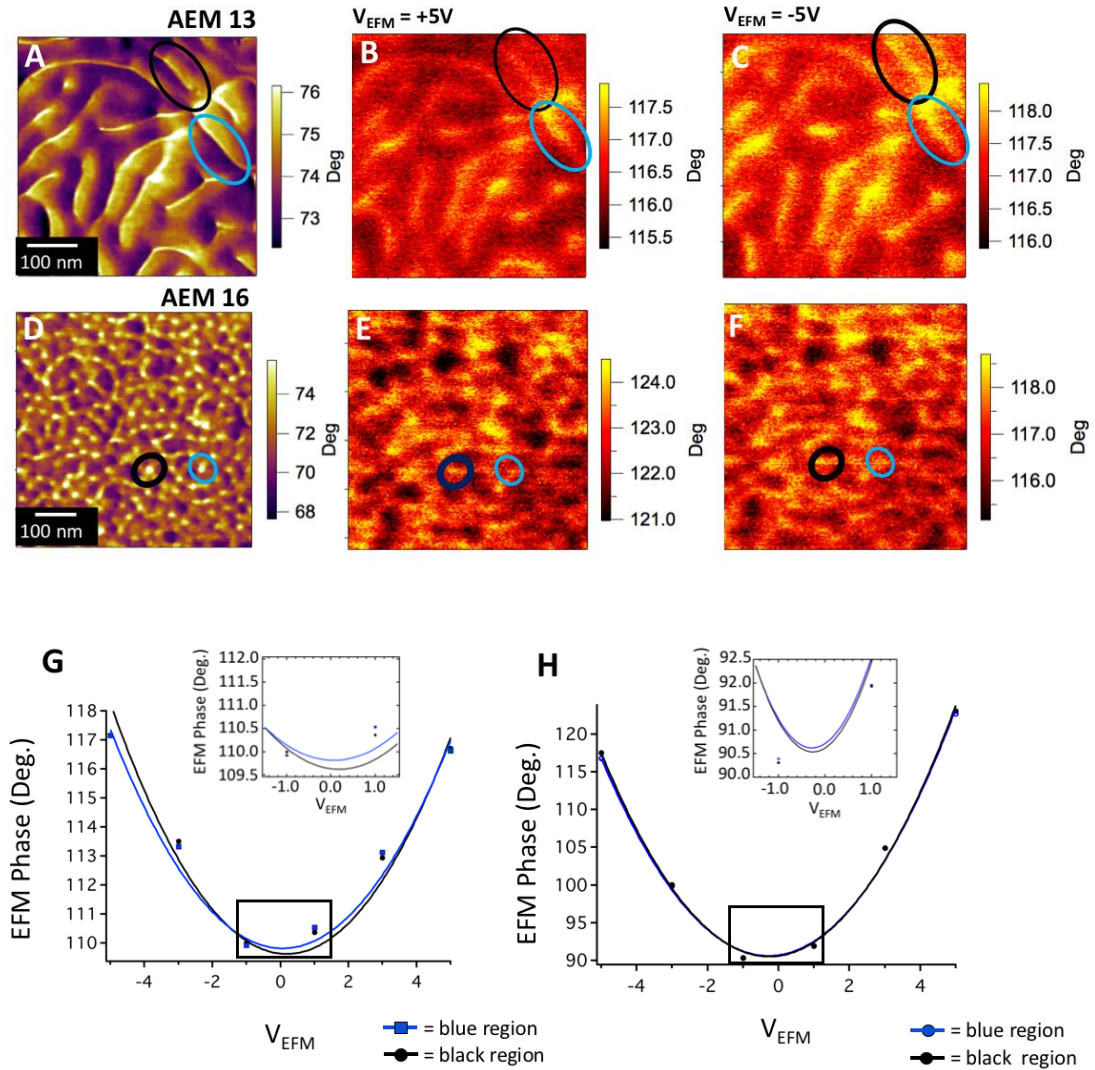


Figure 3. 15 (A) First pass repulsive-mode phase image of AEM 13. EFM images taken in the second pass at (B) $V_{EFM} = +5V$ and (C) $V_{EFM} = -5V$ sample bias. (D) Repulsive-mode phase image of AEM 16 taken in the first pass. EFM images during the second pass at (E) $-5V$ sample bias and (F) $+5V$ sample bias. Parabolic response of EFM phase as a function of V_{EFM} for two regions highlighted (G) in A-C of AEM 13 and (H) in D-F of AEM 16.

Two representative ionic regions of AEM 13 are highlighted in Figure 3.15A-C. The EFM phase was determined by drawing a square box ($20 \text{ nm} \times 20 \text{ nm}$) over the ionic region of interest in the first pass phase image in Igor Pro. The (x, y) spatial coordinates in the first pass correspond to the same coordinates in the second pass EFM phase image, and therefore the square box can be copied onto the second pass EFM image. The statistical average was measured over ~ 100 pixels contained in the square box. This method was applied to the same ionic region of interest for each voltage bias. For example, the blue highlighted region shows a small uniform shift (-0.5°) in EFM phase between the $+5\text{V}$ and -5V image while the black region shows a larger and more negative shift (-1.5°) between the two images. A different EFM phase response as a function of voltage bias was observed for AEM 16. Figure 3.15D shows a repulsive mode phase image of AEM 16. Similar EFM phase contrast can be seen in blue and black highlighted regions at both voltage biases (Figure 3.15E and F), showing a uniform shift in the EFM phase ($+5.9^\circ$) with respect to voltage bias for both regions. Besides, a higher EFM phase shift was observed as expected, since AEM 16 has larger IEC, allowing larger population of charges to be biased towards the surface, which leads to a larger positive shift. Heterogeneity in the EFM phase of AEM 13 can be attributed to “dead-end” ionic channels due to the parallel hydrophobic cylinders that block the chloride from reaching the surface, while homogeneity for AEM 16 can be attributed to identical connected channel structures.

It is important to note that the sign of the shift does not provide adequate information on the channel structure, thus the parabolic EFM behavior of the channels must be analyzed. EFM phase shifts as a function of the bias voltage and can be described mathematically via Equation 3.1.⁵⁸

$$\Delta\Phi = -\frac{Q}{2k} \frac{d^2C}{dz^2} [(V_{EFM} - V_s)^2 - 2(V_{EFM} - V_s)V_q + V_q^2] \quad (3.1)$$

where Q is the quality factor of the cantilever, k is the spring constant of the cantilever, C is the capacitance of the tip-sample system, z is the height above the surface. V_{EFM} is the bias voltage ($V_{EFM} = V_{tip} - V_{sample}$). V_s is the surface potential, which is related to the work function difference between the tip and the sample and is independent of the lift height. We consider V_s to be a constant offset potential and is independent of V_{EFM} . V_q is the potential related to the charge enclosed and is dependent on the lift height. The first term in Equation 3.1 is related to the tip-sample capacitance and induced polarization of the film, which is always an attractive force. The middle term in Equation 3.1 is related to the interaction between the stored charge, q , and the EFM tip apex. The third term is related to the image charge effects, since this is independent of V_{EFM} , we have ignored this interaction from analysis. It is possible to simplify the expression for Equation 3.1 into two terms: a charge force gradient ($\Delta\Phi_q$) that has a linear dependence on V_{EFM} and a capacitive force gradient ($\Delta\Phi_C$) that has a quadratic dependence with V_{EFM} .

$$\Delta\Phi = \Delta\Phi_q + \Delta\Phi_C = AV_{EFM} + BV_{EFM}^2 \quad (3.2)$$

A and B are fitting parameters to the linear and quadratic terms, respectively.

$$B = \frac{Q}{2k} \left(\frac{3\alpha}{(z+d)^4} \right) \quad (3.3)$$

$$A = \frac{-Qq}{2k(z+d)^3} \quad (3.4)$$

Where α is the electric polarizability, d is the film thickness, and q is the stored charge.

For the blue region highlighted in AEM 13, the average EFM phase was measured for each voltage bias and plotted as blue squares shown in Figure 3.15G.³⁹ The data was fit to a quadratic function and the fit curve is shown as the blue line. Similarly, the black region in AEM 13 was plotted as black circles and fit to a quadratic function shown as the

black line. In Figure 3.15G, there are noticeable differences between the blue and black fits. The insets show a close-up of the differences. Furthermore, the analytical expressions shown in Equation 3.3 and 3.4 can be simplified by taking the ratio of A and B, which is dependent on stored charge (q), film thickness (d), and polarizability (α).

$$\frac{A}{B} = \frac{-q(z + d)}{3\alpha} \quad (3.5)$$

Note Equation 3.5 is similar for the ratio expression derived for EFM studies of Nafion[®].³⁹ The EFM phase of Nafion[®] was background subtracted and assumptions regarding the relative permittivity and the charge density of the ionic domains allowed for simplified expressions. Heterogeneity in the A and B fits were due to differences in ionic domain geometry. In this investigation, we can draw similar conclusions, however, we are comparing two membranes of different IEC and film thickness. Therefore, the EFM phase was not background subtracted and the film thickness (d) is included in the expression, which represents a pocket of charge or a connected ionic pathway plus the remaining thickness of the film. The relative permittivity of the ionic domains is also not known. Hence, B was expressed in terms of the polarizability of the film.

For the blue curve, the fitting parameters were $A = -0.036^\circ/V$ and $B = 0.294^\circ/V^2$. Thus, A/B is calculated to be $-0.122 V$. For the black curve in Figure 3.15G, $A = -0.118^\circ/V$, $B = 0.321^\circ/V^2$, and $A/B = -0.368 V$. The differences in A/B between these two regions supports our qualitative depictions shown in Figure 3.14. The black region in AEM 13 shows a large negative A/B which signifies a “dead-end” ionic pathway, while the blue region shifts to less negative, signifying a connected ionic pathway. Both A/B values are negative, which could be due to a negative surface potential, V_s , the potential in the absence of stored charge shown in Equation 3.1. The same analysis was performed on

AEM 16. First, smaller deviation was observed in 3H between quadratic fits for blue and black regions highlighted in images 3D-F. For region 1, $A = 0.632^\circ/V$ and $B = 1.201^\circ/V^2$. For region 2, $A = 0.661^\circ/V$ and $B = 1.176^\circ/V^2$. A/B for these regions are $0.525 V$ and $0.562 V$, respectively.

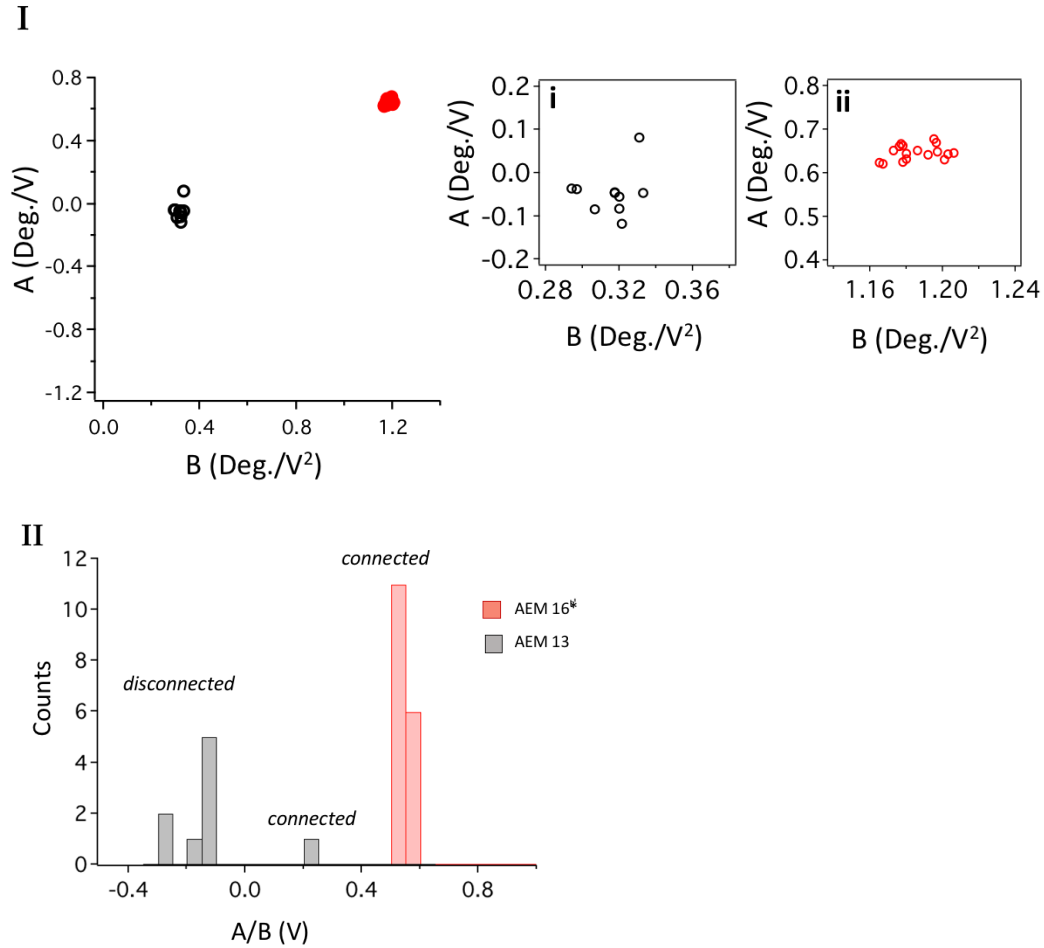


Figure 3. 16 (I) Scatter plot of the linear fit term A vs. quadratic fit term B for several features of AEM 13 in black circles and AEM 16 in red circles. Inset shows a close-up of the scatter plot (I-i) AEM 13 and (I-ii) AEM 16. (II) Histogram of A/B data from (4I) for AEM 13 (gray) and AEM 16 (red).

We continued our investigation of the distribution and parabolic EFM behavior of several ionic domains on AEM 13 and 16. It is important to note that not all ionic domains

were able to be analyzed because of topographic artifacts. These topographical artifacts can contribute to the EFM phase and were thus avoided. In the EFM images that correspond to Figure 3.15A-C, 10 regions of interest were analyzed, while 17 regions of interest were analyzed for Figure 3.15D-F. Figure 3.16I shows scatter plots of fit parameter A versus B for all ionic regions analyzed for AEM 13 and AEM 16, respectively. The inset scatter plots show a close-up of the data highlighting the difference in the variance of AEM 13 (Figure 3.16I-i) and AEM 16 (Figure 3.16I-ii). For AEM 13, points distribute near $A = 0^\circ/V$ and $B = 0.31^\circ/V^2$, while for AEM 16, the fit parameters can be seen near $A = 0.65^\circ/V$ and $B = 1.18^\circ/V^2$. The increase in both fit parameters A and B from AEM 13 to AEM 16 is due to increased IEC. A larger IEC would increase the total amount of stored charge of the membrane and thus increase A, according to Equation 3.4. An increase in the IEC would also make the membrane more polarizable, which would lead to an increase in B according to Equation 3.3. It is important to note that Equation 3.3–3.5 also indicate a dependency on the membrane thickness. The control measurements on the unquaternized membranes have been performed and indicate that decreasing the membrane thickness at a constant charge leads to smaller values of A/B, which is in agreement with Equation 3.5. Because the increase in A/B from AEM 13 (thick membrane) to AEM 16 (thin membrane) is due to the increase in IEC, the IEC plays a more significant role in the measurement of A/B than membrane thickness.

Figure 3.16II shows a histogram of A/B for AEM 13 and AEM 16 regions. AEM 13 shows a broad distribution with a cluster of points below $A/B = 0$, while AEM 16 shows a narrow distribution of $A/B > 0$. The variance in the distribution of A/B is attributed to the variation in ionic pathway connectivity. Similar analysis has been performed to investigate

the channel connectivity of Nafion[®].³⁹ Since the shape of the hydrophilic channels can be approximated as cylinders,¹² isolated cylinder model can be used to interpret EFM data. In the isolated cylinder model, A is proportional to the channel length.⁴⁰ Assuming that charge density is uniform, the variation in A/B is due to variations in channel length. Furthermore, the same model can be applied depending on whether cylinders lay parallel³⁵ or perpendicular.^{36,40} Thus, we were able to conclude that only 1 out of 10 regions of AEM 13 led to a connected channel, while the rest were dead-end channels, and for AEM 16, all regions analyzed led to connected channels, as expected for perpendicular aligned channels.

3.4 Conclusions

Diblock copolymers PIp-PCMS were synthesized by NMP and quaternized with two types of tertiary aromatic phosphines. Membranes with a range of IECs were prepared and their morphologies were analyzed by SAXS, TEM, and AFM. Hexagonal cylinder and BCC morphologies were observed in PIp-P(R₃P⁺)MS membranes, where the ionic block formed the continuous phase. Due to the difference in surface energy between two blocks, moderate IEC membranes showed parallel-aligned channels on the surface, while high IEC showed perpendicular alignment, despite little difference in their bulk morphologies. Given these observations, the higher IEC materials result in surface morphology that is qualitatively similar to those in the bulk. Higher quaternization efficiency with P(Ph)₃ leads to larger d-spacing from SAXS and larger size of the ionic domains from AFM. By partial quaternization, the impact of QL on the phase behavior of PIp-P(R₃P⁺)MS, R = Ph, was investigated. The coulombic interactions and steric repulsion are collectively involved in

accounting for the d-spacing change with increasing QL. The bulk and surface morphologies of PIP-P(R₃P⁺)MS, R = Ph(OMe)₃, as a function of RH were studied, where IEC-dependent change in d-spacing and domain size has been established between dry and humid conditions. A more significant change in the domain spacing on the surface was observed than in the bulk. Morphological reversibility of PIP-P(R₃P⁺)MS membranes was examined by humidity cycling. Full morphology recovery was achieved after cycles of hydration and dehydration, which indicates that the expansion and contraction of channels as a function of RH is a reversible process.

Two AEMs with different IEC were investigated. AEM 13 with low IEC showed a mixture of parallel and perpendicular alignment of channels in the bulk though only parallel alignment on the surface. By contrast, for AEM 16 with higher IEC, perpendicularly aligned channels were observed throughout the bulk and surface. From EFM phase images of both membranes, the EFM phase shift as a function of voltage bias was measured over the ionic domains. From the investigation on the parabolic EFM behavior as a function of voltage bias for the two membranes, variation was observed in the parabolic response of AEM 13 while very little variation was shown in AEM 16. These results suggest that there are a significant number of disconnected channels as a result of the parallel alignment observed in AEM 13, while for AEM 16, highly ordered structure of perpendicular channel alignment leads to a dominant population of connected channels.

Detailed understanding of the relationships between the surface and bulk morphologies can shed light on developing important design principles for future AEM fuel cell membranes.

3.5 References

- (1) Merle, G.; Wessling, M.; Nijmeijer, K. Anion Exchange Membranes for Alkaline Fuel Cells: A Review. *J. Memb. Sci.* **2011**, *377* (1–2), 1–35.
- (2) Varcoe, J. R.; Atanassov, P.; Dekel, D. R.; Herring, A. M.; Hickner, M. A.; Kohl, P. A.; Kucernak, A. R.; Mustain, W. E.; Nijmeijer, K.; Scott, K.; Xu, T.; Zhuang, L. Anion-Exchange Membranes in Electrochemical Energy Systems. *Energy Environ. Sci.* **2014**, *7* (10), 3135–3191.
- (3) Hickner, M. A.; Herring, A. M.; Coughlin, E. B. Anion Exchange Membranes: Current Status and Moving Forward. *J. Polym. Sci. Part B Polym. Phys.* **2013**, *51* (24), 1727–1735.
- (4) Varcoe, J. R.; Slade, R. C. T.; Wright, G. L.; Chen, Y. Steady-State Dc and Impedance Investigations of H₂ / O₂ Alkaline Membrane Fuel Cells with Commercial Pt / C , Ag / C , and Au / C Cathodes. **2006**, *2* (3), 21041–21049.
- (5) Grew, K. N.; Chiu, W. K. S. A Dusty Fluid Model for Predicting Hydroxyl Anion Conductivity in Alkaline Anion Exchange Membranes. *J. Electrochem. Soc.* **2010**, *157* (3), B327.
- (6) Zawodzinski, T. A.; Derouin, C.; Radzinski, S.; Sherman, R. J.; Smith, V. T.; Springer, T. E.; Gottesfeld, S. Water Uptake by and Transport Through Nafion® 117 Membranes. *J. Electrochem. Soc.* **1993**, *140* (4), 1041.
- (7) Paddison, S. J.; Paul, R. The Nature of Proton Transport in Fully Hydrated Nafion®.

- Phys. Chem. Chem. Phys.* **2002**, *4* (7), 1158–1163.
- (8) Choi, P.; Jalani, N. H.; Datta, R. Thermodynamics and Proton Transport in Nafion. *J. Electrochem. Soc.* **2005**, *152* (3), E123.
- (9) Weber, A. Z.; Newman, J. Modeling Transport in Polymer-Electrolyte Fuel Cells. *Chem. Rev.* **2004**, *104* (10), 4679–4726.
- (10) Hsu, W. Y.; Gierke, T. D. Ion Transport and Clustering in Nafion Perfluorinated Membranes. *J. Memb. Sci.* **1983**, *13* (3), 307–326.
- (11) Rubatat, L.; Rollet, A. L.; Gebel, G.; Diat, O. Evidence of Elongated Polymeric Aggregates in Nafion. *Macromolecules* **2002**, *35* (10), 4050–4055.
- (12) Schmidt-Rohr, K.; Chen, Q. Parallel Cylindrical Water Nanochannels in Nafion Fuel-Cell Membranes. *Nat. Mater.* **2007**, *7* (1), 75–83.
- (13) Yan, X.; Gu, S.; He, G.; Wu, X.; Benziger, J. Imidazolium-Functionalized Poly(Ether Ether Ketone) as Membrane and Electrode Ionomer for Low-Temperature Alkaline Membrane Direct Methanol Fuel Cell. *J. Power Sources* **2014**, *250*, 90–97.
- (14) Gu, S.; Skovgard, J.; Yan, Y. S. Engineering the Van Der Waals Interaction in Cross-Linking-Free Hydroxide Exchange Membranes for Low Swelling and High Conductivity. *ChemSusChem* **2012**, *5*, 843–848.
- (15) Disabb-miller, M. L.; Zha, Y.; Decarlo, A. J.; Pawar, M.; Tew, G. N.; Hickner, M. A. Water Uptake and Ion Mobility in Cross-Linked Bis(Terpyridine)Ruthenium-

- Based Anion Exchange Membranes. *Macromolecules* **2013**, *46* (23), 9279–9287.
- (16) Gu, S.; Cai, R.; Luo, T.; Chen, Z.; Sun, M.; Liu, Y.; He, G.; Yan, Y. A Soluble and Highly Conductive Ionomer for High-Performance Hydroxide Exchange Membrane Fuel Cells. *Angew. Chemie - Int. Ed.* **2009**, *48* (35), 6499–6502.
- (17) Noonan, K. J. T.; Hugar, K. M.; Kostalik, H. A.; Lobkovsky, E. B.; Abruña, H. D.; Coates, G. W. Phosphonium-Functionalized Polyethylene: A New Class of Base-Stable Alkaline Anion Exchange Membranes. *J. Am. Chem. Soc.* **2012**, *134* (44), 18161–18164.
- (18) Cotanda, P.; Sudre, G.; Modestino, M. A.; Chen, X. C.; Balsara, N. P. High Anion Conductivity and Low Water Uptake of Phosphonium Containing Diblock Copolymer Membranes. *Macromolecules* **2014**, *47* (21), 7540–7547.
- (19) Li, N.; Leng, Y.; Hickner, M. A.; Wang, C.-Y. Highly Stable, Anion Conductive, Comb-Shaped Copolymers for Alkaline Fuel Cells. *J. Am. Chem. Soc.* **2013**, *135* (27), 10124–10133.
- (20) Zhang, W.; Liu, Y.; Jackson, A. C.; Savage, A. M.; Ertem, S. P.; Tsai, T.-H.; Seifert, S.; Beyer, F. L.; Liberatore, M. W.; Herring, A. M.; Coughlin, E. B. Achieving Continuous Anion Transport Domains Using Block Copolymers Containing Phosphonium Cations. *Macromolecules* **2016**, *49* (13), 4714–4722.
- (21) Kumar, R.; Muthukumar, M. Microphase Separation in Polyelectrolytic Diblock Copolymer Melt: Weak Segregation Limit. *J. Chem. Phys.* **2007**, *126* (21), 214902.

- (22) Rojas, A. A.; Inceoglu, S.; Mackay, N. G.; Thelen, J. L.; Devaux, D.; Stone, G. M.; Balsara, N. P. Effect of Lithium-Ion Concentration on Morphology and Ion Transport in Single-Ion-Conducting Block Copolymer Electrolytes. *Macromolecules* **2015**, *48* (18), 6589–6595.
- (23) Moon, B.; Park, J.; Kim, S.; Minor, A. M.; Hexemer, A.; Balsara, N. P. Control of Domain Orientation in Block Copolymer Electrolyte Membranes at the Interface with Humid Air. *Adv. Mater.* **2009**, *21* (2), 203–208.
- (24) Park, M. J.; Balsara, N. P. Phase Behavior of Symmetric Sulfonated Block Copolymers. *Macromolecules* **2008**, *41* (10), 3678–3687.
- (25) Sing, C. E.; Zwanikken, J. W.; Olvera De La Cruz, M. Electrostatic Control of Block Copolymer Morphology. *Nat. Mater.* **2014**, *13* (7), 694–698.
- (26) Kumar, R.; Muthukumar, M. Microphase Separation in Polyelectrolytic Diblock Copolymer Melt: Weak Segregation Limit. *J. Chem. Phys.* **2017**, *126* (21), 214902.
- (27) Jiang, Y.; Freyer, J. L.; Cotanda, P.; Brucks, S. D.; Killips, K. L.; Bandar, J. S.; Torsitano, C.; Balsara, N. P.; Lambert, T. H.; Campos, L. M. Functional Polyelectrolytes. *Nat. Commun.* **2015**, *6*, 1–7.
- (28) Sing, C. E.; Zwanikken, J. W.; Olvera, M.; Cruz, D. Theory of Melt Polyelectrolyte Blends and Block Copolymers : Phase Behavior , Surface Tension , and Microphase Periodicity Theory of Melt Polyelectrolyte Blends and Block Copolymers : Phase Behavior , Surface Tension , and Microphase Periodicity. *J. Chem. Phys.* **2015**, *142* (3), 034902.

- (29) Sing, C. E.; Olvera, M.; Cruz, D. Polyelectrolyte Blends and Nontrivial Behavior in Effective Flory – Huggins Parameters. *ACS Macro Lett.* **2014**, *3* (8), 698–702.
- (30) Sing, C. E. Development of the Modern Theory of Polymeric Complex Coacervation. *Adv. Colloid Interface Sci.* **2017**, *239*, 2–16.
- (31) Perry, S. L.; Sing, C. E. PRISM-Based Theory of Complex Coacervation: Excluded Volume versus Chain Correlation. *Macromol. Rapid Commun.* **2015**, *48* (14), 5040–5053.
- (32) Irwin, M. T.; Hickey, R. J.; Xie, S.; Bates, F. S.; Lodge, T. P. Lithium Salt-Induced Microstructure and Ordering in Diblock Copolymer/Homopolymer Blends. *Macromolecules* **2016**, *49* (13), 4839–4849.
- (33) Oksana, C.; Liwei, C.; Weng, V.; Yuditsky, L.; Brus, L. E. Quantitative Noncontact Electrostatic Force Imaging of Nanocrystal Polarizability. *J. Phys. Chem. B* **2003**, *107* (7), 1525–1531.
- (34) Yalcin, S. E.; Labastide, J. A.; Sowle, D. L.; Barnes, M. D. Spectral Properties of Multiply Charged Semiconductor Quantum Dots. *Nano Lett.* **2011**, *11* (10), 4425–4430.
- (35) Malvankar, N. S.; Yalcin, S. E.; Tuominen, M. T.; Lovley, D. R. Visualization of Charge Propagation along Individual Pili Proteins Using Ambient Electrostatic Force Microscopy. *Nat. Nanotechnol.* **2014**, *9* (12), 1012–1017.
- (36) Heim, T.; Lmimouni, K.; Vuillaume, D. Ambipolar Charge Injection and Transport

- in a Single Pentacene Monolayer Island NANO LETTERS. *Nano Lett.* **2004**, *4* (11), 2145–2150.
- (37) Schaadt, D. M.; Yu, E. T.; Sankar, S.; Berkowitz, A. E. Charge Storage in Co Nanoclusters Embedded in SiO₂ by Scanning Force Microscopy. *Appl. Phys. Lett.* **1999**, *74*, 472.
- (38) Jaquith, M.; Muller, E. M.; Marohn, J. A. Time-Resolved Electric Force Microscopy of Charge Trapping in Polycrystalline Pentacene. *J. Phys. Chem. B* **2007**, *111* (27), 7711–7714.
- (39) Barnes, A. M.; Buratto, S. K. Imaging Channel Connectivity in Nafion Using Electrostatic Force Microscopy. *J. Phys. Chem. B* **2018**, *122* (3), 1289–1295.
- (40) Mélin, T.; Diesinger, H.; Deresmes, D.; Stiévenard, D. Electric Force Microscopy of Individually Charged Nanoparticles on Conductors: An Analytical Model for Quantitative Charge Imaging. *Phys. Rev. B* **2004**, *69* (3), 035321.
- (41) Harrisson, S.; Couvreur, P.; Nicolas, J. Use of Solvent Effects to Improve Control over Nitroxide-Mediated Polymerization of Isoprene. *Macromol. Rapid Commun.* **2012**, *33* (9), 805–810.
- (42) Lacroix-Desmazes, P.; Delair, T.; Pichot, C.; Boutevin, B. Synthesis of Poly(Chloromethylstyrene-*b*-Styrene) Block Copolymers by Controlled Free-Radical Polymerization. *J. Polym. Sci. Part A Polym. Chem.* **2000**, *38* (21), 3845–3854.

- (43) Nakano, T.; Kawaguchi, D.; Matsushita, Y. Anisotropic Self-Assembly of Gold Nanoparticle Grafted with Polyisoprene and Polystyrene Having Symmetric Polymer Composition. *J. Am. Chem. Soc.* **2013**, *135* (18), 6798–6801.
- (44) Li, W.; Wang, H.; Yu, L.; Morkved, T. L.; Jaeger, H. M. Syntheses of Oligophenylenevinylenes - Polyisoprene Diblock Copolymers and Their Microphase Separation. *Macromolecules* **1999**, *32* (9), 3034–3044.
- (45) Bates, F. S.; Fredrickson, G. H. Block Copolymer Thermodynamics: Theory and Experiment. *Annu. Rev. Phys. Chem.* **1990**, *41* (1), 525–557.
- (46) Hasegawa, H.; Hashimoto, T. Morphology of Block Polymers near a Free Surface. *Macromolecules* **1985**, *18* (3), 589–590.
- (47) Komura, M.; Iyoda, T. AFM Cross-Sectional Imaging of Perpendicularly Oriented Nanocylinder Structures of Microphase-Separated Block Copolymer Films by Crystal-like Cleavage. *Macromolecules* **2007**, *40* (12), 4106–4108.
- (48) Komura, M.; Yoshitake, A.; Komiyama, H.; Iyoda, T. Control of Air-Interface-Induced Perpendicular Nanocylinder Orientation in Liquid Crystal Block Copolymer Films by a Surface-Covering Method. *Macromolecules* **2015**, *48* (3), 672–678.
- (49) Khanna, V.; Cochran, E. W.; Hexemer, A.; Stein, G. E.; Fredrickson, G. H.; Kramer, E. J.; Li, X.; Wang, J.; Hahn, S. F. Effect of Chain Architecture and Surface Energies on the Ordering Behavior of Lamellar and Cylinder Forming Block Copolymers. *Macromolecules* **2006**, *39* (26), 9346–9356.

- (50) O’Dea, J. R.; Economou, N. J.; Buratto, S. K. Surface Morphology of Nafion at Hydrated and Dehydrated Conditions. *Macromolecules* **2013**, *46* (6), 2267–2274.
- (51) Register, R. A.; Marchand, G. R.; Adams, J. L.; Graessley, W. W.; Quiram, D. J. Ordering Dynamics of Compositionally Asymmetric Styrene–Isoprene Block Copolymers. *Macromolecules* **2002**, *29* (8), 2929–2938.
- (52) Kim, J. K.; Lee, H. H.; Ree, M.; Lee, K.-B.; Park, Y. Ordering Kinetics of Cylindrical and Spherical Microdomains in an SIS Block Copolymer by Synchrotron SAXS and Rheology. *Macromol. Chem. Phys.* **1998**, *199* (4), 641–653.
- (53) Economou, N. J.; Barnes, A. M.; Wheat, A. J.; Schaberg, M. S.; Hamrock, S. J.; Buratto, S. K. Investigation of Humidity Dependent Surface Morphology and Proton Conduction in Multi-Acid Side Chain Membranes by Conductive Probe Atomic Force Microscopy. *J. Phys. Chem. B* **2015**, *119* (44), 14280–14287.
- (54) Fang, S. J.; Haplepete, S.; Chen, W.; Helms, C. R.; Edwards, H. Analyzing Atomic Force Microscopy Images Using Spectral Methods. *J. Appl. Phys.* **1998**, *82* (12), 5891.
- (55) Mclean, R. S.; Sauer, B. B. *Tapping-Mode AFM Studies Using Phase Detection for Resolution of Nanophases in Segmented Polyurethanes and Other Block Copolymers*; 1997.
- (56) Kim, S.; Briber, R. M.; Karim, A.; Jones, R. L.; Kim, H.-C. Environment-Controlled Spin Coating To Rapidly Orient Microdomains in Thin Block Copolymer Films. *Macromolecules* **2007**, *40* (12), 4102–4105.

- (57) Gu, X.; Gunkel, I.; Hexemer, A.; Russell, T. P. Controlling Domain Spacing and Grain Size in Cylindrical Block Copolymer Thin Films by Means of Thermal and Solvent Vapor Annealing. *Macromolecules* **2016**, *49* (9), 3373–3381.
- (58) Mélin, T.; Zdrojek, M.; Brunel, D. Electrostatic Force Microscopy and Kelvin Force Microscopy as a Probe of the Electrostatic and Electronic Properties of Carbon Nanotubes. In *Scanning Probe Microscopy in Nanoscience and Nanotechnology*; Springer, Berlin, Heidelberg, 2010; pp 89–128.

CHAPTER 4

MULTI-BLOCK COPOLYMERS OF ISOPRENE AND CHLOROMETHYLSTYRENE SYNTHESIS AND CHARACTERIZATION

1 4.1 Introduction

Polymer architectures have attracted vast research interest. Various synthesis routes have been established to achieve complicated block copolymer structures,¹ and their phase behavior has been well studied by self-consistent field theory (SCFT).² For AB-type block copolymers, even though they are composed of just two types of repeating units, different architectures have been synthesized and studied, linear multi-blocks, combs, stars with diblock arms, hetero-arm stars, H-shaped, etc.¹ It is somewhat surprising that in a morphological perspective, the architectures of AB-type block copolymers have limited impacts on phase behaviors, as shown in Figure 1 for the phase diagrams for three multi-block copolymers. The reason for the similarity is that conceptually if you were to scissor the middle B block of an ABA triblock in half, the free energy is relatively unaffected, thus, its equilibrium phase diagram remains much the same as that of an AB diblock copolymer. This rational applies to other architectures as well. However, the phase boundaries, or order-to-disorder transition, can be shifted significantly by various architectures.^{3,4} Taking di-, tri-, and penta- block copolymers with the same DPs of A and B components as an example, N from the y-axis of the phase diagrams is the number of segments per constituent unit, calculated by the DP of the diblocks formed by cutting all the blocks in the middle.⁴ Therefore, χN of tri- or penta-

block copolymers are 1/2 or 1/4 of that of the diblock copolymer, resulting in drastic difference in the degree of segregation and thus impacting morphologies.

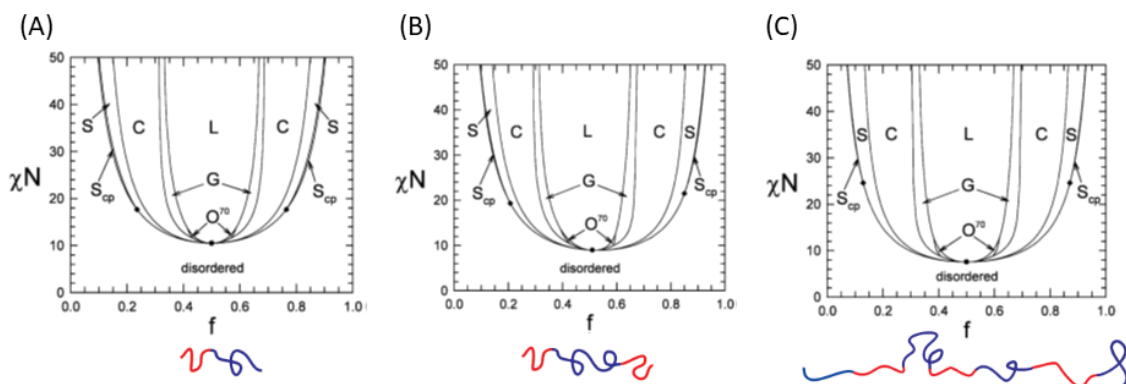


Figure 4. 1 Phase diagram for melts of (A) AB diblock copolymers, (B) ABA triblock copolymers, and (C) infinite linear ABAB... multiblock copolymers. The ordered regions comprise of lamellar (L), cylindrical (C), bcc spherical (S), hcp spherical (S_{cp}), gyroid (G), and Fddd (O⁷⁰) morphologies. ⁴

In spite of the similar phase behavior, various experiments have documented large mechanical differences between di- and tri- block copolymers.⁵⁻¹⁰ Two conformations of the middle block, both loops and bridges, exist in ABA triblock copolymers (Figure 4.2A and B). The proportionalities of looping and bridging are a function of volume fraction (Figure 4.2C). It has been demonstrated that by linking separate interfaces together, the bridges strongly affect mechanical properties. Taking advantages of bridging in triblock copolymers, thermoplastic elastomers for industrial application are usually comprised of two hard outer blocks (high T_g) and a soft midblock (low T_g), therefore, good mechanical property can be achieved by effective stress transfer between glassy domain through the mid-block bridges.

Despite the broad applications of triblock elastomers, the in-depth understanding of morphology-mechanical property relationships is still lacking. Is the classical triblock

design of hard outer blocks and soft middle block the best way to improve mechanical property? If the outer blocks are soft segments, would the bridges formed by the inner hard block bring any positive or negative effect to the overall mechanical properties? Moreover, for ABABA pentablock copolymers, what will the bridging fractions be of the three inner blocks? How does different bridging fractions affect the macroscopic mechanical properties, with either hard or soft outer blocks, respectively?

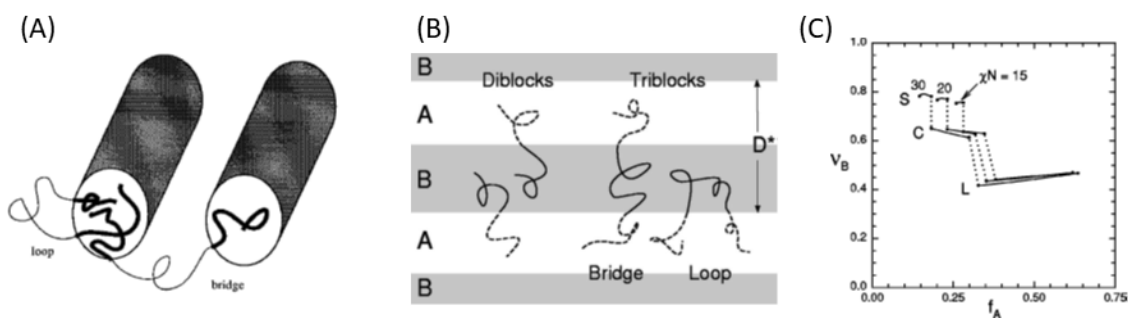


Figure 4. 2 Typical looping and bridging illustration of ABA triblock copolymers in a (A) cylinder morphology and (B) lamellar morphology. (C) Bridging fractions of ABA triblock copolymers as a function of copolymer composition f_A at $\chi N = 15, 20, 30$. The upper, middle, and lower curves correspond to the S, C, and L phases, respectively. The solid dots denote phase transitions, and the dotted lines are simply there to connect curves of the same χN . (Images adapted from Ref. 1 and 8.)

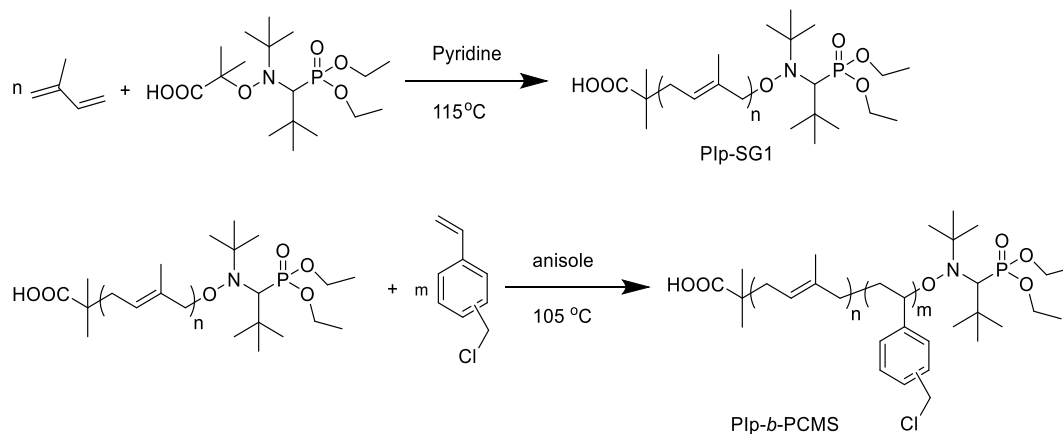
In this study, di-, tri- and penta- block copolymers of isoprene (Ip) and chloromethylstyrene (CMS) were synthesized by two living polymerization methods. Precise control over the structures of all types of block copolymers was achieved. The morphologies were investigated by SAXS and TEM. The experimental results were then compared with simulation study to reveal a detailed understanding of structure-morphology relationship.

2 4.2 Results and Discussion

4.2.1 Synthesis of Diblock Copolymer PIp-*b*-PCMS

In Chapter. 3, diblock copolymer PIp-*b*-PCMS was synthesized by NMP, where *o*-xylene was used as solvent in the second step of chain extension of the PIP macro-initiator by CMS. However, chain transfer to solvent with the benzyl positions of *o*-xylene restricts the living character of NMP, and \bar{D} increased from ~ 1.3 to ~ 1.8 . Anisole, on the other hand, stabilizes the radicals during polymerization as oxygen on the phenyl position is an inert radical acceptor. Therefore, in order to further optimize experimental conditions to obtain better control over polymerization, anisole was used as solvent for polymerization of CMS in diblock copolymer synthesis, as shown in Scheme 4.1.

Scheme 4.1 Synthesis of di-block copolymer PIP-*b*-PCMS



By using anisole as solvent, a light-yellow powder was obtained after precipitation. The yellow color is from the SG1 nitroxide group, which indicates the existence of living chain-ends. Whereas after the polymerization in *o*-xylene, the product is pale white color, which indicates significant chain transfer during polymerization and the loss of SG1 structure on chain-ends. Two diblock copolymers were synthesized by

adjusting the feeding ratio of CMS. The resultant polymers were characterized by GPC and ^1H NMR, as shown in Figure 4.3. The results were listed in Table 4.1. The label “SH” stands for “soft-hard”, indicating the diblock copolymer with the soft PIp block and the hard PCMS block. In Figure 4.3A, GPC traces with unimodal distribution peaks at shorter retention time (higher molecular weight) were observed for both copolymers, compared to that of the hemitelechelic PIp macro-CTA, indicating the formation of PIp-*b*-PCMS diblock copolymers. Two different molecular weights for the PCMS block were obtained, as shown in the Table 4.1. Compared with Chapter 3, a much narrower $D < 1.4$ was obtained for both diblock copolymers after chain extension. The degree of polymerization (DP) of both blocks were calculated from ^1H NMR in Figure 4.3B and the volume fractions of PCMS block were calculated accordingly, based on the DP ratio of two blocks and the densities of the respective homopolymer, PIp and PCMS. ($d_{\text{PIp}} = 0.906 \text{ g/cm}^3$, $d_{\text{PCMS}} = 1.088 \text{ g/cm}^3$)

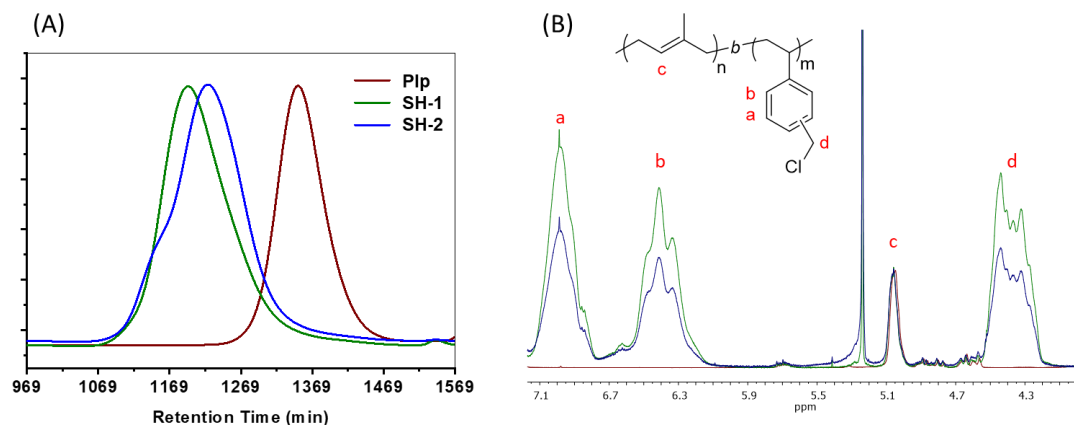


Figure 4. 3 (A) GPC traces and (B) ^1H NMR of PIp-SG1 macro-initiator and PIp-*b*-PCMS.

Table 4. 1 Chemical composition and morphology of diblock copolymer PIp-*b*-PCMS synthesized by NMP.

SH	Composition	N	PIp		PIp- <i>b</i> -PCMS				
			M _n (g/mol)	<i>D</i>	M _n (g/mol)	<i>D</i>	<i>f</i> _{PCMS} (%)	M	d-spacing (nm)
1	PIp ₁₅₉ - <i>b</i> - PCMS ₅₅₂	711	10,900	1.15	32,400	1.27	87	C	21.4
2	PIp ₁₅₉ - <i>b</i> - PCMS ₃₃₇	496			27,100	1.32	80	C	22.5

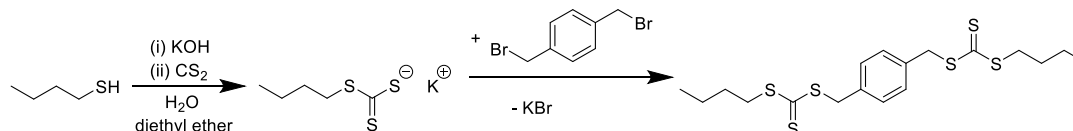
4.2.2 Synthesis of Tri- and Penta-block Copolymers of Ip and CMS

Different approaches have been developed to synthesize triblock copolymers, coupling reactions from diblock copolymers or homopolymers, or by use of difunctional initiator or CTA. Various chemistry can be utilized in coupling reactions,¹¹ such as thiol-ene click,¹² Hiyama coupling,^{13,14} Glaser coupling,¹⁵ etc. Those methods first require the synthesis of macro-precursors, followed by the coupling reactions to build the covalent bond between the blocks in order to achieve the desired triblock architecture. Due to the low reactivity of the macro-precursors during coupling reactions, an alternative strategy is using a difunctional initiator or CTA have been developed. Living polymerization of the first monomer is performed to generate the middle polymer block, followed by chain extension with the second monomer. In this method, designing the difunctional agents is challenging, because the effective reinitiation from the macro-precursor is a significant step for good control of block copolymer synthesis. Synthesis of SG1 based difunctional NMP agent has been conducted by Charleux *et al.*¹⁶ Following the reported procedures, a few trials of SG1 reaction with diene to synthesize di-SG1 initiator have been performed. However, under high temperature (90-120 °C), the radical reaction was not well

controlled and the crude product was difficult to purify. On the other hand, Odian *et al.* have demonstrated that atom transfer radical polymerization (ATRP) route for triblock copolymer synthesis requires the polymerization of the first block to be stopped at relatively low conversion, because the extent of bimolecular termination increases as the monomer concentration decreases.¹⁷ In comparison, synthetic routes to RAFT agents, usually thiocarbonylthio compounds, have been well developed, with initial reports dating as far back as the early 1900s.^{18–20} Since the advent of the RAFT process, the preparation of a vast suite of RAFT agents has been described. A variety of synthesis methods have been developed, such as reaction of a carbodithioate salt with an alkylating agent, thioacylation reactions, thiation of a carboxylic acid or ester, the ketoform reaction, etc.²¹ Different from NMP and ATRP, the living character of RAFT is able to be maintained even at full conversion, due to the unique fragmentation transfer mechanism.²²

Thus, RAFT method was chosen for triblock copolymer syntheses in this study. The difunctional CTA was synthesized based on a previously reported method, the reaction of a carbodithioate salt with alkyl dibromide, as shown in Scheme 4.2.²³

Scheme 4.2 Synthesis of difunctional RAFT CTA



Potassium hydroxide was used to deprotonate butylthiol, which further reacted with carbon disulfide by nucleophilic attack, resulting in carbonotrithioate. Dibromo-*p*-xylene, 0.48 *equiv*, was then added to react with the carbonotrithioate, giving bis-

trithiocarbonates. The crude product was recrystallized from hexane and yellow crystals were obtained in 80% yield.

In order to verify the structure of the difunctional CTA, ESI mass spectrometry was performed (Figure 4.4B). The sodium ion adduct of the molecule was detected in positive ionization mode, with m/z of ~ 457 u/e ($MW = MW_{CTA} + MW_{Na}$). Additionally, in the 1H NMR spectroscopy shown in Figure 4.4A, the splitting, integrations and chemical shifts of each peaks correspond with alkyl chain, benzyl and phenyl protons, respectively. Both characterization methods confirm the successful synthesis of the difunctional CTA, which enables the synthesis of telechelic polymer end-capped with trithiocarbonates.

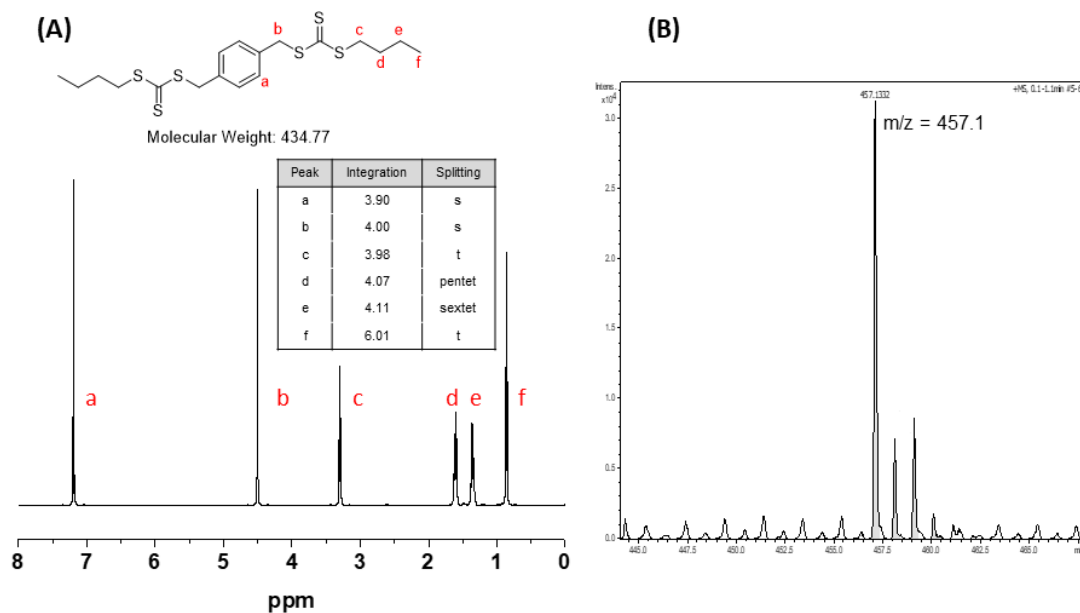


Figure 4. 4 (A) 1H NMR and (B) ESI mass spectra of difunctional CTA.

The synthesis methods of tri- and penta-block copolymers are shown in Scheme 4.3, 4.4 and Scheme 4.5, respectively. The slow rate of polymerization of isoprene (Ip) mediated by RAFT has been reported in the literature. An increase in temperature allows for faster chain propagation, but also leads to a loss of control over radical generation rate

from thermal initiator. To accommodate the increased polymerization temperature, di-*tert*-butylperoxide (dtBP) was chosen for its elongated half-life at 120 °C. Thick-wall Schlenk tubes were carefully sealed after 4 cycles of freeze-pump-thaw to undergo the high-temperature, high-pressure reaction. The polymerization was quenched after 48 hours and resulted in ~32 % conversion, according to ¹H NMR end-group analysis of the homopolymer PIp (Scheme 4.3A).

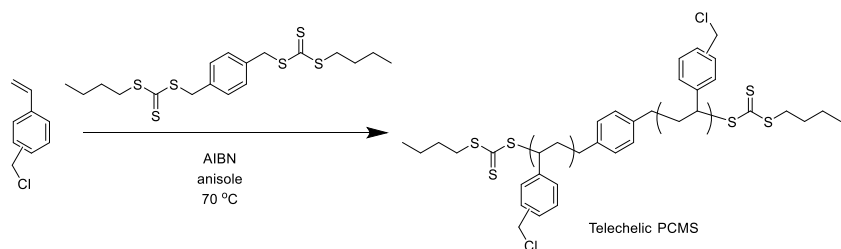
The telechelic PIp was then subjected to chain extension with CMS at 75 °C, using AIBN as initiator (Scheme 4.3B). After 12 hours, the reaction mixture was precipitated in methanol three times and dried under vacuum. The triblock copolymer products appear either as yellow viscous oil or solid depending on molecular weights of both blocks.

The PCMS-*b*-PIp-*b*-PCMS triblock copolymers were again subjected to chain extension reactions by Ip with dtBP at 120 °C, resulting in PIp-*b*-PCMS-*b*-PIp-*b*-PCMS-*b*-PIp pentablock copolymer (Scheme 4.5A).

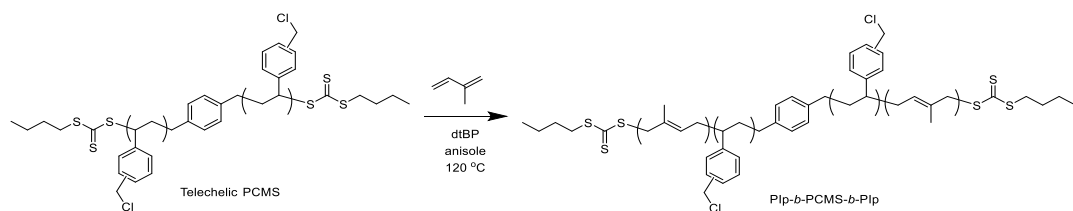
Following a similar synthetic methods, CMS was first polymerized with difunctional CTA (Scheme 4.4A). The telechelic PCMS was then chain extended with Ip to make PIp-*b*-PCMS-*b*-PIp triblock copolymer (Scheme 4.4B), which was able to be chain extended again with CMS to prepare PCMS-*b*-PIp-*b*-PCMS-*b*-PIp-*b*-PCMS pentablock copolymer (Scheme 4.5B).

Scheme 4.3 Synthesis of triblock copolymer **PIp-*b*-PCMS-*b*-PIp**

(A) Synthesis of telechelic PCMS.

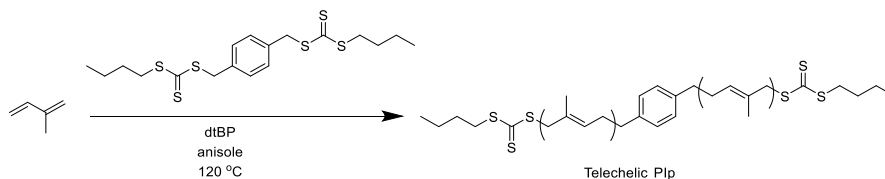


(B) Synthesis of triblock copolymer **PIp-*b*-PCMS-*b*-PIp**.

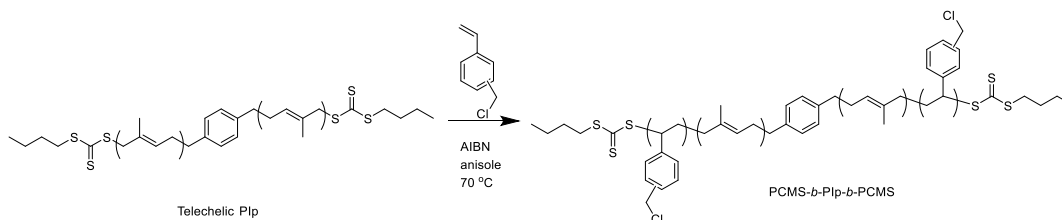


Scheme 4.4 Synthesis of triblock copolymer PCMS-*b*-PIp-*b*-PCMS

(C) Synthesis of telechelic PIp.

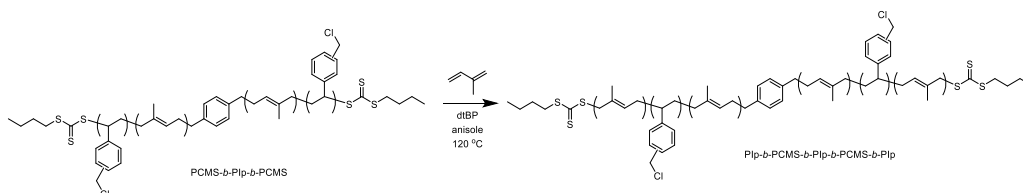


(D) Synthesis of triblock copolymer PCMS-*b*-PIp-*b*-PCMS.

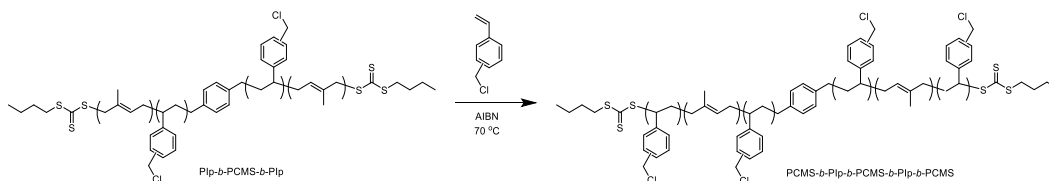


Scheme 4.5 Synthesis of pentablock copolymers

(A) Synthesis of pentablock copolymer PIp-*b*-PCMS-*b*-PIp-*b*-PCMS-*b*-PIp.



(B) Synthesis of pentablock copolymer PCMS-*b*-PIp-*b*-PCMS-*b*-PIp-*b*-PCMS.



The molar ratio between CTA (either difunctional CTA or telechelic macro-CTA) and initiator (either dtBP or AIBN) was kept at 10:1, whereas the feeding ratio of Ip or CMS monomers was adjusted to achieve different molecular weights of PIp and PCMS blocks in tri- or penta-block copolymers. All synthesized block copolymers were labeled with “S” and “H” to indicate the structure formed by the soft PIp block and the hard

PCMS block. For example, the “SHS” series are composed of “soft-hard-soft” triblock copolymers, *i.e.* PIP-*b*-PCMS-*b*-PIp. The molecular weights, dispersities and DPs can be obtained from GPC and ¹H NMR characterization, using the same protocol used for diblock copolymer analysis. The results were listed in Tables 4.2-4.5. The chemical compositions result in a wide range of PCMS volume fractions, from 21% to 89%.

Since the benzylic position of CMS is prone to undergo chain transfer reaction, broadening of the dispersity was observed for chain extension by CMS. Nevertheless, dispersities of all triblock copolymers were less than 1.6 and those of all pentablock copolymers were less than 2.0. The effective fragmentation of the trithiol species on both ends of macro-CTA is accountable for the living character throughout multiple times of chain extension and narrow distribution of resulting block copolymers. Therefore, difunctional CTA has been demonstrated to be a versatile RAFT agent for multi-block copolymer synthesis.

Both drop-casting and spin-coating methods were used to prepare di-, tri- and penta-block copolymer films. For drop-casting, the block polymer solution in chloroform (~100 mg/ml) was drop casted onto a Teflon sheet and allowed to dry. The films were then exposed to saturated THF vapor for solvent annealing for 24 hours before peeling off the Teflon substrate. The thicknesses of the films were ~5 μm. For spin-coating, the block polymer solution in chloroform was spun-cast onto a silver or silicon substrate. The thicknesses of the films depend on solution concentration and films with the thickness of 30, 45 and 60 nm were prepared.

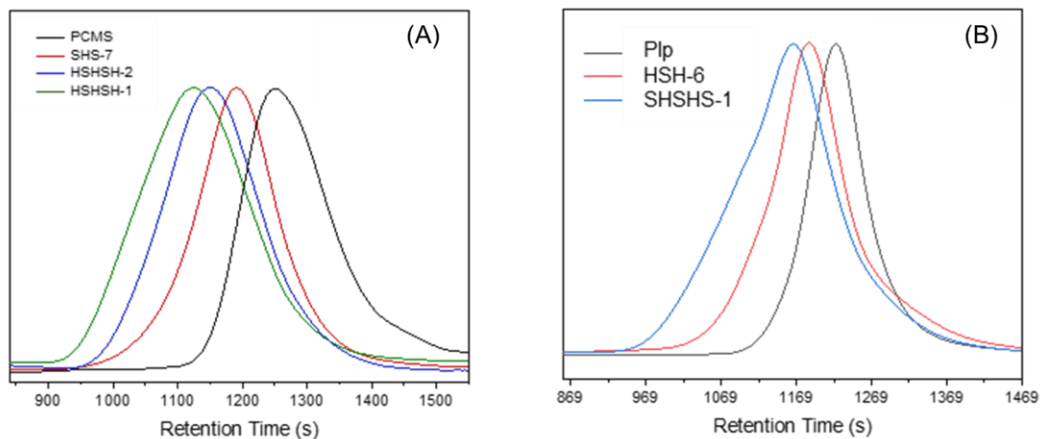


Figure 4. 5 GPC for (A) HSH-6, (B) SHSHS-1, (C) SHS-7 and (D) HSHSH-1.

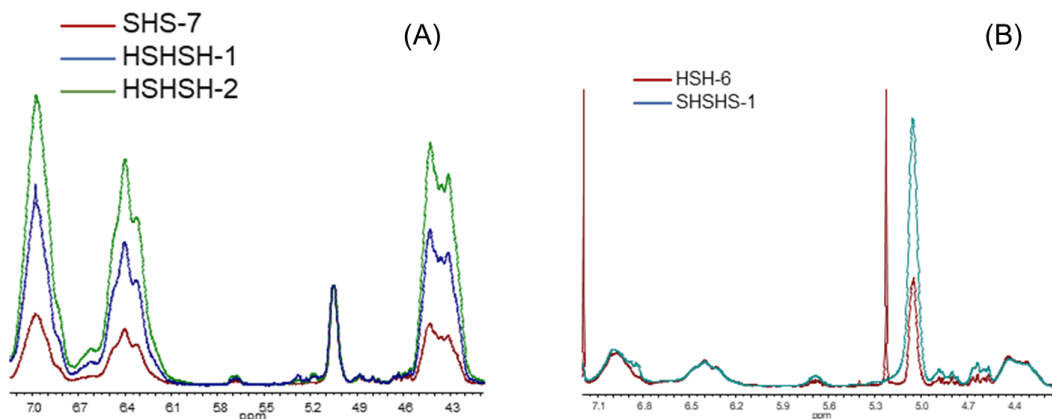


Figure 4. 6 1H NMR for (A) HSH-6, (B) SHSHS-1, (C) SHS-7 and (D) HSHSH-1.

4.2.3 Morphology Investigation of Multi-block Copolymers of Ip and CMS

The morphology of block copolymers was first investigated by SAXS on drop-cast films. The d-spacing spacing, $d = 2\pi/q^*$, was determined for each specimen, where q^* is the primary peak. Morphology was inferred from the higher order peak positions. The d-spacing and morphology results were summarized in Tables 4.1-4.5. Three examples of SAXS profiles for di-, tri- and penta-block copolymers, respectively, are shown in Figure 4.5. For diblock copolymer, SH-1 (Figure 4.5A), up to the

quaternary peak was observed. The peak ratio of $1:\sqrt{3}:\sqrt{7}:\sqrt{9}$ indicates a cylinder morphology, which correspond to the relatively large PCMS volume fraction of 87%, as shown in Table 4.1. For triblock copolymer, SHS-8 (Figure 4.5B), higher order peaks are located at integer multiples of the primary peak, up to the fifth peak, depicting lamellar morphology, which is in agreement with 69% volume fraction of PCMS. Similarly, for pentablock copolymer, SHSHS-1 (Figure 4.5C), lamellar morphology was observed.

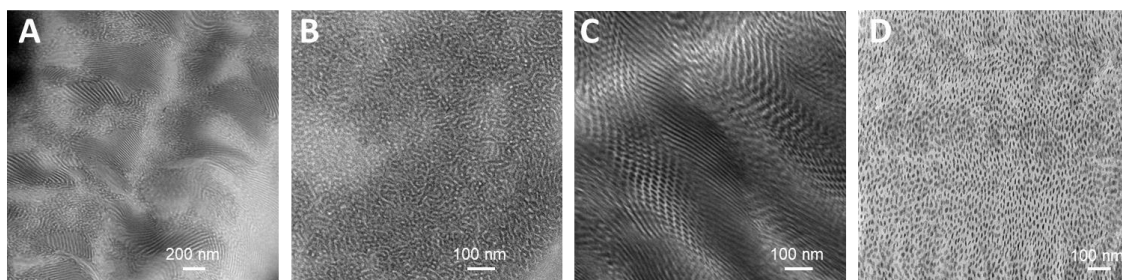


Figure 4. 7 TEM for (A) HSH-6, (B) SHSHS-1, (C) SHS-7 and (D) HSHSH-1.

The morphology was further confirmed by TEM, as shown in Figure 4.6 for examples of two triblock copolymers, as well as two pentablock copolymers obtained by chain extension. All films were microtomed at $-160\text{ }^{\circ}\text{C}$ with a thickness of $\sim 40\text{ nm}$. The specimens were then stained by OsO_4 vapor for 30 min before microscopy. The dark region corresponds to PIP domains in TEM. For HSH-6 (Figure 4.6A), ordered lamellar grains were observed as well as grain boundaries where short-range lamellas with different orientations are observed. The spacing between lamellas was $\sim 30\text{ nm}$. After chain extension, SHSHS-1 (Figure 4.6B), lamellar structures with less aligned orientation were observed. It is also worth noting that the TEM of the pentablock copolymer resembles the grain boundaries in that of the parent triblock copolymer. However, the domain spacing decreased to $\sim 20\text{ nm}$. For SHS-7 (Figure 4.6C), both perpendicular and parallel cylinder structures were observed. From the cross section, the hexagonal packing

of cylinders can be seen. The spacing between cylinders was measured to be ~ 17 nm. After chain extension, the resultant pentablock copolymer, HSHSH-1, displays ordered hexagonally packed cylinder morphology, with domain spacing of ~ 20 nm. Larger volume fraction of PCMS blocks for the pentablock copolymer resulted in larger bright area in TEM, than the triblock copolymer.

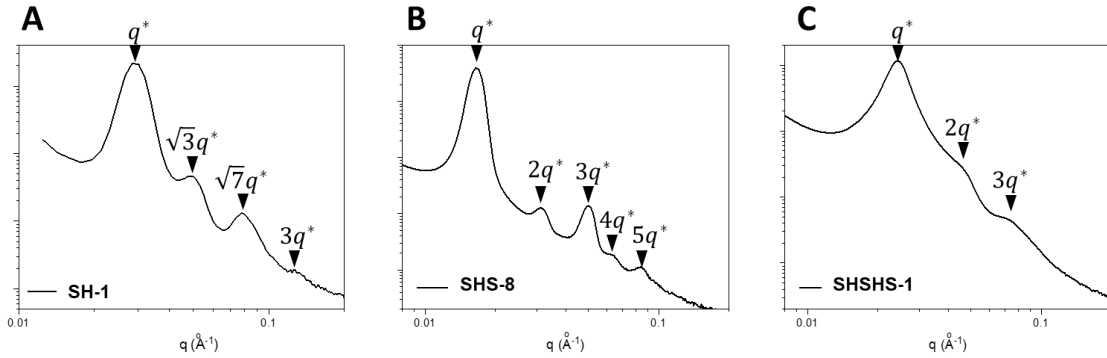


Figure 4. 8 SAXS for (A) SH-1, (B) SHS-8 and (C) SHSHS-1.

Table 4. 2 Chemical composition and morphology of triblock copolymer PCMS-*b*-PIp-*b*-PCMS.

HSH	Composition	N	PIp		PCMS- <i>b</i> -PIp- <i>b</i> -PCMS				
			$M_n^{(1)}$ (g/mol)	$\mathcal{D}^{(1)}$	$M_n^{(1)}$ (g/mol)	$\mathcal{D}^{(1)}$	f_{PCMS} (%) ⁽²⁾	M	d-spacing (nm) ⁽³⁾
1	PCMS ₁₉ - <i>b</i> -PIp ₁₁₀ - <i>b</i> - PCMS ₁₉	73	12,588	1.18	15,405	1.38	37	-	21
2	PCMS ₃₃ - <i>b</i> -PIp ₁₁₀ - <i>b</i> - PCMS ₃₃	112			23,078	1.55	66	-	32
3	PCMS ₃₆ - <i>b</i> -PIp ₁₁₀ - <i>b</i> - PCMS ₃₆	132			30,426	1.44	72	-	30
4	PCMS ₄₂ - <i>b</i> -PIp ₁₁₀ - <i>b</i> - PCMS ₄₂	226			45,770	1.42	85	H	27

5	PCMS ₄₅ - <i>b</i> -PIp ₁₁₀ - <i>b</i> - PCMS ₄₅	286			66,280	1.51	89	H	30
6	PCMS ₁₂₅ - <i>b</i> -PIp ₅₇₃ - <i>b</i> - PCMS ₁₂₅	412	39,900	1.26	47,500	1.45	45	L	38

Table 4. 3 Chemical composition and morphology of pentablock copolymer PIp-*b*-PCMS-*b*-PIp-*b*-PCMS-*b*-PIp.

SHSHS	Composition	N	PIp		PCMS- <i>b</i> -PIp- <i>b</i> -PCMS		PIp- <i>b</i> -PCMS- <i>b</i> -PIp- <i>b</i> -PCMS- <i>b</i> -PIp				
			M _n ⁽¹⁾ (g/mol)	Đ ⁽¹⁾	M _n ⁽¹⁾ (g/mol)	Đ ⁽¹⁾	M _n ⁽¹⁾ (g/mol)	Đ ⁽¹⁾	f _{PCMS} (%) ⁽²⁾	M	d-spacing (nm) ⁽³⁾
1	PIp ₅₆₁ - <i>b</i> -PCMS ₁₂₅ - <i>b</i> -PIp ₅₇₃ - <i>b</i> -PCMS ₁₂₅ - <i>b</i> -PIp ₅₆₁	486	39,900	1.26	47,500	1.45	64,000	1.82	22	L	26

Table 4. 4 Chemical composition and morphology of triblock copolymer PIp-*b*-PCMS-*b*-PIp.

SHS	Composition	N	PCMS		PIp- <i>b</i> -PCMS- <i>b</i> -PIp				
			M _n ⁽¹⁾ (g/mol)	Đ ⁽¹⁾	M _n ⁽¹⁾ (g/mol)	Đ ⁽¹⁾	f _{PCMS} (%) ⁽²⁾	M	d-spacing (nm) ⁽³⁾
1	PIp ₇₃ - <i>b</i> -PCMS ₃₁ - <i>b</i> -PIp ₇₃	88	4,800	1.38	26,300	1.20	29	-	16
2	PIp ₁₁₂ - <i>b</i> -PCMS ₃₁ - <i>b</i> -PIp ₁₁₂	127			29,200	1.29	21	-	18
3	PIp ₂₂ - <i>b</i> -PCMS ₃₇ - <i>b</i> -PIp ₂₂	40	5,600	1.52	7,900	1.31	61	-	13
4	PIp ₉₈ - <i>b</i> -PCMS ₃₇ - <i>b</i> -PIp ₉₈	116			13,400	1.36	26	-	14
5	PIp ₁₈ - <i>b</i> -PCMS ₆₇ - <i>b</i> -PIp ₁₈	52	10,200	1.62	15,700	1.34	78	-	16
6	PIp ₈₆ - <i>b</i> -PCMS ₆₇ - <i>b</i> -PIp ₈₆	119			21,200	1.49	42	L	20

7	PIp ₁₈₄ -b-PCMS ₃₀₈ -b- PIp ₁₈₄	338	47,000	1.31	51,300	1.54	61	L	32
8	PIp ₂₈₉ -b-PCMS ₃₀₈ -b- PIp ₂₈₉	443			65,000	1.52	50	L	38
9	PIp ₂₃₀ -b-PCMS ₃₄₇ -b- PIp ₂₃₀	403	54,400	1.43	60,700	1.49	59	L	40
10	PIp ₃₀₄ -b-PCMS ₃₄₇ -b- PIp ₃₀₄	478			78,900	1.38	52	L	45

Table 4. 5 Chemical composition and morphology of pentablock copolymer PCMS-b-PIp-b-PCMS-b-PIp-b-PCMS.

HSHSH	Composition	N	PCMS		PIp-b-PCMS-b-PIp		PCMS-b-PIp-b-PCMS-b-PIp-b-PCMS				
			M _n ⁽¹⁾ (g/mol)	D ⁽¹⁾	M _n ⁽¹⁾ (g/mol)	D ⁽¹⁾	M _n ⁽¹⁾ (g/mol)	D ⁽¹⁾	f _{PCMS} (%) ⁽²⁾	M	d-spacing (nm) ⁽³⁾
1	PCMS ₄₇₂ -b-PIp ₁₈₄ -b-PCMS ₃₀₈ -b-PIp ₁₈₄ -b- PCMS ₄₇₂	405	47,000	1.31	51,300	1.54	95,700	1.92	86	H	36
2	PCMS ₂₇₇ -b-PIp ₁₈₄ -b-PCMS ₃₀₈ -b-PIp ₁₈₄ -b- PCMS ₂₇₇	308					78,100	1.56	79	H	31

For diblock copolymers with the spherical, cylindrical, or lamellar morphologies, the characteristic spacing has been demonstrated to have the same functional dependence on the volume fraction, N , and the *Flory-Huggins* parameter, χ .²⁴⁻³⁰ In the strong-segregation limit, the lamellar d-spacing for diblock copolymer scales as $d \propto N^{2/3}$.³¹ For symmetrical triblock copolymers, lattice model within a mean-field approximation has shown $d \propto N^{0.68}$.³² The same trend of d-spacing change was observed in the triblock comparison between SHS-7 and SHS-9, both with lamellar morphology and similar

PCMS volume fraction of ~60%. A larger χN in SHS-9 resulted in 8 nm larger d-spacing than SHS-7.

An unexpected phenomenon of d-spacing decreasing after chain extension was observed in SHSHS-1 and HSHSH-2, chain extended from HSH-6 and SHS-7, respectively. Special attention should be paid to the morphology change after chain extension, which might render the d-spacing not comparable. The decreased χN of HSHSH-2 after chain extension might be accountable for the d-spacing decrease. In addition, looping events could happen in all three inner blocks of pentablock copolymers but can only happen in one inner block in triblock copolymers. Therefore, pentablock copolymers could possibly undergo multiple looping, which might lead to d-spacing decreases.

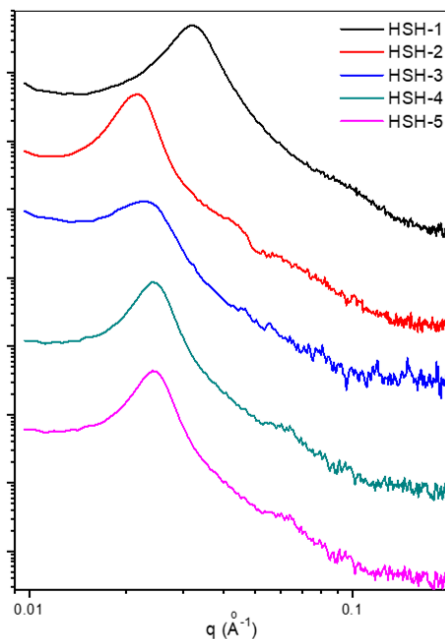


Figure 4. 9 SAXS for weak-segregation SHS samples.

A non-monotonic change of d-spacing with increasing DPs of hard outer blocks was observed, with the same DP of the soft inner block (from SHS-1 to SHS-5). As

shown in Figure 4.7, distinct higher-order peaks were not observed in SAXS profiles for all five samples, indicating they are in the weak segregation limit, which could be accountable for the arbitrary scattering feature sizes. On the contrary, if the DP is large enough to result in strong segregation, chain extension from the same inner block, a larger DP of outer blocks results in a larger d-spacing, as shown in triblocks HSH-7, 8, 9, 10.

Another example revealing the significant impact of χN on the degree of segregation and polymer morphologies can be seen in SHS-3 and SHS-7, with the same PCMS volume fraction of 61%, but different N . A difference was observed in their respective SAXS profiles in Figure 4.8. A larger N of 338 in SHS-7 resulted in distinct higher-order peaks, indicating strong segregation and ordered structure. A decrease of N to 40 led to weak segregation limit, indicated by absence of higher-order peaks in SAXS. Instead, only a broad primary feature was observed.

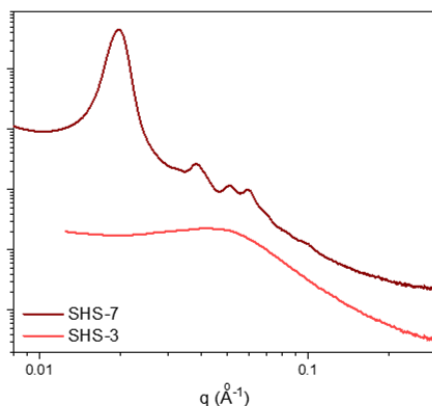


Figure 4. 10 SAXS for weak-segregation SHS-3 with small N and strong-segregation SHS-7 with large χN .

Similar phenomenon was reported in self-consistent field theory (SCFT) study of ABA triblock copolymer.³ As an indicator of the degree of segregation, the interfacial

width between A and B domains were correlated to χN . Small χN leads to the weak segregation limit, indicated by increase in the interfacial width.

Regarding d-spacing change by different volume fractions f_A with the same χN , Matsen *et al.* have established a relationship between d-spacing and volume fraction, with the same χN value of 30, as shown in Figure 4.9.³ D-spacing increases with increasing f_A from ~ 0.15 to ~ 0.35 . Then, a plateau region was observed from f_A of ~ 0.35 to ~ 0.7 , where d-spacing remains constant, followed by a d-spacing decrease with f_A increasing, from ~ 0.7 to ~ 0.85 . Triblocks HSH-6 and SHS-9 with similar N values of ~ 410 , display similar d-spacings, 38 and 40 nm. Because the PCMS volume fractions, 45% and 59%, lay within the plateau of d-spacing versus f_A . In contrast, triblocks SHS-10 and pentablock SHSHS-1 exhibit volume fractions of 22% and 52%, respectively. Therefore, a difference of 19 nm between their d-spacings was seen, regardless of the similar N values of ~ 480 for both. Nevertheless, particular attention should be paid to the polymer architecture difference, *i.e.*, the number of blocks, which might have an influence on d-spacing as well. With the developed synthesis protocol, more experimental data points can be obtained to explore the relationship of d-spacing and volume fraction.

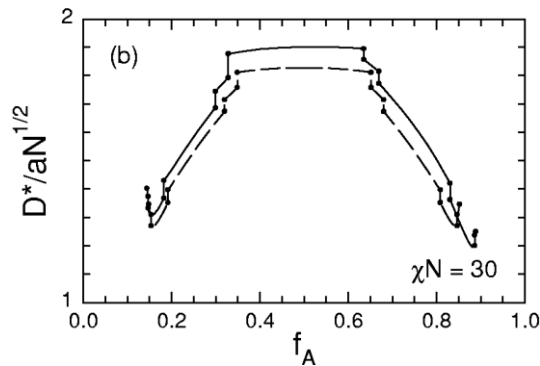


Figure 4. 11 d-spacings D^* as a function of composition f_A at a fixed $\chi N=30$.

(Image adapted from Ref. 97.)

3 4.3 Future Prospective

4.3.1 Mechanical Properties Characterization of the Multi-block Copolymers

The bridging and looping fractions of inner blocks from multi-block copolymers are envisioned to be dependent on the polymer architectures. As a result, mechanical properties, which are closely tied to the effective bridging, will also be affected by polymer architectures. Dynamic mechanical analysis could be performed on all di-, tri-, and penta- block copolymers. From the results, the mechanism of polymer chain configurations affecting mechanical properties may be revealed on a molecular scale.

4.3.2 Investigation on the Morphology of Charged-neutral Multi-block Copolymers

As demonstrated in this chapter, the complexity of block copolymers can be greatly enlarged by increasing the number of blocks. In comparison to the conventional two-dimensional phase diagram for diblock copolymers (Figure 4.1A), other dimensions of block-copolymer-structure related factors are worth exploring. In order to achieve the goal of establishing multi-dimensional phase diagrams for block copolymers, the number of blocks, symmetry, architectures, and the charge fractions will be four variables of interest.

The number of blocks from two to five has been successfully achieved in this study. The inventory of di-, tri- and penta-block copolymers need to be further completed, covering a wider range of volume fraction for each type of polymer structure,

so that volume fraction effect can be normalized for morphology comparison between different copolymers.

Symmetry and architectures can be adjusted via different synthesis methods. With the help of nitroxide-mediated radical polymerization, unsymmetrical triblock copolymers can be synthesized by modulating different DPs of outer blocks. Good control over RAFT agent synthesis as well as living radical polymerization has been demonstrated, thus, more complicated polymer architectures, *i.e.* star, branched, H-shaped, can be obtained using versatile RAFT agents and grafting chemistry.

Regarding the charge effects on block copolymer morphology, the quaternizable benzyl chloride positions on the PCMS block in all synthesized block copolymers of Ip and CMS provide opportunities for installing charges onto these polymer backbones. Based on different molecular weights and parent block copolymer structures, different distribution of charges can be obtained. In addition, different quaternization agents and quaternization ratio can be exploited to investigate the impact from charges on block polyelectrolyte morphology.

4 4.4 Reference

- (1) Bates, F. S.; Schulz, M. F.; Khandpur, A. K.; Förster, S.; Rosedale, J. H.; Almdal, K.; Mortensen, K. Fluctuations, Conformational Asymmetry and Block Copolymer Phase Behaviour. *Faraday Discuss.* **1994**, 98 (0), 7–18.
- (2) Helfand, E. Theory of Inhomogeneous Polymers: Fundamentals of the Gaussian Random-walk Model. *J. Chem. Phys.* **1975**, 62 (3), 999–1005.
- (3) Matsen, M. W. Equilibrium Behavior of Asymmetric ABA Triblock Copolymer

- Melts. *J. Chem. Phys.* **2000**, *113* (13), 5539–5544.
- (4) Matsen, M. W. Effect of Architecture on the Phase Behavior of AB-Type Block Copolymer Melts. *Macromolecules* **2012**, *45* (4), 2161–2165.
- (5) Yamaoka, I.; Kimura, M. Effects of Morphology on Mechanical Properties of a SBS Triblock Copolymer. *Polymer (Guildf)*. **1993**, *34* (21), 4399–4409.
- (6) Ryu, C. Y.; Lee, M. S.; Hajduk, D. A.; Lodge, T. P. Structure and Viscoelasticity of Matched Asymmetric Diblock and Triblock Copolymers in the Cylinder and Sphere Microstructures. *J. Polym. Sci. Part B Polym. Phys.* **1997**, *35* (17), 2811–2823.
- (7) Riise, B. L.; Fredrickson, G. H.; Larson, R. G.; Pearson, D. S. Rheology and Shear-Induced Alignment of Lamellar Diblock and Triblock Copolymers. *Macromolecules* **1995**, *28* (23), 7653–7659.
- (8) McKay, K. W.; Gros, W. A.; Diehl, C. F. The Influence of Styrene–Butadiene Diblock Copolymer on Styrene–Butadiene–Styrene Triblock Copolymer Viscoelastic Properties and Product Performance. *J. Appl. Polym. Sci.* **1995**, *56* (8), 947–958.
- (9) Adams, J. L.; Graessley, W. W.; Register, R. A. Rheology and the Microphase Separation Transition in Styrene-Isoprene Block Copolymers. *Macromolecules* **1994**, *27* (21), 6026–6032.
- (10) Honeker, C. C.; Thomas, E. L. Impact of Morphological Orientation in Determining Mechanical Properties in Triblock Copolymer Systems. *Chem. Mater.* **1996**, *8* (8), 1702–1714.
- (11) Polymeropoulos, G.; Zapsas, G.; Ntetsikas, K.; Bilalis, P.; Gnanou, Y.;

- Hadjichristidis, N. 50th Anniversary Perspective: Polymers with Complex Architectures. *Macromolecules* **2017**, *50* (4), 1253–1290.
- (12) Liu, B.; Quirk, R. P.; Wesdemiotis, C.; Yol, A. M.; Foster, M. D. Precision Synthesis of ω -Branch, End-Functionalized Comb Polystyrenes Using Living Anionic Polymerization and Thiol–Ene “Click” Chemistry. *Macromolecules* **2012**, *45* (23), 9233–9242.
- (13) Iatrou, H.; Siakali-Kioulafa, E.; Hadjichristidis, N.; Roovers, J.; Mays, J. Hydrodynamic Properties of Model 3-Miktoarm Star Copolymers. *J. Polym. Sci. Part B Polym. Phys.* **1995**, *33* (13), 1925–1932.
- (14) Tselikas, Y.; Iatrou, H.; Hadjichristidis, N.; Liang, K. S.; Mohanty, K.; Lohse, D. J. Morphology of Miktoarm Star Block Copolymers of Styrene and Isoprene. *J. Chem. Phys.* **1996**, *105* (6), 2456–2462.
- (15) Polymeropoulos, G.; Bilalis, P.; Hadjichristidis, N. Well-Defined Cyclic Triblock Terpolymers: A Missing Piece of the Morphology Puzzle. *ACS Macro Lett.* **2016**, *5* (11), 1242–1246.
- (16) Nicolas, J.; Charleux, B.; Guerret, O.; Magnet, S. Nitroxide-Mediated Controlled Free-Radical Emulsion Polymerization Using a Difunctional Water-Soluble Alkoxyamine Initiator. Toward the Control of Particle Size, Particle Size Distribution, and the Synthesis of Triblock Copolymers. *Macromolecules* **2005**, *38*, 9963–9973.
- (17) Odian, G. *Principles of Polymerization*; John Wiley & Sons, Ltd, 2004.
- (18) Purvis, J. E.; Jones, H. O.; Tasker, H. S. CCXL. - The Colour and Absorption Spectra of Some Sulphur Compounds. *J. Chem. Soc. {,} Trans.* **1910**, *97*, 2287–

2297.

- (19) Bost, R.; Williams, W. Carbithioic Acid Studies. II. Cyclohexylcarbithioic Acid and Various Derivatives. *J. Am. Chem. Soc.* **1930**, *52* (12), 4991–4992.
- (20) Bost, R.; Mattox, W. Carbithioic Acid Studies. I. Toly-4-Carbithioic Acid and Certain Derivatives. *J. Am. Chem. Soc.* **1930**, *52* (1), 332–335.
- (21) Keddie, D. J.; Moad, G.; Rizzardo, E.; Thang, S. H. RAFT Agent Design and Synthesis. *Macromolecules* **2012**, *45* (13), 5321–5342.
- (22) Perrier, S. 50th Anniversary Perspective: RAFT Polymerization - A User Guide. *Macromolecules* **2017**, *50* (19), 7433–7447.
- (23) Bowes, A.; Mcleary, J. B.; Sanderson, R. D. AB and ABA Type Butyl Acrylate and Styrene Block Copolymers via RAFT-Mediated Miniemulsion Polymerization. *J. Polym. Sci. Part A Polym. Chem.* **2007**, *45* (4), 588–604.
- (24) Chen, L.; Hallinan, D. T.; Elabd, Y. A.; Hillmyer, M. A. Highly Selective Polymer Electrolyte Membranes from Reactive Block Polymers. *Macromolecules* **2009**, *42* (16), 6075–6085.
- (25) Fetters, L. J.; Lohse, D. J.; Richter, D.; Witten, T. A.; Zirkel, A. Connection between Polymer Molecular Weight, Density, Chain Dimensions, and Melt Viscoelastic Properties. *Macromolecules* **1994**, *27* (17), 4639–4647.
- (26) Kennemur, J. G.; Hillmyer, M. A.; Bates, F. S. Synthesis, Thermodynamics, and Dynamics of Poly(4-*Tert*-Butylstyrene-*b*-Methyl Methacrylate). *Macromolecules* **2012**, *45* (17), 7228–7236.
- (27) Schmitt, A. K.; Mahanthappa, M. K. Characteristics of Lamellar Mesophases in Strongly Segregated Broad Dispersity ABA Triblock Copolymers.

- Macromolecules* **2014**, *47* (13), 4346–4356.
- (28) Semenov, A. N. Contribution to the Theory of Microphase Layering in Block-Copolymer Melts. *Sov. Phys.* **1985**, *61* (4), 733–742.
- (29) Widin, J. M.; Kim, M.; Schmitt, A. K.; Han, E.; Gopalan, P.; Mahanthappa, M. K. Bulk and Thin Film Morphological Behavior of Broad Dispersity Poly(Styrene-*b*-Methyl Methacrylate) Diblock Copolymers. *Macromolecules* **2013**, *46* (11), 4472–4480.
- (30) Zalusky, A. S.; Olayo-Valles, R.; Wolf, J. H.; Hillmyer, M. A. Ordered Nanoporous Polymers from Polystyrene–Polylactide Block Copolymers. *J. Am. Chem. Soc.* **2002**, *124* (43), 12761–12773.
- (31) Semenov, A. N. Theory of Block Copolymer Interfaces in the Strong Segregation Limit. *Macromolecules* **1993**, *26* (24), 6617–6621.
- (32) Matsen, M. W.; Schick, M. Lamellar Phase of a Symmetric Triblock Copolymer. *Macromolecules* **1994**, *27* (1), 187–192.

CHAPTER 5

INVESTIGATION ON RADICAL RING-OPENING POLYMERIZATION AND CHARGE TRANSFER OF CYCLIC KETENE ACETALS

5.1 Introduction

Much research has been performed in the last decade on radical ring-opening polymerization (rROP) of cyclic ketene acetals (CKAs) for polyester syntheses, through a radical addition and subsequent ring-opening mechanism.^{1,2} The copolymerization of CKAs with various vinyl monomers enables the preparation of functional polyesters, which have found applications in marine antibiofouling,³ degradable elastomers and adhesives,⁴ bio-degradable micelles/nanoparticles for drug delivery.⁵⁻⁷ Recently, Sumerlin *et al.* reported the alternating copolymerization of CKAs and maleimides with different *N*-substituted groups, demonstrating a synthetic mimic of the precise nature from biological macromolecules.^{8,9} The nearly perfect alternating feature highlights the potential of using CKAs and electron-deficient vinyl comonomers as a new platform to control monomer sequence, and to prepare well-defined polymer architectures.

The alternating tendency during radical copolymerization is dependent on the comonomer's electron affinity and steric effects. Due to the presence of the two conjugated carbonyl groups, the carbon carbon double bond on maleic anhydride and maleimide derivatives are electron poor and sterically hindered. As a result, their homopolymerization and homo-propagation are restricted and the tendency for alternation is increased, especially during the copolymerizations with electron-rich monomers like styrene and vinyl acetate. Maleic anhydride and maleimides have been widely used as

electron acceptor monomers to create various structural patterns and achieve sequence-oriented performance.¹⁰⁻¹⁴ In addition to the AB primary sequence, the AAB alternating sequence was observed by Kamigaito *et al.*, whereby fluoroalcohol solvent was used for the copolymerization of *N*-phenyl maleimide and limonene to facilitate the formation of a bimolecular repeat units of maleimide.¹⁵⁻¹⁷

Despite the resemblance of maleic anhydride to maleimides, the alternating copolymerization with CKA is not applicable to maleic anhydride. Rather, CKA decomposition has been observed with rapid color change at room temperature -- prior to radical polymerization.^{8,9,18} The vast difference in reactivity between CKA and maleic anhydride or maleimides has been attributed to the increased electrophilicity of maleic anhydride in comparison to maleimides. Although the electron transfer and cycloaddition reactions of maleimides as an electron-accepters has also been reported.¹⁹ Due to the electron-rich nature of the CKA olefin, charge-transfer reactions can occur in the presence of electrophilic compounds.²⁰⁻²³ Such reactions of electron donor and acceptor alkenes lead to the formation of a variety of products, including cycloadducts, open-chain adducts, homopolymers, etc.²⁴ Specifically, Hall *et al.* investigated the reactions between 2-methylene-1,3-dioxepane (MDO) and alkenes containing various electron-acceptor groups, where different product structures were characterized and corresponding reaction ratios were quantified.¹⁹

In contrast to the plethora of the studies on the radical copolymerizations of CKA and vinyl-based monomers, an in-depth investigation on these electron-driven “side” reactions between CKA and electrophilic comonomers is still lacking. In this work, we focus on the charge-transfer chemistry between CKAs, as the electron donors, and maleic

anhydride derivatives, as the electron acceptors. These empirical results and computational studies can provide a comprehensive fundamental understanding of the relationship between the structures of the donor-acceptors and the competition between radical copolymerization and charge-transfer reactions. Ultimately, the results can provide crucial insights on monomer design principles in order to fully realize the potentials of desired functionalities during rROP of CKAs and afford a versatile, robust synthetic route for the preparation of functional, degradable and precision copolymers.

5.2 Materials and Methods

Materials. 2,2'-Azobisisobutyronitrile (AIBN, 98%, Sigma-Aldrich) was recrystallized from methanol. All other chemicals were reagent grade purchased from Sigma-Aldrich and used as received.

Synthesis of 5,6-benzo-2-methylene-1,3-dioxepane (BMDO)²⁵

Step 1: synthesis of 5,6-benzo-2-(bromomethyl)-1,3-dioxepane. 1,2-benzenedimethanol (147.1 g, 1.06 mol), bromoacetaldehyde dimethylacetal (180.0 g, 1.06 mol) were mixed as the stock solution. Dioxane (330 g) and *p*-toluenesulfonic acid (1.01 g, 10 mmol) was added to a pre-dried three-neck flask fitted with a Claisen bridge and dropping funnel for collecting methanol. Increase the temperature to 100 °C and start adding the stock solution dropwise over 5 h under nitrogen. Keep effectively recycling dioxane while removing the methanol. When almost all the calculated amount of methanol was collected, the temperature was raised to 120 °C under reduced pressure. After cooling at room temperature, the crude product solidified. The product was dissolved in CHCl₂ and washed with NaHCO₃ solution and water. The solution was then dried over MgSO₄, concentrated,

and recrystallized in a mixture of chloroform and *n*-hexane to give 180.0 g (yield = 80 %) of pale-yellow crystals.

Step 2: synthesis of BMDO. A mixture of 5,6-benzo-2-(bromomethyl)-1,3-dioxepane (180.0 g, 0.74 mol), *t*-BuOK (92.5 g, 0.96 mol) and 800 mL *t*-BuOH were added into a round-bottom flask and allowed to react under nitrogen at 80 °C for 24 h. After cooling to room temperature, the reaction mixture was poured into 2 L of diethyl ether. The insoluble material was removed by passing through Al₂O₃. The diethyl ether was removed, and the crude liquid was distilled under reduced pressure to give a colorless liquid which solidified to white crystals (92.0 g, yield = 77%).

Synthesis of 2-methylene-1,3,6-trioxocane (MTC)^{26,27}

Step 1: synthesis of 2-(bromomethyl)-1,3,6-trioxocane. Diethylene glycol (126.8 g, 1.20 mol), bromoacetaldehyde dimethylacetal (202.0 g, 1.20 mol) were mixed as the stock solution. Dioxane (330 g) and *p*-toluenesulfonic acid (1.14 g, 10 mmol) was added to a pre-dried three-neck flask fitted with a Claisen bridge and dropping funnel for collecting methanol. Increase the temperature to 100 °C and start adding the stock solution dropwise over 5 h under nitrogen. Keep effectively recycling dioxane while removing the methanol. When almost all the calculated amount of methanol was collected, the temperature was raised to 120 °C under reduced pressure. After cooling at room temperature, the crude product was dissolved in CHCl₂ and washed with NaHCO₃ solution and water. The solution was then dried over MgSO₄, concentrated, and distilled under reduced pressure to give 110.0 g (yield = 44 %) product, which solidified into white crystals.

Step 2: synthesis of MTC. A mixture of 2-(bromomethyl)-1,3,6-trioxocane (110.0 g, 0.52 mol) was dissolved in 600 mL THF in a round-bottom flask. The flask was placed in an

ice bath at 0 °C before *t*-BuOK (65.1 g, 0.68 mol) was slowly added over 6 h. The mixture was allowed to warm to room temperature and continue to react under nitrogen for 24 h. Then the reaction mixture was poured into 2 L of diethyl ether. The insoluble material was removed by passing through Al₂O₃. The diethyl ether was removed, and the crude liquid was distilled under reduced pressure to give a colorless liquid (30.0 g, yield = 44 %).

CKA Homopolymerization. Polymerizations of CKA were performed using the molar ratio AIBN : CKA = 1 : 100 in anisole with a total monomer concentration of 2 mol/L at 75 °C. As an example, the homopolymerization of MTC was conducted as follows. MTC (2 g, 15 mmol) and AIBN (25 mg, 0.15 mmol) were dissolved in anisole (5.7 mL) in a 20 mL pre-dried vial. The solution was purged by N₂ for 30 min before placing into an oil bath at 75 °C for 24 h. The polymerization was quenched by placing the vial into an ice bath. Then the solution was precipitated into diethyl ether for three times to remove residual monomers and solvent. The precipitate was collected by filtration and dried under vacuum before further characterization.

CKA Copolymerization with Maleimides. Copolymerizations of CKA and maleimides were performed using the molar ratio AIBN : CKA : maleimide = 1 : 50 : 50 in anisole with a total monomer concentration of 2 mol/L at 75 °C. As an example, the copolymerization of MTC and *N*-propylmaleimide (NPrMI) was conducted as follows. MTC (2 g, 15 mmol), NPrMI (2.35 g, 15 mmol) and AIBN (50 mg, 0.03 mmol) were dissolved in anisole (12 mL) in a 20 mL pre-dried vial. The solution was purged by N₂ for 30 min before placing into an oil bath at 75 °C for 6 h. The polymerization was quenched by placing the vial into an ice bath. Then the solution was precipitated into diethyl ether

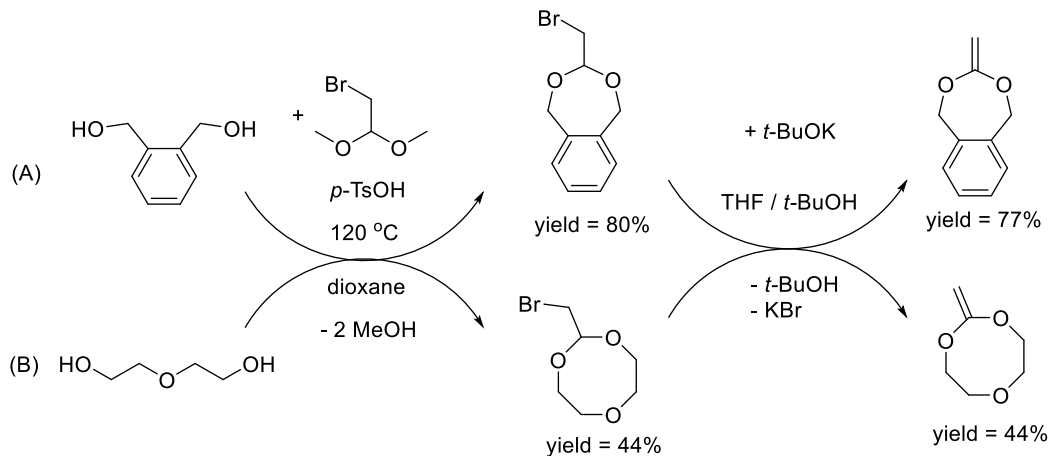
for three times to remove residual monomers and solvent. The precipitate was collected by filtration and dried under vacuum before further characterization.

Characterization. *Gel Permeation Chromatography (GPC).* GPC was performed in THF at a flow rate of 1.0 mL/min using a refractive index detector on a Polymer Laboratories PL-GPC 50 integrated GPC system. *Nuclear Magnetic Resonance (NMR) Spectroscopy.* NMR spectroscopy was performed in 5 mm diameter tubes in deuterated chloroform (CDCl₃) at 25 °C. ¹H NMR spectroscopies were performed on a Bruker 500 spectrometer at 500 MHz (¹H).

5.3 Results and Discussion

During rROP, full ring-opening of CKAs is desirable in order to achieve a degradable backbone with ester groups periodically distributed along the polymer. The synergistic effects from the strain release of the seven-member ring and the enhanced stability of the resultant benzylic radical after ring-opening render 5,6-benzo-2-methylene-1,3-dioxepane (BMDO) to be a promising CKA candidate for aromatic polyester synthesis by rROP.^{1,2} Additionally, due to the strong ring strain, the eight-member ring, 2-methylene-1,3,6-trioxocane (MTC), also exhibits 100% ring-opening during rROP under a broad range of different experimental conditions, which leads to the formation of an aliphatic poly(ester-ether) backbone. Therefore, BMDO and MTC were chosen as standard CKA monomers in this study, for future polyester preparation perspective.

Scheme 5.1 Synthetic routes for the preparation of (A) BMDO and (B) MTC.



The syntheses of the two CKAs were based on the methods reported previously, including ring formation and elimination steps (Scheme 5.1).²⁵⁻²⁷ The CKA structure and purity were confirmed by ^1H NMR in Figures 5.1 and 5.2. During the first ring-formation step, thermodynamically driven intermolecular condensation was recognized to be the main competitive side reaction, which can be effectively hindered. Especially for MTC synthesis, less than 10% yield of the cyclic structure was obtained for the reaction in bulk and poly(acetal-ether) was obtained as the main product (Figure 5.3), presumably because the energy barrier for the formation of the eight-member highly strained ring is much higher. Whereas the reaction in dioxane solution (50 wt%) under the same temperature favors the intramolecular acetal exchange and the yield of the cyclic structure was significantly improved to 50%.

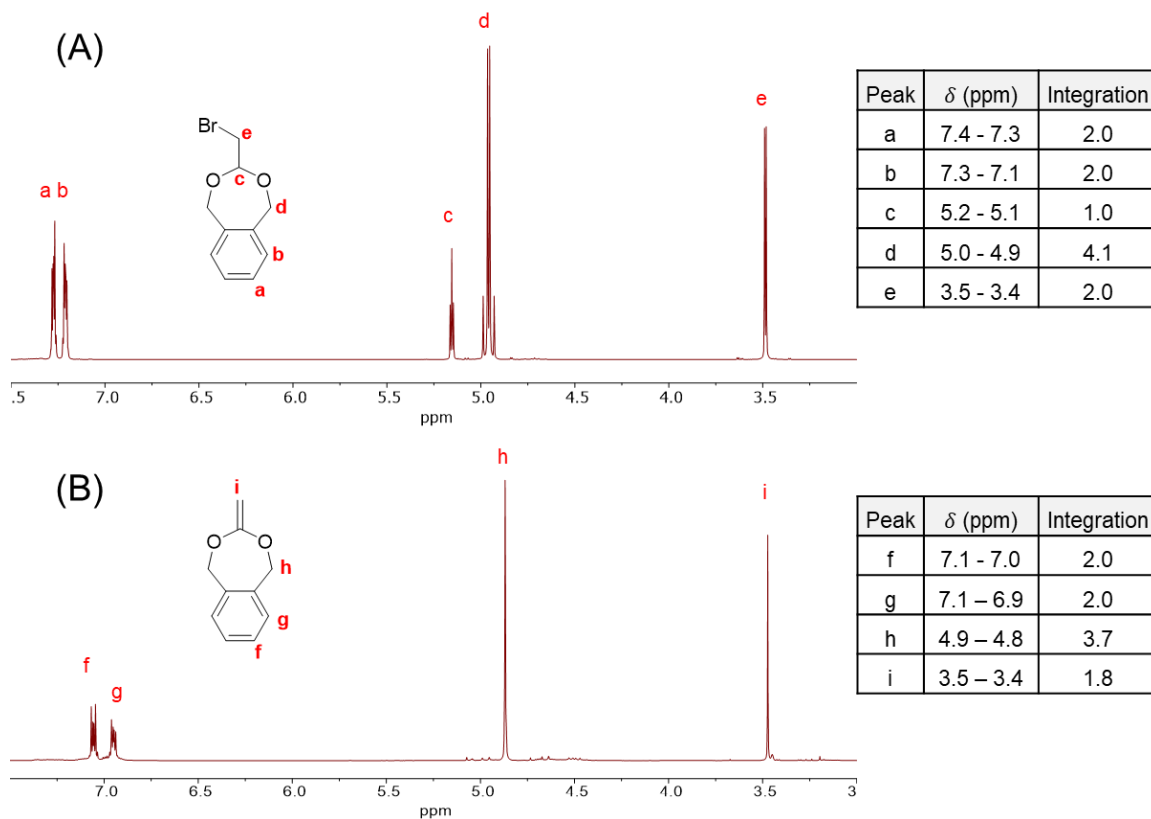


Figure 5. 1 ^1H NMR of (A) 5,6-benzo-2-(bromomethyl)-1,3-dioxepane and (B) BMDO.

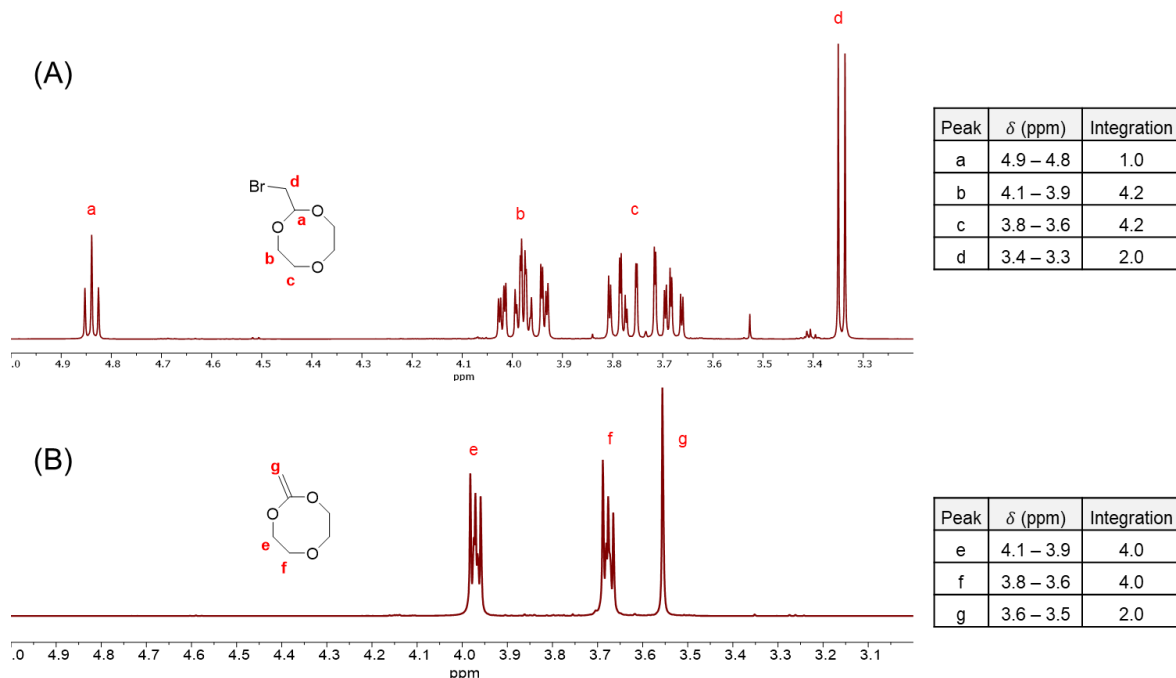


Figure 5. 2 ^1H NMR of (A) 2-(bromomethyl)-1,3,6-trioxocane and (B) MTC.

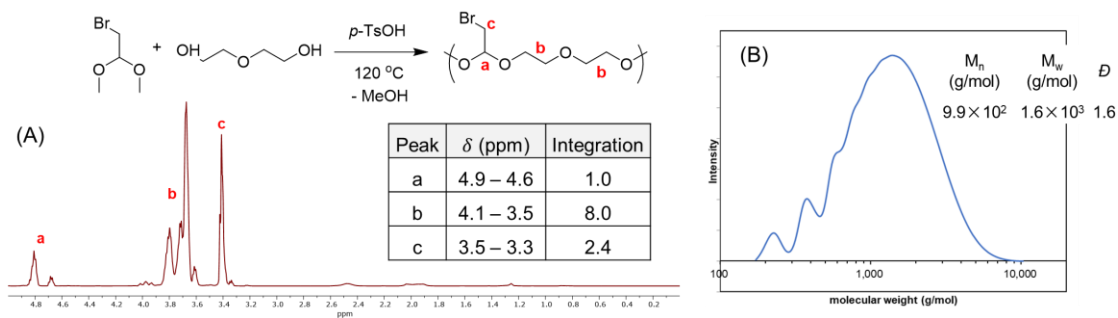


Figure 5. 3 Intermolecular acetal exchange leads to the formation of poly(acetal-ether). (A) ^1H NMR and (B) GPC (polystyrene as the standards) of the resultant poly(acetal-ether).

In order to obtain insights into the detailed reaction pathways between CKAs and various unsaturated cyclic anhydrides, ^1H NMR kinetic study was performed after mixing the THF-d^8 solutions of the two compounds at 25 °C. Selective ^1H NMR spectroscopies of MTC and maleic anhydride reactions are shown in Figure 5.4. The integration evolution

with time of main peaks were analyzed. Monotonic integration decreases for peaks m, n, p ($\delta = 3.88, 3.57, 3.40$ ppm) from MTC were observed, which were used to quantify the decomposition degree (%) with time and calculate the half-life time ($t_{1/2}$) of MTC. The full decomposition of MTC was observed after 5 days. Peak i_1 ($\delta = 1.86$ ppm) increased with time, indicating continuous formation of the new product. Peak i_2 ($\delta = 1.75$ ppm) appeared immediately after mixing the donor-acceptor pair and gradually decrease with time, indicating the formation and consumption of an unstable intermediate with a short half-life time. Peaks i_3 ($\delta = 1.31$ ppm) exhibited an integration increase at the first 2 days, followed by an integration plateau and subsequent decrease, which might be from the orthoester intermediate with a longer half-life time. After the full decomposition of MTC, the main decomposition products were summarized in Figure 5.4.

The same kinetic ^1H NMR experiments were performed on the reactions between MTC or BMDO with the three unsaturated cyclic anhydrides. The spectra are shown in Figure 5.5 – 5.6 and the calculated $t_{1/2}$ results are listed in Table 5.1. Because of an additional electron donating methyl group, a longer $t_{1/2}$ of the CKA was observed in the presence of citraconic anhydride than that with maleic anhydride. Itaconic anhydride is an isomer of citraconic anhydride, with a less electrophilic alkene. Nevertheless, it induced the fastest CKA decomposition.

It is known that isomerization of itaconic anhydride can occur upon heating, or with the presence of electrophiles, such as pyridine and amines, resulting in citraconic anhydride, a thermodynamically more stable structure.^{28–30} Herein, CKAs might serve as a base catalyst for the itaconic anhydride rearrangement. As shown in Figures 5.5 and 5.6, common diacid products from unsaturated cyclic anhydride degradation and the [2+2]

cycloaddition products were observed in the reactions either with citraconic anhydride or itaconic anhydride, which indicate the rearrangement of itaconic anhydride to citraconic anhydride in the presence of MTC.

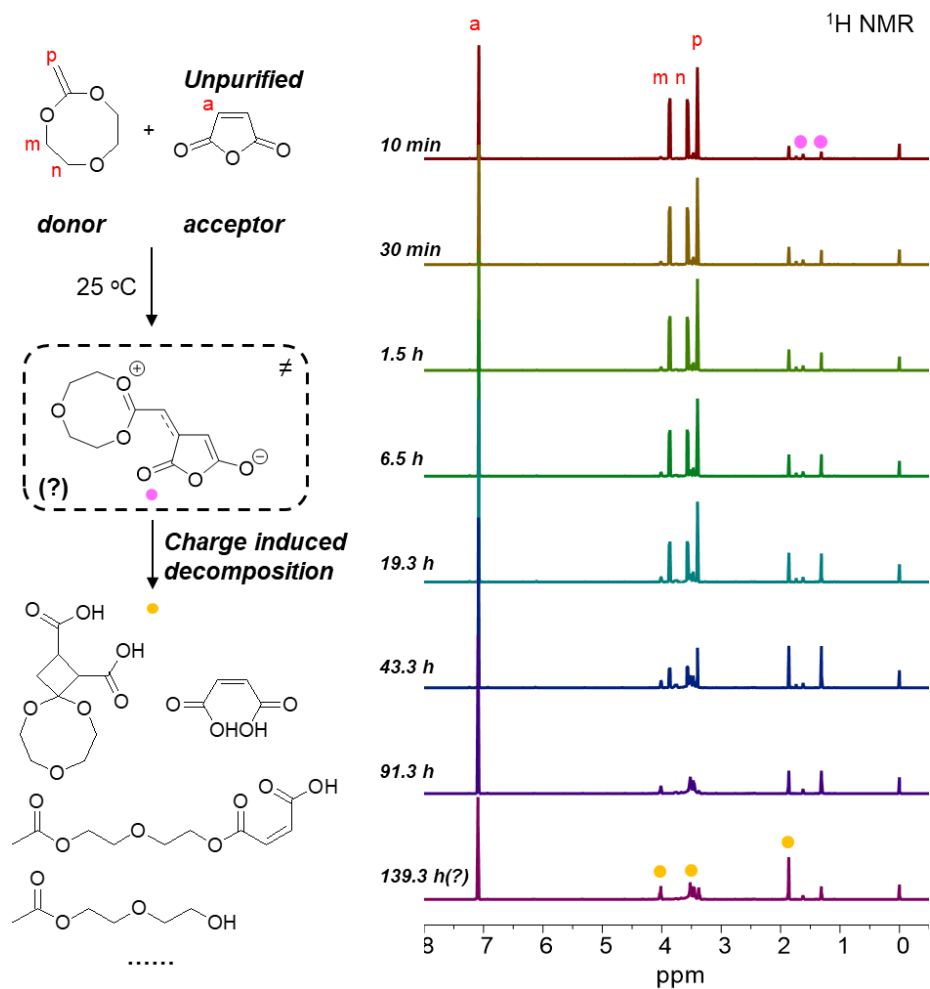


Figure 5. 4 Kinetic characterization of the reactions between MTC and maleic anhydride by ^1H NMR in 1 mol/L *d*-THF solution at 25 °C, the possible intermediate and decomposition products annotated.

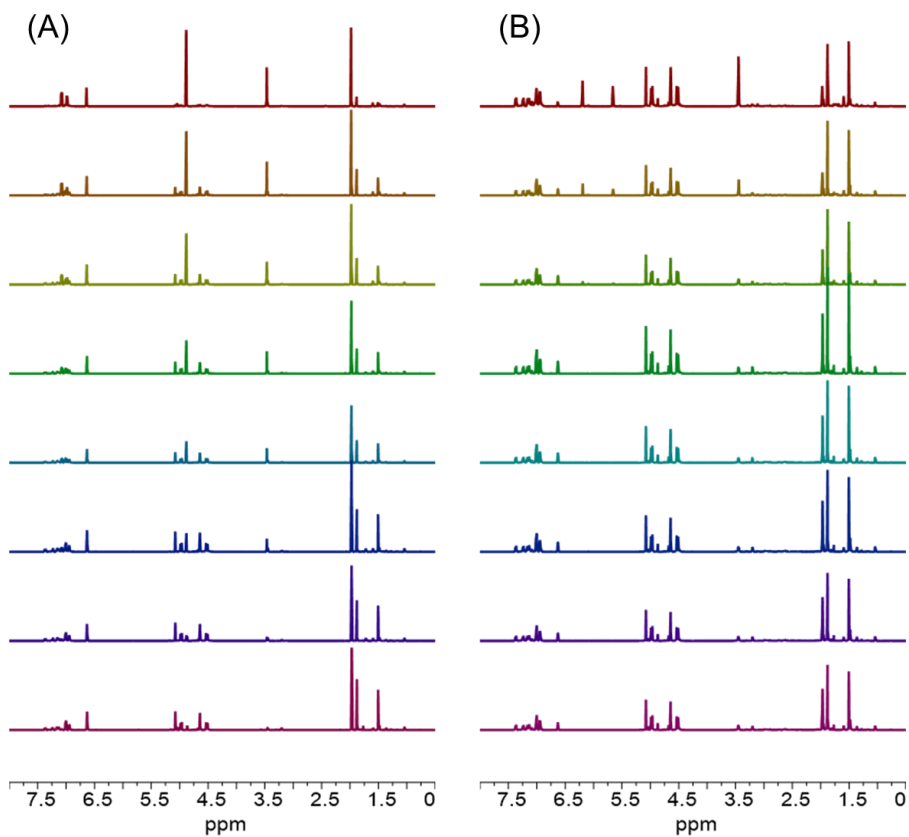


Figure 5. 5 Kinetic characterization of the reactions between MTC and (A) citraconic anhydride, (B) itaconic anhydride by ^1H NMR in 1 mol/L *d*-THF solution at 25 °C.

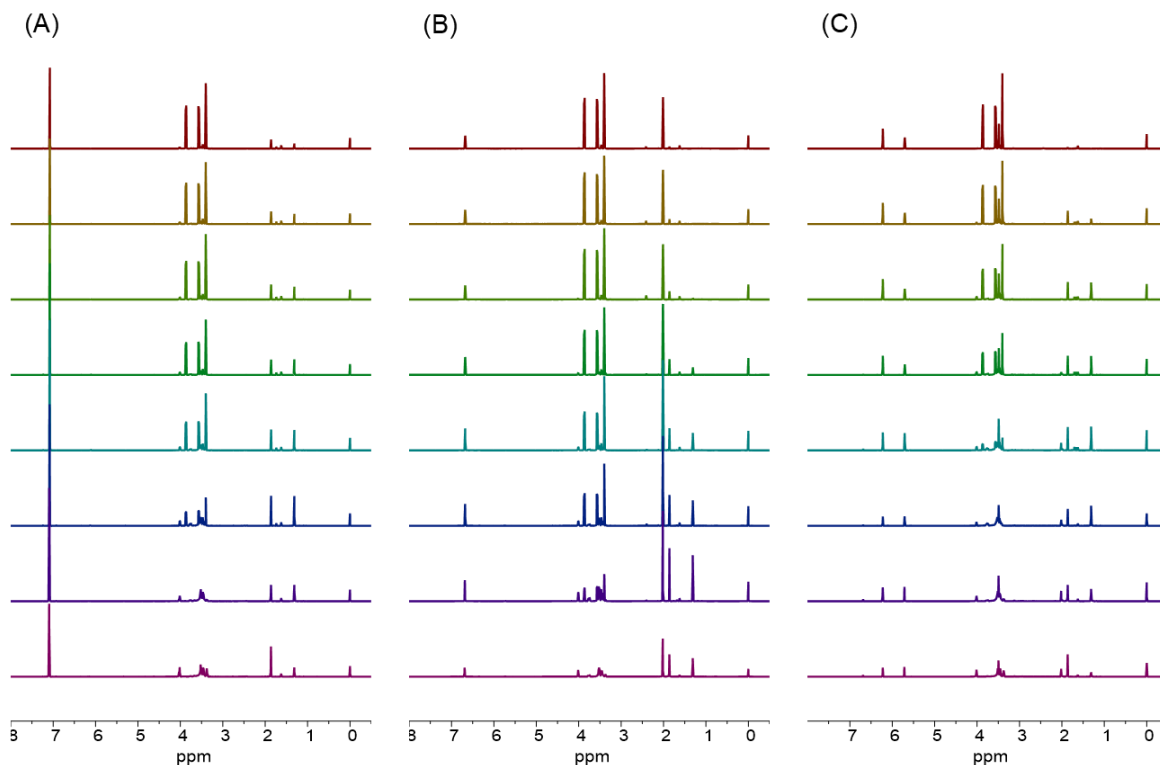


Figure 5. 6 Kinetic ^1H NMR of the reactions between BMDO and (A) maleic anhydride, (B) citraconic anhydride, and (C) itaconic anhydride in 1 mol/L d-THF solution at 25 °C.

Time-dependent color change was observed during the reactions between CKAs and unsaturated cyclic anhydrides. Therefore, real-time optical absorption in the range of 400-700 nm was monitored after mixing the CKA and unsaturated cyclic anhydride species, as shown in Figure 5.7. Charge-transfer complexes with discernible optical absorption formed within one hour after mixing BMDO with either maleic anhydride or citraconic anhydride, which exhibit similar optical properties with two absorption maxima locating at ~ 540 and 575 nm. Whereas the absorption band with similar wavelengths appeared after 24 hours for the reactions between MTC and either maleic anhydride or

citraconic anhydride, indicating a slower charge-transfer complex formation kinetics. The charge transfer between CKAs and itaconic anhydride resulted in very different optical absorption spectra. A maximum at ~417 nm for BMDO was observed within an hour, in company with a shoulder. In the case of MTC, an absorption band at ~430 nm appeared after an hour in the presence of itaconic anhydride, which continued to increase over the next 24 hours. From the onset of an absorption spectrum, the corresponding bandgap value of specific intermediates can be calculated. Quantitative analysis results from kinetic ^1H NMR and real-time optical absorption characterizations were summarized in Table 1. Higher bandgaps were observed for the charge-transfer complex formed from CKA and itaconic anhydride, than the other two unsaturated cyclic anhydrides.

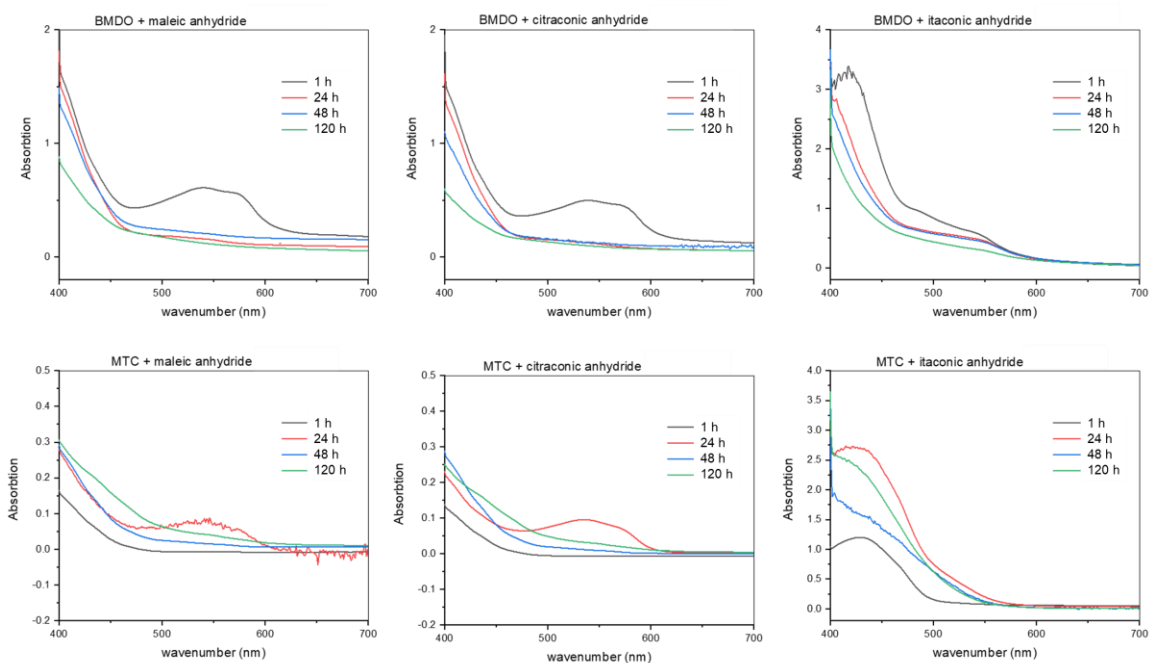


Figure 5. 7 Real-time absorption characterization of the reactions between CKAs and unsaturated cyclic anhydrides.

Table 5. 1 the half-life time ($t_{1/2}$) of CKAs and optical bandgap values of the intermediates during the charge-transfer reactions between CKAs and unsaturated cyclic anhydrides in THF (0.5 mol/L).

CKA	unsaturated cyclic anhydrides	$t_{1/2}^a$ (h)	λ_{max} (nm)	Bandgap ^b (eV)
BMDO	Maleic anhydride	0.5	540, 575	1.95
	Citraconic anhydride	6.8	540, 575	1.95
	Itaconic anhydride	< 0.2	417	2.07
MTC	Maleic anhydride	34	540	2.02
	Citraconic anhydride	49	540	2.03
	Itaconic anhydride	10	430	2.42 (1h) 2.14 (1d)

^a $t_{1/2}$, half-life time of CKA, was calculated from kinetic ¹H NMR.

^bBandgap values were calculated from the onset of the absorption spectra.

With one more extra methyl group, 2,3-dimethylmaleic anhydride exhibits higher electron density than citraconic anhydride and the radical copolymerization with MTC took place with decent yield, using AIBN as the initiator at 75 °C, during which no color change was observed. However, limited by the slower radical polymerization rate of BMDO than MTC, the charge-transfer prevails upon the same temperature in the presence of radical species and very low yield of polymer was obtained with M_n less than 1,000 g/mol. The

solution of BMDO and 2,3-dimethylmaleic anhydride stays colorless at room temperature but a vibrant red color was observed at a temperature of 75 °C.

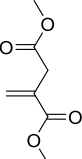
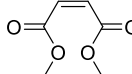
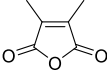
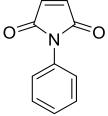
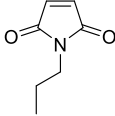
The copolymerization of CKA with maleimides with various substitutive groups were performed under the same experimental conditions. It has been demonstrated that replacing the anhydride oxygen with nitrogen can significantly influence the competition between radical mediated polymerization and charge transfer in the presence of initiating radical source from AIBN.^{8,9} There is no discernable color change observed during the copolymerization with *N*-phenyl maleimide or *N*-propyl maleimide.

Another way to tune the electron density is by modifying the anhydride on unsaturated cyclic anhydrides. In comparison with maleic anhydride, two methoxycarbonyl groups on dimethyl maleate exhibit less electron withdrawing effect on the alkene. As a result, dimethyl maleate with either BMDO or MTC can yield quantitative copolymerization at 75 °C in the presence of radicals.

Similarly, by changing the anhydride to esters, the copolymerization of CKA and dimethyl itaconate successfully proceeded without discernable color changes during the polymerization process. The acyclic structure of dimethyl itaconate resembles methyl methacrylate and the copolymerization are anticipated to yield random copolymer structures. It has been demonstrated that both electron density and cyclic versus acyclic “structural factors” can influence the competition between charge transfer and radical mediated polymerization.

The copolymers of CKA and electron deficient vinyl comonomers were characterized by GPC, where much larger molecular weights were obtained for MTC copolymers than BMDO, as shown in Table 5.2.

Table 5. 2 Molecular weights and DP ratios of the copolymers of CKA and electron deficient comonomers.

Comonomer ^a		ITDE	DME	DMMAAnH	NPhMI	NPrMI
CKA						
MTC	M_n^b (g/mol)	15,300	15,300	1,100	5,900	19,400
	$\frac{DP_{CKA}}{DP_{comonomer}}^c$	1 : 1	1 : 1	1 : 1.5	1 : 1	1 : 2
BMDO	M_n^b (g/mol)	1,300	1,300	-	2,600	4,700
	$\frac{DP_{CKA}}{DP_{comonomer}}^c$	1 : 1	1 : 1		1 : 1	1 : 2

^aThe abbreviations of the comonomers. ITDE, dimethyl itaconate. DME, dimethyl maleate.

DMMAAnH, 2,3-dimethylmaleic anhydride. NPhMI, N-phenyl maleimide. NPrMI, N-propyl maleimide.

^bNumber average molecular weights, M_n , were characterized from THF GPC, using polystyrene standards.

^cThe degree of polymerization (DP) ratios between CKA and comonomers were calculated from ¹H NMR, peak assignments based on 2D NMR techniques, including DEPT-135, COSY, HMQC, etc.

5.4 Conclusion

The charge transfer side reactions can rapidly consume polymerizable alkene groups on CKAs and bring deleterious effects during rROP, which significantly limit their application. From the *in situ* ¹H NMR investigation, the half-life time of BMDO was measured to be 10 min in 1 mol/L solution at room temperature with the presence of maleic

anhydride. The charge transfer reactions with citraconic anhydride and itaconic anhydride also exhibit fast kinetics, with the half-life time within 30 min. In future investigations on the radical and electron-driven reaction competitions of CKA monomers and various comonomers will be performed. The results can provide valuable insights on monomer molecular design and polymerization condition optimization in order to mitigate the charge transfer and promote radical polymerization. Ultimately, the versatility of rROP will be significantly enhanced and the technique can be applied to a boarder range of monomer systems for the preparation of innovative degradable polymer compositions suitable for various applications.

5.5 Reference

- (1) Tardy, A.; Nicolas, J.; Gimes, D.; Lefay, C.; Guillaneuf, Y. Radical Ring-Opening Polymerization: Scope, Limitations, and Application to (Bio) Degradable Materials. *Chem. Rev.* **2017**, *117*, 1319–1406.
- (2) Agarwal, S. Chemistry, Chances and Limitations of the Radical Ring-Opening Polymerization of Cyclic Ketene Acetals for the Synthesis of Degradable Polyesters. *Polym. Chem.* **2010**, *1* (7), 953–964.
- (3) Zhou, X.; Xie, Q.; Ma, C.; Chen, Z.; Zhang, G. Inhibition of Marine Biofouling by Use of Degradable and Hydrolyzable Silyl Acrylate Copolymer. *Ind. Eng. Chem. Res.* **2015**, *54* (39), 9559–9565.
- (4) Grabe, N.; Zhang, Y.; Agarwal, S. Degradable Elastomeric Block Copolymers Based on Polycaprolactone by Free-Radical Chemistry. *Macromol. Chem. Phys.* **2011**, *212* (13), 1327–1334.

- (5) Jin, Q.; Maji, S.; Agarwal, S. Novel Amphiphilic, Biodegradable, Biocompatible, Cross-Linkable Copolymers: Synthesis, Characterization and Drug Delivery Applications. *Polym. Chem.* **2012**, *3* (10), 2785–2793.
- (6) Cai, T.; Chen, Y.; Wang, Y.; Wang, H.; Liu, X.; Jin, Q.; Agarwal, S.; Ji, J. Functional 2-Methylene-1,3-Dioxepane Terpolymer: A Versatile Platform to Construct Biodegradable Polymeric Prodrugs for Intracellular Drug Delivery. *Polym. Chem.* **2014**, *5* (13), 4061–4068.
- (7) Cai, T.; Chen, Y.; Wang, Y.; Wang, H.; Liu, X.; Jin, Q.; Agarwal, S.; Ji, J. One-Step Preparation of Reduction-Responsive Biodegradable Polymers as Efficient Intracellular Drug Delivery Platforms. *Macromol. Chem. Phys.* **2014**, *215* (19), 1848–1854.
- (8) Hill, M. R.; Guégain, E.; Tran, J.; Figg, C. A.; Turner, A. C.; Nicolas, J.; Sumerlin, B. S. Radical Ring-Opening Copolymerization of Cyclic Ketene Acetals and Maleimides Affords Homogeneous Incorporation of Degradable Units. *ACS Macro Lett.* **2017**, *6* (10), 1071–1077.
- (9) Hill, M. R.; Kubo, T.; Goodrich, S. L.; Figg, C. A.; Sumerlin, B. S. Alternating Radical Ring-Opening Polymerization of Cyclic Ketene Acetals: Access to Tunable and Functional Polyester Copolymers. *Macromolecules* **2018**, *51* (14), 5079–5084.
- (10) Lutz, J.-F.; Ouchi, M.; Liu, D. R.; Sawamoto, M. Sequence-Controlled Polymers. *Science (80-.)*. **2013**, *341* (6146), 1238149.
- (11) Baradel, N.; Shishkan, O.; Srichan, S.; Lutz, J.-F. Synthesis of Sequence-Controlled Copolymers Using Time-Regulated Additions of N-Substituted Maleimides in Styrenic Radical Polymerizations. In *Sequence-Controlled Polymers: Synthesis*,

Self-Assembly, and Properties; ACS Symposium Series; American Chemical Society, 2014; Vol. 1170, pp 119-131 SE – 8.

- (12) Ouchi, M.; Badi, N.; Lutz, J. F.; Sawamoto, M. Single-Chain Technology Using Discrete Synthetic Macromolecules. *Nat. Chem.* **2011**, *3* (12), 917–924.
- (13) Badi, N.; Lutz, J.-F. Sequence Control in Polymer Synthesis. *Chem. Soc. Rev.* **2009**, *38* (12), 3383–3390.
- (14) Huang, J.; Turner, S. R. Recent Advances in Alternating Copolymers: The Synthesis, Modification, and Applications of Precision Polymers. *Polymer (Guildf)*. **2017**, *116*, 572–586.
- (15) Satoh, K.; Matsuda, M.; Nagai, K.; Kamigaito, M. AAB-Sequence Living Radical Chain Copolymerization of Naturally Occurring Limonene with Maleimide: An End-to-End Sequence-Regulated Copolymer. *J. Am. Chem. Soc.* **2010**, *132* (29), 10003–10005.
- (16) Matsuda, M.; Satoh, K.; Kamigaito, M. Periodically Functionalized and Grafted Copolymers via 1:2-Sequence- Regulated Radical Copolymerization of Naturally Occurring Functional Limonene and Maleimide Derivatives. *Macromolecules* **2013**, *46* (14), 5473–5482.
- (17) Soejima, T.; Satoh, K.; Kamigaito, M. Main-Chain and Side-Chain Sequence-Regulated Vinyl Copolymers by Iterative Atom Transfer Radical Additions and 1:1 or 2:1 Alternating Radical Copolymerization. *J. Am. Chem. Soc.* **2016**, *138* (3), 944–954.
- (18) Spick, M. P.; Bingham, N. M.; Li, Y.; De Jesus, J.; Costa, C.; Bailey, M. J.; Roth, P. J. Fully Degradable Thioester-Functional Homo- And Alternating Copolymers

Prepared through Thiocarbonyl Addition-Ring-Opening RAFT Radical Polymerization. *Macromolecules* **2020**, *53* (2), 539–547.

- (19) Johnston, K.; Padias, A. B.; Bates, R. B.; Hall, H. K. Cycloadditions of Ketene Diethyl Acetal and 2-Methylene-1,3-Dioxepane to Electrophilic Alkenes. *Langmuir* **2003**, *19* (16), 6416–6421.
- (20) Yamamoto, S. I.; Sanda, F.; Endo, T. Cationic Polymerization of Cyclic Ketene Acetals via Zwitterion Formation with Cyanoallene. *J. Polym. Sci. Part A Polym. Chem.* **2000**, *38* (11), 2075–2081.
- (21) Agarwal, S.; Kumar, R. Synthesis of High-Molecular-Weight Tulipalin-A-Based Polymers by Simple Mixing and Heating of Comonomers. *Macromol. Chem. Phys.* **2011**, *212* (6), 603–612.
- (22) Yokozawa, T.; Takagi, J.; Endo, T. A Novel Polymerization Process. Spontaneous Block Copolymerization of 2-Methylene-4-Phenyl-1,3-Dioxolane with β -Propiolactone through Zwitterionic Mechanism. *J. Polym. Sci. Part C Polym. Lett.* **1990**, *28* (9), 279–283.
- (23) Yokozawa, T.; Takagi, J.; Endo, T. Polymerization of Methyl Methacrylate with a Cyclic Ketene Acetal as Catalyst via Zwitterionic Mechanism. *Die Makromol. Chemie, Rapid Commun.* **1991**, *12* (9), 553–557.
- (24) Hall, H. K.; Buyle Padias, A. Bond Forming Initiation of “Charge-Transfer” Polymerizations and the Accompanying Cycloadditions. *Acc. Chem. Res.* **1997**, *30* (8), 322–329.
- (25) Bailey, W. J.; Ni, Z.; Wu, S. R. Free Radical Ring-Opening Polymerization of 4,7-Dimethyl-2-Methylene-1,3-Dioxepane and 5,6-Benzo-2-Methylene-1,3-

- Dioxepane. *Macromolecules* **1982**, *15* (3), 711–714.
- (26) Gmbh, E. D.; Technologies, C. Synthesis of Amorphous Aliphatic Polyester-Ether Homo- and Copolymers by Radical Polymerization of Ketene Acetals. *Polymer (Guildf)*. **2010**, *48*, 1973–1978.
- (27) Hiracuri, Y.; Tokiwa, Y. Synthesis of Copolymers Composed of 2-methylene-1,3,6-trioxocane and Vinyl Monomers and Their Enzymatic Degradation. *J. Polym. Sci. Part A Polym. Chem.* **1993**, *31* (12), 3159–3163.
- (28) Galanti, M. C.; Galanti, A. V. Kinetic Study of the Isomerization of Itaconic Anhydride to Citraconic Anhydride. *J. Org. Chem.* **1982**, *47* (8), 1572–1574.
- (29) Modzelewska-Banachiewicz, B.; Paprocka, R.; Mazur, L.; Saczewski, J.; Kutkowska, J.; Stepień, D. K.; Cyrański, M. Experimental and Theoretical Study on the Reaction of N³-Phenyl- (Pyridin-2-Yl)Carbohydrazonamide with Itaconic Anhydride. *J. Mol. Struct.* **2012**, *1022*, 211–219.
- (30) Galanti, A. V.; Keen, B. T.; Pater, R. H.; Scola, D. Mechanism of Amine Catalyzed Isomerization of Itaconic Anhydride To Citraconic Anhydride: Citraconamic Acid Formation. *J. Polym. Sci. A1*. **1981**, *19* (9), 2243–2253.

CHAPTER 6

CONCLUSIONS AND PERSPECTIVE

6.1 Polyelectrolyte Coacervates in Electrospinning

The diffusion behavior of polyelectrolytes in salt-free solutions were investigated in Chapter 2. The complexation of oppositely charged polymers with additional salt can lead to a unique liquid-liquid phase separation.^{1,2} The polymer rich phase, a so-called coacervate, can be electrospun for nano-fiber fabrication from aqueous solutions.^{3,4} Conventionally, electrospinning has been limited to polymers with relatively high molecular weights.⁵ We investigated polymer coacervate systems prepared by methacryloyl-based polyelectrolytes with DP 10 ~ 500 and demonstrated that the inherent electrostatic interactions in coacervates enables the electrospinning of oligomers (Figure 6.1).⁶ This demonstrated the capability to decouple polymer molecular weight and entanglement requirements for electrospinning. This finding will shed light on new material design and processing possibilities, for example to include drug molecules and amino acids and proteins bio-based materials.

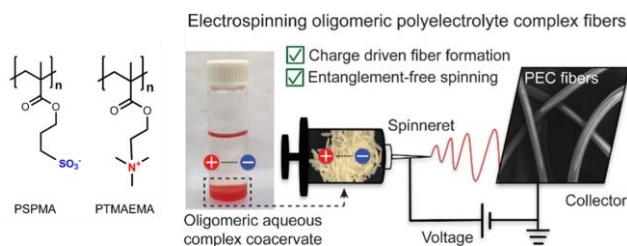


Figure 6. 1 Chemical structures of polyelectrolytes used for methacryloyl-based coacervate preparation. Electrostatic interactions in coacervates can facilitate the formation of a continuous fiber jet during electrospinning.

(Image reproduced from reference ⁵)

6.2 Interactions in Polymer Composite Systems

In addition to block copolymer membrane systems demonstrated in Chapters 3 and 4, polymer–metal nanocomposites have also been a growing field of material research with potential as semiconductors, high-strength materials, flexible electronics, catalysts or electrocatalysts, sensors, biocompatible materials and in additive manufacturing applications.^{7–9} We investigated the interactions between silver nanoparticles and PCMS-*b*-polycyclooctene-*b*-PCMS (PCMS-*b*-PCOE-*b*-PCMS) triblock copolymers, and the ionomers derived from quaternization of the PCMS outer blocks with various tertiary amines to form cations.¹⁰ As shown in Figure 6.2, the interactions between silver particles with the phenyl rings, cations and unsaturation from PCOE bring significant impacts on crystallization behaviors and water contents. The continuation of this line of study could provide further design principles for ionomer structural design and synthesis for integration with specific electrocatalyst particles.

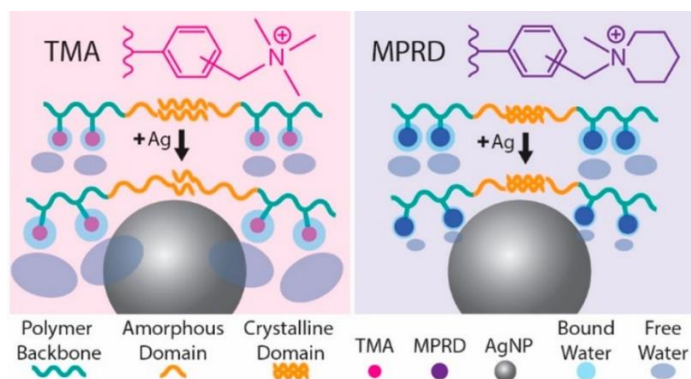


Figure 6. 2 Water absorption and crystallinity of polymer-silver composites were highly dependent on cation species.

(Image taken from reference ¹⁰)

6.3 CKA Charge-Transfer versus Radical Co-Polymerization with Anhydride Containing Comonomers.

As demonstrated in Chapter 5, the attempt at copolymerizing CKA with maleic anhydride or itaconic anhydride without pre-purification of the anhydride comonomers did not yield copolymers. Previously, the copolymerization of MTC and sublimed maleic anhydride was reported by Hiraguri *et al.*¹¹ Therefore, we performed sublimation on maleic anhydride and itaconic anhydride. The subsequent copolymerization with MTC in anhydrous anisole yielded copolymers successfully without color change. It is hypothesized that trace amount of water or residual acid present in crude anhydride containing comonomers might be a catalyst for the charge-transfer with CKA. Therefore, purification by sublimation can be a feasible approach to hinder charge-transfer and promote radical copolymerization. Additionally, charge-transfer kinetics are dependent on temperature, solvent polarity, etc. Different experimental conditions, such as using non-polar solvent, might be beneficial for radical mediated polymerization and are worth investigating. The addition of a third vinyl comonomer to anhydride containing monomer and CKA can significantly change the radical polymerization kinetics in a terpolymerization system and leverage the competition between radical and charge mediated reactions.

6.4 CKA Monomer Synthesis

One of the factors that limits the application of rROP technique introduced in Chapter 5 at an industrial scale lies in the difficulties in the synthesis and storage of CKA monomers.¹² The synthesis approach adopted in Chapter 5 has been effectively used in the

literature, yet with overall yield less than 60 %. The conditions are relatively harsh, involving the use of halogenated reagents and moisture-sensitive procedures. The obtained CKA monomers are highly sensitive, prone to hydrolysis as are traditional acetals. They can also undergo nucleophilic attacks due to the electrophilicity induced by ketene acetal, as demonstrated in Chapter 5. Moreover, CKAs can self-polymerize by cationic polymerization upon contact with glass surfaces during distillation,¹³ also upon storage, which can be inhibited by the addition of a small amount pyridine (1–2 mol%).¹⁴

In addition to the haloacetal route adopted in Chapter 5, other CKA synthesis effort has been explored that use alternative protocols. Among these, the carbonate route, initially proposed by Petasis *et al.*,¹⁵ has recently been revised and improved.^{16,17} The Petasis chemistry relies on a carbonate intermediate formation from a diol, in the presence of triphosgene or ethylchloroformate as the catalyst, followed by olefination using the Petasis reagent (Figure 6.3 A, B). There are other halogen free synthetic approaches reported by McElvain *et al.*, where ketene acetals were prepared from ortho-ester pyrolysis at a high temperature.^{18,19} (Figure 6.3 C, D) A Pinner reaction based approach has been investigated for the synthesis of a five-member ring CKA from acetonitrile and ethylene glycol.²⁰

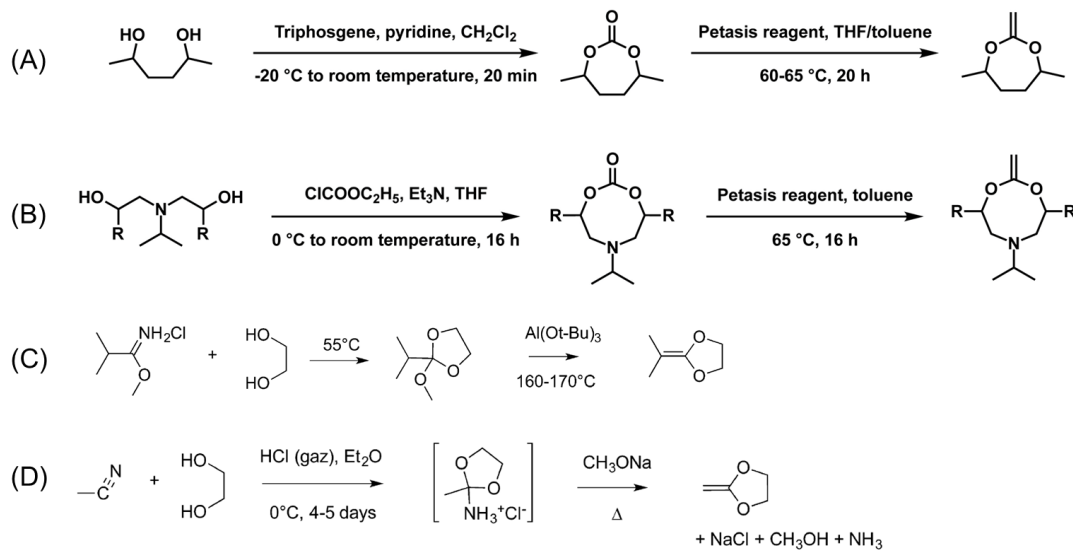


Figure 6. 3 CKA syntheses based on (A) carbonate route using triphosgene,²¹ (B) carbonate route using ethylchloroformate,¹⁷ (C) ortho-ester pyrolysis¹⁸ and (D) Pinner reaction.²⁰

(Image reproduced from reference ¹⁷⁻²¹)

The development of efficient monomer CKA syntheses is very crucial for the implementation of rROP technique in industry. Although the haloacetal approach has been the route investigated and adopted the most, limitations remain, such as the use of halogenated agents and large quantity of organic solvents required, both of these factors raise “green” chemical processing concerns. Other alternative synthesis routes discussed above have been reported decades ago. Yet much less attention has been paid to the further improvement and evaluation. Therefore, CKA synthesis can be a significant aspect worth exploring.

6.5 Reference

- (1) Sing, C. E.; Perry, S. L. Recent Progress in the Science of Complex Coacervation.

Soft Matter **2020**, *16* (12), 2885–2914.

- (2) Spruijt, E.; Leermakers, F. A. M.; Fokkink, R.; Schweins, R.; van Well, A. A.; Cohen Stuart, M. A.; van der Gucht, J. Structure and Dynamics of Polyelectrolyte Complex Coacervates Studied by Scattering of Neutrons, X-Rays, and Light. *Macromolecules* **2013**, *46* (11), 4596–4605.
- (3) Meng, X.; Perry, S. L.; Schiffman, J. D. Complex Coacervation: Chemically Stable Fibers Electrospun from Aqueous Polyelectrolyte Solutions. *ACS Macro Lett.* **2017**, *6* (5), 505–511.
- (4) Meng, X.; Schiffman, J. D.; Perry, S. L. Electrospinning Cargo-Containing Polyelectrolyte Complex Fibers: Correlating Molecular Interactions to Complex Coacervate Phase Behavior and Fiber Formation. *Macromolecules* **2018**, *51* (21), 8821–8832.
- (5) De Gennes, P. G. Dynamics of Entangled Polymer Solutions. I. The Rouse Model. *Macromolecules* **1976**, *9* (4), 587–593.
- (6) Meng, X.; Du, Y.; Liu, Y.; Coughlin, E. B.; Perry, S. L.; Schiffman, J. D. Electrospinning Fibers from Oligomeric Complex Coacervates: No Chain Entanglements Needed. *Macromolecules* **2021**, *54*, 5033–5042.
- (7) Rosi, N. L.; Mirkin, C. A. Nanostructures in Biodiagnostics. *Chem. Rev.* **2005**, *105* (4), 1547–1562.
- (8) Murphy, C. J.; Sau, T. K.; Gole, A. M.; Orendorff, C. J.; Gao, J.; Gou, L.; Hunyadi, S. E.; Li, T. Anisotropic Metal Nanoparticles: Synthesis, Assembly, and Optical Applications. *J. Phys. Chem. B* **2005**, *109* (29), 13857–13870.
- (9) Kamat, P. V. Photophysical, Photochemical and Photocatalytic Aspects of Metal

- Nanoparticles. *J. Phys. Chem. B* **2002**, *106* (32), 7729–7744.
- (10) Buggy, N. C.; Du, Y.; Kuo, M. C.; Gasvoda, R. J.; Seifert, S.; Agarwal, S.; Coughlin, E. B.; Herring, A. M. Investigating Silver Nanoparticle Interactions with Quaternary Ammonium Functionalized Triblock Copolymers and Their Effect on Midblock Crystallinity. *ACS Appl. Polym. Mater.* **2020**, *2* (11), 4914–4923.
- (11) Hiraguri, Y.; Katase, K.; Tokiwa, Y. Synthesis of Biodegradable Detergent Builder by Alternating Copolymerization of 2-Methylene-1,3,6-Trioxocane and Maleic Anhydride. *J. Macromol. Sci. Part A Pure Appl. Chem.* **2007**, *44* (8), 893–897.
- (12) Pesenti, T.; Nicolas, J. 100th Anniversary of Macromolecular Science Viewpoint: Degradable Polymers from Radical Ring-Opening Polymerization: Latest Advances, New Directions, and Ongoing Challenges. *ACS Macro Lett.* **2020**, *9* (12), 1812–1835.
- (13) Schulze, T.; Klemm, E. Investigations on Free Radical Polymerization of Phenyl-substituted 2-methylene-1,3-dioxanes. *Die Angew. Makromol. Chemie* **1995**, *229* (1), 123–132.
- (14) Bailey, W.; Wu, S.-R.; Ni, Z. Synthesis and Free Radical Ring-opening Polymerization of 2-methylene-4-phenyl-1,3-dioxolane. *Die Makromol. Chemie* **1982**, *183* (8), 1913–1920.
- (15) Petasis, N. A.; Lu, S.-P. Methylenations of Heteroatom-Substituted Carbonyls with Dimethyl Titanocene. *Tetrahedron Lett.* **1995**, *36* (14), 2393–2396.
- (16) Ho, H. T.; Montembault, V.; Rollet, M.; Aboudou, S.; Mabrouk, K.; Pascual, S.; Fontaine, L.; Gigmes, D.; Phan, T. N. T. Radical Ring-Opening Polymerization of Novel Azlactone-Functionalized Vinyl Cyclopropanes. *Polym. Chem.* **2020**, *11*

- (24), 4013–4021.
- (17) Folini, J.; Huang, C.-H.; Anderson, J. C.; Meier, W. P.; Gaitzsch, J. Novel Monomers in Radical Ring-Opening Polymerisation for Biodegradable and PH Responsive Nanoparticles. *Polym. Chem* **2019**, *10*, 5285.
- (18) McElvain, S. M.; Aldridge, C. L. Ketene Acetals. XXXI. Dimethylketene Ethyleneacetal. *J. Am. Chem. Soc.* **1953**, *75* (16), 3993–3996.
- (19) McElvain, S. M.; Nelson, J. W. The Preparation of Orthoesters. *J. Am. Chem. Soc.* **1942**, *64* (8), 1825–1827.
- (20) Argade, A. B.; Joglekar, B. R. A Short and Simple Synthesis of Ketene Acetals. *Synth. Commun.* **1993**, *23* (14), 1979–1984.
- (21) Gaitzsch, J.; Welsch, P. C.; Folini, J.; Schoenenberger, C.-A.; Anderson, J. C.; Meier, W. P. Revisiting Monomer Synthesis and Radical Ring Opening Polymerization of Dimethylated MDO towards Biodegradable Nanoparticles for Enzymes. *Eur. Polym. J.* **2018**, *101*, 113–119.

BIBLIOGRAPHY

- (1) Hoover, M. F. Cationic Quaternary Polyelectrolytes—A Literature Review. *J. Macromol. Sci. Part A - Chem.* **1970**, *4* (6), 1327–1418.
- (2) Holliday, L. *Ionic Polymers*; Applied Science Publishers: London, 1975.
- (3) Eisenberg, A.; King, M. Ion-Containing Polymers: Physical Properties and Structure (Chapter I - Introduction); Academic Press, 1977; pp 1–14.
- (4) Chen, Q.; Bao, N.; Wang, J.-H. H. H.; Tunic, T.; Liang, S.; Colby, R. H. Linear Viscoelasticity and Dielectric Spectroscopy of Ionomer/Plasticizer Mixtures: A Transition from Ionomer to Polyelectrolyte. *Macromolecules* **2015**, *48* (22), 8240–8252.
- (5) Eisenberg, A.; Rinaudo, M. Polyelectrolytes and Ionomers. *Polym. Bull.* **1990**, *24* (6), 671.
- (6) Dobrynin, A. V.; Rubinstein, M. Theory of Polyelectrolytes in Solutions and at Surfaces. *Prog. Polym. Sci.* **2005**, *30* (11), 1049–1118.
- (7) Eisenberg, A.; Kim, J.-S. *Introduction to Ionomers*; Wiley: New York, 1998.
- (8) Colby, R. H. Structure and Linear Viscoelasticity of Flexible Polymer Solutions: Comparison of Polyelectrolyte and Neutral Polymer Solutions. *Rheol. Acta* **2010**, *49* (5), 425–442.
- (9) De Gennes, P.-G.; Pincus, P.; Velasco, R. M.; Brochard, F. Remarks on Polyelectrolyte Conformation. *J. Phys.* **1976**, *37* (12), 1461–1473.

- (10) Muthukumar, M. 50th Anniversary Perspective: A Perspective on Polyelectrolyte Solutions. *Macromolecules* **2017**, *50* (24), 9528–9560.
- (11) Fuoss, R. M. Viscosity Function for Polyelectrolytes. *J. Polym. Sci.* **1948**, *3* (4), 603–604.
- (12) Prabhu, V. M. Counterion Structure and Dynamics in Polyelectrolyte Solutions. *Curr. Opin. Colloid Interface Sci.* **2005**, *10* (1), 2–8.
- (13) Sedláč, M. What Can Be Seen by Static and Dynamic Light Scattering in Polyelectrolyte Solutions and Mixtures? *Langmuir* **1999**, *15* (12), 4045–4051.
- (14) Nishida, K.; Kaji, K.; Kanaya, T.; Shibano, T. Added Salt Effect on the Intermolecular Correlation in Flexible Polyelectrolyte Solutions: Small-Angle Scattering Study. *Macromolecules* **2002**, *35* (10), 4084–4089.
- (15) Jia, D.; Muthukumar, M. Effect of Salt on the Ordinary-Extraordinary Transition in Solutions of Charged Macromolecules. *J. Am. Chem. Soc.* **2019**, *141* (14), 5886–5896.
- (16) Sehgal, A.; Seery, T. A. P. The Ordinary–Extraordinary Transition Revisited: A Model Polyelectrolyte in a Highly Polar Organic Solvent. *Macromolecules* **1998**, *31* (21), 7340–7346.
- (17) Förster, S.; Schmidt, M. Polyelectrolytes in Solution. *Adv. Polym. Sci.* **1995**, *120*, 51–133.
- (18) Muthukumar, M. Collective Dynamics of Semidilute Polyelectrolyte Solutions with

Salt. *J. Polym. Sci. Part B Polym. Phys.* **2019**, *57*, 1263–1269.

- (19) Lin, S. -C S.-C.; Lee, W. I.; Schurr, J. M. Brownian Motion of Highly Charged Poly(L-lysine). Effects of Salt and Polyion Concentration. *Biopolymers* **1978**, *17* (4), 1041–1064.
- (20) Chen, K.; Zheng, K.; Xu, G.; Yang, J.; Zhao, J. Diffusive Motion of Single Polyelectrolyte Molecules under Electrostatic Repulsion. *Macromolecules* **2019**, *52* (10), 3925–3934.
- (21) Sehgal, A.; Seery, T. A. P. The Ordinary-Extraordinary Transition Revisited: A Model Polyelectrolyte in a Highly Polar Organic Solvent. *Macromolecules* **1998**, *31* (21), 7340–7346.
- (22) Sedláč, M.; Amis, E. J. Dynamics of Moderately Concentrated Salt-Free Polyelectrolyte Solutions: Molecular Weight Dependence. *J. Chem. Phys.* **1992**, *96* (1), 817–825.
- (23) Prabhu, V. M.; Muthukumar, M.; Wignall, G. D.; Melnichenko, Y. B. Dimensions of Polyelectrolyte Chains and Concentration Fluctuations in Semidilute Solutions of Sodium-Poly(Styrene Sulfonate) as Measured by Small-Angle Neutron Scattering. *Polymer (Guildf)*. **2001**, *42* (21), 8935–8946.
- (24) Zhang, Y.; Douglas, J. F.; Ermi, B. D.; Amis, E. J. Influence of Counterion Valency on the Scattering Properties of Highly Charged Polyelectrolyte Solutions. *J. Chem. Phys.* **2001**, *114* (7), 3299–3313.

- (25) Prabhu, V. M.; Muthukumar, M.; Wignall, G. D.; Melnichenko, Y. B. Polyelectrolyte Chain Dimensions and Concentration Fluctuations near Phase Boundaries. *J. Chem. Phys.* **2003**, *119* (7), 4085–4098.
- (26) Förster, S.; Schmidt, M.; Antonietti, M. Static and Dynamic Light Scattering by Aqueous Polyelectrolyte Solutions: Effect of Molecular Weight, Charge Density and Added Salt. *Polymer (Guildf)*. **1990**, *31* (5), 781–792.
- (27) Levy, A.; Andelman, D.; Orland, H. Dielectric Constant of Ionic Solutions: A Field-Theory Approach. *Phys. Rev. Lett.* **2012**, *108* (22), 227801.
- (28) Yethiraj, A. Liquid State Theory of Polyelectrolyte Solutions. *J. Phys. Chem. B* **2009**, *113* (6), 1539–1551.
- (29) Yethiraj, A. Theory for Chain Conformations and Static Structure of Dilute and Semidilute Polyelectrolyte Solutions. *J. Chem. Phys.* **1998**, *108* (3), 1184–1192.
- (30) Mahalik, J. P.; Muthukumar, M. Langevin Dynamics Simulation of Polymer-Assisted Virus-like Assembly. *J. Chem. Phys.* **2012**, *136* (13), 135101.
- (31) Liu, S.; Muthukumar, M. Langevin Dynamics Simulation of Counterion Distribution around Isolated Flexible Polyelectrolyte Chains. *J. Chem. Phys.* **2002**, *116* (22), 9975–9982.
- (32) Shew, C.-Y.; Yethiraj, A. Monte Carlo Simulations and Self-Consistent Integral Equation Theory for Polyelectrolyte Solutions. *J. Chem. Phys.* **1999**, *110* (11), 5437–5443.

- (33) Muthukumar, M. Ordinary-Extraordinary Transition in Dynamics of Solutions of Charged Macromolecules. *Proc. Natl. Acad. Sci. U. S. A.* **2016**, *113* (45), 12627–12632.
- (34) Osada, Y.; Honda, K.; Ohta, M. Control of Water Permeability by Mechanochemical Contraction of Poly(Methacrylic Acid)-Grafted Membranes. *J. Memb. Sci.* **1986**, *27* (3), 327–338.
- (35) Tarvainen, T.; Svarfvar, B.; Åkerman, S.; Savolainen, J.; Karhu, M.; Paronen, P.; Järvinen, K. Drug Release from a Porous Ion-Exchange Membrane in Vitro. *Biomaterials* **1999**, *20* (22), 2177–2183.
- (36) Åkerman, S.; Viinikka, P.; Svarfvar, B.; Järvinen, K.; Kontturi, K.; Näsman, J.; Urtti, A.; Paronen, P. Transport of Drugs across Porous Ion Exchange Membranes. *J. Control. Release* **1998**, *50* (1), 153–166.
- (37) Sershen, S.; West, J. Implantable, Polymeric Systems for Modulated Drug Delivery. *Adv. Drug Deliv. Rev.* **2003**, *55* (3), 439.
- (38) Jeong, B.; Kim, S. W.; Bae, Y. H. Thermosensitive Sol-Gel Reversible Hydrogels. *Adv. Drug Deliv. Rev.* **2002**, *54* (1), 37–51.
- (39) Rossi, N. A. A.; Constantinescu, I.; Brooks, D. E.; Scott, M. D.; Kizhakkedathu, J. N. Enhanced Cell Surface Polymer Grafting in Concentrated and Nonreactive Aqueous Polymer Solutions. *J. Am. Chem. Soc.* **2010**, *132* (10), 3423–3430.
- (40) Rossi, N. A. A.; Constantinescu, I.; Kainthan, R. K.; Brooks, D. E.; Scott, M. D.;

- Kizhakkedathu, J. N. Red Blood Cell Membrane Grafting of Multi-Functional Hyperbranched Polyglycerols. *Biomaterials* **2010**, *31* (14), 4167–4178.
- (41) Mansouri, S.; Merhi, Y.; Winnik, F. M.; Tabrizian, M. Investigation of Layer-by-Layer Assembly of Polyelectrolytes on Fully Functional Human Red Blood Cells in Suspension for Attenuated Immune Response. *Biomacromolecules* **2011**, *12* (3), 585–592.
- (42) Wang, D.; Toyofuku, W. M.; Scott, M. D. The Potential Utility of Methoxypoly(Ethylene Glycol)-Mediated Prevention of Rhesus Blood Group Antigen RhD Recognition in Transfusion Medicine. *Biomaterials* **2012**, *33* (10), 3002–3012.
- (43) Wang, B.; Wang, G.; Zhao, B.; Chen, J.; Zhang, X.; Tang, R. Antigenically Shielded Universal Red Blood Cells by Polydopamine-Based Cell Surface Engineering. *Chem. Sci.* **2014**, *5* (9), 3463–3468.
- (44) Scott, M. D.; Murad, K. L.; Koumpouras, F.; Talbot, M.; Eaton, J. W. Chemical Camouflage of Antigenic Determinants: Stealth Erythrocytes. *Proc. Natl. Acad. Sci.* **1997**, *94* (14), 7566 LP – 7571.
- (45) Zhao, Y.; Fan, M.; Chen, Y.; Liu, Z.; Shao, C.; Jin, B.; Wang, X.; Hui, L.; Wang, S.; Liao, Z.; Ling, D.; Tang, R.; Wang, B. Surface-Anchored Framework for Generating RhD-Epitope Stealth Red Blood Cells. *Sci. Adv.* **2020**, *6* (12), 1–12.
- (46) Howell, J. A.; Nyström, M. Fouling Phenomena BT - Membranes in Bioprocessing: Theory and Applications; Howell, J. A., Sanchez, V., Field, R. W., Eds.; Springer

Netherlands: Dordrecht, 1993; pp 203–241.

- (47) Dalsin, J. L.; Messersmith, P. B. Bioinspired Antifouling Polymers. *Mater. Today* **2005**, *8* (9), 38–46.
- (48) Rana, D.; Matsuura, T. Surface Modifications for Antifouling Membranes. *Chem. Rev.* **2010**, *110* (4), 2448–2471.
- (49) Combe, C.; Molis, E.; Lucas, P.; Riley, R.; Clark, M. M. The Effect of CA Membrane Properties on Adsorptive Fouling by Humic Acid. *J. Memb. Sci.* **1999**, *154* (1), 73–87.
- (50) Ulbricht, M.; Richau, K.; Kamusewitz, H. Chemically and Morphologically Defined Ultrafiltration Membrane Surfaces Prepared by Heterogeneous Photo-Initiated Graft Polymerization | Part 11 of the Series: Photomodification of Ultrafiltration Membranes. *Colloids Surfaces A Physicochem. Eng. Asp.* **1998**, *138* (2), 353–366.
- (51) Kato, K.; Sano, S.; Ikada, Y. Protein Adsorption onto Ionic Surfaces. *Colloids Surfaces B Biointerfaces* **1995**, *4* (4), 221–230.
- (52) Susanto, H.; Ulbricht, M. Photografted Thin Polymer Hydrogel Layers on PES Ultrafiltration Membranes: Characterization, Stability, and Influence on Separation Performance. *Langmuir* **2007**, *23* (14), 7818–7830.
- (53) White, A.; Jiang, S. Local and Bulk Hydration of Zwitterionic Glycine and Its Analogues through Molecular Simulations. *J. Phys. Chem. B* **2011**, *115* (4), 660–667.

- (54) Hower, J. C.; Bernardis, M. T.; Chen, S.; Tsao, H.-K.; Sheng, Y.-J.; Jiang, S. Hydration of “Nonfouling” Functional Groups. *J. Phys. Chem. B* **2009**, *113* (1), 197–201.
- (55) Kurtz, I. S.; Sui, S.; Hao, X.; Huang, M.; Perry, S. L.; Schiffman, J. D. Bacteria-Resistant, Transparent, Free-Standing Films Prepared from Complex Coacervates. *ACS Appl. Bio Mater.* **2019**, *2* (9), 3926–3933.
- (56) Leng, C.; Huang, H.; Zhang, K.; Hung, H.-C.; Xu, Y.; Li, Y.; Jiang, S.; Chen, Z. Effect of Surface Hydration on Antifouling Properties of Mixed Charged Polymers. *Langmuir* **2018**, *34* (22), 6538–6545.
- (57) Bazuin, C. G.; Eisenberg, A. Ion-Containing Polymers: Ionomers. *J. Chem. Educ.* **1981**, *58* (11), 938–943.
- (58) Taubert, A.; Winey, K. I. Imaging and X-Ray Microanalysis of a Poly(Ethylene-Ran-Methacrylic Acid) Ionomer Melt Neutralized with Sodium. *Macromolecules* **2002**, *35* (19), 7419–7426.
- (59) Buitrago, C. F.; Jenkins, J. E.; Opper, K. L.; Aitken, B. S.; Wagener, K. B.; Alam, T. M.; Winey, K. I. Room Temperature Morphologies of Precise Acid- and Ion-Containing Polyethylenes. *Macromolecules* **2013**, *46* (22), 9003–9012.
- (60) Seitz, M. E.; Chan, C. D.; Opper, K. L.; Baughman, T. W.; Wagener, K. B.; Winey, K. I. Nanoscale Morphology in Precisely Sequenced Poly(Ethylene-Co-Acrylic Acid) Zinc Ionomers. *J. Am. Chem. Soc.* **2010**, *132* (23), 8165–8174.

- (61) Nagayama, K.; Kapur, J.; Morris, B. A. Influence of Two-Phase Behavior of Ethylene Ionomers on Diffusion of Water. *J. Appl. Polym. Sci.* **2020**, *137*, 48929.
- (62) Zhou, N. C.; Chan, C. D.; Winey, K. I. Reconciling STEM and X-Ray Scattering Data To Determine the Nanoscale Ionic Aggregate Morphology in Sulfonated Polystyrene Ionomers. *Macromolecules* **2008**, *41* (16), 6134–6140.
- (63) Castagna, A. M.; Wang, W.; Winey, K. I.; Runt, J. Influence of the Degree of Sulfonation on the Structure and Dynamics of Sulfonated Polystyrene Copolymers. *Macromolecules* **2010**, *43* (24), 10498–10504.
- (64) Castagna, A. M.; Wang, W.; Winey, K. I.; Runt, J. Influence of Cation Type on Structure and Dynamics in Sulfonated Polystyrene Ionomers. *Macromolecules* **2011**, *44* (13), 5420–5426.
- (65) Yang, S.; Sun, K.; Risen Jr., W. M. Preparation and Thermal Characterization of the Glass Transition Temperatures of Sulfonated Polystyrene-Metal Ionomers. *J. Polym. Sci. Part B Polym. Phys.* **1990**, *28* (10), 1685–1697.
- (66) Weiss, R. A.; Fitzgerald, J. J.; Kim, D. Viscoelastic Behavior of Lightly Sulfonated Polystyrene Ionomers. *Macromolecules* **1991**, *24* (5), 1071–1076.
- (67) Enokida, J. S.; Tanna, V. A.; Winter, H. H.; Coughlin, E. B. Progression of the Morphology in Random Ionomers Containing Bulky Ammonium Counterions. *Macromolecules* **2018**, *51* (18), 7377–7385.
- (68) Enokida, J. S.; Hu, W.; Fang, H.; Morgan, B. F.; Beyer, F. L.; Winter, H. H.;

- Coughlin, E. B. Modifying the Structure and Dynamics of Ionomers through Counterion Sterics. *Macromolecules* **2020**, *53* (5), 1767–1776.
- (69) Nandi, A.; DuttaGupta, M.; Banthia, A. K. Sulfonated Polybutadiene Ionomer Templates Nanonickel Composite. *Mater. Lett.* **2002**, *52* (3), 203–205.
- (70) Matsuura, H.; Eisenberg, A. Glass Transitions of Ethyl Acrylate-Based Ionomers. *J. Polym. Sci. Polym. Phys. Ed.* **1976**, *14* (7), 1201–1209.
- (71) Chen, Q.; Tudryn, G. J.; Colby, R. H. Ionomer Dynamics and the Sticky Rouse Model. *J. Rheol. (N. Y. N. Y.)* **2013**, *57* (5), 1441–1462.
- (72) Page, K. A.; Landis, F. A.; Phillips, A. K.; Moore, R. B. SAXS Analysis of the Thermal Relaxation of Anisotropic Morphologies in Oriented Nafion Membranes. *Macromolecules* **2006**, *39* (11), 3939–3946.
- (73) Nguyen, H.-D.; Jestin, J.; Porcar, L.; Iojoiu, C.; Lyonard, S. Aromatic Copolymer/Nafion Blends Outperforming the Corresponding Pristine Ionomers. *ACS Appl. Energy Mater.* **2018**, *1* (2), 355–367.
- (74) Barnes, A. M.; Buratto, S. K. Imaging Channel Connectivity in Nafion Using Electrostatic Force Microscopy. *J. Phys. Chem. B* **2018**, *122* (3), 1289–1295.
- (75) Hickner, M. A. Water-Mediated Transport in Ion-Containing Polymers. *J. Polym. Sci. Part B Polym. Phys.* **2012**, *50* (1), 9–20.
- (76) Wang, F.; Hickner, M.; Kim, Y. S.; Zawodzinski, T. A.; McGrath, J. E. Direct Polymerization of Sulfonated Poly(Arylene Ether Sulfone) Random (Statistical)

- Copolymers: Candidates for New Proton Exchange Membranes. *J. Memb. Sci.* **2002**, *197* (1), 231–242.
- (77) Paul, M.; Park, H. B.; Freeman, B. D.; Roy, A.; McGrath, J. E.; Riffle, J. S. Synthesis and Crosslinking of Partially Disulfonated Poly(Arylene Ether Sulfone) Random Copolymers as Candidates for Chlorine Resistant Reverse Osmosis Membranes. *Polymer (Guildf)*. **2008**, *49* (9), 2243–2252.
- (78) Van der Bruggen, B.; Vandecasteele, C. Distillation vs. Membrane Filtration: Overview of Process Evolutions in Seawater Desalination. *Desalination* **2002**, *143* (3), 207–218.
- (79) Varcoe, J. R.; Atanassov, P.; Dekel, D. R.; Herring, A. M.; Hickner, M. A.; Kohl, P. A.; Kucernak, A. R.; Mustain, W. E.; Nijmeijer, K.; Scott, K.; Xu, T.; Zhuang, L. Anion-Exchange Membranes in Electrochemical Energy Systems. *Energy Environ. Sci.* **2014**, *7* (10), 3135–3191.
- (80) Hickner, M. A. Ion-Containing Polymers: New Energy & Clean Water. *Mater. Today* **2010**, *13* (5), 34–41.
- (81) Asano, N.; Aoki, M.; Suzuki, S.; Miyatake, K.; Uchida, H.; Watanabe, M. Aliphatic/Aromatic Polyimide Ionomers as a Proton Conductive Membrane for Fuel Cell Applications. *J. Am. Chem. Soc.* **2006**, *128* (5), 1762–1769.
- (82) Einsla, B. R.; Hong, Y.-T.; Seung Kim, Y.; Wang, F.; Gunduz, N.; McGrath, J. E. Sulfonated Naphthalene Dianhydride Based Polyimide Copolymers for Proton-Exchange-Membrane Fuel Cells. I. Monomer and Copolymer Synthesis. *J. Polym.*

Sci. Part A Polym. Chem. **2004**, 42 (4), 862–874.

- (83) Fang, J.; Guo, X.; Harada, S.; Watari, T.; Tanaka, K.; Kita, H.; Okamoto, K. Novel Sulfonated Polyimides as Polyelectrolytes for Fuel Cell Application. 1. Synthesis, Proton Conductivity, and Water Stability of Polyimides from 4,4'-Diaminodiphenyl Ether-2,2'-Disulfonic Acid. *Macromolecules* **2002**, 35 (24), 9022–9028.
- (84) Genies, C.; Mercier, R.; Sillion, B.; Cornet, N.; Gebel, G.; Pineri, M. Soluble Sulfonated Naphthalenic Polyimides as Materials for Proton Exchange Membranes. *Polymer (Guildf)*. **2001**, 42 (2), 359–373.
- (85) Ghassemi, H.; McGrath, J. E. Synthesis and Properties of New Sulfonated Poly(p-Phenylene) Derivatives for Proton Exchange Membranes. I. *Polymer (Guildf)*. **2004**, 45 (17), 5847–5854.
- (86) Fujimoto, C. H.; Hickner, M. A.; Cornelius, C. J.; Loy, D. A. Ionomeric Poly(Phenylene) Prepared by Diels–Alder Polymerization: Synthesis and Physical Properties of a Novel Polyelectrolyte. *Macromolecules* **2005**, 38 (12), 5010–5016.
- (87) Schuster, M.; Kreuer, K.-D.; Andersen, H. T.; Maier, J. Sulfonated Poly(Phenylene Sulfone) Polymers as Hydrolytically and Thermooxidatively Stable Proton Conducting Ionomers. *Macromolecules* **2007**, 40 (3), 598–607.
- (88) Karlsson, L. E.; Jannasch, P. Polysulfone Ionomers for Proton-Conducting Fuel Cell Membranes: Sulfoalkylated Polysulfones. *J. Memb. Sci.* **2004**, 230 (1), 61–70.
- (89) Merle, G.; Wessling, M.; Nijmeijer, K. Anion Exchange Membranes for Alkaline

- Fuel Cells: A Review. *J. Memb. Sci.* **2011**, 377 (1–2), 1–35.
- (90) Hickner, M. A.; Herring, A. M.; Coughlin, E. B. Anion Exchange Membranes: Current Status and Moving Forward. *J. Polym. Sci. Part B Polym. Phys.* **2013**, 51 (24), 1727–1735.
- (91) Gottesfeld, S.; Dekel, D. R.; Page, M.; Bae, C.; Yan, Y.; Zelenay, P.; Kim, Y. S. Anion Exchange Membrane Fuel Cells: Current Status and Remaining Challenges. *J. Power Sources* **2018**, 375, 170–184.
- (92) Couture, G.; Alaaeddine, A.; Boschet, F.; Ameduri, B. Polymeric Materials as Anion-Exchange Membranes for Alkaline Fuel Cells. *Prog. Polym. Sci.* **2011**, 36 (11), 1521–1557.
- (93) Panchal, S. S.; Vasava, D. V. Biodegradable Polymeric Materials: Synthetic Approach. *ACS Omega* **2020**, 5 (9), 4370–4379.
- (94) Luo, Z.; Wu, Y. L.; Li, Z.; Loh, X. J. Recent Progress in Polyhydroxyalkanoates-Based Copolymers for Biomedical Applications. *Biotechnol. J.* **2019**, 1900283, 1–16.
- (95) Koller, M. Polyhydroxyalkanoate Biosynthesis at the Edge of Water Activity-Haloarchaea as Biopolyester Factories. *Bioengineering* **2019**, 6 (2), 34.
- (96) Herron, J. S.; King, J. D.; White, D. C. Recovery of Poly- β -Hydroxybutyrate from Estuarine Microflora. *Appl. Environ. Microbiol.* **1978**, 35 (2), 251 LP – 257.
- (97) Luo, S.; Netravali, A. N. Interfacial and Mechanical Properties of Environment-

- Friendly 'green' Composites Made from Pineapple Fibers and Poly(Hydroxybutyrate-Co-Valerate) Resin. *J. Mater. Sci.* **1999**, *34* (15), 3709–3719.
- (98) Carr, N. G. The Occurrence of Poly- β -Hydroxybutyrate in the Blue-Green Alga, *Chlorogloea Fritschii*. *Biochim. Biophys. Acta - Biophys. Incl. Photosynth.* **1966**, *120* (2), 308–310.
- (99) Wallen, L. L.; Rohwedder, W. K. Poly-. Beta.-Hydroxyalkanoate from Activated Sludge. *Environ. Sci. Technol.* **1974**, *8* (6), 576–579.
- (100) Lemoigne, M. Etudes Sur L'autolyse Microbienne Acidification Par Formation D'acide β -Oxybutyrique. *Ann. Inst. Pasteur* **1925**, *39*, 144–173.
- (101) Roy, I.; Visakh, P. M. *Polyhydroxyalkanoate (PHA) Based Blends, Composites and Nanocomposites*; Royal Society of Chemistry, 2014; Vol. 30.
- (102) Knani, D.; Gutman, A. L.; Kohn, D. H. Enzymatic Polyesterification in Organic Media. Enzyme-Catalyzed Synthesis of Linear Polyesters. I. Condensation Polymerization of Linear Hydroxyesters. II. Ring-Opening Polymerization of ϵ -Caprolactone. *J. Polym. Sci. Part A Polym. Chem.* **1993**, *31* (5), 1221–1232.
- (103) Pellis, A.; Comerford, J. W.; Weinberger, S.; Guebitz, G. M.; Clark, J. H.; Farmer, T. J. Enzymatic Synthesis of Lignin Derivable Pyridine Based Polyesters for the Substitution of Petroleum Derived Plastics. *Nat. Commun.* **2019**, *10* (1), 1762.
- (104) Eichhorn, S. J.; Dufresne, A.; Aranguren, M.; Marcovich, N. E.; Capadona, J. R.;

Rowan, S. J.; Weder, C.; Thielemans, W.; Roman, M.; Renneckar, S.; Gindl, W.; Veigel, S.; Keckes, J.; Yano, H.; Abe, K.; Nogi, M.; Nakagaito, A. N.; Mangalam, A.; Simonsen, J.; et al. *Review: Current International Research into Cellulose Nanofibres and Nanocomposites*; 2010; Vol. 45.

- (105) Wohlhauser, S.; Delepierre, G.; Labet, M.; Morandi, G.; Thielemans, W.; Weder, C.; Zoppe, J. O. Grafting Polymers from Cellulose Nanocrystals: Synthesis, Properties, and Applications. *Macromolecules* **2018**, *51* (16), 6157–6189.
- (106) Heinze, T.; Liebert, T. Unconventional Methods in Cellulose Functionalization. *Prog. Polym. Sci.* **2001**, *26* (9), 1689–1762.
- (107) Carvalho, L. C. R.; Queda, F.; Santos, C. V. A.; Marques, M. M. B. Selective Modification of Chitin and Chitosan: En Route to Tailored Oligosaccharides. *Chem. - An Asian J.* **2016**, *11* (24), 3468–3481.
- (108) Kurita, K.; Mori, S.; Nishiyama, Y.; Harata, M. N-Alkylation of Chitin and Some Characteristics of the Novel Derivatives. *Polym. Bull.* **2002**, *48* (2), 159–166.
- (109) Kurita, K.; Kojima, T.; Nishiyama, Y.; Shimojoh, M. Synthesis and Some Properties of Nonnatural Amino Polysaccharides: Branched Chitin and Chitosan. *Macromolecules* **2000**, *33* (13), 4711–4716.
- (110) Kurita, K.; Akao, H.; Yang, J.; Shimojoh, M. Nonnatural Branched Polysaccharides: Synthesis and Properties of Chitin and Chitosan Having Disaccharide Maltose Branches. *Biomacromolecules* **2003**, *4* (5), 1264–1268.

- (111) Silvernail, C. M.; Yao, L. J.; Hill, L. M. R.; Hillmyer, M. A.; Tolman, W. B. Structural and Mechanistic Studies of Bis(Phenolato)Amine Zinc(II) Catalysts for the Polymerization of ϵ -Caprolactone. *Inorg. Chem.* **2007**, *46* (16), 6565–6574.
- (112) Gou, M.; Gong, C.; Zhang, J.; Wang, X.; Wang, X.; Gu, Y.; Guo, G.; Chen, L.; Luo, F.; Zhao, X.; Wei, Y.; Qian, Z. Polymeric Matrix for Drug Delivery: Honokiol-Loaded PCL-PEG-PCL Nanoparticles in PEG-PCL-PEG Thermosensitive Hydrogel. *J. Biomed. Mater. Res. Part A* **2010**, *93A* (1), 219–226.
- (113) Lowe, J. R.; Martello, M. T.; Tolman, W. B.; Hillmyer, M. A. Functional Biorenewable Polyesters from Carvone-Derived Lactones. *Polym. Chem.* **2011**, *2* (3), 702–708.
- (114) Fraser, C.; Hillmyer, M. A.; Gutierrez, E.; Grubbs, R. H. Degradable Cyclooctadiene/Acetal Copolymers: Versatile Precursors to 1,4-Hydroxytelechelic Polybutadiene and Hydroxytelechelic Polyethylene. *Macromolecules* **1995**, *28* (21), 7256–7261.
- (115) Hilf, S.; Kilbinger, A. F. M. Heterotelechelic Ring-Opening Metathesis Polymers. *Macromolecules* **2010**, *43* (1), 208–212.
- (116) Hilf, S.; Kilbinger, A. F. M. Sacrificial Synthesis of Hydroxy-Telechelic Metathesis Polymers via Multiblock-Copolymers. *Macromolecules* **2009**, *42* (4), 1099–1106.
- (117) Hilf, S.; Grubbs, R. H.; Kilbinger, A. F. M. Sacrificial Synthesis of Hydroxy-Functionalized ROMP Polymers: An Efficiency Study. *Macromolecules* **2008**, *41* (16), 6006–6011.

- (118) Hilf, S.; Berger-Nicoletti, E.; Grubbs, R. H.; Kilbinger, A. F. M. Monofunctional Metathesis Polymers via Sacrificial Diblock Copolymers. *Angew. Chemie - Int. Ed.* **2006**, *45* (47), 8045–8048.
- (119) Chang, C. C.; Emrick, T. Functional Polyolefins Containing Disulfide and Phosphoester Groups: Synthesis and Orthogonal Degradation. *Macromolecules* **2014**, *47* (4), 1344–1350.
- (120) Nagarkar, A. A.; Crochet, A.; Fromm, K. M.; Kilbinger, A. F. M. Efficient Amine End-Functionalization of Living Ring-Opening Metathesis Polymers. *Macromolecules* **2012**, *45* (11), 4447–4453.
- (121) Shieh, P.; Nguyen, H. V. T.; Johnson, J. A. Tailored Silyl Ether Monomers Enable Backbone-Degradable Polynorbornene-Based Linear, Bottlebrush and Star Copolymers through ROMP. *Nat. Chem.* **2019**, *11* (12), 1124–1132.
- (122) Hilf, S.; Kilbinger, A. F. M. Thiol-Functionalized ROMP Polymers via Sacrificial Synthesis. *Macromolecules* **2009**, *42* (12), 4127–4133.
- (123) Tivant, P.; Turq, P.; Drifford, M.; Magdelenat, H.; Menez, R. Effect of Ionic Strength on the Diffusion Coefficient of Chondroitin Sulfate and Heparin Measured by Quasielastic Light Scattering. *Biopolymers* **1983**, *22* (2), 643–662.
- (124) Meller, A.; Nivon, L.; Branton, D. Voltage-Driven DNA Translocations through a Nanopore. *Phys. Rev. Lett.* **2001**, *86* (15), 3435–3438.
- (125) Muthukumar, M. Phase Diagram of Polyelectrolyte Solutions: Weak Polymer

- Effect. *Macromolecules* **2002**, *35* (24), 9142–9145.
- (126) Lee, C.-L.; Muthukumar, M. Phase Behavior of Polyelectrolyte Solutions with Salt. *J. Chem. Phys.* **2009**, *130* (2), 24904.
- (127) Mori, S. Secondary Effects in Aqueous Size Exclusion Chromatography of Sodium Poly(Styrenesulfonate) Compounds. *Anal. Chem.* **1989**, *61* (6), 530–534.
- (128) Liu, Y.; Fratini, E.; Baglioni, P.; Chen, W.-R.; Chen, S.-H. Effective Long-Range Attraction between Protein Molecules in Solutions Studied by Small Angle Neutron Scattering. *Phys. Rev. Lett.* **2005**, *95* (11), 118102.
- (129) Sedláč, M.; Amis, E. J. Concentration and Molecular Weight Regime Diagram of Salt-Free Polyelectrolyte Solutions as Studied by Light Scattering. *J. Chem. Phys.* **1992**, *96* (1), 826–834.
- (130) Scheler, U. NMR on Polyelectrolytes. *Curr. Opin. Colloid Interface Sci.* **2009**, *14* (3), 212–215.
- (131) Holappa, S.; Karesoja, M.; Shan, J.; Tenhu, H. Solution Properties of Linear and Branched Block Copolymers Consisting of Acidic and PEO Blocks. *Macromolecules* **2002**, *35* (12), 4733–4738.
- (132) Sinha, V. R.; Singla, A. K.; Wadhawan, S.; Kaushik, R.; Kumria, R.; Bansal, K.; Dhawan, S. Chitosan Microspheres as a Potential Carrier for Drugs. *Int. J. Pharm.* **2004**, *274* (1), 1–33.
- (133) Kumar, M. N. V. R.; Muzzarelli, R. A. A.; Muzzarelli, C.; Sashiwa, H.; Domb, A.

- J. Chitosan Chemistry and Pharmaceutical Perspectives. *Chem. Rev.* **2004**, *104* (12), 6017–6084.
- (134) Gondi, S. R.; Vogt, A. P.; Sumerlin, B. S. Versatile Pathway to Functional Telechelics via RAFT Polymerization and Click Chemistry. *Macromolecules* **2007**, *40* (3), 474–481.
- (135) Bouhadir, G.; Legrand, N.; Quiclet-Sire, B.; Zard, S. Z. A New Practical Synthesis of Tertiary S-Alkyl Dithiocarbonates and Related Derivatives. *Tetrahedron Lett.* **1999**, *40* (2), 277–280.
- (136) Moad, G.; Chong, Y. K.; Postma, A.; Rizzardo, E.; Thang, S. H. Advances in RAFT Polymerization: The Synthesis of Polymers with Defined End-Groups. *Polymer (Guildf)*. **2005**, *46* (19), 8458–8468.
- (137) Perrier, S. 50th Anniversary Perspective: RAFT Polymerization - A User Guide. *Macromolecules* **2017**, *50* (19), 7433–7447.
- (138) Keddie, D. J.; Moad, G.; Rizzardo, E.; Thang, S. H. RAFT Agent Design and Synthesis. *Macromolecules* **2012**, *45* (13), 5321–5342.
- (139) Weidner, S. M.; Trimpin, S. Mass Spectrometry of Synthetic Polymers. *Anal. Chem.* **2008**, *80* (12), 4349–4361.
- (140) Cohen, Y.; Avram, L.; Frish, L. Diffusion NMR Spectroscopy in Supramolecular and Combinatorial Chemistry: An Old Parameter - New Insights. *Angew. Chemie - Int. Ed.* **2005**, *44* (4), 520–554.

- (141) Stuart, M. A. C.; Hofs, B.; Voets, I. K.; Keizer, A. De. Assembly of Polyelectrolyte-Containing Block Copolymers in Aqueous Media. *Curr. Opin. Colloid Interface Sci.* **2005**, *10*, 30–36.
- (142) Varcoe, J. R.; Slade, R. C. T.; Wright, G. L.; Chen, Y. Steady-State Dc and Impedance Investigations of H₂ / O₂ Alkaline Membrane Fuel Cells with Commercial Pt / C , Ag / C , and Au / C Cathodes. *J. Phys. Chem. B* **2006**, *2* (3), 21041–21049.
- (143) Grew, K. N.; Chiu, W. K. S. A Dusty Fluid Model for Predicting Hydroxyl Anion Conductivity in Alkaline Anion Exchange Membranes. *J. Electrochem. Soc.* **2010**, *157* (3), B327.
- (144) Zawodzinski, T. A.; Derouin, C.; Radzinski, S.; Sherman, R. J.; Smith, V. T.; Springer, T. E.; Gottesfeld, S. Water Uptake by and Transport Through Nafion® 117 Membranes. *J. Electrochem. Soc.* **1993**, *140* (4), 1041.
- (145) Paddison, S. J.; Paul, R. The Nature of Proton Transport in Fully Hydrated Nafion®. *Phys. Chem. Chem. Phys.* **2002**, *4* (7), 1158–1163.
- (146) Choi, P.; Jalani, N. H.; Datta, R. Thermodynamics and Proton Transport in Nafion. *J. Electrochem. Soc.* **2005**, *152* (3), E123.
- (147) Weber, A. Z.; Newman, J. Modeling Transport in Polymer-Electrolyte Fuel Cells. *Chem. Rev.* **2004**, *104* (10), 4679–4726.
- (148) Hsu, W. Y.; Gierke, T. D. Ion Transport and Clustering in Nafion Perfluorinated

Membranes. *J. Memb. Sci.* **1983**, *13* (3), 307–326.

- (149) Rubatat, L.; Rollet, A. L.; Gebel, G.; Diat, O. Evidence of Elongated Polymeric Aggregates in Nafion. *Macromolecules* **2002**, *35* (10), 4050–4055.
- (150) Schmidt-Rohr, K.; Chen, Q. Parallel Cylindrical Water Nanochannels in Nafion Fuel-Cell Membranes. *Nat. Mater.* **2007**, *7* (1), 75–83.
- (151) Yan, X.; Gu, S.; He, G.; Wu, X.; Benziger, J. Imidazolium-Functionalized Poly(Ether Ether Ketone) as Membrane and Electrode Ionomer for Low-Temperature Alkaline Membrane Direct Methanol Fuel Cell. *J. Power Sources* **2014**, *250*, 90–97.
- (152) Gu, S.; Skovgard, J.; Yan, Y. S. Engineering the Van Der Waals Interaction in Cross-Linking-Free Hydroxide Exchange Membranes for Low Swelling and High Conductivity. *ChemSusChem* **2012**, *5*, 843–848.
- (153) Disabb-miller, M. L.; Zha, Y.; Decarlo, A. J.; Pawar, M.; Tew, G. N.; Hickner, M. A. Water Uptake and Ion Mobility in Cross-Linked Bis(Terpyridine)Ruthenium-Based Anion Exchange Membranes. *Macromolecules* **2013**, *46* (23), 9279–9287.
- (154) Gu, S.; Cai, R.; Luo, T.; Chen, Z.; Sun, M.; Liu, Y.; He, G.; Yan, Y. A Soluble and Highly Conductive Ionomer for High-Performance Hydroxide Exchange Membrane Fuel Cells. *Angew. Chemie - Int. Ed.* **2009**, *48* (35), 6499–6502.
- (155) Noonan, K. J. T.; Hugar, K. M.; Kostalik, H. A.; Lobkovsky, E. B.; Abruña, H. D.; Coates, G. W. Phosphonium-Functionalized Polyethylene: A New Class of Base-

- Stable Alkaline Anion Exchange Membranes. *J. Am. Chem. Soc.* **2012**, *134* (44), 18161–18164.
- (156) Cotanda, P.; Sudre, G.; Modestino, M. A.; Chen, X. C.; Balsara, N. P. High Anion Conductivity and Low Water Uptake of Phosphonium Containing Diblock Copolymer Membranes. *Macromolecules* **2014**, *47* (21), 7540–7547.
- (157) Li, N.; Leng, Y.; Hickner, M. A.; Wang, C.-Y. Highly Stable, Anion Conductive, Comb-Shaped Copolymers for Alkaline Fuel Cells. *J. Am. Chem. Soc.* **2013**, *135* (27), 10124–10133.
- (158) Zhang, W.; Liu, Y.; Jackson, A. C.; Savage, A. M.; Ertem, S. P.; Tsai, T.-H.; Seifert, S.; Beyer, F. L.; Liberatore, M. W.; Herring, A. M.; Coughlin, E. B. Achieving Continuous Anion Transport Domains Using Block Copolymers Containing Phosphonium Cations. *Macromolecules* **2016**, *49* (13), 4714–4722.
- (159) Kumar, R.; Muthukumar, M. Microphase Separation in Polyelectrolytic Diblock Copolymer Melt: Weak Segregation Limit. *J. Chem. Phys.* **2007**, *126* (21), 214902.
- (160) Rojas, A. A.; Inceoglu, S.; Mackay, N. G.; Thelen, J. L.; Devaux, D.; Stone, G. M.; Balsara, N. P. Effect of Lithium-Ion Concentration on Morphology and Ion Transport in Single-Ion-Conducting Block Copolymer Electrolytes. *Macromolecules* **2015**, *48* (18), 6589–6595.
- (161) Moon, B.; Park, J.; Kim, S.; Minor, A. M.; Hexemer, A.; Balsara, N. P. Control of Domain Orientation in Block Copolymer Electrolyte Membranes at the Interface with Humid Air. *Adv. Mater.* **2009**, *21* (2), 203–208.

- (162) Park, M. J.; Balsara, N. P. Phase Behavior of Symmetric Sulfonated Block Copolymers. *Macromolecules* **2008**, *41* (10), 3678–3687.
- (163) Sing, C. E.; Zwanikken, J. W.; Olvera De La Cruz, M. Electrostatic Control of Block Copolymer Morphology. *Nat. Mater.* **2014**, *13* (7), 694–698.
- (164) Kumar, R.; Muthukumar, M. Microphase Separation in Polyelectrolytic Diblock Copolymer Melt: Weak Segregation Limit. *J. Chem. Phys.* **2017**, *126* (21), 214902.
- (165) Jiang, Y.; Freyer, J. L.; Cotanda, P.; Brucks, S. D.; Killops, K. L.; Bandar, J. S.; Torsitano, C.; Balsara, N. P.; Lambert, T. H.; Campos, L. M. Functional Polyelectrolytes. *Nat. Commun.* **2015**, *6*, 1–7.
- (166) Sing, C. E.; Zwanikken, J. W.; Olvera, M.; Cruz, D. Theory of Melt Polyelectrolyte Blends and Block Copolymers : Phase Behavior , Surface Tension , and Microphase Periodicity Theory of Melt Polyelectrolyte Blends and Block Copolymers : Phase Behavior , Surface Tension , and Microphase Periodicity. *J. Chem. Phys.* **2015**, *142* (3), 034902.
- (167) Sing, C. E.; Olvera, M.; Cruz, D. Polyelectrolyte Blends and Nontrivial Behavior in Effective Flory – Huggins Parameters. *ACS Macro Lett.* **2014**, *3* (8), 698–702.
- (168) Sing, C. E. Development of the Modern Theory of Polymeric Complex Coacervation. *Adv. Colloid Interface Sci.* **2017**, *239*, 2–16.
- (169) Perry, S. L.; Sing, C. E. PRISM-Based Theory of Complex Coacervation: Excluded Volume versus Chain Correlation. *Macromol. Rapid Commun.* **2015**, *48* (14), 5040–

5053.

- (170) Irwin, M. T.; Hickey, R. J.; Xie, S.; Bates, F. S.; Lodge, T. P. Lithium Salt-Induced Microstructure and Ordering in Diblock Copolymer/Homopolymer Blends. *Macromolecules* **2016**, *49* (13), 4839–4849.
- (171) Oksana, C.; Liwei, C.; Weng, V.; Yuditsky, L.; Brus, L. E. Quantitative Noncontact Electrostatic Force Imaging of Nanocrystal Polarizability. *J. Phys. Chem. B* **2003**, *107* (7), 1525–1531.
- (172) Yalcin, S. E.; Labastide, J. A.; Sowle, D. L.; Barnes, M. D. Spectral Properties of Multiply Charged Semiconductor Quantum Dots. *Nano Lett.* **2011**, *11* (10), 4425–4430.
- (173) Malvankar, N. S.; Yalcin, S. E.; Tuominen, M. T.; Lovley, D. R. Visualization of Charge Propagation along Individual Pili Proteins Using Ambient Electrostatic Force Microscopy. *Nat. Nanotechnol.* **2014**, *9* (12), 1012–1017.
- (174) Heim, T.; Lmimouni, K.; Vuillaume, D. Ambipolar Charge Injection and Transport in a Single Pentacene Monolayer Island NANO LETTERS. *Nano Lett.* **2004**, *4* (11), 2145–2150.
- (175) Schaadt, D. M.; Yu, E. T.; Sankar, S.; Berkowitz, A. E. Charge Storage in Co Nanoclusters Embedded in SiO₂ by Scanning Force Microscopy. *Appl. Phys. Lett.* **1999**, *74*, 472.
- (176) Jaquith, M.; Muller, E. M.; Marohn, J. A. Time-Resolved Electric Force Microscopy

- of Charge Trapping in Polycrystalline Pentacene. *J. Phys. Chem. B* **2007**, *111* (27), 7711–7714.
- (177) Mélin, T.; Diesinger, H.; Deresmes, D.; Stiévenard, D. Electric Force Microscopy of Individually Charged Nanoparticles on Conductors: An Analytical Model for Quantitative Charge Imaging. *Phys. Rev. B* **2004**, *69* (3), 035321.
- (178) Harrisson, S.; Couvreur, P.; Nicolas, J. Use of Solvent Effects to Improve Control over Nitroxide-Mediated Polymerization of Isoprene. *Macromol. Rapid Commun.* **2012**, *33* (9), 805–810.
- (179) Lacroix-Desmazes, P.; Delair, T.; Pichot, C.; Boutevin, B. Synthesis of Poly(Chloromethylstyrene-*b*-Styrene) Block Copolymers by Controlled Free-Radical Polymerization. *J. Polym. Sci. Part A Polym. Chem.* **2000**, *38* (21), 3845–3854.
- (180) Nakano, T.; Kawaguchi, D.; Matsushita, Y. Anisotropic Self-Assembly of Gold Nanoparticle Grafted with Polyisoprene and Polystyrene Having Symmetric Polymer Composition. *J. Am. Chem. Soc.* **2013**, *135* (18), 6798–6801.
- (181) Li, W.; Wang, H.; Yu, L.; Morkved, T. L.; Jaeger, H. M. Syntheses of Oligophenylenevinylenes - Polyisoprene Diblock Copolymers and Their Microphase Separation. *Macromolecules* **1999**, *32* (9), 3034–3044.
- (182) Hasegawa, H.; Hashimoto, T. Morphology of Block Polymers near a Free Surface. *Macromolecules* **1985**, *18* (3), 589–590.

- (183) Bates, F. S.; Fredrickson, G. H. Block Copolymer Thermodynamics: Theory and Experiment. *Annu. Rev. Phys. Chem.* **1990**, *41* (1), 525–557.
- (184) Khanna, V.; Cochran, E. W.; Hexemer, A.; Stein, G. E.; Fredrickson, G. H.; Kramer, E. J.; Li, X.; Wang, J.; Hahn, S. F. Effect of Chain Architecture and Surface Energies on the Ordering Behavior of Lamellar and Cylinder Forming Block Copolymers. *Macromolecules* **2006**, *39* (26), 9346–9356.
- (185) Komura, M.; Iyoda, T. AFM Cross-Sectional Imaging of Perpendicularly Oriented Nanocylinder Structures of Microphase-Separated Block Copolymer Films by Crystal-like Cleavage. *Macromolecules* **2007**, *40* (12), 4106–4108.
- (186) Komura, M.; Yoshitake, A.; Komiyama, H.; Iyoda, T. Control of Air-Interface-Induced Perpendicular Nanocylinder Orientation in Liquid Crystal Block Copolymer Films by a Surface-Covering Method. *Macromolecules* **2015**, *48* (3), 672–678.
- (187) O’Dea, J. R.; Economou, N. J.; Buratto, S. K. Surface Morphology of Nafion at Hydrated and Dehydrated Conditions. *Macromolecules* **2013**, *46* (6), 2267–2274.
- (188) Register, R. A.; Marchand, G. R.; Adams, J. L.; Graessley, W. W.; Quiram, D. J. Ordering Dynamics of Compositionally Asymmetric Styrene–Isoprene Block Copolymers. *Macromolecules* **2002**, *29* (8), 2929–2938.
- (189) Kim, J. K.; Lee, H. H.; Ree, M.; Lee, K.-B.; Park, Y. Ordering Kinetics of Cylindrical and Spherical Microdomains in an SIS Block Copolymer by Synchrotron SAXS and Rheology. *Macromol. Chem. Phys.* **1998**, *199* (4), 641–653.

- (190) Economou, N. J.; Barnes, A. M.; Wheat, A. J.; Schaberg, M. S.; Hamrock, S. J.; Buratto, S. K. Investigation of Humidity Dependent Surface Morphology and Proton Conduction in Multi-Acid Side Chain Membranes by Conductive Probe Atomic Force Microscopy. *J. Phys. Chem. B* **2015**, *119* (44), 14280–14287.
- (191) Fang, S. J.; Haplepete, S.; Chen, W.; Helms, C. R.; Edwards, H. Analyzing Atomic Force Microscopy Images Using Spectral Methods. *J. Appl. Phys.* **1998**, *82* (12), 5891.
- (192) Mclean, R. S.; Sauer, B. B. *Tapping-Mode AFM Studies Using Phase Detection for Resolution of Nanophases in Segmented Polyurethanes and Other Block Copolymers*; 1997.
- (193) Kim, S.; Briber, R. M.; Karim, A.; Jones, R. L.; Kim, H.-C. Environment-Controlled Spin Coating To Rapidly Orient Microdomains in Thin Block Copolymer Films. *Macromolecules* **2007**, *40* (12), 4102–4105.
- (194) Gu, X.; Gunkel, I.; Hexemer, A.; Russell, T. P. Controlling Domain Spacing and Grain Size in Cylindrical Block Copolymer Thin Films by Means of Thermal and Solvent Vapor Annealing. *Macromolecules* **2016**, *49* (9), 3373–3381.
- (195) Mélin, T.; Zdrojek, M.; Brunel, D. Electrostatic Force Microscopy and Kelvin Force Microscopy as a Probe of the Electrostatic and Electronic Properties of Carbon Nanotubes. In *Scanning Probe Microscopy in Nanoscience and Nanotechnology*; Springer, Berlin, Heidelberg, 2010; pp 89–128.
- (196) Bates, F. S.; Schulz, M. F.; Khandpur, A. K.; Förster, S.; Rosedale, J. H.; Almdal,

- K.; Mortensen, K. Fluctuations, Conformational Asymmetry and Block Copolymer Phase Behaviour. *Faraday Discuss.* **1994**, *98* (0), 7–18.
- (197) Helfand, E. Theory of Inhomogeneous Polymers: Fundamentals of the Gaussian Random-walk Model. *J. Chem. Phys.* **1975**, *62* (3), 999–1005.
- (198) Matsen, M. W. Equilibrium Behavior of Asymmetric ABA Triblock Copolymer Melts. *J. Chem. Phys.* **2000**, *113* (13), 5539–5544.
- (199) Matsen, M. W. Effect of Architecture on the Phase Behavior of AB-Type Block Copolymer Melts. *Macromolecules* **2012**, *45* (4), 2161–2165.
- (200) Yamaoka, I.; Kimura, M. Effects of Morphology on Mechanical Properties of a SBS Triblock Copolymer. *Polymer (Guildf)*. **1993**, *34* (21), 4399–4409.
- (201) Ryu, C. Y.; Lee, M. S.; Hajduk, D. A.; Lodge, T. P. Structure and Viscoelasticity of Matched Asymmetric Diblock and Triblock Copolymers in the Cylinder and Sphere Microstructures. *J. Polym. Sci. Part B Polym. Phys.* **1997**, *35* (17), 2811–2823.
- (202) Riise, B. L.; Fredrickson, G. H.; Larson, R. G.; Pearson, D. S. Rheology and Shear-Induced Alignment of Lamellar Diblock and Triblock Copolymers. *Macromolecules* **1995**, *28* (23), 7653–7659.
- (203) McKay, K. W.; Gros, W. A.; Diehl, C. F. The Influence of Styrene–Butadiene Diblock Copolymer on Styrene–Butadiene–Styrene Triblock Copolymer Viscoelastic Properties and Product Performance. *J. Appl. Polym. Sci.* **1995**, *56* (8), 947–958.

- (204) Adams, J. L.; Graessley, W. W.; Register, R. A. Rheology and the Microphase Separation Transition in Styrene-Isoprene Block Copolymers. *Macromolecules* **1994**, *27* (21), 6026–6032.
- (205) Honeker, C. C.; Thomas, E. L. Impact of Morphological Orientation in Determining Mechanical Properties in Triblock Copolymer Systems. *Chem. Mater.* **1996**, *8* (8), 1702–1714.
- (206) Polymeropoulos, G.; Zapsas, G.; Ntetsikas, K.; Bilalis, P.; Gnanou, Y.; Hadjichristidis, N. 50th Anniversary Perspective: Polymers with Complex Architectures. *Macromolecules* **2017**, *50* (4), 1253–1290.
- (207) Liu, B.; Quirk, R. P.; Wesdemiotis, C.; Yol, A. M.; Foster, M. D. Precision Synthesis of ω -Branch, End-Functionalized Comb Polystyrenes Using Living Anionic Polymerization and Thiol–Ene “Click” Chemistry. *Macromolecules* **2012**, *45* (23), 9233–9242.
- (208) Iatrou, H.; Siakali-Kioulafa, E.; Hadjichristidis, N.; Roovers, J.; Mays, J. Hydrodynamic Properties of Model 3-Miktoarm Star Copolymers. *J. Polym. Sci. Part B Polym. Phys.* **1995**, *33* (13), 1925–1932.
- (209) Tselikas, Y.; Iatrou, H.; Hadjichristidis, N.; Liang, K. S.; Mohanty, K.; Lohse, D. J. Morphology of Miktoarm Star Block Copolymers of Styrene and Isoprene. *J. Chem. Phys.* **1996**, *105* (6), 2456–2462.
- (210) Polymeropoulos, G.; Bilalis, P.; Hadjichristidis, N. Well-Defined Cyclic Triblock Terpolymers: A Missing Piece of the Morphology Puzzle. *ACS Macro Lett.* **2016**, *5*

- (11), 1242–1246.
- (211) Nicolas, J.; Charleux, B.; Guerret, O.; Magnet, S. Nitroxide-Mediated Controlled Free-Radical Emulsion Polymerization Using a Difunctional Water-Soluble Alkoxyamine Initiator. Toward the Control of Particle Size, Particle Size Distribution, and the Synthesis of Triblock Copolymers. *Macromolecules* **2005**, *38*, 9963–9973.
- (212) Odian, G. *Principles of Polymerization*; John Wiley & Sons, Ltd, 2004.
- (213) Purvis, J. E.; Jones, H. O.; Tasker, H. S. CCXL. - The Colour and Absorption Spectra of Some Sulphur Compounds. *J. Chem. Soc. {,} Trans.* **1910**, *97*, 2287–2297.
- (214) Bost, R.; Williams, W. Carbithioic Acid Studies. II. Cyclohexylcarbithioic Acid and Various Derivatives. *J. Am. Chem. Soc.* **1930**, *52* (12), 4991–4992.
- (215) Bost, R.; Mattox, W. Carbithioic Acid Studies. I. Toly-4-Carbithioic Acid and Certain Derivatives. *J. Am. Chem. Soc.* **1930**, *52* (1), 332–335.
- (216) Bowes, A.; Mcleary, J. B.; Sanderson, R. D. AB and ABA Type Butyl Acrylate and Styrene Block Copolymers via RAFT-Mediated Miniemulsion Polymerization. *J. Polym. Sci. Part A Polym. Chem.* **2007**, *45* (4), 588–604.
- (217) Chen, L.; Hallinan, D. T.; Elabd, Y. A.; Hillmyer, M. A. Highly Selective Polymer Electrolyte Membranes from Reactive Block Polymers. *Macromolecules* **2009**, *42* (16), 6075–6085.
- (218) Fetters, L. J.; Lohse, D. J.; Richter, D.; Witten, T. A.; Zirkel, A. Connection between

- Polymer Molecular Weight, Density, Chain Dimensions, and Melt Viscoelastic Properties. *Macromolecules* **1994**, *27* (17), 4639–4647.
- (219) Kennemur, J. G.; Hillmyer, M. A.; Bates, F. S. Synthesis, Thermodynamics, and Dynamics of Poly(4-*Tert*-Butylstyrene-*b*-Methyl Methacrylate). *Macromolecules* **2012**, *45* (17), 7228–7236.
- (220) Schmitt, A. K.; Mahanthappa, M. K. Characteristics of Lamellar Mesophases in Strongly Segregated Broad Dispersity ABA Triblock Copolymers. *Macromolecules* **2014**, *47* (13), 4346–4356.
- (221) Semenov, A. N. Contribution to the Theory of Microphase Layering in Block-Copolymer Melts. *Sov. Phys.* **1985**, *61* (4), 733–742.
- (222) Widin, J. M.; Kim, M.; Schmitt, A. K.; Han, E.; Gopalan, P.; Mahanthappa, M. K. Bulk and Thin Film Morphological Behavior of Broad Dispersity Poly(Styrene-*b*-Methyl Methacrylate) Diblock Copolymers. *Macromolecules* **2013**, *46* (11), 4472–4480.
- (223) Zalusky, A. S.; Olayo-Valles, R.; Wolf, J. H.; Hillmyer, M. A. Ordered Nanoporous Polymers from Polystyrene–Polylactide Block Copolymers. *J. Am. Chem. Soc.* **2002**, *124* (43), 12761–12773.
- (224) Semenov, A. N. Theory of Block Copolymer Interfaces in the Strong Segregation Limit. *Macromolecules* **1993**, *26* (24), 6617–6621.
- (225) Matsen, M. W.; Schick, M. Lamellar Phase of a Symmetric Triblock Copolymer.

Macromolecules **1994**, 27 (1), 187–192.

- (226) Tardy, A.; Nicolas, J.; Gimes, D.; Lefay, C.; Guillaneuf, Y. Radical Ring-Opening Polymerization: Scope, Limitations, and Application to (Bio) Degradable Materials. *Chem. Rev.* **2017**, 117, 1319–1406.
- (227) Agarwal, S. Chemistry, Chances and Limitations of the Radical Ring-Opening Polymerization of Cyclic Ketene Acetals for the Synthesis of Degradable Polyesters. *Polym. Chem.* **2010**, 1 (7), 953–964.
- (228) Zhou, X.; Xie, Q.; Ma, C.; Chen, Z.; Zhang, G. Inhibition of Marine Biofouling by Use of Degradable and Hydrolyzable Silyl Acrylate Copolymer. *Ind. Eng. Chem. Res.* **2015**, 54 (39), 9559–9565.
- (229) Grabe, N.; Zhang, Y.; Agarwal, S. Degradable Elastomeric Block Copolymers Based on Polycaprolactone by Free-Radical Chemistry. *Macromol. Chem. Phys.* **2011**, 212 (13), 1327–1334.
- (230) Jin, Q.; Maji, S.; Agarwal, S. Novel Amphiphilic, Biodegradable, Biocompatible, Cross-Linkable Copolymers: Synthesis, Characterization and Drug Delivery Applications. *Polym. Chem.* **2012**, 3 (10), 2785–2793.
- (231) Cai, T.; Chen, Y.; Wang, Y.; Wang, H.; Liu, X.; Jin, Q.; Agarwal, S.; Ji, J. Functional 2-Methylene-1,3-Dioxepane Terpolymer: A Versatile Platform to Construct Biodegradable Polymeric Prodrugs for Intracellular Drug Delivery. *Polym. Chem.* **2014**, 5 (13), 4061–4068.

- (232) Cai, T.; Chen, Y.; Wang, Y.; Wang, H.; Liu, X.; Jin, Q.; Agarwal, S.; Ji, J. One-Step Preparation of Reduction-Responsive Biodegradable Polymers as Efficient Intracellular Drug Delivery Platforms. *Macromol. Chem. Phys.* **2014**, *215* (19), 1848–1854.
- (233) Hill, M. R.; Guégain, E.; Tran, J.; Figg, C. A.; Turner, A. C.; Nicolas, J.; Sumerlin, B. S. Radical Ring-Opening Copolymerization of Cyclic Ketene Acetals and Maleimides Affords Homogeneous Incorporation of Degradable Units. *ACS Macro Lett.* **2017**, *6* (10), 1071–1077.
- (234) Hill, M. R.; Kubo, T.; Goodrich, S. L.; Figg, C. A.; Sumerlin, B. S. Alternating Radical Ring-Opening Polymerization of Cyclic Ketene Acetals: Access to Tunable and Functional Polyester Copolymers. *Macromolecules* **2018**, *51* (14), 5079–5084.
- (235) Lutz, J.-F.; Ouchi, M.; Liu, D. R.; Sawamoto, M. Sequence-Controlled Polymers. *Science* (80-.). **2013**, *341* (6146), 1238149.
- (236) Baradel, N.; Shishkan, O.; Srichan, S.; Lutz, J.-F. Synthesis of Sequence-Controlled Copolymers Using Time-Regulated Additions of N-Substituted Maleimides in Styrenic Radical Polymerizations. In *Sequence-Controlled Polymers: Synthesis, Self-Assembly, and Properties*; ACS Symposium Series; American Chemical Society, 2014; Vol. 1170, pp 119-131 SE – 8.
- (237) Ouchi, M.; Badi, N.; Lutz, J. F.; Sawamoto, M. Single-Chain Technology Using Discrete Synthetic Macromolecules. *Nat. Chem.* **2011**, *3* (12), 917–924.
- (238) Badi, N.; Lutz, J.-F. Sequence Control in Polymer Synthesis. *Chem. Soc. Rev.* **2009**,

38 (12), 3383–3390.

- (239) Huang, J.; Turner, S. R. Recent Advances in Alternating Copolymers: The Synthesis, Modification, and Applications of Precision Polymers. *Polymer (Guildf)*. **2017**, *116*, 572–586.
- (240) Satoh, K.; Matsuda, M.; Nagai, K.; Kamigaito, M. AAB-Sequence Living Radical Chain Copolymerization of Naturally Occurring Limonene with Maleimide: An End-to-End Sequence-Regulated Copolymer. *J. Am. Chem. Soc.* **2010**, *132* (29), 10003–10005.
- (241) Matsuda, M.; Satoh, K.; Kamigaito, M. Periodically Functionalized and Grafted Copolymers via 1:2-Sequence- Regulated Radical Copolymerization of Naturally Occurring Functional Limonene and Maleimide Derivatives. *Macromolecules* **2013**, *46* (14), 5473–5482.
- (242) Soejima, T.; Satoh, K.; Kamigaito, M. Main-Chain and Side-Chain Sequence-Regulated Vinyl Copolymers by Iterative Atom Transfer Radical Additions and 1:1 or 2:1 Alternating Radical Copolymerization. *J. Am. Chem. Soc.* **2016**, *138* (3), 944–954.
- (243) Spick, M. P.; Bingham, N. M.; Li, Y.; De Jesus, J.; Costa, C.; Bailey, M. J.; Roth, P. J. Fully Degradable Thioester-Functional Homo- And Alternating Copolymers Prepared through Thiocarbonyl Addition-Ring-Opening RAFT Radical Polymerization. *Macromolecules* **2020**, *53* (2), 539–547.
- (244) Johnston, K.; Padias, A. B.; Bates, R. B.; Hall, H. K. Cycloadditions of Ketene

- Diethyl Acetal and 2-Methylene-1,3-Dioxepane to Electrophilic Alkenes. *Langmuir* **2003**, *19* (16), 6416–6421.
- (245) Yamamoto, S. I.; Sanda, F.; Endo, T. Cationic Polymerization of Cyclic Ketene Acetals via Zwitterion Formation with Cyanoallene. *J. Polym. Sci. Part A Polym. Chem.* **2000**, *38* (11), 2075–2081.
- (246) Agarwal, S.; Kumar, R. Synthesis of High-Molecular-Weight Tulipalin-A-Based Polymers by Simple Mixing and Heating of Comonomers. *Macromol. Chem. Phys.* **2011**, *212* (6), 603–612.
- (247) Yokozawa, T.; Takagi, J.; Endo, T. A Novel Polymerization Process. Spontaneous Block Copolymerization of 2-Methylene-4-Phenyl-1,3-Dioxolane with β -Propiolactone through Zwitterionic Mechanism. *J. Polym. Sci. Part C Polym. Lett.* **1990**, *28* (9), 279–283.
- (248) Yokozawa, T.; Takagi, J.; Endo, T. Polymerization of Methyl Methacrylate with a Cyclic Ketene Acetal as Catalyst via Zwitterionic Mechanism. *Die Makromol. Chemie, Rapid Commun.* **1991**, *12* (9), 553–557.
- (249) Hall, H. K.; Buyle Padias, A. Bond Forming Initiation of “Charge-Transfer” Polymerizations and the Accompanying Cycloadditions. *Acc. Chem. Res.* **1997**, *30* (8), 322–329.
- (250) Bailey, W. J.; Ni, Z.; Wu, S. R. Free Radical Ring-Opening Polymerization of 4,7-Dimethyl-2-Methylene-1,3-Dioxepane and 5,6-Benzo-2-Methylene-1,3-Dioxepane. *Macromolecules* **1982**, *15* (3), 711–714.

- (251) Gmbh, E. D.; Technologies, C. Synthesis of Amorphous Aliphatic Polyester-Ether Homo- and Copolymers by Radical Polymerization of Ketene Acetals. *Polymer (Guildf)*. **2010**, *48*, 1973–1978.
- (252) Hiracuri, Y.; Tokiwa, Y. Synthesis of Copolymers Composed of 2-methylene-1,3,6-trioxocane and Vinyl Monomers and Their Enzymatic Degradation. *J. Polym. Sci. Part A Polym. Chem.* **1993**, *31* (12), 3159–3163.
- (253) Galanti, M. C.; Galanti, A. V. Kinetic Study of the Isomerization of Itaconic Anhydride to Citraconic Anhydride. *J. Org. Chem.* **1982**, *47* (8), 1572–1574.
- (254) Modzelewska-Banachiewicz, B.; Paprocka, R.; Mazur, L.; Saczewski, J.; Kutkowska, J.; Stepień, D. K.; Cyrański, M. Experimental and Theoretical Study on the Reaction of N3-Phenyl- (Pyridin-2-Yl)Carbohydrazonamide with Itaconic Anhydride. *J. Mol. Struct.* **2012**, *1022*, 211–219.
- (255) Galanti, A. V.; Keen, B. T.; Pater, R. H.; Scola, D. Mechanism of Amine Catalyzed Isomerization of Itaconic Anhydride To Citraconic Anhydride: Citraconamic Acid Formation. *J. Polym. Sci. A1*. **1981**, *19* (9), 2243–2253.
- (256) Ramakrishna, S.; Fujihara, K.; Teo, W.-E.; Yong, T.; Ma, Z.; Ramaseshan, R. Electrospun Nanofibers: Solving Global Issues. *Mater. Today* **2006**, *9* (3), 40–50.
- (257) Mirjalili, M.; Zohoori, S. Review for Application of Electrospinning and Electrospun Nanofibers Technology in Textile Industry. *J. Nanostructure Chem.* **2016**, *6* (3), 207–213.

- (258) Mingjun, C.; Youchen, Z.; Haoyi, L.; Xiangnan, L.; Yumei, D.; Bubakir, M. M.; Weimin, Y. An Example of Industrialization of Melt Electrospinning: Polymer Melt Differential Electrospinning. *Adv. Ind. Eng. Polym. Res.* **2019**, *2* (3), 110–115.
- (259) Persano, L.; Camposeo, A.; Tekmen, C.; Pisignano, D. Industrial Upscaling of Electrospinning and Applications of Polymer Nanofibers: A Review. *Macromol. Mater. Eng.* **2013**, *298* (5), 504–520.
- (260) De Gennes, P. G. Dynamics of Entangled Polymer Solutions. I. The Rouse Model. *Macromolecules* **1976**, *9* (4), 587–593.
- (261) Meng, X.; Du, Y.; Liu, Y.; Coughlin, E. B.; Perry, S. L.; Schiffman, J. D. Electrospinning Fibers from Oligomeric Complex Coacervates: No Chain Entanglements Needed. *Macromolecules* **2021**, *54*, 5033–5042.
- (262) Rosi, N. L.; Mirkin, C. A. Nanostructures in Biodiagnostics. *Chem. Rev.* **2005**, *105* (4), 1547–1562.
- (263) Murphy, C. J.; Sau, T. K.; Gole, A. M.; Orendorff, C. J.; Gao, J.; Gou, L.; Hunyadi, S. E.; Li, T. Anisotropic Metal Nanoparticles: Synthesis, Assembly, and Optical Applications. *J. Phys. Chem. B* **2005**, *109* (29), 13857–13870.
- (264) Kamat, P. V. Photophysical, Photochemical and Photocatalytic Aspects of Metal Nanoparticles. *J. Phys. Chem. B* **2002**, *106* (32), 7729–7744.
- (265) Buggy, N. C.; Du, Y.; Kuo, M. C.; Gasvoda, R. J.; Seifert, S.; Agarwal, S.; Coughlin, E. B.; Herring, A. M. Investigating Silver Nanoparticle Interactions with Quaternary

Ammonium Functionalized Triblock Copolymers and Their Effect on Midblock Crystallinity. *ACS Appl. Polym. Mater.* **2020**, 2 (11), 4914–4923.

- (266) Pesenti, T.; Nicolas, J. 100th Anniversary of Macromolecular Science Viewpoint: Degradable Polymers from Radical Ring-Opening Polymerization: Latest Advances, New Directions, and Ongoing Challenges. *ACS Macro Lett.* **2020**, 9 (12), 1812–1835.
- (267) Schulze, T.; Klemm, E. Investigations on Free Radical Polymerization of Phenyl-substituted 2-methylene-1,3-dioxanes. *Die Angew. Makromol. Chemie* **1995**, 229 (1), 123–132.
- (268) Bailey, W.; Wu, S.-R.; Ni, Z. Synthesis and Free Radical Ring-opening Polymerization of 2-methylene-4-phenyl-1,3-dioxolane. *Die Makromol. Chemie* **1982**, 183 (8), 1913–1920.
- (269) Petasis, N. A.; Lu, S.-P. Methylenations of Heteroatom-Substituted Carbonyls with Dimethyl Titanocene. *Tetrahedron Lett.* **1995**, 36 (14), 2393–2396.
- (270) Ho, H. T.; Montembault, V.; Rollet, M.; Aboudou, S.; Mabrouk, K.; Pascual, S.; Fontaine, L.; Gigmes, D.; Phan, T. N. T. Radical Ring-Opening Polymerization of Novel Azlactone-Functionalized Vinyl Cyclopropanes. *Polym. Chem.* **2020**, 11 (24), 4013–4021.
- (271) Folini, J.; Huang, C.-H.; Anderson, J. C.; Meier, W. P.; Gaitzsch, J. Novel Monomers in Radical Ring-Opening Polymerisation for Biodegradable and PH Responsive Nanoparticles. *Polym. Chem* **2019**, 10, 5285.

- (272) McElvain, S. M.; Aldridge, C. L. Ketene Acetals. XXXI. Dimethylketene Ethyleneacetal. *J. Am. Chem. Soc.* **1953**, *75* (16), 3993–3996.
- (273) McElvain, S. M.; Nelson, J. W. The Preparation of Orthoesters. *J. Am. Chem. Soc.* **1942**, *64* (8), 1825–1827.
- (274) Argade, A. B.; Joglekar, B. R. A Short and Simple Synthesis of Ketene Acetals. *Synth. Commun.* **1993**, *23* (14), 1979–1984.
- (275) Gaitzsch, J.; Welsch, P. C.; Folini, J.; Schoenenberger, C.-A.; Anderson, J. C.; Meier, W. P. Revisiting Monomer Synthesis and Radical Ring Opening Polymerization of Dimethylated MDO towards Biodegradable Nanoparticles for Enzymes. *Eur. Polym. J.* **2018**, *101*, 113–119.